

# Modeling mammalian metabolism using novel stable isotopic techniques

By

Mohsin Rahim

Dissertation

Submitted to the Faculty of the  
Graduate School of Vanderbilt University  
in partial fulfillment of the requirements  
for the degree of

DOCTOR OF PHILOSOPHY

in

Chemical and Biomolecular Engineering

August 31, 2021

Nashville, Tennessee

Approved:

Jamey D. Young, Ph.D.

John T. Wilson, Ph.D.

Ethan S. Lippmann, Ph.D.

Richard M. O'Brien, Ph.D.

*To my mother, for all the sacrifices she made to get me here.*

## ACKNOWLEDGEMENTS

My last six years at Vanderbilt have allowed me to grow as a scientist and a person, and I owe this success to the support of many people. First and foremost, I would like to thank my advisor, Jamey Young, for his incredible mentorship, support, and encouragement in helping me develop as a scientist. I came into his lab with basic biology skills and almost no laboratory experience. Over these six years, he has challenged me to think critically and encouraged me to venture outside of my comfort zone, learning more about not only mathematical modeling but also mammalian physiology. I am also truly grateful for his financial support, for having my back, and for his colossal patience as I struggled during my six months to obtain a simple linear calibration curve. Additionally, I would like to thank my undergraduate mentors and professors, Farzan Aminian, Joshua Schwartz, and Wilson Terrell; thank you for nurturing my scientific curiosity and for encouraging me to apply to graduate school. I am also thankful for the guidance of my dissertation committee members: Richard O'Brien, John Wilson and Ethan Lippmann. My first project involved significant collaboration with Richard and Karin Bosma at the O'Brien lab, and I am very grateful for their patience and support as I learned so much while working on that specific project.

The Young lab will forever have a special place in my heart for me, thanks to all its brilliant members that I got to interact with, learn from and had the pleasure of teaching. It really has been incredible working and hanging out with lab mates such as Sarah Sacco, Ian Cheah, Piyoosh Babele, Bo Wang, Baltazar Zuniga, Javier Gomez, Rachel Moen, and Tomasz Bednarski; from summer outings to relay races, it really has been quite the ride. I am grateful for Irina Trenary for all her help and patience over the years as she taught me how to pipette, perform cell culture, and most importantly, for keeping the lab always stocked up, even during a pandemic. I would also like to thank my good friend, Amy Zheng for always lending an ear and

for discussing all things flux analysis and for sharing spicy Vanderbilt gossip. It gives me great comfort and ease that I am leaving my projects in the hands of a very competent and inquisitive scientist and friend, Deveena Banerjee; given her work ethic, she is destined for great things. And finally, a special thank you to my great friend and mentor Clinton Hasenour. I think it would be an understatement to say that he shaped my graduate school experience, scientifically and socially. The projects that he set up are the backbone of this dissertation and will continue to shape the physiology side of the Young Lab.

My experience at Vanderbilt would not have been the same without some of the lifelong friends that I have made here. Jonah Rosch, I think had we not become friends in our first year of grad school, I doubt I would have stayed in the program for longer than a year. Our friendship and time together completely changed my graduate school experience, thank you for always being there. Kyle Garland, Allison Bosworth, Katie Ozgun, Ella Hoogenboezem, Richard Darcy, Dushyant Barpaga, Michael Marin, and to all my friends who I did not mention here, your friendship really made living in Nashville and surviving through graduate school an incredible experience and I could not have asked for better friends. Also, I am blessed to have two very caring college friends, Hinna Hassan and Kevin Gaughan; thank you for all your encouragement and motivation during college and graduate school. Last and most importantly, I would like to thank my very special friend, Prarthana Patil. Her unwavering love and support encouraged me to become a better scientist and a better person; I truly could not have done this PhD without her by my side.

I am incredibly grateful to have a very loving and caring family. I am truly thankful for my host parents, Barbara and John Greene, without their help and support I never would have even made it through college, let alone apply to graduate school. My siblings, Ahsan Rahim and Anum Rahim, thank you for your moral support, pep talks and de-stressing family vacations. Finally, and most of all, I would like to thank my parents for affording me the opportunities that they themselves did not get. Thank you for all your sacrifices and patience. I am eternally grateful for my mother's love and constant support, for her sacrifices and for praying for me at every step of the way.

## TABLE OF CONTENTS

DEDICATION .....	ii
ACKNOWLEDGEMENTS .....	iii
LIST OF TABLES .....	x
LIST OF FIGURES .....	xi
LIST OF ABBREVIATIONS .....	xv
1. INTRODUCTION .....	1
2. BACKGROUND AND LITERATURE REVIEW .....	7
2.1 Mammalian Metabolism .....	7
2.2 Metabolic Flux Analysis .....	8
2.2.1 Experimental Design Considerations for MFA .....	8
2.2.2 Isotomer measurement techniques .....	10
2.2.3 Data modeling and analysis of isotope labeling experiments .....	13
2.3 Applications of Metabolic Flux Analysis in physiology .....	15
2.3.1 Liver Metabolism .....	16
2.3.2 Pancreatic Metabolism .....	18
2.3.3 Cardiac and skeletal muscle metabolism .....	20
2.3.4 Multi-tissue metabolic flux analysis .....	21
2.4 Conclusions .....	21
3. G6PC2 negatively regulates glucose oxidation and insulin secretion in $\beta$ -cells .....	23
3.1 Abstract .....	23
3.2 Introduction .....	24
3.3 Methods .....	26
3.3.1 Cell culture .....	26
3.3.2 Generation of G6pc2 knockout (KO) and control $\beta$ TC3 cells .....	26
3.3.3 Isotope labelling studies .....	28
3.3.4 Extraction of metabolites and GC-MS analyses .....	28
3.3.5 Extracellular uptake and excretion rates .....	29
3.3.6 $^{13}\text{C}$ Metabolic flux analysis .....	29
3.3.7 Intracellular and media insulin quantification .....	30
3.3.8 Intracellular metabolite quantification and assessment of redox markers .....	30
3.3.9 Glucose cycling .....	31
3.3.10 Measurement of cytoplasmic calcium .....	32
3.3.11 Gene expression analysis .....	32

3.3.12 Statistical analyses .....	32
3.4 Results.....	33
3.4.1 $\beta$ TC3 cell line is a representative in vitro model to study the effects of G6pc2 on $\beta$ -cell metabolism.....	33
3.4.2 Generation and validation of $\beta$ TC3 G6pc2 knockout cells.....	34
3.4.3 Assessment of metabolic fluxes reveals increased oxidative metabolism due to loss of G6PC2 .....	38
3.4.4 Knockout of <i>G6pc2</i> promotes a reduced cytosolic redox potential in $\beta$ TC3 cells.....	41
3.5 Discussion .....	44
3.6 Acknowledgements.....	50
3.7 APPENDIX: Supplemental figures and tables.....	51
4. <i>In vivo</i> Estimates of Liver Metabolic Fluxes Assessed by $^{13}\text{C}$ -Propionate and $^{13}\text{C}$ -Lactate are Impacted by Tracer Recycling and Equilibrium Assumptions .....	63
4.1 Abstract.....	63
4.2 Introduction.....	64
Figure 4.1: Metabolic flux analysis (MFA) determines fluxes through model-based regression of isotope labeling measurements.....	66
4.3 Methods.....	67
4.3.1 <i>In vivo</i> Procedures in the Mouse.....	67
4.3.2 Metabolite Extraction, Derivatization, and GC-MS .....	67
4.3.3 Metabolic Flux Analysis (MFA).....	68
4.3.4 Correction of Liver Oxaloacetate Isotopomers to Account for $^{13}\text{CO}_2$ Recycling .....	69
4.3.5. Calculation of Percent Equilibration in the 4C reactions of the CAC .....	70
4.3.6. Quantification and Statistical Analysis.....	71
4.4 Results.....	71
4.4.1 Secondary Tracer Effects Influence Estimates of Liver Pyruvate Cycling.....	71
4.4.2 Incongruent Hepatic Flux Estimates are Obtained with Base Models of $^{13}\text{C}_3\text{Lac}/^2\text{H}$ and $^{13}\text{C}_3\text{Prop}/^2\text{H}$ Tracers .....	72
4.4.3 $^{13}\text{C}_3\text{Lac}$ Infusion without $^2\text{H}$ Tracers Enables Rigorous Testing of Base Model Assumptions. 72	
4.4.4 Model Expansion to Account for Extrahepatic Metabolism Significantly Alters Pyruvate Cycle and CAC Fluxes.....	76
4.4.5 Expanded Two-Compartment Models Provide Consistent Hepatic Flux Estimates Using $^{13}\text{C}_3\text{Prop}/^2\text{H}$ and $^{13}\text{C}_3\text{Lac}/^2\text{H}$ Tracers <i>In Vivo</i> .....	79
4.5 Discussion .....	82
4.6 Acknowledgements.....	86
4.7 Appendix: Supplemental figures and tables.....	87

5. Multi-tissue $^2\text{H}/^{13}\text{C}$ flux analysis reveals reciprocal upregulation of renal gluconeogenesis in hepatic PEPCK-C knockout mice .....	101
5.1 Abstract .....	101
5.2 Introduction.....	102
5.3 Methods.....	103
5.3.1 In vivo Procedures in the Mouse .....	103
5.3.2 Gene Expression Analysis .....	104
5.3.3 Western Blotting.....	105
5.3.4 Glucagon Measurement .....	105
5.3.5 Metabolite Extraction, Derivatization, and GC-MS .....	105
5.3.6 $^2\text{H}/^{13}\text{C}$ Metabolic Flux Analysis (MFA) .....	106
5.3.7 Statistical Analysis.....	107
5.3.8 Study approval .....	107
5.4 Results.....	108
5.4.1 Development of a novel liver-kidney multi-compartment model to quantify glucose-producing fluxes <i>in vivo</i> .....	108
5.4.2 Liver PEPCK-C KO mice exhibit significant renal gluconeogenesis compared to WT littermates .....	110
5.4.3 Results from the dual organ liver-kidney model are consistent with whole-body flux estimates and previous NMR-based $^2\text{H}/^{13}\text{C}$ studies.....	112
5.5 Discussion .....	116
5.6 Acknowledgements.....	121
5.7 Appendix: Supplemental figures and tables.....	123
6. Simultaneous <i>in vivo</i> multi-organ fluxomics in obese mice .....	134
6.1 Abstract .....	134
6.2 Introduction.....	135
6.3 Methods.....	137
6.3.1 Experimental model and subject details.....	137
6.3.2 <i>In vivo</i> procedures in the mouse.....	137
6.3.3 Metabolite extraction, derivatization, and GC-MS.....	138
6.3.4 Multi-tissue metabolic flux analysis (MFA).....	139
6.3.5 Multi-omics analysis.....	140
6.3.6 Gene expression analysis .....	141
6.3.7 Quantification of tissue and plasma metabolites and assessment of redox markers.....	141
6.3.8 Liver histology, plasma analyses and body composition measurements.....	142
6.3.9 Statistical Analysis.....	142

6.4 Results.....	144
6.4.1 Simultaneous flux assessment of hepatic, cardiac and skeletal muscle reveals organ-specific metabolic signatures of obesity.....	144
6.4.2 Genetic, metabolite and redox changes during the hepatic response to increasing steatosis and fibrosis .....	146
6.4.3 Myocardial oxidative glucose metabolism is elevated despite an upregulation in fatty acid oxidation .....	149
6.4.4 Reduced skeletal muscle mitochondrial fluxes are associated with dysregulation of multiple metabolic pathways.....	151
6.4.5 Multi-omics analysis reveals tissue specific biomarkers for obesity .....	153
6.5 Discussion .....	156
6.5.1 Limitations of the study .....	161
6.6 Acknowledgements.....	162
6.7 Appendix: Supplemental figures and tables.....	163
7. INCA 2.0: a tool for integrated, dynamic modeling of NMR- and MS-based isotopomer measurements and rigorous metabolic flux analysis .....	176
7.1 Abstract.....	176
7.2 Introduction.....	177
7.3 Methods.....	179
7.3.1 Animals Care .....	179
7.3.2 Heart perfusions and metabolite extractions.....	179
7.3.3 NMR and GC-MS analysis of plasma glucose .....	180
7.3.4 NMR analysis of cardiac tissue extracts .....	181
7.3.5 Tracer simulation and flux estimation using tcaSIM/tcaCALC.....	181
7.3.8 EMU modeling of NMR isotopomers in INCA.....	182
7.3.7 Metabolic flux analysis (MFA).....	183
7.4 Results.....	184
7.4.1 INCA 2.0 tracer simulations predict <sup>13</sup> C NMR isotopomer ratios consistent with tcaSIM .....	184
7.4.2 Regression of <sup>13</sup> C NMR isotopomer ratios in INCA 2.0 estimates cardiac fluxes consistent with tcaCALC .....	185
7.4.3 Flux estimation using dynamic <sup>13</sup> C NMR datasets improves cardiac flux precision.....	188
7.4.4 Integration of MS and NMR datasets improves precision of in vivo hepatic flux estimates... ..	190
7.5 Discussion .....	193
7.6 Acknowledgements.....	196
7.7 Appendix: Supplemental figures and tables.....	197
8. CONCLUSIONS AND FUTURE WORK .....	210



8.1 Conclusions.....	210
8.2 Recommendations for future work.....	212
LIST OF REFERENCES .....	218
APPENDIX OF DETAILED PROTOCOLS.....	239
Metabolite extraction from plasma .....	239
Metabolite extraction from frozen tissues.....	240
RNA and protein extraction from cells .....	241
Di-O-isopropylidene propionate derivatization of glucose.....	244
MOX-TBDMS derivatization of metabolite extracts.....	246
Designing TIDE primers and performing TIDE analysis to quantify efficiency for CRISPR/Cas9 knockout.....	247

## LIST OF TABLES

### CHAPTER 3

Table 3A.1: Pancreatic $\beta$ -cell metabolic reaction network for $^{13}\text{C}$ MFA. (Related to Fig. 3.4-3.6 and Table 3A.2) .....	60
Table 3A.2: GC-MS fragment ions of measured metabolites regressed using the metabolic model for MFA. (Related to Fig. 3.4-3.6, S3, 3A.5-3A.7 and Table 3A.1) .....	62

### CHAPTER 4

Table 4A.1: Base reaction network for $^2\text{H}/^{13}\text{C}$ MFA. Related to Figures 4.2D, 4.2E and 4A.1 .....	94
Table 4A.2: Comparison of selected flux estimates between base and expanded models of $^{13}\text{C}/^2\text{H}$ studies. Related to Figures 4.2 and 4.5, 4A.1 and 4A.7. ....	95
Table 4A.3: Expanded reaction network for $^{13}\text{C}$ MFA. Related to Figures 4.4, 4A.4 and 4A.6. ....	97
Table 4A.4: Expanded reaction network for $^2\text{H}/^{13}\text{C}$ MFA. Related to Figures 4.5 and 4A.7. ....	99
Table 4A.5: Measured GC-MS fragment ions. Related to all Figures. ....	100

### CHAPTER 5

Table 5A.1: Dual organ metabolic reaction network for $^2\text{H}/^{13}\text{C}$ MFA. ....	128
Table 5A.2: GC-MS fragment ions of measured metabolites regressed using the metabolic model for MFA. ....	130
Table 5A.3: Metabolic fluxes in the liver and kidneys of WT and KO mice (Related to Fig. 5.3) .....	131

### CHAPTER 6

Table 6A.1: Multi-organ metabolic reaction network for $^{13}\text{C}$ MFA. ....	172
Table 6A.2: GC-MS fragment ions of measured metabolites regressed using the multi-tissue metabolic model. ....	175

### CHAPTER 7

Table 7A.1: Metabolic parameters used to simulate cardiac metabolism in tcaSIM. All relative fluxes are normalized to citrate synthase (=1). ....	206
Table 7A.2: Cardiac metabolic reaction network constructed in INCA 2.0 for comparison against tcaSIM and tcaCALC. ....	207
Table 7A.3: Isotopomers simulated by tcaSIM and INCA 2.0. ....	208
Table 7A.4: Pool sizes of glycolytic and citric acid cycle metabolites in the heart used for dynamic simulations .....	209

# LIST OF FIGURES

## CHAPTER 1

Figure 1.1: Metabolic model expansion helps reduce isotope-specific differences.....	4
Figure 1.2: Simultaneous assessment of metabolic fluxes in PEPCK-C knockout mice shows reciprocity between the liver and kidneys in maintaining euglycemia. ....	5

## CHAPTER 3

Figure 3.1: Validation of $\beta$ TC3 cell line as a representative model to study metabolic regulation by <i>G6pc2</i> .....	34
Figure 3.2: Generation of $\beta$ TC3 <i>G6pc2</i> knockout and control cell lines using CRISPR-Cas9 .....	35
Figure 3.3: Knockout of <i>G6pc2</i> in $\beta$ TC3 cells leads to increased GSIS.....	36
Figure 3.4: MFA in $\beta$ TC3 <i>G6pc2</i> WT and KO cells shows increased absolute flux through glycolytic and mitochondrial pathways .....	37
Figure 3.5: Metabolic fluxes relative to net glucose uptake reveal flux rerouting through NADPH producing reactions .....	39
Figure 3.6: Knockout of <i>G6pc2</i> promotes a reduced redox potential in $\beta$ TC3 cells.....	43
Figure 3.7: Schematic illustrating the effect of <i>G6pc2</i> KO on oxidative metabolism, energetics, and insulin secretion of $\beta$ TC3 cells .....	45
Figure 3A.1 Measurement of glucose uptake and release fluxes in INS-1 832/13 rat insulinoma cells.....	51
Figure 3A.2: Cycled abundance in two biological replicates of <i>G6pc2</i> WT and KO $\beta$ TC3 single cell clones at 5 and 11 mM glucose concentrations.....	52
Figure 3A.3: Atom percentage enrichment (APE) in metabolites over time to determine isotopic steady state in isotope labelling experiments .....	53
Figure 3A.4: Extracellular uptake and excretion rates in <i>G6pc2</i> WT and KO $\beta$ TC3 cells.....	54
Figure 3A.5 :Enrichment of glycolytic metabolites in <i>G6pc2</i> WT and KO $\beta$ TC3 cells labeled with [1,2- <sup>13</sup> C <sub>2</sub> ]glucose .....	55
Figure 3A.6: Enrichment of CAC metabolites in <i>G6pc2</i> WT and KO $\beta$ TC3 cells labeled with 2 mM [U- <sup>13</sup> C <sub>5</sub> ]glutamine.....	56
Figure 3A.7: Metabolic fluxes relative to net glucose uptake in <i>G6pc2</i> WT and KO $\beta$ TC3 cells.....	57
Figure 3A.8:Intracellular metabolite abundance in <i>G6pc2</i> WT and KO $\beta$ TC3 cells labeled with 2 mM [U- <sup>13</sup> C <sub>5</sub> ]glutamine.....	58
Figure 3A.9: Enrichment patterns in glycolytic metabolites after incubation with 2 mM [U- <sup>13</sup> C <sub>5</sub> ]glutamine .....	59

## CHAPTER 4

Figure 4.1: Metabolic flux analysis (MFA) determines fluxes through model-based regression of isotope labeling measurements.....	66
--	----

Figure 4.2: Base model shows evidence of secondary tracer effects and provides different estimates of hepatic fluxes for $^{13}\text{C}_3\text{Lac}/^2\text{H}$ and $^{13}\text{C}_3\text{Prop}/^2\text{H}$ tracers .....	73
Figure 4.3: Testing the assumptions of secondary tracer effects and fumarate/oxaloacetate equilibration in $^{13}\text{C}_3\text{Lac}$ infusion study .....	74
Figure 4.4: Expansion of base model in mice infused with $^{13}\text{C}_3\text{Lac}$ only.....	78
Figure 4.5: Comparison of $^{13}\text{C}_3\text{Lac}/^2\text{H}$ and $^{13}\text{C}_3\text{Prop}/^2\text{H}$ isotopes for hepatic flux estimation using expanded models of metabolism.....	81
Figure 4A.1: Regression of base model to specific measurement sets. Related to Figures 4.2, 4A.2, and Table 4A.1.....	87
Figure 4A.2: Confidence interval widths in dual tracer models. Related to Figures 4.2 and 4.5 .....	88
Figure 4A.3: Mass isotopomer measurements for plasma and liver metabolites. Related to Figures 3, 4, S4, S5, S6, and Tables S3 and S5. ....	89
Figure 4A.4: Expansion of models in mice infused with $^{13}\text{C}_3\text{Lac}$ . Related to Figures 4, S3, S5 and Tables S3 and S5 .....	90
Figure 4A.5: Confidence interval widths in $^{13}\text{C}_3\text{Lac}$ studies. Related to Figures 4.4, 4A.4 and 4A.6.....	91
Figure 4A. 6: Testing the assumption of low $V_{\text{PDHL}}$ flux during fasting with $^{13}\text{C}_3\text{Lac}$ . Related to Figure 4.4B, 4A.3, 4A.5, and Tables 4A.3 and 4A.5 .....	92
Figure 4A.7: Comparison of $^{13}\text{C}_3\text{Lac}/^2\text{H}$ and $^{13}\text{C}_3\text{Prop}/^2\text{H}$ isotopes for hepatic flux estimates using expanded models of metabolism. Related to Figures 4.5, 4A.2, and Tables 4A.2 and 4A.4 .....	93

## CHAPTER 5

Figure 5.1. Mass isotopomer distributions (MIDs) of liver, kidney, and plasma metabolites.....	109
Figure 5.2. Liver-kidney multi-compartment model enables quantification of tissue-specific fluxes using $^2\text{H}/^{13}\text{C}$ metabolic flux analysis (MFA).....	111
Figure 5.3: Liver PEPCK-C KO mice exhibit significant renal gluconeogenesis compared to WT littermates.....	113
Figure 5.4: Comparison of flux estimates between the dual-organ model and a previously developed single-compartment model. ....	115
Figure 5.5: Metabolic pathways affected by knockout of hepatic PEPCK-C.....	116
Figure 5A.1: Measured and predicted fractional enrichments of liver metabolites for WT and KO mice. ....	123
Figure 5A.2: Measured and predicted fractional enrichments of kidney metabolites for WT and KO mice. ....	124
Figure 5A.3: Measured and predicted fractional enrichments of plasma glucose for WT and KO mice. ....	125
Figure 5A.4: Mean hepatic and renal fluxes with 95% confidence intervals represented as error bars. ...	126
Figure 5A.5: Protein expression of Pck1 (PEPCK-C) and Pck2 (PEPCK-M) in the liver and kidney.....	127

## CHAPTER 6

Figure 6.1: Hepatic, cardiac and skeletal muscle fluxes reveal organ specific metabolic signatures of obesity .....	143
---	-----

Figure 6.2: Genetic, metabolite and redox changes support increased hepatic flux measured in obesogenic mice.....	148
Figure 6.3: Myocardial oxidative glucose metabolism is elevated despite an upregulation in fatty acid oxidation under obesity.....	150
Figure 6.4: Obese mice have reduced mitochondrial flux in the skeletal muscle along with dysregulation of multiple metabolic pathways .....	152
Figure 6.5: Multi-omics analysis reveals tissue specific biomarkers for obesity.....	154
Figure 6A.1: Hyperphagic mice show phenotypic signatures of obesity along with impaired glucose metabolism.....	163
Figure 6A.2: Hepatic and skeletal muscle fluxes but not cardiac fluxes are affected by hyperphagia.....	164
Figure 6A.3: Changes in hepatic genes and metabolite due to obesity.....	165
Figure 6A.4: Significantly affected genes in the livers of obese mice.....	166
Figure 6A.5: Genetic and metabolite changes in the cardiac muscle of obese mice .....	167
Figure 6A.6: Genetic and metabolite changes in the gastrocnemius muscle of obese mice.....	168
Figure 6A.7: Genetic and metabolite changes in the vastus muscle of obese mice.....	169
Figure 6A.8: Supervised and unsupervised multivariate analysis confirms the robustness of tissue specific biomarkers identified using sPLS-DA analysis .....	170
Figure 6A.9: Multi-omics analysis reveals gastrocnemius specific biomarkers for obesity.....	171

## CHAPTER 7

Figure 7.1 Simulation of $^{13}\text{C}$ NMR isotopomer ratios using tcaSIM and INCA 2.0 .....	186
Figure 7.2: Regression of cardiac fluxes using glutamate isotopomers in tcaCALC and INCA 2.0 shows good agreement when fitting data from $[1,6-^{13}\text{C}_2]\text{glucose}$ and $[\text{U}-^{13}\text{C}]\text{LCFA}$ tracers.....	187
Figure 7.3: INST-MFA of dynamic $^{13}\text{C}$ NMR measurements provides more precise estimation of cardiac fluxes.....	189
Figure 7.4: Combining NMR and GC-MS measurements in INCA 2.0 improves precision of in vivo hepatic flux estimates .....	192
Figure 7A.1: Comparison of simulated NMR isotopomers using tcaSIM and INCA 2.0 .....	197
Figure 7A.2: Comparison of measured glutamate isotopomers against those predicted by tcaCALC and INCA 2.0.....	198
Figure 7A.3: Dynamic and steady-state $^{13}\text{C}$ NMR glutamate isotopomer ratios .....	199
Figure 7A.4: Dynamic and steady-state $^{13}\text{C}$ NMR aspartate isotopomer ratios.....	200
Figure 7A.5: Dynamic and steady-state NMR alanine Isotopomers.....	201
Figure 7A.6: Formation of glutamate, aspartate and alanine isotopomers over time in the heart when $[1-^{13}\text{C}]\text{acetate}$ is administered as a tracer. ....	202
Figure 7A.7: Formation of glutamate, aspartate and alanine isotopomers over time in the heart when $[2-^{13}\text{C}]\text{acetate}$ is administered as a tracer. ....	203
Figure 7A.8: Formation of glutamate, aspartate and alanine isotopomers over time in the heart when $[\text{U}-^{13}\text{C}_2]\text{acetate}$ is administered as a tracer. ....	204

Figure 7A.9: Estimation of cardiac fluxes using steady-state versus dynamic NMR isotopomer measurements.....205

CHAPTER 8

Figure 8.1: Metabolic effect of *G6pc2* KO in primary mice islets .....213  
Figure 8.2: Metabolic fluxes in the liver and kidneys of *MC4R<sup>-/-</sup>* KO mice.....217

## LIST OF ABBREVIATIONS

2PG	2-phosphoglycerate
3PG/3PGA	3-phosphoglycerate/3-phosphoglyceric acid
6PGDH	6-phosphogluconate dehydrogenase
$\alpha$ -KG	$\alpha$ -ketoglutarate
AcCoA	Acetyl CoA
Ala	Alanine
Asp	Aspartate
AV	Arteriovenous
BCAA	Branch chain amino acids
BPG	Bisphosphoglycerate
CAC	Citric Acid Cycle
CAM	Cardiovascular-associated mortality
Cit	Citrate
CO <sub>2</sub>	Carbon Dioxide
CS	Citrate synthase
D	Doublet
DHAP	Dihydroxyacetone phosphate
DiO	Di-isopropylidene propionate
E4P	Erythrose 4-phosphate
EMU	Elementary mass unit
Enol	Enolase
ER	Endoplasmic reticulum
ESI	Electron spray ionization
ETA	Extracellular Time-Course Analysis
F16BP	Fructose 1,6-bisphosphate
F6P	Fructose-6-phosphate
FACS	fluorescence activated cell sorting
FBG	Fasting blood glucose
FFA	Free fatty acid
FH	Fumarate Hydratase
FPI	Fasting plasma insulin
Fum	Fumarate
G3P	Glycerol-3-phosphate
G3PP	Glycerol-3-phosphate phosphatase
G6P	Glucose-6-phosphate
G6PC	Glucose-6-phosphatase catalytic subunit

G6PDH	Glucose-6-phosphate dehydrogenase
GAP	Glucose-6-phosphatase catalytic subunit
GC	Gas Chromatography
GCGR	Glucagon receptor
GK	Glucokinase
Gln	Glutamine
Glu	Glutamate
GRX1	Glutaredoxin
GSH	Glutathione
GSIS	Glucose stimulated insulin secretion
GSSG	Glutathione disulfide
GWAS	Genome-wide association studies
H&E	Hematoxylin and eosin
HTS	home-built superconducting
IDDM	Insulin dependent diabetes mellitus
IDH	Isocitrate dehydrogenase
IGRP	Islet-specific glucose-6-phosphatase catalytic subunit-related protein
ILE	Isotope labelling experiment
INCA	Isotopomer Network Compartmental Analysis
INST-MFA	isotopically nonstationary MFA
KO	Knockout
KRHB	Krebs-Ringer HEPES buffer
Lac	Lactate
LC	Liquid Chromatography
LDH	Lactate dehydrogenase
MAG	Monoacetone glucose
Mal	Malate
MC4R	Glycerol-4-Phosphate
MDH	Malate dehydrogenase
ME	Malic enzyme
MFA	Metabolic flux analysis
MID	mass isotopomer distribution
MIDA	Mass isotopomer distribution analysis
MMPC	Mouse Metabolic Phenotyping Center
Mox-TBDMS	Methyloxime tert-butyldimethylsilyl
MRS	Magnetic resonance spectroscopy
MS	Mass spectrometry
NADH	Reduced nicotinamide adenine dinucleotide
NADPH	Reduced nicotinamide adenine dinucleotide phosphate



NAFLD	Non-alcoholic fatty liver disease
NASH	Non-alcoholic steatohepatitis
NIDDM	Non-insulin dependent diabetes mellitus
NMR	Nuclear magnetic resonance
Oac	Oxaloacetate
PC	Pyruvate carboxylase
PCA	Perchloric acid
PCK/PEPCK	Glycerol-C-Phosphate
PDH	Pyruvate dehydrogenase
PEP	Phosphoenolpyruvate
PEPCK-C	Cytosolic phosphoenolpyruvate carboxykinase
PEPCK-M	Mitochondrial phosphoenolpyruvate carboxykinase
PINTA	Positional isotopomer NMR tracer analysis
PK	Pyruvate kinase
PPP	Pentose phosphate pathway
PSP	Phosphoserine phosphatase
PYGL	Liver glycogen Phosphorylase
PYGM	Muscle glycogen Phosphorylase
Pyr	Pyruvate
Q	Quartet
S7P	Sedoheptulose-7-phosphate
SCS	Succinyl coenzyme A synthetase
SEM	Standard error of the mean
SENPI	Sentrin/SUMO-specific protease 1
Ser	Serine
SERCA	sarco-endoplasmic reticulum calcium ATPase
sPLS-DA	Sparse partial least-squares discriminate analysis
SSR	Sum of squared residuals
Suc	Succinate
T2D	Glycerol-2-Phosphate
TCA	Tricarboxylic acid
TIDE	Tracking of Indels by DEcomposition
ToF	Time of flight
TPI	Triosephosphate isomerase
WD	Western diet
WT	Wild type

## 1. INTRODUCTION

The overall theme of this dissertation is the development of organ specific metabolic models and application of stable isotope based metabolic flux analysis (MFA) to uncover the molecular mechanisms and metabolic regulation in animal and human physiology. Over the past several decades, biochemists have been successful in describing the general network of reactions that comprise cell metabolism. While the basic architecture of central carbon metabolism is known, the regulation of these pathways in physiological and pathological conditions complicates identification of the enzymes most amenable to therapeutic intervention [1]. Despite advancement in molecular biology techniques, metabolism is often considered at the level of individual reactions where most studies examine changes in enzyme expression or relative changes in metabolite levels to interrogate metabolism [2], [3]. While this offers some insight into the metabolic phenotype of the system, metabolic flux is better characterized when the flow of multiple metabolites through metabolic networks is studied simultaneously [4]. The combination of these techniques with the use of isotope-labeled tracers enables quantification of dynamic pathway operation inside living cells and tissues using metabolic flux analysis [4], [5]. The majority of this dissertation focuses on constructing metabolic modeling strategies and applying MFA to characterize and understand the metabolic regulation in overnutritive states such as hyperglycemia and obesity. Furthermore, I provide examples on integrating measurements from two analytical platforms, mass spectrometry and nuclear magnetic resonance spectroscopy, in the flux analysis software tool INCA to assess cardiac and hepatic fluxes.

Worldwide obesity has tripled since 1975, and in 2016, 1.9 billion adults were overweight and 650 million obese. Among these obese individuals, more than 422 million had diabetes [6], [7]. Obesity is linked with non-alcoholic fatty liver disease (NAFLD) and is strongly associated with type 2 diabetes mellitus and cardiovascular diseases [8]–[10]. Despite important advances, there is a critical knowledge gap in accurately modelling the progression and regulation of these metabolic diseases in a physiologically relevant state. The research shown in this dissertation focuses on the development of novel metabolic flux

model and provides four physiological applications of these techniques. First, it provides an in-depth understanding of the metabolic effects of the G6pc2 enzyme and hyperglycemia on glucose oxidation and insulin secretion in  $\beta$ -cells. Second, it examines the impact of Cori cycling and secondary tracer effects on mathematically modeling hepatic and extrahepatic fluxes *in vivo*. Third, I provide a dual-organ metabolic model to simultaneously assess hepatic and renal fluxes. Lastly, the dual organ model is further expanded to understand the effects of increasing adiposity on the skeletal and cardiac muscle and their communication with the liver *in vivo*. The research shown here is significant because it provides novel metabolic models to understand glucose-stimulated insulin secretion, non-alcoholic fatty liver disease and cardiometabolic disorders; metabolic conditions that are signatures of type 2 diabetes, obesity and cardiovascular disease. Thus, the outcomes of this research will not only increase our fundamental understanding of the metabolic syndrome but will also have broad positive impact on the field of diabetes, obesity and cardiovascular disease.

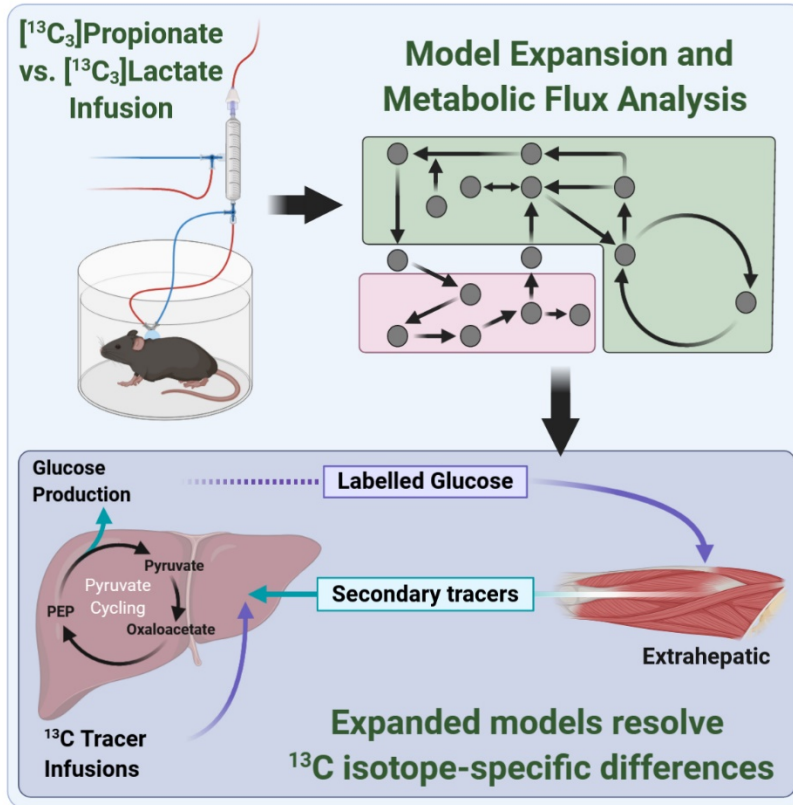
This dissertation is divided into the following chapters:

**Chapter 2** reviews previous studies that detail the development and advancements in experimental, analytical and computation tools that enable flux characterization. I then review the applications of these technologies in assessing hepatic, pancreatic, cardiac, and skeletal muscle metabolism.

**Chapter 3** assesses the metabolic effects of G6pc2 on glycolytic and mitochondrial fluxes under euglycemic and hyperglycemic conditions in pancreatic cell lines. CRISPR/Cas9 gene editing and metabolic flux analysis were used to study the metabolism of  $\beta$ TC3 cells, a murine pancreatic  $\beta$ -cell line, and examine the role of *G6pc2* in regulating glycolytic and mitochondrial fluxes. I found that deletion of *G6pc2* led to substantial elevations in net glucokinase and citrate synthase fluxes. Intracellular insulin content and GSIS were enhanced by up to  $\sim 2$  fold along with increased cytosolic redox potential and reductive carboxylation flux. Importantly, normalization of fluxes to the net glucose uptake rate showed

increased flux through a couple of NADPH producing pathways in the CAC, independent of elevated glycolytic flux. These results suggest that G6PC2 also regulates CAC pathways, separate from its modulation of glycolysis. These results demonstrate that *G6pc2* regulates GSIS by modulating not only glycolysis but also citric acid cycle (CAC) activity in  $\beta$ -cells.

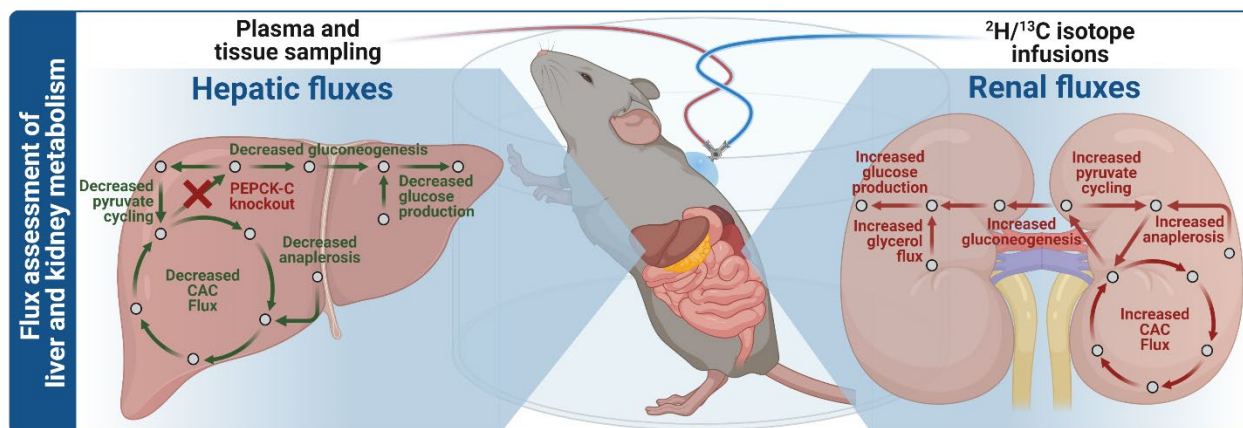
**Chapter 4** tests the validity of key assumptions used to model stable isotope labeling of liver metabolism *in vivo*. I examined an important controversy surrounding the estimates of liver CAC and gluconeogenesis fluxes using a flexible modeling platform that enables rigorous testing of standard assumptions. The results show that liver pyruvate cycling fluxes are incongruent between different  $^{13}\text{C}$  tracers in models with conventional assumptions. When models are expanded to include more labeling measurements and fewer constraining assumptions, however, liver pyruvate cycling is significant, and inconsistencies in hepatic flux estimates using [ $^{13}\text{C}_3$ ]lactate and [ $^{13}\text{C}_3$ ]propionate isotopes emanate, in part, from peripheral tracer recycling and incomplete isotope equilibration within the citric acid cycle (Fig. 1.1). Furthermore, this study paves the way for conducting *in vivo* isotope labeling studies and analyzing hepatic and extrahepatic contributions simultaneously.



**Figure 1.1: Metabolic model expansion helps reduce isotope-specific differences**

**Chapter 5** details the development and application of a novel stable isotope approach to simultaneously quantify hepatic and renal gluconeogenic and oxidative metabolic fluxes *in vivo*. Hepatic gluconeogenesis from phosphoenolpyruvate was disrupted via liver-specific knockout of cytosolic PEPCK (KO). Hepatic and renal fluxes were assessed by integrating the isotopic enrichment of plasma and tissue metabolites from mice infused with <sup>2</sup>H/<sup>13</sup>C isotopes in a multi-compartment metabolic model. Hepatic gluconeogenesis and glucose production were reduced in KO mice, yet whole-body glucose production and arterial glucose were unaffected. Glucose homeostasis was maintained by a compensatory rise in renal glucose production and gluconeogenesis. Renal oxidative metabolic fluxes of KO mice increased to sustain the energetic and metabolic demands of elevated gluconeogenesis (Fig 1.2). These results show the reciprocity of the liver and kidney in maintaining glucose homeostasis by regulating gluconeogenic flux through PEPCK-C. This

is the first study to simultaneously assess the metabolic fluxes in multiple organs from a single mouse *in vivo*.



**Figure 1.2: Simultaneous assessment of metabolic fluxes in PEPCK-C knockout mice shows reciprocity between the liver and kidneys in maintaining euglycemia.**

**Chapter 6** describes the development of an MFA-based approach to simultaneously quantify metabolic fluxes in the liver, heart, and skeletal muscle in a single mouse *in vivo*. This method was applied to several cohorts of mice to examine the nature of metabolic dysfunction in obese animals. Diet-induced obesity caused an increase in gluconeogenesis and endogenous glucose production from the liver and was accompanied by elevations in glycolytic and mitochondrial cardiac fluxes, whereas CAC activity in the skeletal muscle was significantly reduced. These results challenge the fuel selection hypothesis proposed by the Randle cycle. The metabolic model devised in this study will have significant applications in better characterizing non-communicable diseases, (patho)physiology, and drug metabolism.

**Chapter 7** demonstrates the ability of INCA 2.0, an updated version of our in-house MFA software package, to simulate and regress mass spectrometry (MS) and nuclear magnetic resonance (NMR) based isotopomer measurements to assess metabolic fluxes. Using physiologically relevant cardiac and hepatic metabolic models, I tested and validated the capabilities of INCA 2.0. The results show that INCA 2.0 can simulate and regress steady-state and dynamic NMR measurements to precisely estimate cardiac fluxes.

Furthermore, the combination of  $^{13}\text{C}$  NMR and MS datasets improved the precision of estimated fluxes. Overall, the ability to regress fluxes using both measurement modalities in the same mathematical model is expected to aid in the design of more sophisticated isotope labelling studies and allow for significant advancements in the fields of metabolic engineering, cell culture, and mammalian physiology.

**Chapter 8** concludes the dissertation with a summary of the main findings and presents ideas for the possible extension of these projects.

## 2. BACKGROUND AND LITERATURE REVIEW

Some sections are taken from *Current Opinion in Biotechnology* (2021). 71:1-8.

### 2.1 Mammalian Metabolism

In mammalian cells, energy metabolism can be divided into two types of pathways: catabolic pathways and anabolic pathways [11]. Catabolism involves metabolic processes that break down molecules to obtain energy and nutrients, whereas anabolism involves the synthesis of complex molecules for cell growth, repair, signaling, and storage of energy [12]. Some of the fundamental catabolic pathways are glycolysis, glycogenolysis, TCA cycle,  $\beta$ -oxidation and proteolysis where energy sources such as sugar, fatty acid and proteins are broken down to produce energy in the form of ATP or reduced NAD(P)H co-factors. Anabolic pathways such as gluconeogenesis, glycogenesis, lipogenesis, and amino acid synthesis are activated to produce energy storage molecules such as glycogen and triglycerides when the body is in a state of positive energy balance [12]. However, even under negative energy balance, anabolic pathways are active in specific organs to generate fuels for other tissues. For example, under conditions of fasting or starvation, the liver synthesizes glucose and ketone bodies via anabolic processes such as gluconeogenesis and ketogenesis, to be consumed by the heart, brain, and muscle [13]. Therefore, mammalian metabolism involves constant crosstalk between organs and tissues that have varying fuel needs and consumption rates.

Although the fundamental metabolic currency remains the same across cell types, the metabolic requirements of cells are dictated by their tissue-specific functions and environment. For example, T-lymphocytes reprogram their metabolic pathways from reliance on  $\beta$ -oxidation and the CAC to using glycolytic, pentose phosphate, and glutaminolytic pathways to proliferate upon stimulation of an immune response [14]. In contrast, differentiated cardiomyocytes do not proliferate and rely more heavily on oxidative phosphorylation to produce ATP and fulfill their intensive energy demands [15]. In many cell types, metabolism varies over time and switches upon the energy needs of the cell. CHO cells for example



switch from lactate production to lactate consumption and upregulate their pentose pathway and CAC flux when secreting large amounts of recombinant antibody during the production phase of industrial bioprocesses [16]. Therefore, the physiology of each tissue requires different ratios of metabolic substrates and thus cannot be modelled using the same metabolic networks and constraints.

## **2.2 Metabolic Flux Analysis**

While biochemical analysis can be used to study enzyme expression and metabolite concentration, these measurements rely upon the assumption that functional outputs of metabolism are directly related to intermediate concentrations [2], [3]. Metabolic flux analysis circumvents these drawbacks and can be used to decipher the contribution of different pathways to supply metabolic demands for energy and molecular building blocks. To perform MFA, cells are fed an isotopically labeled substrate. Cell metabolism is then quenched and intracellular metabolites are extracted [17], [18]. NMR spectroscopy or MS approaches are then used to measure the incorporation of the labeled substrate atoms into downstream metabolites. The relative abundance of various labeling patterns in the metabolites depends directly on the relative fluxes in cellular metabolism [19]. Using computational methods, MFA combines intracellular labeling data with extracellular uptake and secretion fluxes to generate flux maps to describe changes in metabolism across different experimental conditions. Systemic flux maps therefore provide functional information on the dynamic metabolic state of cells and their response to various perturbations [20]. Several experimental, analytical, and computational considerations need to be taken into account prior to performing metabolic flux analysis in mammalian systems.

### **2.2.1 Experimental Design Considerations for MFA**

Proper selection of metabolic tracer(s) is critical for quantifying specific pathway activities, since it ultimately determines the quality (i.e., precision and accuracy) of flux results that can be obtained [21]. Single tracer experiments, while simpler to analyze and interpret, seldom provide sufficient information to

resolve fluxes through multiple overlapping pathways. Thus, the choice of isotopic tracer varies depending upon the pathway being investigated. Generally,  $^{13}\text{C}$  glucose tracers are best for determining fluxes in upper metabolism (e.g., glycolysis and PPP), while  $^{13}\text{C}$  glutamine tracers typically produce better resolution of fluxes in lower parts of metabolism (e.g., TCA cycle and reductive carboxylation) [22], [23]. Most  $^{13}\text{C}$  MFA models for *in vitro* studies include all major metabolic pathways of central carbon metabolism such as glycolysis, pentose phosphate pathway (PPP), TCA cycle, as well as any relevant reactions that connect these pathways [24]. To quantify these pathways *in vitro*, typically parallel labeling experiments with different tracers are performed and all the data are integrated into a single comprehensive flux model [16], [22]. For example, parallel labeling experiments with  $[1,2-^{13}\text{C}_2]\text{glucose}$  and  $[\text{U}-^{13}\text{C}_5]\text{glutamine}$  have proven to be particularly informative and complementary [16], [22]. When conducting parallel labeling experiments, it is important that the only difference between the experiments is the choice of labeled substrate, i.e., the concentrations of all nutrients in the media must be the same for all experiments [25]. In addition to quantifying intracellular metabolic fluxes, it is vital to also measure extracellular fluxes which represent the crosstalk between the cells and their environment. Typically, extracellular fluxes are measured by dividing the rate of change in metabolite concentration over time by the integrated viable cell count [26]. Specialized software packages such as ETA can aid in the calculation of these external rates [27]. After conducting labelling experiments, cells are extracted using organic solvents and metabolite pool sizes and isotopic enrichments are analyzed using analytical platforms such as a GC-MS.

Quantification of *in vivo* fluxes is much more challenging, mainly due to the requirement of sophisticated mathematical models and computational tools to deconvolute the complicated enrichment patterns that emerge as a result of multiple simultaneous tracers. Additionally, assessment of extracellular exchange rates and determination of the contributions from different cell/tissue types from *in vivo* studies remains a major challenge. In the past, due to a lack of computational techniques, initial *in vivo* metabolic studies used a single tracer to accurately delineate a particular flux, however, this approach was rather inefficient and

provided minimal information [28]. By leveraging advancements in the field of optimal experiment design [24], modern *in vivo* MFA studies typically infuse a cocktail of different isotope tracers that have been tailored to the pathways of interest. Administration of multiple stable isotopes to rodents has enabled the concurrent assessment of glycolytic/gluconeogenic, TCA cycle, and anaplerotic fluxes in liver and cardiac tissue [29], [30], thus minimizing the number of animals required for comprehensive studies of *in vivo* metabolism. Similar approaches have been adapted to human subjects, where combined administration of  $^2\text{H}$  and  $^{13}\text{C}$  tracers has been used to quantify glucose turnover, hepatic TCA cycle activity and ketone turnover during starvation [31] or obesity [32]. However, the high cost, administrative burden, and minimally invasive sampling required for human subjects research have meanwhile prompted innovation and miniaturization of surgical procedures required for *in vivo* metabolic tracer studies in rodents. For example, implantation of dual arterial-venous catheters has enabled simultaneous tracer infusion and plasma sampling in conscious, unrestrained mice [33]. Such techniques are critically important for *in vivo* studies of metabolism, since physiological alterations caused by anesthesia or stress at the time of sample collection can lead to unacceptable variability that obscures the experimental effects under investigation.

### 2.2.2 Isotopomer measurement techniques

Metabolic flux analysis can help distinguish flux contributions from different metabolic pathways based on specific labeling patterns, detectable by MS or NMR spectroscopy methods. MS platforms such as GC-MS, LC-MS and tandem MS/MS systems have significantly higher sensitivity ( $\sim\text{pmol}$  to  $\text{nmol}$  range) and can precisely determine the total unenriched and enriched fractions of a metabolite pool [34]. However, MS-based systems do not directly provide positional enrichment information unless the metabolite is subjected to extensive chemical degradation or source/collision-induced fragmentation. Instead, MS systems output the relative abundance of chemical species that differ in the number of heavy atoms incorporated (i.e.,  $M+0$ ,  $M+1$ ,  $M+2$ , etc.), which can then be used to determine the mass isotopomer distribution (MID) of a given metabolite [35].

MS-based platforms can detect low-abundance metabolites with much higher sensitivity compared to NMR instruments and are thus becoming increasingly popular for *in vivo* flux characterization, especially for mouse studies and other situations where sample volumes are limited [29]. Mass spectrometry-based metabolite enrichment analysis gained traction in the early to mid-90s, when GC–MS based isotopomer analysis was used for quantification of metabolic fluxes in perfused rat livers and hearts by measuring the labeling patterns of different intermediary metabolites [35]–[37]. Due to its high sensitivity, MS based methods quickly gained popularity, with studies quantifying anaplerosis in rat hearts for pyruvate, lactate, succinate, citrate, fumarate, and malate [37]. Additionally, increased stability of metabolites with suitable derivatization methods enabled the quantification of compounds ranging from pmol to nmol within a particular sample [38]. However, due to limited instrument sensitivity to detect low isotope enrichments (<0.1%), mass spectrometry could only resolve isotopomer pools to a minor extent [39]. Due to a higher noise threshold, only unlabeled versus labeled fractions of lactate, alanine, glutamine, and glutamate were determined by Katz et al. [40].

Recently, gas chromatography-mass spectrometry (GC-MS), widely used for measuring semi-volatile compounds such as fatty acids and organic acids, has experienced a renaissance due to improvements in sample derivatization techniques [41] and addition of tandem MS (MS/MS) [42] and time of flight (ToF) capabilities [43]. The advent of electrospray ionization (ESI) has concurrently revolutionized the use of liquid chromatography (LC)-MS and LC-MS/MS in biomedical applications, chiefly due to its versatility and limited sample preparation requirements [44], [45]. The ability of high-resolution MS to distinguish between  $^2\text{H}$ -labeled and  $^{13}\text{C}$ -labelled metabolites based on their mass defects allows contributions from multiple tracers to be directly quantified in the same sample [46]. Fragmentation of parent metabolites by MS/MS instruments can provide additional information about the position of labeled atoms in isotopically enriched metabolites [47]. Therefore, high-resolution MS/MS analysis combines some of the most attractive features of NMR—extensive positional labeling information and ability to distinguish different

isotopic nuclei—with the high sensitivity that is achievable by MS instruments. Such enhancements enable accurate measurement of metabolite abundance and isotope enrichment from plasma and tissues samples collected from *in vivo* tracer experiments [48], [49].

NMR spectroscopy has a different data output from GC- or LC-MS systems, one that provide distinct positional information pertaining to metabolite enrichment patterns. For example,  $^{13}\text{C}$  NMR provides two types of information: (i) relative signal intensity from different  $^{13}\text{C}$ -enriched carbon positions in a molecule and (ii) the relative intensity of the various multiplets within a resonance signal (due to interaction between adjacent  $^{13}\text{C}$  nuclei, also known as  $^{13}\text{C}$ - $^{13}\text{C}$  coupling) [50]. While  $^{13}\text{C}$  NMR does not specify the total amount of labeled and unlabeled fraction, other modalities such as  $^1\text{H}$ - $^{13}\text{C}$  NMR can be used to overcome this limitation and quantify the fractional enrichment of  $^{13}\text{C}$  atoms bound to hydrogen at specific molecular positions [51]. Together, this information can be used to determine the position-specific  $^{13}\text{C}$  labelling in a measured metabolite, even when the isotopic enrichment is as low as 0.1%. However,  $^{13}\text{C}$  NMR spectroscopy has two major limitations when applied to measure stable isotope enrichment. First, it does not directly determine the unenriched (i.e., M+0) fraction of the metabolite pool. Second, it has limited sensitivity to detect low-abundance metabolites, e.g., present at lower than  $\mu\text{mol}$  amounts [34]. This limitation typically restricts the application of  $^{13}\text{C}$  NMR to measurements of highly abundant intracellular metabolites, such as glutamate and aspartate.

Early attempts at isotopomer analysis relied on measurements of a small number of highly abundant metabolites (e.g., glucose, lactate, glutamine, alanine) using NMR spectroscopy [52]. Since then,  $^{13}\text{C}$  and  $^1\text{H}$  NMR have been widely applied for determination of isotope labeling patterns [53]–[57].  $^1\text{H}$ - $^{13}\text{C}$  COSY NMR spectroscopy enables the determination of isotopomers of a compound yielding maximal possible information. For example, this technique was used for isotopomer determination of amino acids from protein hydrolysates of *Escherichia coli* [58], [59]. More importantly, NMR's use in studying cardiac and hepatic fluxes gained significant traction in the early 90s. NMR based approaches were preferred for *in vivo*

isotopomer analysis because of their ability to assess position-specific isotope enrichments and directly distinguish  $^2\text{H}$  and  $^{13}\text{C}$  nuclei [50], [51], [60]–[64]. However, labeling patterns of intermediary metabolites usually occurring at low concentrations were difficult to obtain directly by NMR, which allowed mass spectrometry methods to gain popularity in the mid-2000s.

Recent advancements in NMR based techniques, however, have helped revitalize the technique by reducing sample size requirements and expanding measurements to include previously undetectable metabolites. An underappreciated aspect of NMR is its ability to accurately quantify low isotope enrichments (e.g., 0.1%) that are below the noise threshold of typical MS measurements [65]. This is a major advantage for some *in vivo* studies, especially in human subjects, where cost and safety constraints limit the total amount of tracer that can be administered. Overall, the two analytical platforms have extensively, yet independently, been used to collect isotopomer data and assess metabolic fluxes *in vitro* and *in vivo*.

### **2.2.3 Data modeling and analysis of isotope labeling experiments**

Isotope labelling experiments (ILEs) rely on the enzymatic rearrangement of substrate atoms in unique and predictable ways. Consequently, the enrichment patterns that emerge in downstream products after tracer administration encode detailed information about the activity of upstream metabolic pathways and their relative fluxes. Under certain conditions, it is possible to infer information about the pathway activity or metabolite turnover by qualitatively assessing the isotope enrichment data. However, due to the intricate rearrangement of substrate atoms through intersecting metabolic pathways, mathematical models are often necessary to determine metabolic fluxes from isotope labeling data. This is especially true when analyzing complex datasets involving multiple tracers [65], integrating measurements of numerous metabolites and their adducts [66] or derivatives [29], and accounting for the added complexity of reversible isotope exchange [67] and secondary tracer recycling [48] that inevitably occur during *in vivo* tracer studies. Under

these circumstances, intuitive inspection of the isotope labeling data can often lead to erroneous or incomplete conclusions.

Metabolic models used for MFA are specific to the system under investigation. Each reaction in the model is associated with an annotated enzyme or transport process, and atom rearrangements are assigned to each reaction based on its biochemical mechanism. This information is used to enumerate mass balances and isotopomer balances that describe the conservation of atoms within the metabolic network. In some cases, these balances can be distilled to closed-form equations that relate isotope enrichment measurements to pathway fluxes. While convenient to use, these simplified equations involve implicit assumptions and approximations that may not be appropriate or fully validated under the conditions of interest. An alternative approach uses least-squares regression to obtain a best-fit flux solution that provides optimal agreement between model-predicted and experimentally determined isotopomer measurements. The model parameters are iteratively adjusted, and the balance equations are repeatedly solved until the measurement residuals are minimized [68].

Quantification of fluxes using metabolic flux analysis involves solving a non-linear regression problem to obtain a set of metabolic fluxes that best reproduces the measured isotope labeling patterns and external rates. Over the last decade, many software tools have been developed for performing these  $^{13}\text{C}$ -MFA calculations, including INCA [69], Metran [70], OpenFLUX2 [71], OpenMebius [72], and WUFlux [73]. All of these software packages are based on the EMU framework [20], [74] and use various optimization strategies to find the optimal solution by minimizing the sum of squared residuals. After the estimation of fluxes, it is vital to ascertain that the goodness-of-fit is satisfactory by evaluating the magnitude of the sum-of-squared residuals (SSR) value [75]. If the model is adequate, and the experimental data contain only random measurement errors, the minimized SSR value is a stochastic variable described by a  $\chi^2$ -distribution. The number of degrees of freedom is equal to the number of independent measurements  $n$  minus the number of fitted parameters  $p$ . The acceptable range of SSR values is between  $\chi^2_{\alpha/2}(n-p)$  and  $\chi^2_{1-\alpha/2}(n-p)$ , where  $\alpha$

is a chosen threshold value, typically,  $\alpha = 0.05$  for 95% confidence. If the minimized SSR value is too high, i.e., there is significant disagreement between the measured data and the best-fit model predictions, then the flux solution must be rejected, and flux analysis assumptions must be re-assessed [26].

Model-based regression approaches account for the complexities of *in vivo* stable isotope experiments and can rigorously test assumptions used in the calculation of metabolic fluxes. The availability of flexible software tools for simulating metabolic tracer experiments [76], extracting isotopic enrichments from metabolomics datasets [77], and estimating fluxes from isotopomer measurements [69], [70], [78] now make sophisticated MFA workflows increasingly practicable. Comprehensive isotopomer modeling has the potential to reconcile apparently divergent results and identify flux estimates that are sensitive to methodological differences or, conversely, are robust to a variety of study designs and assumptions [48]. The large amount of isotopomer data obtainable from each sample results in a highly overdetermined flux solution that can be statistically assessed to detect errors in measurements or model formulation [79]. Furthermore, regression approaches can accommodate a broad range of modeling assumptions, isotope tracers, and measurement inputs without the need to introduce *ad hoc* mathematical approximations. As a result, models for *in vivo* MFA can be readily adapted to a broad range of study designs and physiological conditions.

### **2.3 Applications of Metabolic Flux Analysis in physiology**

Most obesity-associated diseases such as type 2 diabetes and non-alcoholic fatty liver disease are characterized by metabolic dysfunction. Yet, even when metabolic changes are not the underlying cause of a disease, metabolic dysregulation is closely connected with the progression of many major pathologies such as cancer, cardiomyopathy, and neurodegenerative disorders. Therefore, studying altered metabolic pathways holds tremendous potential for determining therapeutic targets and diagnostic markers. Over the past several decades, there have been continuous efforts to utilize stable-isotope-based flux analysis to



assess metabolism in specific tissues, both *in vitro* and *in vivo*. Because this dissertation focuses on construction of metabolic models pertaining to the liver, pancreas, cardiac and skeletal muscle, the following sections summarize the efforts made to characterize metabolism in those particular tissues.

### 2.3.1 Liver Metabolism

The value of MFA has been most evident in the field of hepatology research because the liver is a metabolic hub of the body. Using hepatic cell lines and primary hepatocytes, *in vitro* experiments have helped elucidate the effects of hormones, amino acids, and drugs in a highly controlled environment [80]. For example, our group has shown that N-acetylcysteine scavenges ROS, phenformin inhibits mitochondrial activity and BAPTA chelates intracellular calcium in cultured hepatocytes [81], [82]. While *in vitro* studies are more economical and help elucidate the fundamental molecular mechanisms within a specific cell type, they fail to capture the inherent complexity of organ systems that interact with other tissues through exchange of metabolites or signaling proteins that control their metabolic state. Therefore, decades of work have helped generate methods to assess hepatic metabolism *in vivo* and are summarized below.

Prior to the use of MFA, several different approaches were employed to study intermediary hepatic fluxes *in vivo*. Spanning over several decades, invasive techniques such as arteriovenous (AV) measurements were used to calculate gluconeogenic and glycogenolytic contributions to glucose production [83]–[85]. To minimize surgical requirements and improve reproducibility of data [85], [86],  $^{13}\text{C}$  NMR spectroscopy and isotope tracer analyses were used to quantify net hepatic glycogenolysis and gluconeogenesis in human subjects [87], [88]. A more generalizable version of this technique called mass isotopomer distribution analysis (MIDA), which does not require direct measurements of precursor pool enrichment, was used to assess hepatic gluconeogenesis [89]–[93]. In the mid-90s, methods using deuterated water ( $^2\text{H}_2\text{O}$ ) gained popularity due to the limited technical requirements and cross-species applicability [63], [94], [95]. In this approach, the  $^2\text{H}$  fractional enrichments bound to C2, C5, and C6 carbon positions of the monoacetone

glucose (MAG) derivative of plasma glucose were used to calculate the relative hepatic flux contributions from gluconeogenesis and glycogenolysis [63], [94]–[98]. Stable or radioactive glucose tracers were co-administered with  $^2\text{H}_2\text{O}$  to quantify absolute rates of gluconeogenesis and glycogenolysis [61].

By coupling  $^{13}\text{C}$  and  $^2\text{H}_2\text{O}$  tracers, several studies implemented this methodology to assess hepatic fluxes in a variety of hormonal, genetic, and nutritional states [86], [87], [99]–[104]. For example, Wajngot et al. used deuterated water and [6,6- $^2\text{H}_2$ ]glucose to show that gluconeogenesis contributed more to glucose production in diabetic individuals than in control subjects [102]. Furthermore, this coupling of multiple isotopic tracers has enabled the investigation of anaplerotic, cataplerotic, and oxidative metabolism in the liver [2], [29], [51], [99]–[101], [105]–[108]. To simultaneously quantify hepatic glucose and energy producing fluxes, the Burgess group devised an isotopomer analysis method that used the position-specific resolution of  $^2\text{H}$ - and  $^{13}\text{C}$ -NMR of plasma glucose to assess the influence of genes, nutritive states, and therapeutics on hepatic fluxes in mice [2], [109], [110] and humans [32], [99].

While the application of metabolic flux analysis in physiology is nascent, the field of quantifying hepatic fluxes spans many decades [36], [40], [118]–[120], [62], [111]–[117]. These methods rely upon simplifying assumptions, tracer selection and closed-form analytical equations that estimate fluxes benefiting from these assumptions [121]. Recently, regression based metabolic flux analysis approaches have gained popularity with flexibility in testing modeling assumptions and incorporation of multiple tracers and measurement inputs. These studies leverage the GC-MS based fragmentation of plasma glucose to assess hepatic gluconeogenic and CAC fluxes in microvolumes of plasma collected from conscious, unrestrained mice [29]. These methods are further aided with the development of flexible MFA software, like INCA [69], to allow for the introduction of additional reactions, testing of assumptions, and simulation of MIDs of intermediary metabolites. Lately, these networks have been used to test the recycling of  $^{13}\text{CO}_2$  [29], measurement of ketogenesis [122], and cross-validation of NMR datasets with GC-MS-based MIDs [65].

### 2.3.2 Pancreatic Metabolism

The main function of pancreatic islet  $\beta$ -cells is to synthesize and secrete insulin at appropriate rates to control blood glucose within a narrow range. Glucose stimulated insulin secretion (GSIS) is biphasic. While the  $K_{ATP}$  channel-dependent pathway is critical for activating the first phase of GSIS, significant amounts of insulin are secreted in the second ( $K_{ATP}$  independent) phase of insulin secretion, which is regulated by glucose metabolism and several fuel secretagogues [123]. Studies using carbon isotope tracing by NMR and mass spectrometry techniques have demonstrated that the anaplerotic flux of pyruvate to oxaloacetate via pyruvate carboxylase (PC) is strongly responsive to changes in extracellular glucose and GSIS in  $\beta$ -cells [124]–[127]. Inhibition of pyruvate carboxylase by phenylacetic acid in the INS-1 cell line and rat islets leads to inhibition of GSIS [128]–[131]. Anaplerotic flux is connected with NADPH production via malic enzyme (ME) and through a reductive carboxylation pathway recently uncovered in  $\beta$ -cells through the application of stable isotope flux methods [132]. NADPH is a key modulator of the amplifying insulin pathway because it converts GSSG to GSH, which elicits insulin granule exocytosis via sentrin/SUMO-specific protease-1 (SENP1) [133], [134].

NADPH production is also thought to be modulated by the pentose monophosphate shunt pathway (PPP), which is also considered as a potential regulator of GSIS. The inhibition of the NADPH-generating enzymes of the pathway, namely glucose-6-phosphate dehydrogenase (G6PDH) [135] or 6-phosphogluconate dehydrogenase (6PGDH) [136], results in impaired GSIS. However, the role of the PPP in regulating GSIS via NADPH is debated and is proposed to be connected to nucleotide production [135]–[137]. Future studies benefiting from the use of stable isotope metabolic tracing methods may be required to determine the pathway's contribution to NADPH production. Another pathway connected with amplifying GSIS is the phosphoenolpyruvate (PEP) cycle. The cycle connects the production of mitochondrial GTP, generated by succinyl-CoA synthase (SCS) during glucose stimulation, to its utilization by the mitochondrial isoform

of phosphoenolpyruvate carboxykinase (PEPCK-M) [138], [139]. The generation of the very high free energy PEP molecule is suggested to allow the  $\beta$ -cell to continue to synthesize ATP as a direct product of the pyruvate kinase reaction, even at maximum mitochondrial oxidative phosphorylation potential [57]. While metabolic flux studies have revealed an approximate doubling of PEPCK-M flux when comparing cells expressing GTP-dependent SCS to those expressing ATP-dependent SCS, no differences in oxidative flux of glucose to the TCA cycle through pyruvate dehydrogenase or in anaplerotic flux via PC have been found between the two groups of cells [140]. New findings indicate the PEP cycle might be connected with the first phase of insulin secretion along with pyruvate kinase [141].

Recently, an islet specific enzyme, G6PC2, has been implicated in regulating fasting blood glucose levels and GSIS [142]. Previous work from our group has shown that G6PC2, along with glucokinase (GK), form a futile substrate cycle where G6PC2 de-phosphorylates G6P, generated by GK, back into glucose [142], [143]. This suggests that G6PC2, in conjunction with GK, may regulate glycolytic flux and consequently affect the glucose sensitivity of GSIS [142]. Various observations support this model. Glucose-6-phosphatase activity [142] and glucose cycling [144] are abolished in *G6pc2* knockout (KO) islets and *G6pc2* KO mice exhibit reduced fasting blood glucose (FBG) with no change in fasting plasma insulin (FPI) compared to wild-type (WT) controls as a consequence of a leftward shift in the dose response curve for GSIS [142]. *G6pc2* KO islets incubated for short durations (<2h) in sub-maximal glucose also show higher glycolytic flux and increased GSIS compared to islets isolated from WT littermates [142], [145]. These prior results suggest that *G6pc2* negatively regulates GSIS by opposing flux through glycolysis, but the effect of *G6pc2* deletion on other downstream pathways that control insulin release, such as the TCA cycle and PPP is unknown. Genetic studies in humans have generated data that indicate that G6PC2 may regulate pulsatile insulin secretion [146], [147], which suggests that G6PC2 may regulate aspects of beta cell metabolism other than glycolysis. Overall, insulin secretion is intricately regulated via many pathways,

and an important area for future studies includes the simultaneous assessment of multiple metabolic pathway fluxes to reveal their metabolic control of insulin secretion.

### 2.3.3 Cardiac and skeletal muscle metabolism

Dysregulation in cardiac metabolism is closely associated with heart disease. To quantify the substrate preferences in the perfused heart, sophisticated  $^{13}\text{C}$  NMR techniques have been developed [50], [148]–[150]. These methods help assess the relative contributions of pyruvate, fatty acid, and ketone body oxidation to AcCoA formation, which is the primary fuel for the heart. Leveraging the platform used for estimating hepatic fluxes, initial attempts to quantify cardiac fluxes have relied upon measurements of glutamate enrichment in hearts perfused with  $^{13}\text{C}$  labelled precursors. Subsequent efforts combined the use of GC-MS and NMR datasets and implemented isotopomer analysis to assess cardiac substrate usage. An important aspect that is analyzed in cardiac metabolism is the concerted regulation of pyruvate dehydrogenase (PDH) and fatty acid oxidation that is required to maintain supplies of AcCoA. In order to measure the myocardial PDH flux, hyperpolarized magnetic resonance spectroscopy have enabled the *in vivo* quantification of pyruvate dehydrogenase in the heart [151], [152]. More recently, a rigorous MFA based approach was applied to labeling data acquired from a prior study [15] to assess energy metabolism in perfused hearts [153]. Overall, these studies show that cardiac metabolism is intricately balanced between glucose and fatty acid metabolism, and shifts in substrate usage often occur in various forms of injury to the myocardium [154], [155].

Skeletal muscle is considered to be a major tissue involved in the maintenance of glucose homeostasis because its contribution to glucose uptake is  $\approx 75\%$  of the total contribution of peripheral tissues [156], and it is the main tissue responsible for insulin-dependent glucose utilization. Using  $^{13}\text{C}$  magnetic resonance spectroscopy (MRS) and analysis of  $^{13}\text{C}$  isotopomers of glutamate, early studies characterizing skeletal muscle metabolism focused on determining the primary oxidative substrates [157]. Building on these

findings, follow-up studies used  $^{13}\text{C}$  NMR to assess anaplerotic fluxes in isolated skeletal muscles [158], [159]. Recent studies, using noninvasive MRS, have assessed the substrate oxidation rates of skeletal muscles using plasma enrichments *in vivo* [160]. Furthermore, these studies have shown that offspring of type 2 diabetic patients have impaired mitochondrial substrate oxidation in the skeletal muscle [161]. While  $^{13}\text{C}/^{31}\text{P}$  NMR techniques have been used to assess mitochondrial energy coupling [162], use of metabolic flux analysis to quantify skeletal muscle metabolism has been limited.

#### **2.3.4 Multi-tissue metabolic flux analysis**

While the work highlighted above focuses on assessing fluxes in a single tissue, recent technological advancements have enabled the assessment of circulating fluxes between multiple tissues *in vivo*. There is an increasing motivation to evaluate the major sources of carbon for each tissue. Recent stable isotope infusion studies show that circulating lactate is a major carbon shuttle between numerous tissues in the body and may serve as the primary fuel for TCA cycle metabolism [163]. Contrastingly, others have shown that glucose, not lactate, is the dominant source of oxidative metabolism [164] and glycerol may be a major contributor of ‘new’ glucose synthesized during fasting [165]. Furthermore, recent work suggests that lactate is produced rapidly from glucose by certain muscle tissues, whereas many other tissues rely heavily on stored glycogen rather than glucose to sustain glycolytic metabolism *in vivo* [166]. Also, evaluation of fifteen nutrient tracers on circulating fluxes shows that glucose-lactate and triglyceride-glycerol-fatty acid cycles carry most of the carbon around the body [167]. These innovative approaches indicate an emerging trend towards assessing metabolic exchanges between multiple tissues and provide an opportunity to simultaneously resolve intermediary metabolism within those tissues.

### **2.4 Conclusions**

Advancements in experimental, analytical, and computational techniques have enabled the resolution and quantification of a wider range of metabolic pathways using MFA. Decades of work in the fields of hepatic,

pancreatic and muscle metabolism have furthered our understanding of tissue-specific metabolism. Using these technical and physiological advancements, in the remaining chapters of this dissertation I describe the development of *in vitro* and *in vivo* metabolic models and complementary experimental workflows to investigate the regulation of mammalian metabolism using stable isotope-based MFA.

### 3. G6PC2 negatively regulates glucose oxidation and insulin secretion in $\beta$ -cells

#### 3.1 Abstract

Elevated fasting blood glucose (FBG) is associated with increased risks of developing type 2 diabetes (T2D) and cardiovascular-associated mortality. G6PC2, a predominantly islet-specific glucose-6-phosphatase catalytic subunit that converts glucose-6-phosphate (G6P) to glucose, has been linked with variations in FBG in genome-wide association studies (GWAS). Deletion of *G6pc2* in mice leads to lower FBG without affecting fasting plasma insulin levels *in vivo*. At 5 mM glucose *G6pc2* knockout (KO) islets exhibit no glucose cycling, increased glycolytic flux and enhanced glucose-stimulated insulin secretion (GSIS). However, the broader effects of *G6pc2* KO on  $\beta$ -cell metabolism and redox regulation are unknown. Here we used CRISPR/Cas9 gene editing and metabolic flux analysis in  $\beta$ TC3 cells, a murine pancreatic  $\beta$ -cell line, to examine the role of *G6pc2* in regulating glycolytic and mitochondrial fluxes. We found that deletion of *G6pc2* led to a 67% and 62% increase in glycolytic and citric acid cycle flux at 5 and 11 mM glucose concentrations, respectively. Intracellular insulin content and GSIS were enhanced by up to ~2 fold along with increased cytosolic redox potential and reductive carboxylation flux. Normalization of fluxes relative to net glucose uptake revealed upregulation in two NADPH producing pathways in the CAC; reductive carboxylation and malic enzyme flux were increased by 32% and 67%, respectively. These results demonstrate that *G6pc2* regulates GSIS by modulating not only glycolysis but also citric acid cycle (CAC) activity in  $\beta$ -cells. Furthermore, our results provide support for a new paradigm wherein glucokinase and G6PC2 together regulate glycolytic flux and glucose oxidation, and thereby exert control over GSIS. Overall, our findings implicate G6PC2 as a novel therapeutic target for enhancing insulin secretion and lowering FBG, which would benefit individuals with prediabetes, T2D and obesity.



### 3.2 Introduction

Glucose-6-phosphatase, a multi-component system located in the endoplasmic reticulum (ER), catalyzes the conversion of glucose-6-phosphate (G6P) to glucose [168]. This enzyme system is composed of several integral membrane proteins including a G6P transporter, encoded by *SLC37A4*, which carries the substrate from the cytosol to the ER lumen. Once in the ER, G6P is hydrolyzed by a glucose-6-phosphatase catalytic subunit (G6PC) to glucose and inorganic phosphate, and these products are subsequently transported to the cytosol. Three G6PC isoforms, encoded by *G6PC1*, *G6PC2*, and *G6PC3*, have been identified and are selectively expressed in different tissues [145], [168]. *G6PC1* is predominantly expressed in the liver and kidneys where it catalyzes the terminal step in endogenous glucose production through gluconeogenesis and glycogenolysis. *G6PC3* is highly expressed in the kidneys, testis, skeletal muscle, and brain [168] where it functions to eliminate the noncanonical metabolite, 1,5-anhydroglucitol-6-phosphate [169]. *G6PC2*, also known as the islet-specific glucose-6-phosphatase catalytic subunit-related protein (IGRP), is predominantly expressed in pancreatic islet  $\beta$ -cells [168].

Previous work from our group has shown that G6PC2, along with glucokinase (GK), form a futile substrate cycle where G6PC2 de-phosphorylates G6P, generated by GK, back into glucose. This suggests that G6PC2, in conjunction with GK, may regulate glycolytic flux and consequently affect the glucose sensitivity of glucose stimulated insulin secretion (GSIS) [142]. Various observations support this model. Glucose-6-phosphatase activity [142] and glucose cycling [144] are abolished in *G6pc2* knockout (KO) islets and *G6pc2* KO mice exhibit reduced fasting blood glucose (FBG) with no change in fasting plasma insulin (FPI) compared to wild-type (WT) controls as a consequence of a leftward shift in the dose response curve for GSIS [142]. *G6pc2* KO islets incubated for short durations (<2h) in sub-maximal glucose also show higher glycolytic flux and increased GSIS compared to islets isolated from WT littermates [142], [145]. These prior results suggest that *G6pc2* negatively regulates GSIS by opposing flux through glycolysis but the effect of *G6pc2* deletion on other downstream pathways that control insulin release, such as the

citric acid cycle (CAC) and pentose phosphate pathway (PPP) is unknown. Genetic studies in humans have generated data that indicate that G6PC2 may regulate pulsatile insulin secretion [146], which suggests that G6PC2 may regulate aspects of beta cell metabolism other than glycolysis.

To better understand the role of *G6pc2* in  $\beta$ -cells, we describe here the application of  $^{13}\text{C}$  metabolic flux analysis (MFA) to assess global changes in glucose and oxidative metabolism in response to *G6pc2* deletion. MFA is a stable isotope-based approach that relies on the inherent assumption that the system under investigation is at metabolic steady state. However, obtaining sufficient isotope enrichment to enable precise flux estimation in cell culture systems often requires extended incubation times ( $\geq 24\text{h}$ ) [26]. Unfortunately, prolonged culture of primary islets causes gradual loss of their *in vivo* metabolic phenotype [144], resulting in no apparent differences in net glucose uptake or media insulin concentration between WT and *G6pc2* KO islets [143]. To minimize the confounding effects of phenotypic instability and cellular heterogeneity that complicate *ex vivo* studies of primary islets, we used a pancreatic mouse  $\beta$ -cell line ( $\beta\text{TC3}$ ) to examine the metabolic effects of *G6pc2* loss.

We applied CRISPR-Cas9 gene editing to generate stable *G6pc2* KO and WT  $\beta\text{TC3}$  cell lines for MFA studies. We also developed a mathematical model to assess isotope labeling measurements and quantify flux through the major pathways of glycolysis, PPP, CAC, and anaplerosis in  $\beta$ -cells. Metabolic fluxes were estimated by simultaneously regressing isotope enrichment measurements from 21 unique metabolite fragment ions and 13 extracellular uptake and excretion rates obtained from WT and KO cells incubated with  $^{13}\text{C}$  isotopes. The results indicate that *G6pc2* deletion leads to a significant increase in oxidative fluxes and GSIS. A 65% increase in glycolytic and CAC activity was accompanied by up to a ~2-fold upregulation in intracellular insulin content and GSIS. Furthermore, we observed an increase in the cytosolic NADPH:NADP<sup>+</sup> ratio along with a 2-fold flux increase through the reductive carboxylation pathway from glutamine to citrate. Importantly, normalization of fluxes to the net glucose uptake rate showed increased flux through a couple of NADPH producing pathways in the CAC, independent of elevated glycolytic flux.

These results suggest that G6PC2 also regulates CAC pathways, separate from its modulation of glycolysis. More broadly, these data suggest that G6PC2 could be a potential target for enhancing insulin secretion and lowering FBG in individuals with prediabetes, type 2 diabetes (T2D) and obesity.

### **3.3 Methods**

#### **3.3.1 Cell culture**

The  $\beta$ TC3 cell line was cultured in RPMI 1640 medium (ThermoFisher; Cat no. 11875-093) supplemented with 10% fetal bovine serum (Sigma; Cat. No. F2442) and 1X penicillin-streptomycin (Gibco; Cat. No. 15140122). Rat islet-derived INS1-832/13 cells were cultured in RPMI medium supplemented with 10% fetal bovine serum, 0.05 mM  $\beta$ -mercaptoethanol, and 1X penicillin-streptomycin. All cells were cultured at 37°C in a 5% CO<sub>2</sub> humid atmosphere.

#### **3.3.2 Generation of G6pc2 knockout (KO) and control $\beta$ TC3 cells**

*G6pc2* KO and control Cas9-expressing  $\beta$ TC3 cells were generated in a multi-step process. We first generated a variant  $\beta$ TC3 cell line that stably expresses Cas9. To achieve this, cells were washed twice with Dulbecco's phosphate-buffered saline (Gibco; Cat. No. 14190144), dissociated with TrypLE Select Enzyme (Gibco; Cat. No. 12563029) and collected as a single-cell suspension. Cell density was measured, and cells were then transduced in a 12-well plate with a lentivirus encoding Edit-R mKate2-tagged Cas9 nuclease at a multiplicity of infection (MOI) of 2.0 under conditions specified by the manufacturer (Dharmacon; Cat. No. VCAS11863). This virus confers constitutive mKate2-tagged Cas9 expression driven by the CMV promoter. By utilizing a 2A self-cleaving peptide, both the fluorescent mKate2 reporter and Cas9 are expressed within the same mRNA strand and translated into two separate proteins. Antibiotic-free complete growth medium (RPMI 1640 (Gibco; Cat. No. 11875093), supplemented with 10% FBS (Sigma; Cat. No. F2442) was added to the transduced cells at a 1:3 volume ratio (transduction media: antibiotic-free complete growth media) after 5 hours, and medium was changed every 48 hours. Once cells

reached a confluency of ~5 million cells/well (~6 days), they were dissociated with TrypLE Select Enzyme and resuspended in phenol-red free RPMI medium (Gibco; Cat. No. 11835030) supplemented with 10 mM HEPES buffer (Gibco; Cat. No. 15630106) and antibiotic-antimycotic solution (Gibco; Cat. No. 15240062). Transduction and Cas9 integration were confirmed under a fluorescence microscope prior to fluorescence activated cell sorting (FACS). Cells with high fluorescence signal were clonally sorted onto 96-well plates using a 5-laser FACS Aria III (BD Biosciences) with a 100  $\mu$ m nozzle. Sorted cells were collected in 150  $\mu$ L per well antibiotic-containing complete RPMI 1640 growth medium (Gibco; Cat. No. 11875093) supplemented with 10% FBS (Sigma; Cat. No. F2442), 10 mM HEPES (Gibco; Cat. No. 15630080), and 1X penicillin-streptomycin (Gibco, Cat. No. 15140122). Clones were supplemented with an additional 100  $\mu$ L of antibiotic-containing complete growth medium per well approximately 24 hours after sorting. Medium was changed with antibiotic-containing complete growth media every 48 hours. mKate2-tagged Cas9-expressing clones were identified using fluorescent image analysis (Leica Microscope Dmi8 and ImageJ). The clones showing the highest fluorescent signal were selected for further analysis and experimental use.

To generate knockouts, *G6pc2* crRNA (Cat. Nos. CM-065306-01, CM-065306-02, CM-065306-03) and synthetic tracrRNA (Cat. No. U-002005-20) were ordered from Dharmacon and resuspended according to the manufacturer's instructions. Cas9-expressing  $\beta$ TC3 cells (~10,000 cells per well in 4 wells of a 24-well plate) were incubated with 25 nM crRNA, 25 nM tracrRNA, and Dharmafect 1 reagent (Cat. No. T-2001-01) in antibiotic-free RPMI medium (Gibco; Cat. No. 11875093) for 48 hours at 37°C. After 48 hours, the cells were switched to antibiotic-containing complete growth medium, allowed to recover and then subjected to another round of crRNA:tracrRNA delivery. After three rounds of transfection, the  $\beta$ TC3 cells were expanded and prospectively analyzed for *G6pc2* expression and activity by TIDE (Tracking of Indels by Decomposition) analysis [170] and a stable isotope-based glucose cycling assay [143], respectively. The isolate with the highest KO efficiency and lowest glucose cycling was selected for use in subsequent studies.

### 3.3.3 Isotope labelling studies

Prior to labelling experiments, *G6pc2* WT and KO  $\beta$ TC3 cells were washed with PBS and passaged twice in glucose-free RPMI media supplemented with 10% dialyzed FBS and 5- or 11 mM glucose on 10-cm plates. After the second passage,  $\beta$ TC3 cells were grown to ~60% confluency, washed twice with PBS and incubated for 24h in RPMI media supplemented with dialyzed FBS and 2 mM [U- $^{13}\text{C}_5$ ] glutamine plus unlabeled 5- or 11 mM glucose, or with 5- or 11 mM [1,2- $^{13}\text{C}_2$ ] glucose plus 2 mM unlabeled glutamine. Post incubation, media and cells were harvested and subjected to further analyses as described below.

### 3.3.4 Extraction of metabolites and GC-MS analyses

Intracellular metabolites from  $\beta$ TC3 cells were extracted as previously described [171]. Briefly, intracellular metabolism was quenched with 2 mL of  $-80\text{ }^\circ\text{C}$  methanol, and cells were scraped into a mixture of 1:1:1 chloroform, methanol, and water. Twenty  $\mu\text{L}$  of 5-mM norvaline and 5-mM [U- $^{13}\text{C}_6,^2\text{H}_7$ ]glucose was spiked as an internal standard for metabolite quantification. The aqueous phase was split into two parts, dried, and processed to form either methyloxime *tert*-butyldimethylsilyl (Mox-TBDMS) derivatives of organic and amino acids [172] or the di-isopropylidene propionate (DiO) derivative of glucose [41]. Media metabolites were quantified by adding 20  $\mu\text{L}$  of 5-mM norvaline in 50  $\mu\text{L}$  of media followed by cold acetone precipitation. Calibration standards with known amounts of each metabolite were prepared and derivatized simultaneously with the extracted samples for absolute quantification of metabolite abundances. Derivatized samples were analyzed by GC-MS. Sample volumes of 1  $\mu\text{L}$  were injected in a 5:1 split in an Agilent 7890A gas chromatography system equipped with two HP-5 ms (15 m x 0.25 mm x 0.25  $\mu\text{m}$ ; Agilent J&W Scientific) capillary columns and interfaced with an Agilent 5977C mass spectrometer. Previously defined temperature programs for Mox-TBDMS [172] and DiO [29] derivatives were used for data collection. Derivative peaks were integrated using a custom MATLAB function [143] to obtain mass isotopomer distributions (MIDs) for the metabolite fragment ions shown in

Table S1. Measurement uncertainty was assessed by calculating the root-mean-square deviation between the MID of unlabeled standards and the theoretical MID computed from the known abundances of naturally occurring isotopes. Absolute metabolite abundances were normalized to the total number of cells present at the time of sample collection.

### 3.3.5 Extracellular uptake and excretion rates

Extracellular uptake and excretion rates of  $\beta$ TC3 cells were determined in triplicate growth experiments. Ten-centimeter tissue culture dishes were seeded at a density of 150,000 cells/mL in 10 mL of RPMI media supplemented with 5- or 11 mM glucose. After incubating parallel dishes for 12h, 24h, 48h, or 72h, extracellular media was collected and stored at -80 °C for further analysis while the cells were washed with PBS, detached using 0.05% Trypsin-EDTA (Gibco; Cat no. 25300062) and counted using a Cedex XS cell counter (Roche; Cat no. 702070001). Concentrations of media metabolites were then analyzed using GC-MS (see *Extraction of metabolites and GC-MS analyses*). We integrated the media metabolite concentrations and cell counts at each timepoint into our previously developed MATLAB-based software package Extracellular Time-Course Analysis (ETA) to quantify cell-specific uptake and excretion rates of measured metabolites [27]. The spontaneous degradation of glutamine to ammonia and pyrrolidonecarboxylic acid was included in the specific rate calculations and the degradation rate was determined to be  $0.0031 \text{ h}^{-1}$  by measuring glutamine disappearance in control cell-free plates. Evaporation rates determined in these control plates were found to be negligible in comparison to cell-specific metabolic rates.

### 3.3.6 $^{13}\text{C}$ Metabolic flux analysis

$^{13}\text{C}$  MFA was performed by minimizing the sum-of-squared residuals (SSR) between model-simulated and experimentally determined measurements. The Isotopomer Network Compartmental Analysis (INCA) software package [69] was used to develop a model of  $\beta$ -cell metabolism (Table S1) and estimate fluxes by

fitting the model to the experimental datasets. Extracellular uptake rates and metabolite enrichment measurements were provided as inputs into the INCA model for flux analysis of  $\beta$ TC3 cell cultures. The standard error in these measurements was set to either the root-mean-square deviation of the unenriched control samples or the standard error of the mean (SEM) obtained from biological replicates, whichever was greater. Best-fit metabolic flux solutions were determined for each experiment by least-squares regression of the experimental measurements to the isotopomer network model. To ensure that a global solution was obtained, flux estimations were repeated a minimum of 25 times from randomized initial guesses. A chi-square test was used to assess goodness-of-fit, and a sensitivity analysis was performed to determine 95% confidence intervals associated with the calculated flux values. Although the metabolic model does not directly capture the flux through G6PC2 ( $V_{G6PC2}$ ), the combination of  $^{13}\text{C}$  metabolite enrichments and net glucose uptake measurements help estimate the net flux through glucokinase ( $V_{GK\text{ Net}}$ ) where  $V_{GK\text{ Net}} = V_{GK} - V_{G6PC2}$ .

### **3.3.7 Intracellular and media insulin quantification**

A previously described [173] islet insulin extraction protocol was adapted to measure insulin content within  $\beta$ TC3 cells. Approximately 5 million  $\beta$ TC3 WT and KO cells were washed 4 times with ice-cold PBS, prior to 48-hour refrigeration in 300  $\mu\text{L}$  of acid alcohol (1 mL concentrated HCl; 110 mL 95% ethanol). After incubation for 48h, the extract was centrifuged for 10 minutes at 2000 RPM at 4°C. Lastly, 200  $\mu\text{L}$  of supernatant was collected and stored at -20°C for insulin analysis. Insulin from cell extracts and media was quantified using radioimmunoassay (Millipore) by the Vanderbilt Diabetes Research and Training Center Hormone Assay Core.

### **3.3.8 Intracellular metabolite quantification and assessment of redox markers**

Intracellular metabolites from 8-10 million  $\beta$ TC3 WT and KO cells were extracted as defined above (see *Extraction of metabolites and GC-MS analyses*). Absolute quantification of metabolite amount was

performed by running calibration standards along with extracted samples. Cell counts in biological replicates were assessed after detaching and counting them using 0.05% Trypsin-EDTA (Gibco; Cat no. 25300062) and Cedex XS cell counter (Roche; Cat no. 702070001), respectively. Metabolite amount was normalized to total volume estimated using cell counts and assuming an average volume of a  $\beta$ -cell of approximately  $1100 \mu\text{m}^3$  from previous studies [174]. For analysis of ammonium, 300  $\mu\text{L}$  sample was diluted by dH<sub>2</sub>O to 1.5 mL and then analyzed using an Ammonia Gas Sensing Electrode (Cat. No. 9512BNWP, Thermo Fisher Scientific, MA, USA) according to the manual. Cytosolic and mitochondrial redox state were estimated using enzymatic equilibrium relations described elsewhere [175]. The cytosolic NADH/NAD<sup>+</sup> was estimated from lactate dehydrogenase equilibrium (i.e.  $\text{cNADH/NAD}^+ = [\text{Lactate}]/[\text{Pyruvate}] \times 1/K_{\text{LDH}}$ ; where  $K_{\text{LDH}} = 1.11 \times 10^{-4}$ ). Similarly, cytosolic NADPH/NADP<sup>+</sup> was estimated from malate dehydrogenase equilibrium ( $\text{cNADPH/NADP}^+ = [\text{Malate}]/[\text{Pyruvate}][\text{CO}_2] \times K_{\text{MDH}}$ ; where  $K_{\text{MDH}} = 34.4 \times 10^3 \text{ uM}$ ). Lastly, mitochondrial NADPH/NADP<sup>+</sup> was estimated from glutamate dehydrogenase equilibrium ( $\text{mNADPH/NADP}^+ = [\text{Glutamate}]/[\alpha\text{-ketoglutarate}][\text{NH}_4^+] \times K_{\text{GDH}}$ ; where  $K_{\text{GDH}} = 2.49 \times 10^{-3} \text{ mM}$ ) [175].

### 3.3.9 Glucose cycling

Glucose cycling in  $\beta\text{TC3}$  and INS1-832/13 cells was measured using our previously defined approach [143]. Briefly, 8-10 million cells were incubated for 24 or 72 hr 37°C in RPMI 1640 medium containing 5 mM or 11 mM glucose in 10-cm dishes. Cells were incubated in either naturally labeled glucose or [1,2,3,4,5,6,6-<sup>2</sup>H<sub>7</sub>]glucose (Cambridge Isotope Laboratories; Cat no. DLM-2062). Following the 24 or 72 hr incubation, the supernatant was collected for glucose derivatization and GC-MS analysis (see *Extraction of metabolites and GC-MS analyses*). The glucose MID was quantified, and absolute glucose concentration was determined through comparison to a standard curve. Glucose cycling and glucose uptake rates were calculated as described previously [143].



### 3.3.10 Measurement of cytoplasmic calcium

$\beta$ TC3 WT and KO cells were cultured in RPMI with 5mM glucose or 11mM glucose for 24h at 37°C, 5% CO<sub>2</sub> in 35 mm tissue culture dishes. Cells were loaded with 2  $\mu$ M Fura-2, AM (Invitrogen, Waltham, MA) for 25 min. Cells were then washed, incubated (for 15 min), and perfused with Krebs-Ringer HEPES buffer (KRHB) containing (mM) 119.0 NaCl, 4.7 KCl, 2.5 CaCl<sub>2</sub>, 1.2 MgSO<sub>4</sub>, 1.2 KH<sub>2</sub>PO<sub>4</sub>, and 10.0 HEPES (pH 7.35 adjusted by NaOH) supplemented with either 5 mM glucose or 11 mM glucose. Baseline Ca<sup>2+</sup> levels was recorded at glucose concentrations indicated in the figure legends.  $\beta$ TC3 K<sub>ATP</sub> channels were subsequently inhibited with 100  $\mu$ M tolbutamide in KRHB; only cells that showed functional K<sub>ATP</sub> channels as determined by tolbutamide-induced Ca<sub>2+</sub> influx were analyzed. Fura-2 AM Ca<sup>2+</sup> fluorescence (excited at 488 nm) was measured at 340 nm and 380 nm (F<sub>340</sub>/F<sub>380</sub>) every 5s as an indicator of intracellular Ca<sup>2+</sup> using a Ti2 microscope (Nikon, Tokyo, Japan) and a back-illuminated sCMOS Prime 95B camera (Teledyne Photometrics, Tucson, AZ, USA).

### 3.3.11 Gene expression analysis

RNA was isolated from ~2 million  $\beta$ TC3 cells using QIAshredder (Qiagen, Cat no. 79656) and RNeasy Mini Kit (Qiagen, Cat no. 74104), according to manufacturer protocols. To perform quantitative real-time PCR analysis, cDNA was synthesized using the iScript cDNA synthesis kit (Bio-Rad, Cat no. 1708891). Next, this cDNA was diluted tenfold with DI water, mixed with previously defined primer sequences [145] (Integrated DNA Technologies) and iQ SYBR Green Supermix (Bio-Rad, Hercules, CA) and analyzed on a CFX96 Real-Time PCR System (Bio-Rad, Hercules, CA). Gene expression was normalized to *Ppia* using the 2<sup>- $\Delta$ Ct</sup> method [176].

### 3.3.12 Statistical analyses

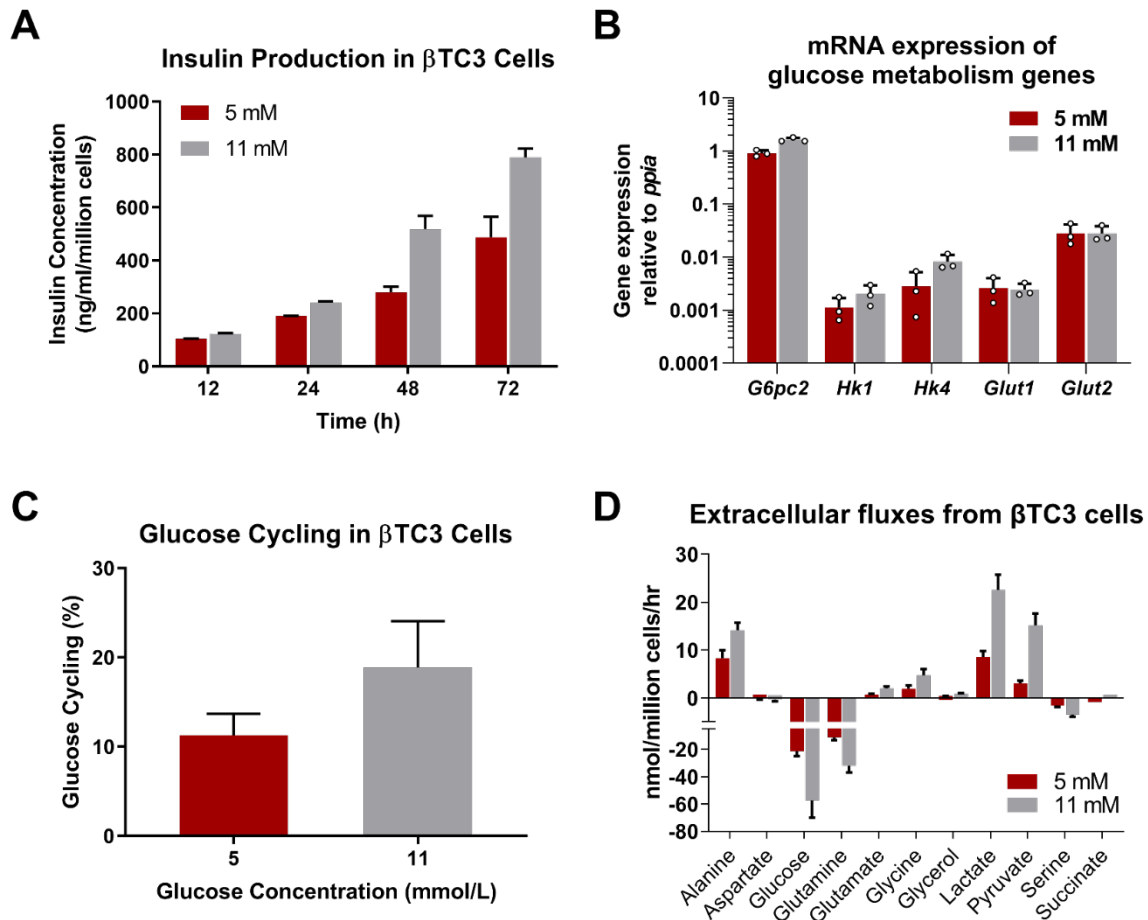
Unless otherwise specified, data are presented as means  $\pm$  SEM. Differences between groups were tested using an unpaired parametric t-test without assuming consistent standard deviations (Welch's t-test). Unless

otherwise stated in figure legends, significant differences were defined as follows: \*\*\* $p < 0.01$ , \*\* $p < 0.05$ , and \* $p < 0.1$ .

### 3.4 Results

#### 3.4.1 $\beta$ TC3 cell line is a representative in vitro model to study the effects of G6pc2 on $\beta$ -cell metabolism

Prior to conducting metabolic studies on  $\beta$ TC3 cells, we validated that the cell line has characteristics suitable for studying the function of G6PC2. We examined expression of *G6pc2*, *Gck* (HK IV) and *Slc2a2*. *Gck* and *Slc2a2* encode glucokinase and the GLUT2 glucose transporter, respectively [177]. All 3 genes were expressed in  $\beta$ TC-3 cells and their expression was not dependent on glucose concentrations. (Fig. 3.1A). We also verified that glucose cycling (Fig. 3.1B), a functional readout of G6PC2 activity, was present at levels comparable to those previously measured in primary islets at 5 mM (~10%) and 11 mM (~20%) glucose concentrations [143], [178]. In contrast, glucose cycling studies in INS1-832/13 cells (Fig. 3A.1A-D), a rat insulinoma cell line, showed negligible glucose cycling ( $\leq 3\%$ ) and net release of glucose (~1 nmol/ $10^6$  cells/hr), further validating that *G6pc2* is a pseudogene in rats [179]. Lastly, uptake and excretion rates of metabolites connected to central carbon metabolism roughly doubled when the glucose concentration was increased from 5 to 11 mM (Fig. 3.1C) and this was associated with a linear increase in insulin secretion over 72h (Fig. 3.1D). These results indicate that  $\beta$ -cell specific features are conserved within  $\beta$ TC3 cells, making the cell line a representative model for our studies investigating the effects of G6PC2 on metabolism.

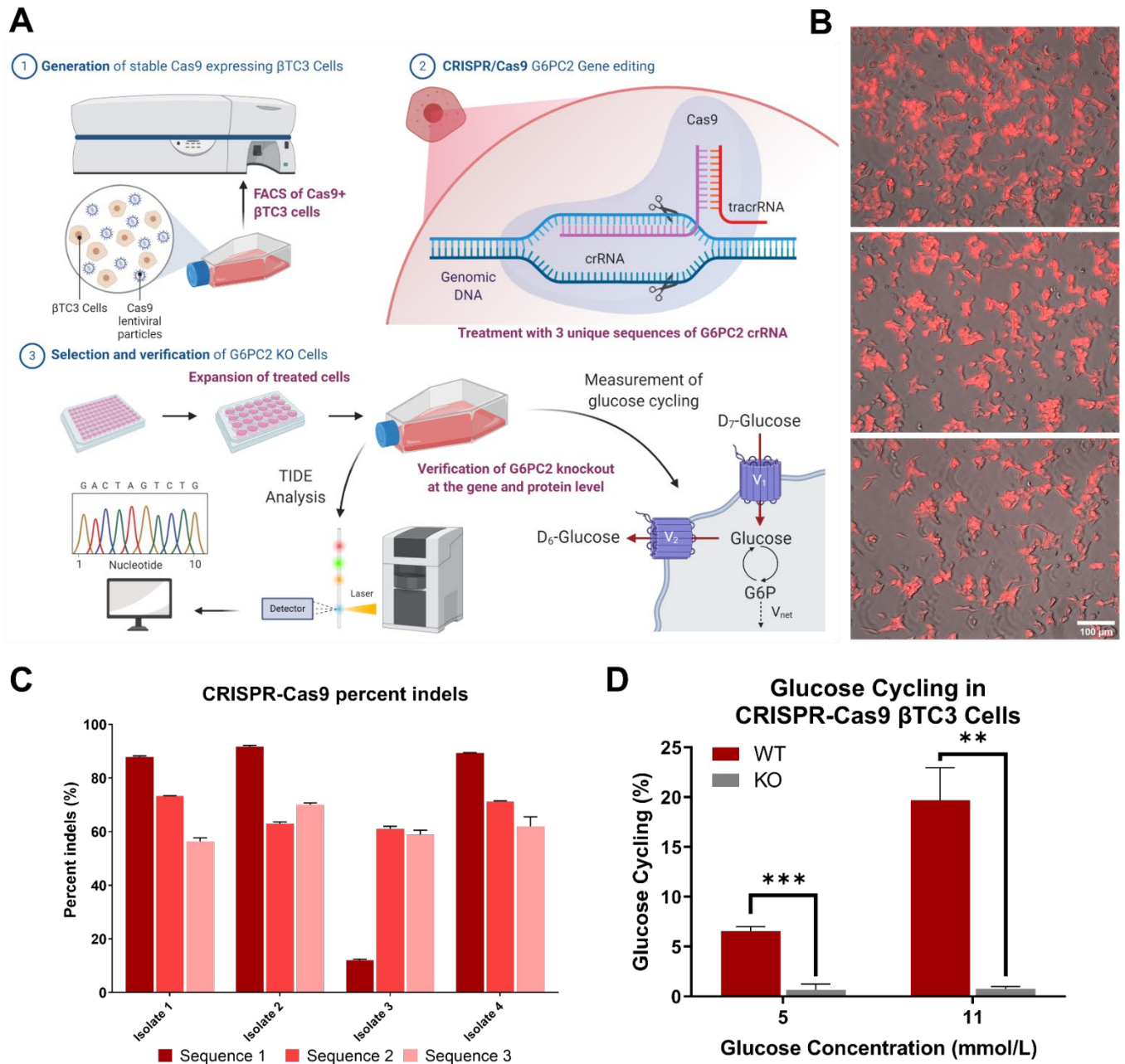


**Figure 3.1: Validation of  $\beta$ TC3 cell line as a representative model to study metabolic regulation by *G6pc2***

- A) Media insulin content over time for  $\beta$ TC3 cells incubated at 5 and 11 mM glucose concentrations. Data represent means $\pm$ SEM (n=3).
- B) mRNA expression of genes regulating glucose metabolism. Data represent means $\pm$ SEM (n=3) relative to expression of the housekeeping gene *ppia*.
- C) Estimated percentage glucose cycling in  $\beta$ TC3 cells at 5 and 11 mM glucose concentrations. Data represent means $\pm$ SEM (n=3).
- D) Extracellular uptake and excretion rates measured in  $\beta$ TC3 cells incubated at 5 and 11 mM glucose concentrations. Positive values represent net excretion while negative values indicate net uptake. Data represent means $\pm$ SEM (n=3).

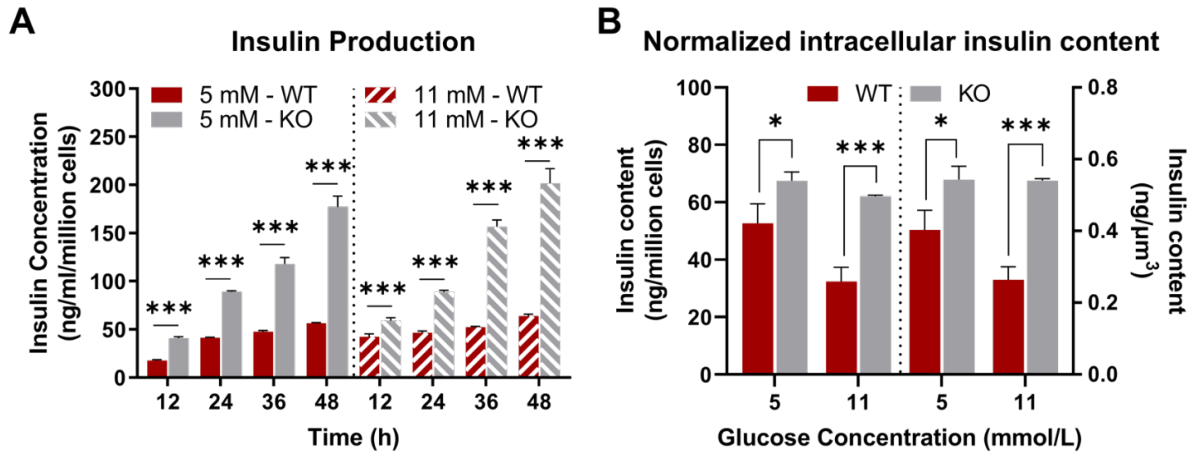
### 3.4.2 Generation and validation of $\beta$ TC3 *G6pc2* knockout cells

To examine the effects of *G6pc2* deletion in  $\beta$ TC3 cells, we engineered *G6pc2* knockout (KO) and control (WT) cell lines by using the CRISPR/Cas9 gene editing technique. We first generated a  $\beta$ TC3 cell line with constitutive Cas9 expression using lentiviral transduction (Fig. 3.2A). The highest Cas9-expressing  $\beta$ TC3 single cell clones were identified using fluorescence-activated cell sorting (FACS) followed by



**Figure 3.2: Generation of βTC3 G6pc2 knockout and control cell lines using CRISPR-Cas9**

- A) Schematic providing an overview of βTC3 *G6pc2* KO cell line development using CRISPR-Cas9 (See *Experimental procedures* for details).
- B) mKate2 and brightfield superimposed images from 3 biological replicates of βTC3 cells expressing Cas9 protein. The single cell clone with the highest mKate2 fluorescence, shown here, was selected for CRISPR RNA transfection
- C) TIDE analysis showing the total percentage of insertions and deletions (indels) around 3 different loci targeted with three different CRISPR RNA sequences in four biological replicates of the single cell clone shown in Fig 2B.
- D) Verification of loss of *G6pc2* functional activity in KO cells by measurement of glucose cycling (see Ref. 7 for details) at 5 and 11 mM glucose concentrations. Cas9 expressing single cell clone from Fig. 2B was used as βTC3 wild-type (WT) control. Data represent means±SEM, \*\*\*p<0.01, \*\*p<0.05 (n=3).

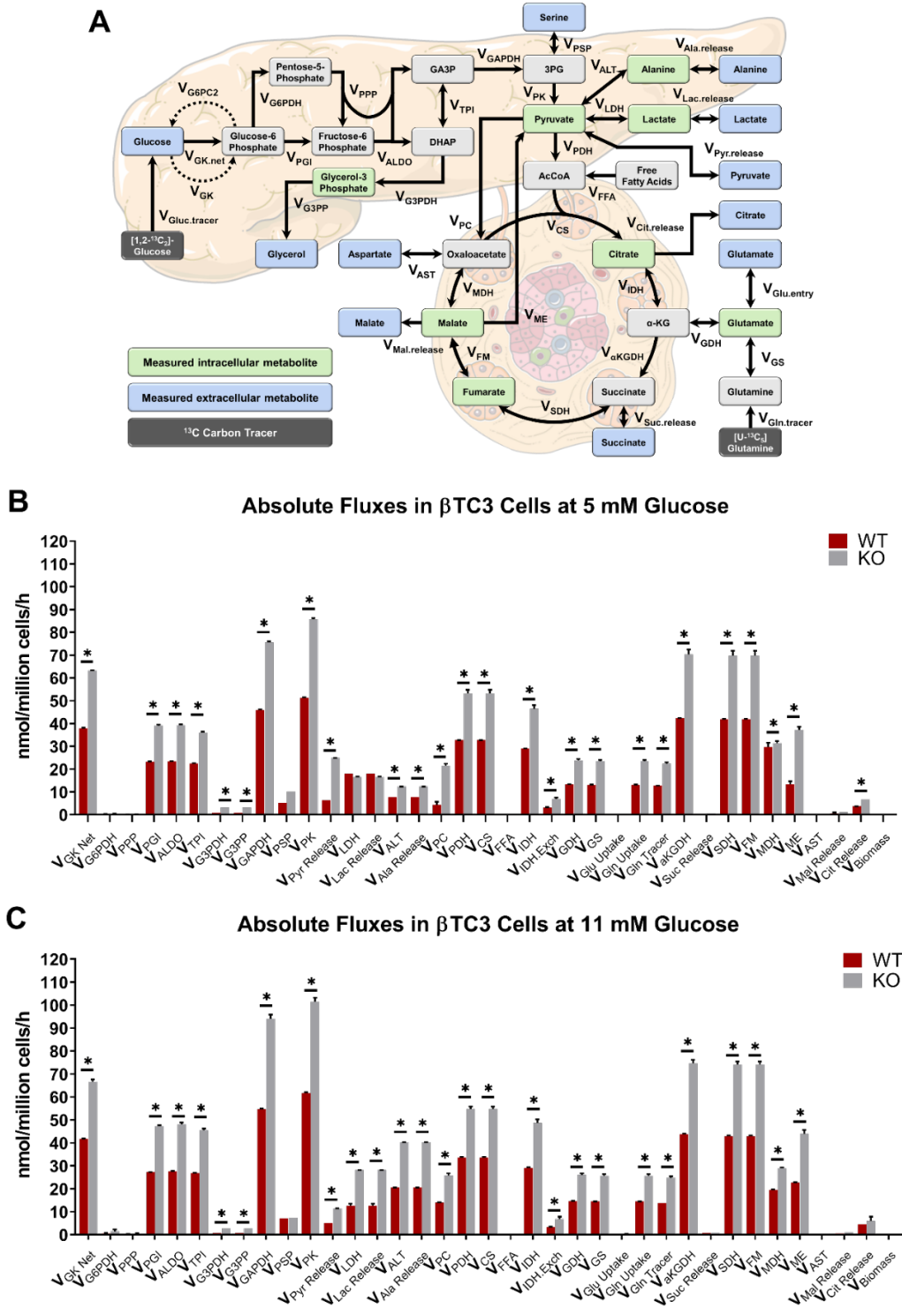


**Figure 3.3: Knockout of *G6pc2* in  $\beta$ TC3 cells leads to increased GSIS**

A) Insulin production normalized to cell count at 5 mM (left) and 11 mM (right) glucose concentrations in  $\beta$ TC3 *G6pc2* WT and KO cells. Data represent means $\pm$ SEM, \*\*\* $p$ <0.01, \*\* $p$ <0.05 (n=4).

B) Intracellular insulin content normalized to cell count (left) and to total surface area (right) at 5 and 11 mM glucose concentrations in  $\beta$ TC3 *G6pc2* WT and KO cells. Data represent means $\pm$ SEM, \*\*\* $p$ <0.01, \* $p$ <0.10 (n=4).

immunofluorescent imaging (Fig. 3.2B). To generate KO cells, three unique synthetic gRNA (crRNA:tracrRNA conjugates, each targeting a specific cut site) were delivered to the highest Cas9-expressing single cell clone using lipofection. To generate WT control cells, only tracrRNA was delivered to the highest Cas9 expressing single cell clone. using the same transfection protocol. After three rounds of gRNA or tracrRNA treatment, four biological isolates were expanded and analyzed using the Tracking of Indels by DEcomposition (TIDE) genomic assessment tool to quantify the percentage knockout (see *Experimental procedures* for details). Computational assessment of Sanger-sequenced genomic DNA showed all three cut sites were predicted to have indel formations with biological isolates 2 and 4 having >90% indel formation at the first cut site (Fig. 3.2C), which is highly indicative of efficient knockout. To confirm loss of G6PC2 functional activity, we measured glucose cycling in KO isolates 2 and 4. Our results indicate that glucose cycling was almost completely abolished (Fig. 3.2D) with negligible glucose release flux (Fig. 3A.2D) in the KO cells at 5 and 11 mM glucose concentrations. Additionally, there was no change in the cycled abundance of glucose over time in either KO isolate, whereas an 8-10% increase was observed in WT isolates within 24h of incubation (Fig. 3A.2A-B). The total glucose uptake flux (Fig. 3A.2C) trended higher in the KO isolates, however the differences were not significant.



**Figure 3.4: MFA in  $\beta$ TC3 *G6pc2* WT and KO cells shows increased absolute flux through glycolytic and mitochondrial pathways**

- A) Flux network representing oxidative  $\beta$ TC3 metabolism constructed in INCA (14). Measured media metabolites are shown in blue while measured intracellular metabolites are highlighted in green.
- B) Absolute extra- and intracellular fluxes in *G6pc2* WT and KO  $\beta$ TC3 cells at 5 mM glucose concentration estimated using MFA. Data represent means $\pm$ SEM, \* $p < 0.05$  (n=3).
- C) Absolute extra- and intracellular fluxes in *G6pc2* WT and KO  $\beta$ TC3 cells at 11 mM glucose concentration estimated using MFA. Data represent means $\pm$ SEM, \* $p < 0.05$  (n=3).

To further validate our novel cell model, we measured intracellular and media insulin concentration in *G6pc2* WT and KO cells at 5 and 11 mM glucose concentrations. Contrary to primary islets, where longer incubation times (>24h) led to normalization of GSIS in KO cells due to metabolic adaptation [143], we saw a consistent elevation of media insulin production by  $\beta$ TC3 KO cells compared to WT cells at both glucose concentrations examined (Fig. 3.3A). Measurement of intracellular insulin content also showed that KO cells not only secreted more insulin but also stored more insulin per cell and per cell surface area (Fig. 3.3B). Collectively, these results demonstrate that the engineered  $\beta$ TC3 KO cell clones had negligible G6PC2 activity and therefore provided a cellular model of *G6pc2* deletion. These results also further support our previously published results characterizing G6PC2 as a negative regulator of GSIS [142].

### **3.4.3 Assessment of metabolic fluxes reveals increased oxidative metabolism due to loss of G6PC2**

To elucidate the underlying mechanisms responsible for increased GSIS in *G6pc2* KO cells, we developed a  $\beta$ -cell specific mathematical model to determine metabolic fluxes from  $^{13}\text{C}$  labeling measurements. Stable isotope studies were initially conducted on parental  $\beta$ TC3 cells to determine the optimal tracers and incubation times required to reach isotopic steady state. These studies showed that glycolytic metabolites reached isotopic steady within 24h of incubation with  $[\text{U-}^{13}\text{C}_6]\text{glucose}$  (Fig. 3A.3A) whereas CAC metabolites did not reach isotopic steady state even after 72h of labeling (Fig. 3A.3B). In contrast to analyses with  $[\text{U-}^{13}\text{C}_6]\text{glucose}$ , using  $[\text{U-}^{13}\text{C}_5]\text{glutamine}$  isotopic steady state  $^{13}\text{C}$  enrichment of CAC metabolites was achieved between 12 and 24h of incubation (Fig. 3A.3C). Based on these data, we determined that parallel labelling experiments with  $[1,2\text{-}^{13}\text{C}_2]\text{glucose}$  and  $[\text{U-}^{13}\text{C}_5]\text{glutamine}$  for 24h would provide an optimal experimental design for steady-state MFA. These tracers were previously shown to produce measurements that are highly sensitivity to fluxes in glycolysis/PPP and CAC, respectively [24]. A metabolic model including glycolysis and the oxidative PPP was developed (Fig. 3.4A, Table S1) using previously established carbon atom transitions [24]. CAC metabolism was modeled using both oxidative





and reductive pathways (Fig. 3.4A, Table S1), the latter of which has been shown to promote GSIS in rat islets [132]. In addition to measurements of extracellular uptake and excretion rates (Fig. 3A.4), measured mass isotopomer distributions (MIDs) of several media and intracellular metabolites (Fig 3A.5, 3A.6) were also provided as inputs to the metabolic model in order to estimate intracellular fluxes using MFA (see *Experimental procedures* for details).

Similar to other mammalian cells [180], glucose and glutamine were the major carbon substrates utilized by  $\beta$ TC3 cells and were metabolized largely via the mitochondrial CAC (Fig. 3.4B-C). Excretion of overflow products (lactate, pyruvate, alanine and citrate) represented a minor fate for disposal of excess carbon (Fig. 3.4B-C, S4). Negligible fluxes were detected through oxidative PPP and to the overflow products aspartate, glycerol, malate, and succinate. Glycolytic and mitochondrial fluxes were substantially elevated in *G6pc2* KO cells compared to WT cells at both glucose concentrations examined. At 5 mM glucose, glycolytic ( $V_{PK}$ ) and mitochondrial ( $V_{CS}$ ) fluxes were ~67% and ~62% higher compared to WT cells (Fig. 3.4B), respectively. Increased oxidative fluxes were accompanied by a ~1.7 fold increase in serine ( $V_{PSP}$ ) and glutamine anaplerosis ( $V_{Gln.entry}$ ). Additionally, we observed significant increases in the excretion fluxes of pyruvate, alanine and citrate, but not lactate (Fig. 3.4B, 3A.4A). We observed similar increases in oxidative fluxes at 11 mM glucose, with glycolytic ( $V_{PK}$ ) and CAC ( $V_{CS}$ ) fluxes increased by ~60% and 56%, respectively, compared to WT cells (Fig. 3.4C). Anaplerosis from glutamine, but not serine, was ~1.8 fold higher in KO cells compared to WT cells. We also observed significant increases in the excretion fluxes of pyruvate, alanine and lactate, but not citrate (Fig. 3.4C).

While we saw a significant elevation in absolute glycolytic and mitochondrial fluxes in KO cells (Fig 3.5A), it was important to determine whether there were metabolic effects arising from the loss of G6PC2 that were independent of increased glycolysis. To accomplish that, we normalized all metabolic fluxes to the net glucokinase flux ( $V_{GK_{Net}}$ ). This normalization revealed more subtle changes in the relative distribution of glycolytic flux within KO cells. In particular, relative fluxes through pyruvate carboxylase

( $V_{PC}/V_{GK\ Net}$ ) and malic enzyme ( $V_{ME}/V_{GK\ Net}$ ) were increased in combination with a decrease in  $V_{MDH}/V_{GK}$  at both glucose concentrations (Fig. 3.5B-C, 3A.7A-B). In addition, we observed a shift in overflow products from increased pyruvate excretion at 5 mM glucose concentration, to increased pyruvate, lactate and alanine release at 11 mM glucose concentration, potentially due to a shift in the redox state of the KO cells (Fig 3.5B).

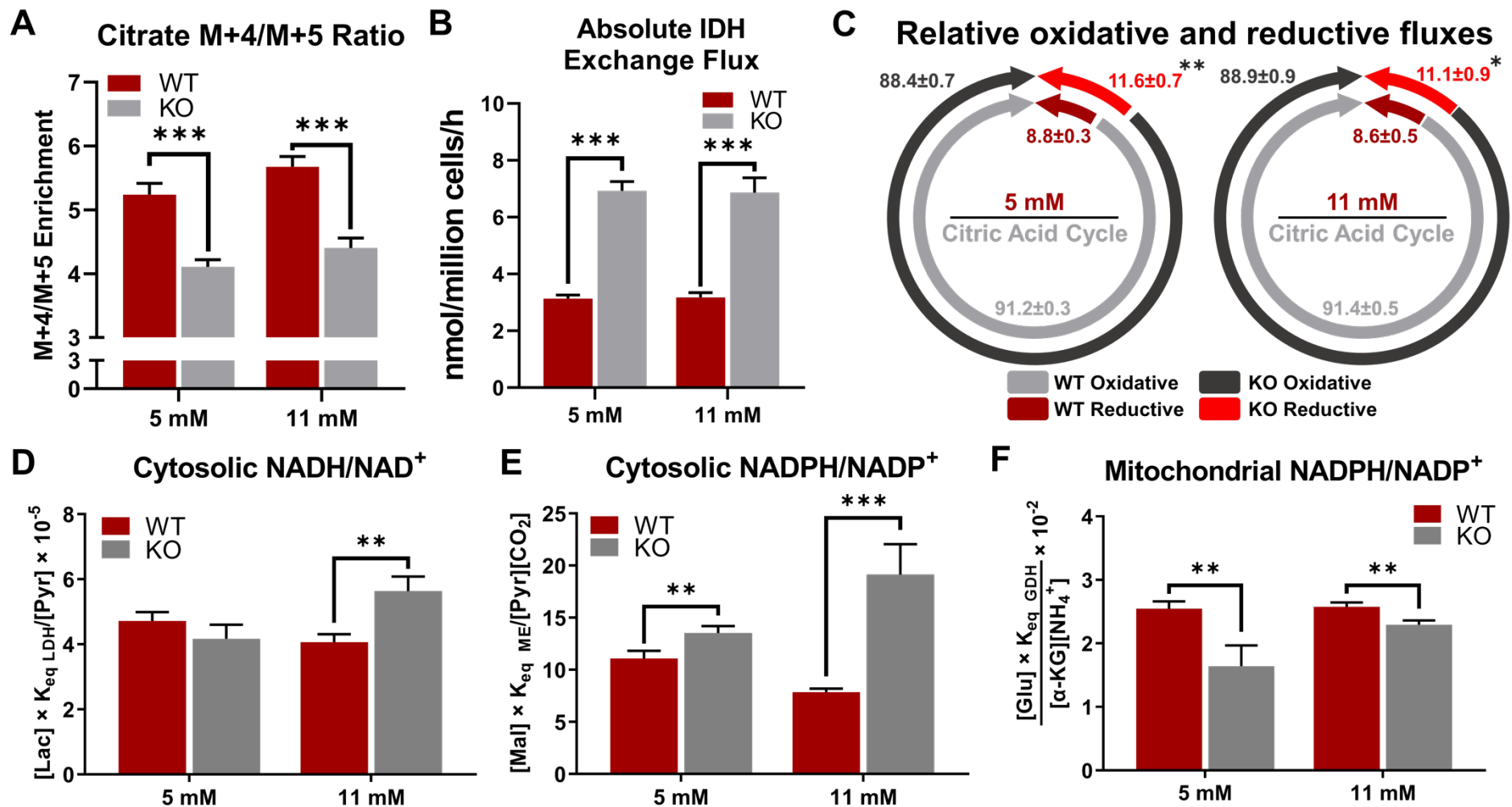
Interestingly, this normalization relative to net glucokinase flux also showed that the exchange flux between citrate and  $\alpha$ -ketoglutarate ( $\alpha$ -KG) was significantly elevated at both glucose concentrations, suggesting increased reductive activity of isocitrate dehydrogenase (IDH). Reductive carboxylation flux through mitochondrial IDH2 has been proposed as a mechanism that drives NADPH production by cytosolic IDH1, which acts as a coupling factor to regulate insulin secretion [132]. While our analysis cannot distinguish contributions from cytosolic and mitochondrial isoforms to the total IDH exchange flux, increased cycling between citrate and  $\alpha$ -KG is consistent with enhanced redox coupling between IDH1/2 in KO cells (Fig 3.5C). Furthermore, similar to data obtained in primary KO islets [142], we measured a significant elevation in baseline cytoplasmic calcium levels within the KO cells at 5 and 11 mM glucose concentrations (Fig 3.5D). Overall, these results show that deletion of *G6pc2* leads to a broad acceleration in glycolytic and mitochondrial metabolism, primarily by rerouting more glucose and glutamine towards oxidative pathways that supply ATP and redox cofactors linked to GSIS.

#### **3.4.4 Knockout of *G6pc2* promotes a reduced cytosolic redox potential in $\beta$ TC3 cells**

Our assessment of metabolic fluxes suggested the activation of reductive IDH flux and NADPH-producing pathways that have previously been implicated in augmenting GSIS [132], [181]. To further investigate the increase in reductive carboxylation seen in KO cells, we analyzed the MID of intracellular citrate (Fig. 3.6A). Oxidation of labelled glutamine through the forward progression of the CAC results in M+4 enrichment of citrate. In contrast, M+5 citrate is indicative of reductive carboxylation of  $\alpha$ -KG by IDH2

[132]. A significantly lower (M+4)/(M+5) ratio was observed in KO cells, consistent with a 2-fold increase in IDH exchange flux estimated by  $^{13}\text{C}$  MFA at both glucose concentrations (Fig. 3.6B). To test if the increased IDH exchange flux is secondary to increased mitochondrial flux, we normalized the metabolic fluxes to CAC activity ( $V_{\text{CS}}$ ). Even after this normalization, the reductive IDH flux was significantly higher in KO cells compared to the WT cells at both glucose concentrations (Fig. 3.6C). This shows that if equal amount of carbon enters in the CAC of WT and KO cells, a higher percentage is routed through the reductive carboxylation pathway.

The redox state of  $\beta$ -cells during glucose stimulation is tightly correlated with their capacity for GSIS [132], [182]. Therefore, using classical equations and metabolite concentrations (see *Experimental procedures*) [175], we determined the metabolic redox state in WT and KO cells. Cytosolic NADH/NAD<sup>+</sup> was unchanged at 5 mM glucose concentration but was increased at 11 mM glucose concentration (Fig. 3.6D). This is consistent with a 55% decrease in pyruvate excretion flux (Fig. 3A.4A-B) along with a 60% increase in  $V_{\text{LDH}}/V_{\text{GK}}$  flux in KO cells (Fig. 3.5A) from 5 to 11 mM glucose concentration. Additionally, increased malic enzyme and IDH activity was associated with significant elevation in cytosolic NADPH/NADP<sup>+</sup> ratios at both 5- and 11 mM glucose concentrations (Fig. 3.6E). In agreement with the increase in cytosolic NADPH/NADP<sup>+</sup> ratio, the mitochondrial NADPH/NADP<sup>+</sup> fraction was reduced in the KO cells at both glucose concentrations (Fig. 3.6F). These results can be explained by the increase in IDH exchange flux, which has been proposed as a mechanism to transfer reductant (in the form of NADPH) from the mitochondria to the cytosol through the concerted action of IDH1/2 isozymes and the mitochondrial citrate/isocitrate carrier [132]. Importantly, flux through the reductive carboxylation and the malic enzyme pathways was upregulated by 67% and 32% in the KO cells, respectively, independent of the elevated glucose uptake rate (Fig. 3.5C). Overall, these results show that ablation of *G6pc2* alters the cytosolic and mitochondrial redox state through upregulation of pathways connected with cytosolic NAD(P)H production, separate from its effects on glycolytic metabolism.



**Figure 3.6: Knockout of G6pc2 promotes a reduced redox potential in  $\beta$ TC3 cells**

A) Ratio of M+4/M+5 isotopomer enrichment in *G6pc2* WT and KO  $\beta$ TC3 cells labeled with [U-<sup>13</sup>C<sub>5</sub>]glutamine at 5 and 11 mM glucose concentrations. Data represent means±SEM, \*\*\*p<0.01 (n=3).

B) Absolute exchange flux through isocitrate dehydrogenase ( $V_{\text{IDH Exch}}$ ) in *G6pc2* WT and KO  $\beta$ TC3 cells labeled with [U-<sup>13</sup>C<sub>5</sub>]glutamine at 5 and 11 mM glucose concentrations. Data represent means±SEM, \*\*\*p<0.01 (n=3).

C) Oxidative ( $V_{\text{IDH Net}}$ ) and reductive fluxes ( $V_{\text{IDH Exch}}$ ) relative to total citrate synthase flux ( $V_{\text{CS}}$ ) in *G6pc2* WT and KO  $\beta$ TC3 cells labeled with [U-<sup>13</sup>C<sub>5</sub>]glutamine at 5 and 11 mM glucose concentrations. Data represent means±SEM, \*\*p<0.05, \*p<0.10 (n=3).

D) Cytosolic NADH/NAD<sup>+</sup> assessed by pyruvate/lactate ratio in *G6pc2* WT and KO  $\beta$ TC3 cells at 5 and 11 mM glucose concentrations. Data represent means±SEM, \*\*p<0.05 (n=3)

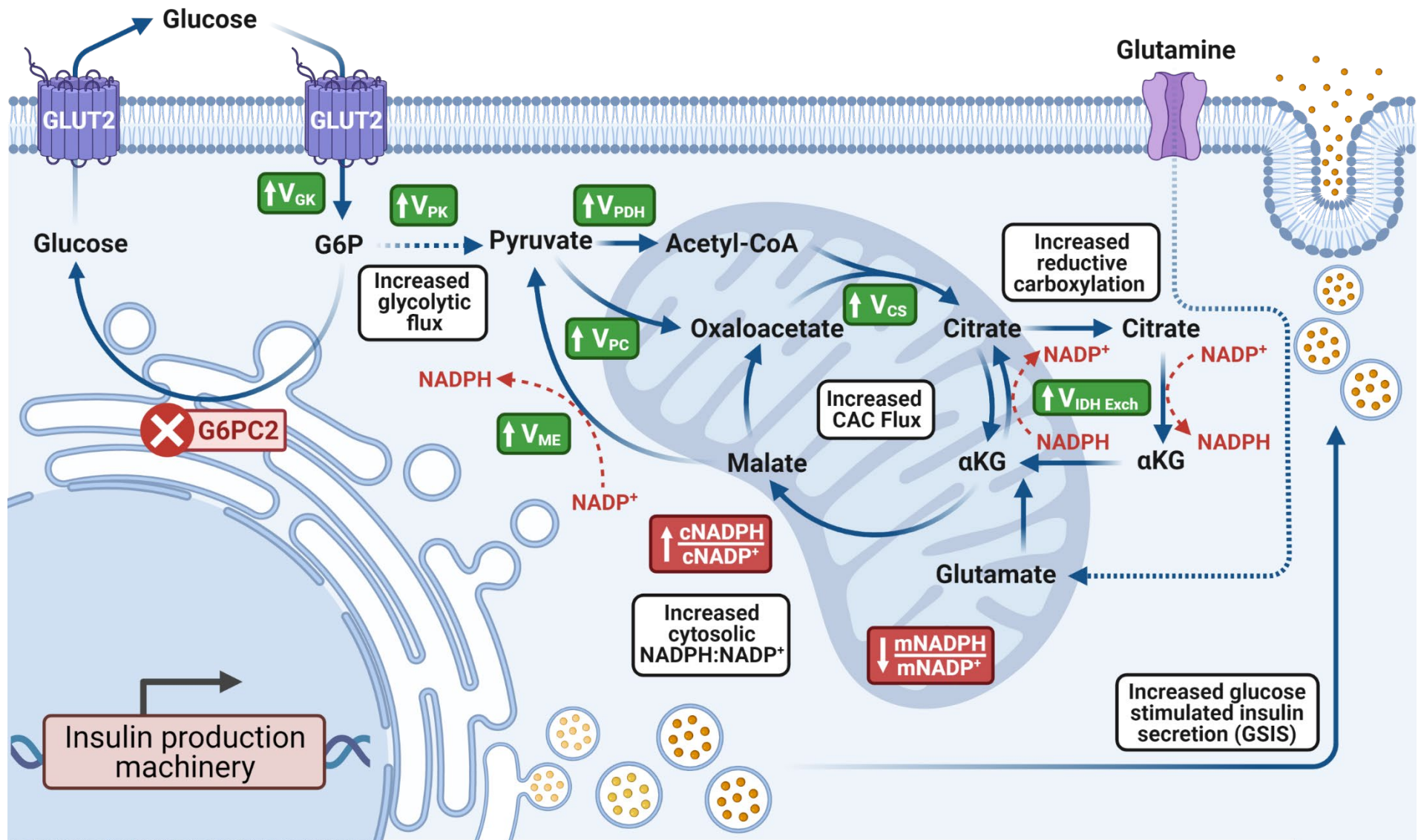
E) Cytosolic NADPH/NADP<sup>+</sup> assessed by malate/pyruvate ratio in *G6pc2* WT and KO  $\beta$ TC3 cells at 5 and 11 mM glucose concentrations. Data represent means±SEM, \*\*\*p<0.01, \*\*p<0.05 (n=3).

F) Mitochondrial redox state (NAPDH/NADP<sup>+</sup>) indicated by the [ $\alpha$ -KG][NH<sub>4</sub>]/[Glu] ratio in *G6pc2* WT and KO  $\beta$ TC3 cells at 5 and 11 mM glucose concentrations. Data represent means±SEM, \*\*\*p<0.01, \*p<0.10 (n=3)

### 3.5 Discussion

Prior studies on G6PC2 have shown that it negatively regulates glucose stimulated insulin secretion and elevates fasting blood glucose *in vivo* [142]. However, while G6PC2 is predicted to control the fate of G6P, its effect on islet metabolism remains largely unknown. Here, using a mathematical modeling approach, we have quantified the metabolic effect of G6PC2 on  $\beta$ -cell metabolism and GSIS. Our results show that deletion of *G6pc2* not only affects glycolytic flux but also, as expected, increases CAC flux. However, even after normalizing for the increased glycolytic flux, an increase in CAC flux and NADPH producing pathways is still apparent (Fig. 3.7). As observed in *G6pc2* KO islets, we see that the deletion of *G6pc2* in  $\beta$ TC-3 cells increases GSIS. More importantly, we show, again by normalizing for the increased glycolytic flux, that while this increase in GSIS is largely fueled by elevated glycolytic flux, it is also bolstered by the influence of G6PC2 on downstream mitochondrial pathways. Additionally, these findings again challenge the existing dogma that GK alone regulates glycolytic flux and show that G6PC2 plays a pivotal role in glucose sensitivity of  $\beta$ -cells.

Our results here extend the previous findings on the metabolic control exerted by glucokinase on glycolysis [183], [184]. Our revised model here suggests that GK and G6PC2 together help regulate glycolytic flux, as the loss of the latter increases glycolytic flux and insulin secretion. Glycolytic flux and insulin secretion in  $\beta$ -cells have also been associated with the pentose monophosphate shunt, which is an important generator of NADPH and precursor nucleotides [135], [140]. Our metabolic model showed minimal oxidative flux through the pentose phosphate pathway in both WT and KO cells, although we did see a significant increase in the ratio of cytosolic NADPH to  $\text{NADP}^+$ . Also, our model estimated significant upregulation of pyruvate kinase flux ( $V_{\text{PK}}$ ), which recently has been implicated as a dominant regulatory node of glycolysis and insulin secretion [141]. The increase seen in  $V_{\text{PK}}$  in our steady-state metabolic model is secondary to the increase in  $V_{\text{GK Net}}$ , indicative of the latter stage of the 2-state model proposed by Lewandowski et. al [141]. While others have suggested mitochondrial GTP and PEP cycling as insulin amplifying signals [138], [185],



**Figure 3.7: Schematic illustrating the effect of G6pc2 KO on oxidative metabolism, energetics, and insulin secretion of  $\beta$ TC3 cells**

Ablation of G6pc2 leads to increased glycolytic and citric acid cycle (CAC) flux. Cyclic flux through IDH and other putative NADPH-producing pathways is also upregulated along with an increase and a decrease in cytosolic(c) and mitochondrial(m) NADPH:NADP<sup>+</sup> ratios, respectively. A combination of these metabolic perturbations, previously associated with increased GSIS (23), result in enhanced insulin production and release. Created with BioRender.com

we measured negligible enrichment in PEP post incubation with  $^{13}\text{C}_5$  glutamine labelled media (Fig. 3A.9). PEP cycle and PEPCK-M have been shown to be active prior to membrane depolarization [141], whereas our model captures oxidative steady-state metabolism after depolarization and calcium entry when PDH and CAC flux is high and PEPCK-M activity is minimized.

As expected, increasing the glucose concentration in the parental, WT and KO  $\beta$ TC3 cells led to an overall increase in the uptake and excretion fluxes. Several potential pathways have been implicated in regulating excess-fuel detoxification in  $\beta$ -cells, including pyruvate, lactate, alanine, glutamate and more recently, free fatty acids (FFA) and glycerol [186], [187]. The recent discovery of a mammalian glycerol-3-phosphate phosphatase (G3PP) has been associated with linear increases in glycerol production with increasing glucose concentrations within murine pancreatic islets [186], [188]. The inclusion of this pathway, along with the enrichment measurements of glycerol-3-phosphate and glycerol, in our metabolic model showed a >2-fold increase in glycerol release flux in KO cells at both glucose concentrations (Fig. 3.4B-C, 3A.4A-B). However, compared to other metabolites, the overflow of carbon through G3PP was still limited in magnitude. Instead, we saw that increased oxidative metabolism in KO cells is supported by an increase in the net uptake and excretion of several glycolytic metabolites centered around the pyruvate node (Fig. 3A.4). At lower glucose concentrations, relative to  $V_{\text{GK net}}$ , only pyruvate release was significantly elevated with a decrease in  $V_{\text{LDH}}$  and no changes in alanine excretion (Fig 3.5B). However, at higher glucose concentrations, we saw an increase  $V_{\text{Pyr release}}/V_{\text{GK net}}$ ,  $V_{\text{LDH}}/V_{\text{GK net}}$  and  $V_{\text{ALT}}/V_{\text{GK net}}$  in the KO cells (Fig 3.5B, 3A.4B). This is consistent with recent findings [187], wherein  $\beta$ -cells pyruvate responds most strongly to increasing fuel pressure, potentially to maintain redox equilibrium. Interestingly, the metabolic flux analysis results (Fig. 3.4B-C) also showed a concurrent increase in glutamine uptake flux with rising glucose concentrations, fueling increased CAC activity along with glycolysis. These results indicate that despite the loss of G6PC2, a tight coupling between glycolysis and mitochondrial metabolism is maintained, a hallmark of  $\beta$ -cells [189].

While G6PC2 is closely connected with glycolysis, our studies also showed the upregulation of several mitochondrial pathways, independent of increased glucose uptake rate, associated with enhancements in insulin secretion. Similar to our results (Fig. 3.7), increased anaplerosis through pyruvate carboxylase [126], enhanced pyruvate recycling via malic enzyme [190] and upregulation of reductive flux through the isocitrate–IDH1/IDH2 pathway [132] have all been associated with upregulation in GSIS. Consistent with increased flux from  $V_{ME}$  and  $V_{IDH}$ , we also measured an increase in cytosolic NADPH:NADP<sup>+</sup> ratio along with a slight but significant decrease in mitochondrial NADPH:NADP<sup>+</sup> ratio. Cytosolic NADPH production has previously been shown to drive the reduction of glutathione (GSH) by GSH reductase [133], [191]. This leads to the activation of glutaredoxin (GRX1), which mediates the reduction and activation of sentrin/SUMO-specific protease 1 (SENP1) [133]. SENP1 then acts as a deSUMOylase that removes SUMO peptides from secretory granule-trafficking proteins to enhance insulin exocytosis [192]. Increased flux through NADPH producing pathways due to the loss of G6PC2 (Fig. 3.5C) thus may be responsible for increased GSIS in the KO cells (Fig. 3.3). Additionally, at higher glucose concentrations, we also saw an increase in cytosolic NADH:NAD<sup>+</sup> ratio along with upregulation of  $V_{LDH}$  and  $V_{Lac\ Release}$ , factors indicative of hyperglycemia [193]. Together these results indicate that reductive CAC flux, an important coupling factor that regulates insulin secretion [132], is increased upon the loss of G6PC2.

Since G6PC2 is an islet specific isoform of glucose-6-phosphatase, it can directly control the concentration of G6P present in the  $\beta$ -cells. Elevated G6P levels can lead to a reduction in the calcium accumulation in the endoplasmic reticulum through the metabolite's ability to lower sarco-endoplasmic reticulum calcium ATPase (SERCA) activity [194]. More importantly, inhibition of glucose-6-phosphatase has been shown to lower Ca<sup>2+</sup> sequestration in endoplasmic reticulum of permeabilized islets [195]. Therefore, glycolytic and mitochondrial flux increases seen here (Fig 3.5A,C) due to the knockout of G6PC2 may directly be associated with changes in calcium signaling in the ER and the cytosol of  $\beta$ TC3 cells. Regulation of mitochondrial pathways by calcium, through allosteric interactions or otherwise, is well understood for



many enzymes in central carbon metabolism. Increased calcium levels are known to activate multiple dehydrogenases in the CAC, such as isocitrate dehydrogenase and  $\alpha$ -ketoglutarate dehydrogenase, stimulating the respiratory chain and ATP supply [196]. More importantly, consistent with our results (Fig. 3.5D), previous studies in *G6pc2* KO mice islets have also shown elevated cytoplasmic calcium levels along with enhanced glycolytic flux [142], [145]. Our flux, cytoplasmic calcium and redox results here suggest that G6PC2, through the suppression of calcium signaling, exerts control not only on glycolytic but also mitochondrial metabolism. Future studies will focus on better understanding the role of G6PC2 on calcium signaling in the ER and the cytosol.

Several genome-wide association studies (GWAS) have identified multiple genetic variants in *G6PC2* to be associated with fasting blood glucose levels [197], [198], with studies suggesting that single nucleotide polymorphisms (SNPs) in *G6PC2* affect RNA splicing [199], protein expression [200] and DNA methylation [201]. Consistent with previous findings [142] and our results, a recent study in human EndoC- $\beta$ H1 cell line shows that knockdown of G6PC2 increases insulin secretion at submaximal glucose concentrations [202]. However, contrary to the results of Ng et al. [202], our study shows an increase, as opposed to a decrease, in intracellular insulin content upon ablation of *G6pc2*. A different result was seen in *G6pc2* KO islets where no change in intracellular insulin content was observed despite increased insulin secretion [142]. These apparently inconsistent results may partly be explained by differences in the duration of glucose stimulation. Unlike Pound. et. al. [142] and Ng et al. [202], where the cells were exposed to glucose for 30 minutes to an hour, in our study we incubated the cells in glucose for 24h. This may have resulted in increased insulin mRNA transcription and translation, since longer incubations have been shown to upregulate proinsulin mRNA levels [203].

Our metabolic model (Fig. 3.4A, Table 3A.1) relies upon some fundamental modelling assumptions that introduce some inherent limitations. Firstly, we assume that the citrate enrichment is equivalent to that of isocitrate. This is a safe assumption since no carbon rearrangements are known to occur at the aconitase

reaction at equilibrium [204]. Secondly, the oxidative IDH reaction modeled in our network does not differentiate between the flux through cytosolic IDH (IDH1) and mitochondrial IDH (IDH2/3) and represents the total flux through both enzymes. Given the identical carbon transitions between IDH isoforms, deconvolution of these pathways is inherently challenging and future studies requiring the expression of exogenous reporter systems may be needed to resolve compartment specific IDH fluxes [205]. Third, use of only glucose and pyruvate measurements, two metabolites typically used to assess the contribution of PPP to glycolysis [206], provided limited resolution of pentose phosphate pathway (PPP) flux. Future studies, benefiting from the use of LC-MS/MS platforms, will be needed to measure enrichment in pentose intermediates to better resolve the intermediary fluxes within the pathway. Finally, although all data pertaining to knockout of *G6pc2* confirms its role as a negative regulator of oxidative metabolism, operation of the pathways described herein remains to be tested in primary mouse and human islets. These studies are feasible but challenging in light of the longer incubation times needed for  $^{13}\text{C}$ -MFA, leading to *ex vivo* culture adaptations, feedback effects due to media insulin build up along with functional heterogeneity of human islet aliquots obtained from different donors.

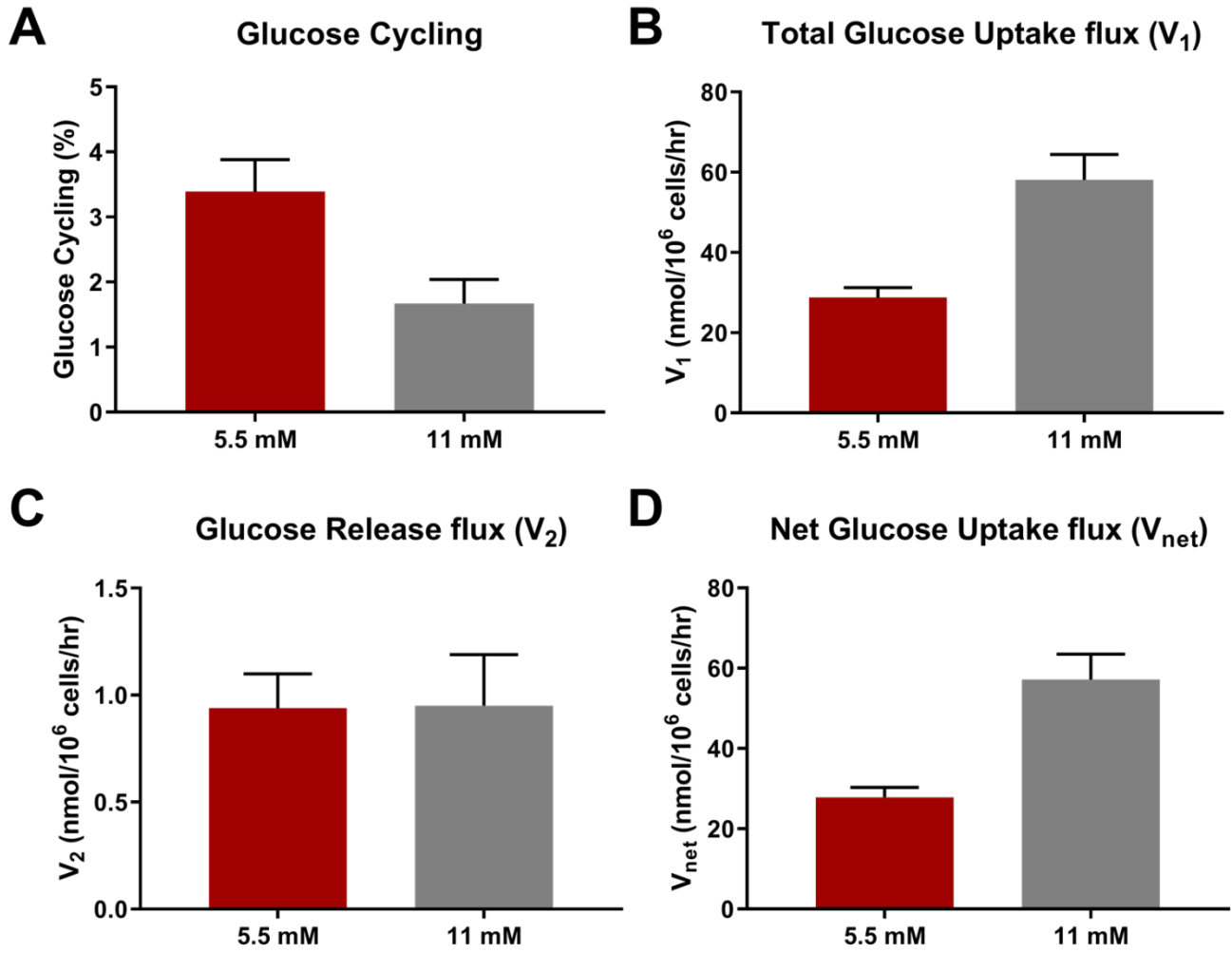
In conclusion, the data presented in this study show that G6PC2 acts as a negative regulator of oxidative metabolism and GSIS. Our findings suggest that G6PC2, together with GK, regulates glycolysis, citric acid cycle activity and pathways that control NADPH and insulin production. More importantly, these results validate our hypothesis that knockout of *G6pc2* causes a leftward shift in the dose-response curve for GSIS and is a potential target for enhancing insulin secretion. Since elevated *G6PC2* expression is associated with increased FBG levels and thus heightened risk for cardiovascular-associated mortality (CAM) *in vivo* [199], [207], our study also suggests that G6PC2 inhibitors would be useful for lowering FBG and the risk of CAM. However, one needs to be judicious in interpreting these findings as recent studies suggest that under specific physiological conditions, such as prolonged fasting and ketogenic feeding, G6PC2 offers protection against hypoglycemia [178]. Future studies will involve understanding the direct and/or indirect

signals that result in the metabolic changes brought about by the deletion of *G6pc2*. Finally, deeper exploration of the potential role of G6PC2 in development of, or compensation for,  $\beta$  cell failure in T2D remains to be explored in genetic and dietary animal models.

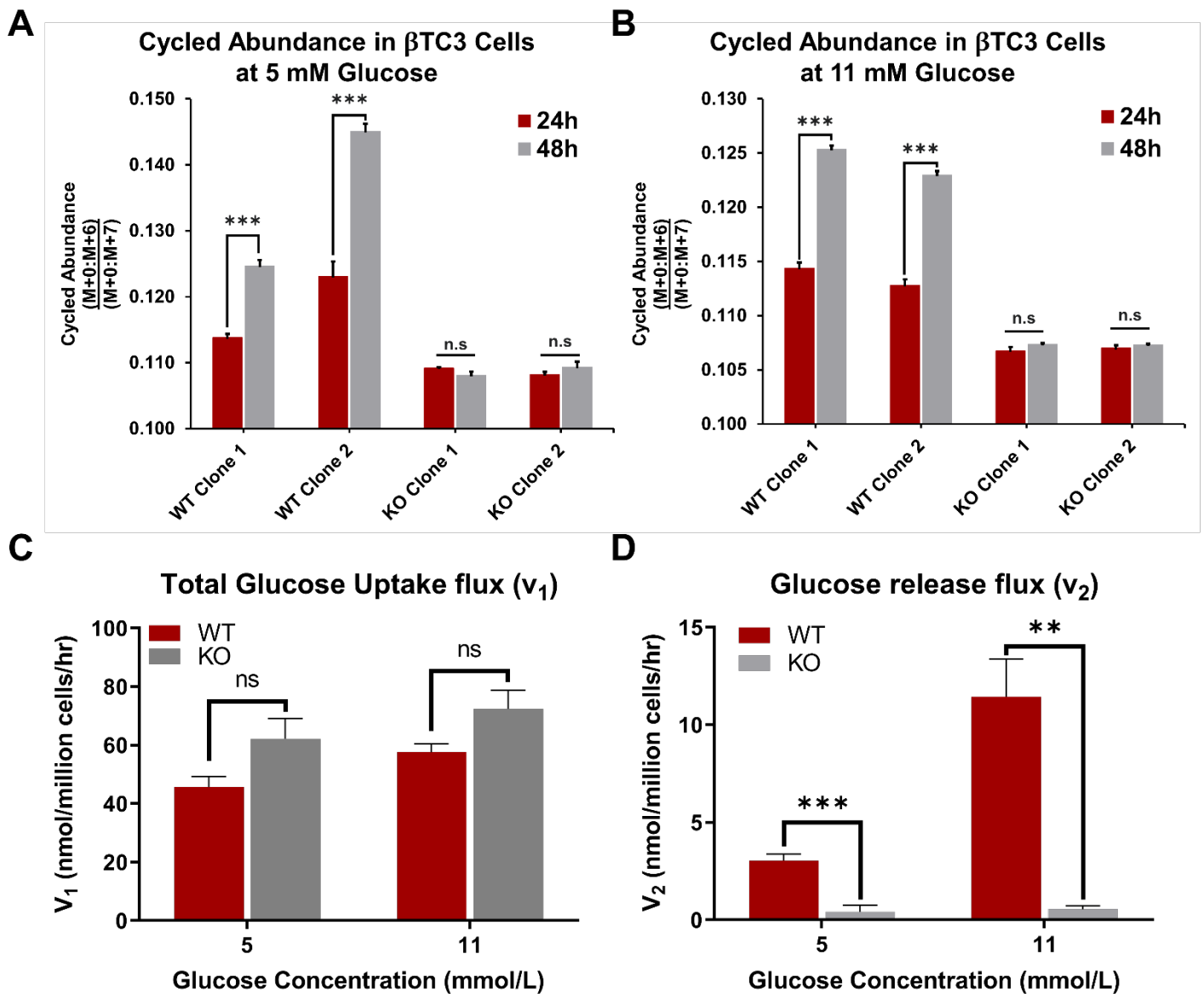
### **3.6 Acknowledgements**

We thank Susan Hajizadeh for performing insulin assays. This research was supported by the following grants: J.D.Y DK106348; R.O'B., DK92589. The measurement of media insulin by the Vanderbilt Hormone Assay & Analytical Services Core were supported by NIH grant P60 DK20593 awarded to the Vanderbilt Diabetes Research Training Center. Additionally, we would like to thank the Jacobson lab, in particular Arya Nakhe, for obtaining cytosolic calcium measurements.

3.7 APPENDIX: Supplemental figures and tables

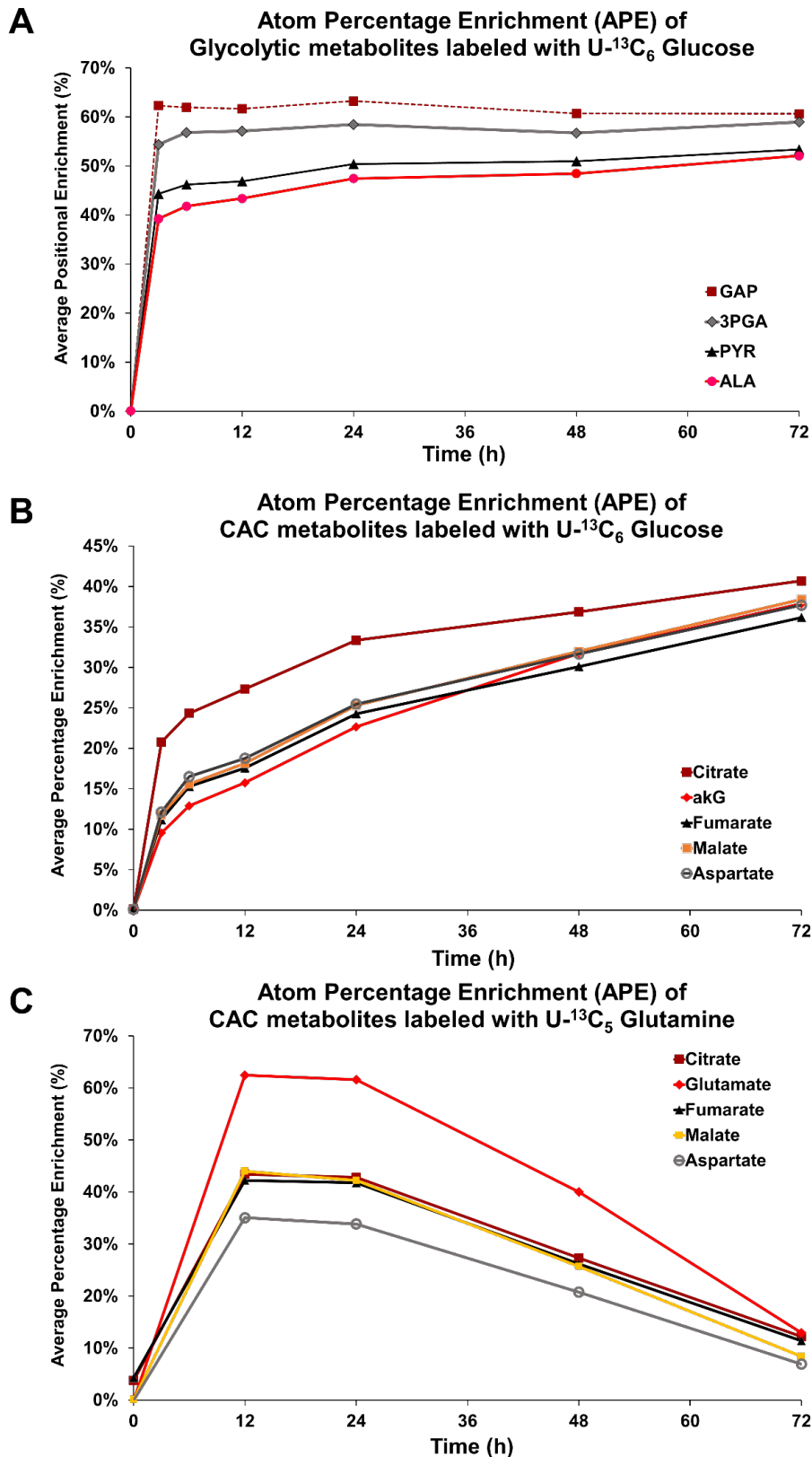


**Figure 3A.1 Measurement of glucose uptake and release fluxes in INS-1 832/13 rat insulinoma cells**  
Measurement of (A) glucose cycling, (B) total glucose uptake flux ( $v_1$ ), (C) total glucose release flux ( $v_2$ ), and (D) net glucose uptake flux ( $v_{net}$ ) at 5 and 11 mM glucose concentrations in INS-1 832/13 cells. Data represent means $\pm$ SEM (n=3).



**Figure 3A.2: Cycled abundance in two biological replicates of *G6pc2* WT and KO  $\beta$ TC3 single cell clones at 5 and 11 mM glucose concentrations**

Cycled abundance, which is the ratio M+0:M+6 isotopomers to M+0:M+7 isotopomers, measured in cell media taken at 24h and 48h after incubation with [1,2,3,4,5,6, $^2$ H $_7$ ]glucose at (A) 5 mM and (B) 11 mM glucose concentrations. Data represent means $\pm$ SEM, \*\*\* $p$ <0.01 (n=3). (C) Total glucose uptake flux ( $v_1$ ) and (D) Total glucose release flux ( $v_2$ ) measured in  $\beta$ TC3 *G6pc2* WT and KO cells. Data represent means $\pm$ SEM (n=3).

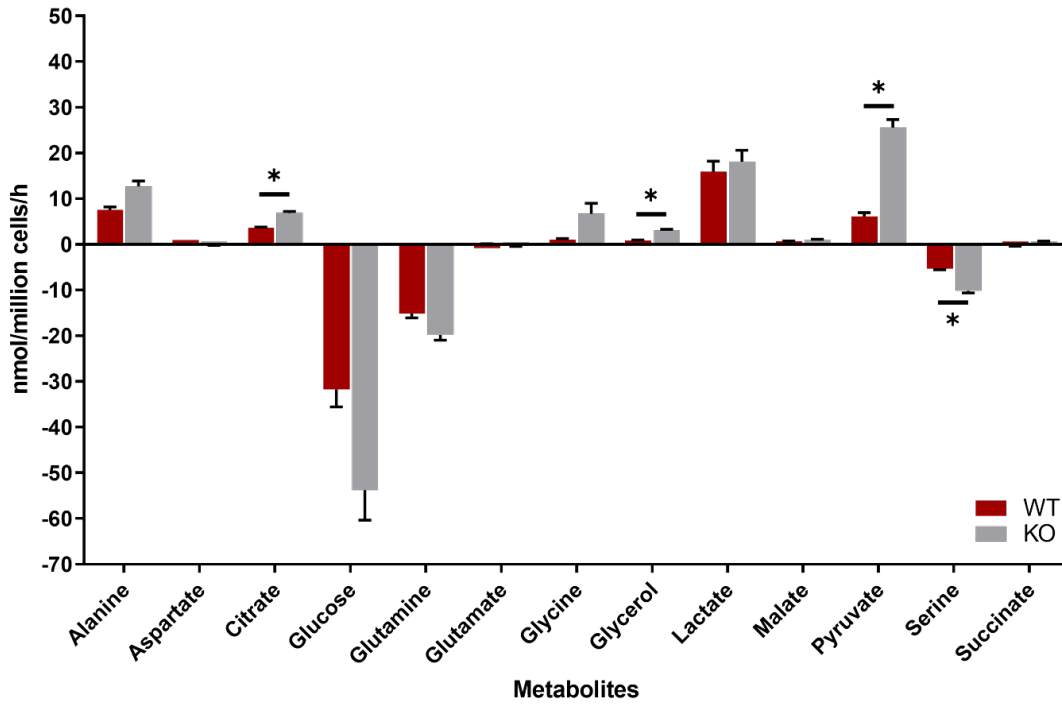
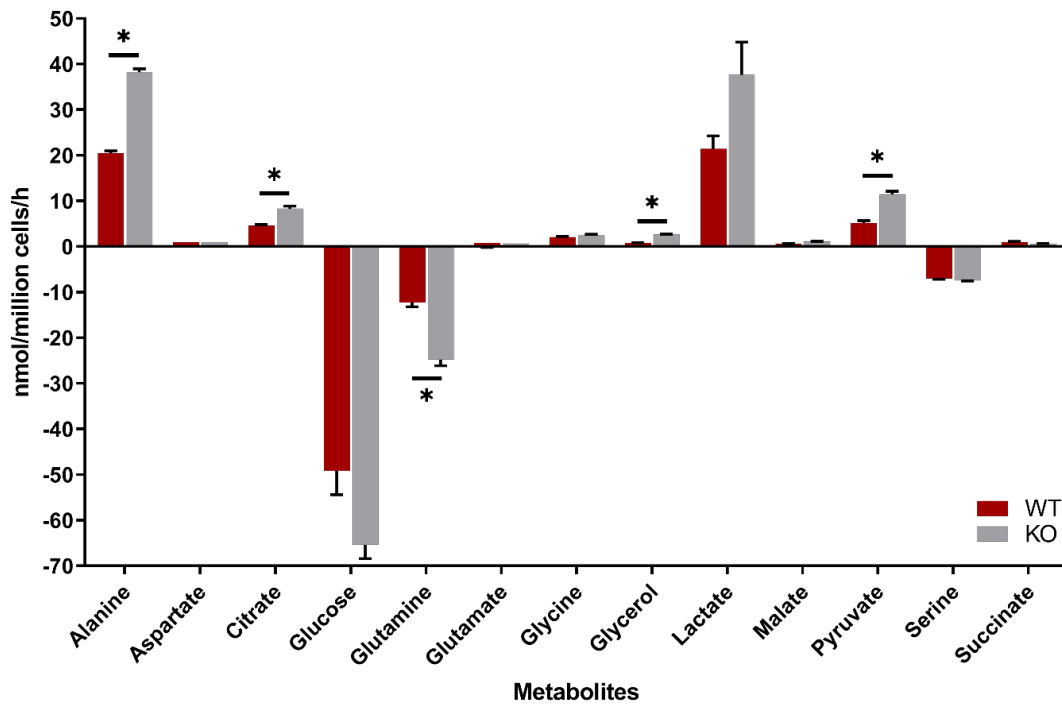


**Figure 3A.3: Atom percentage enrichment (APE) in metabolites over time to determine isotopic steady state in isotope labelling experiments**

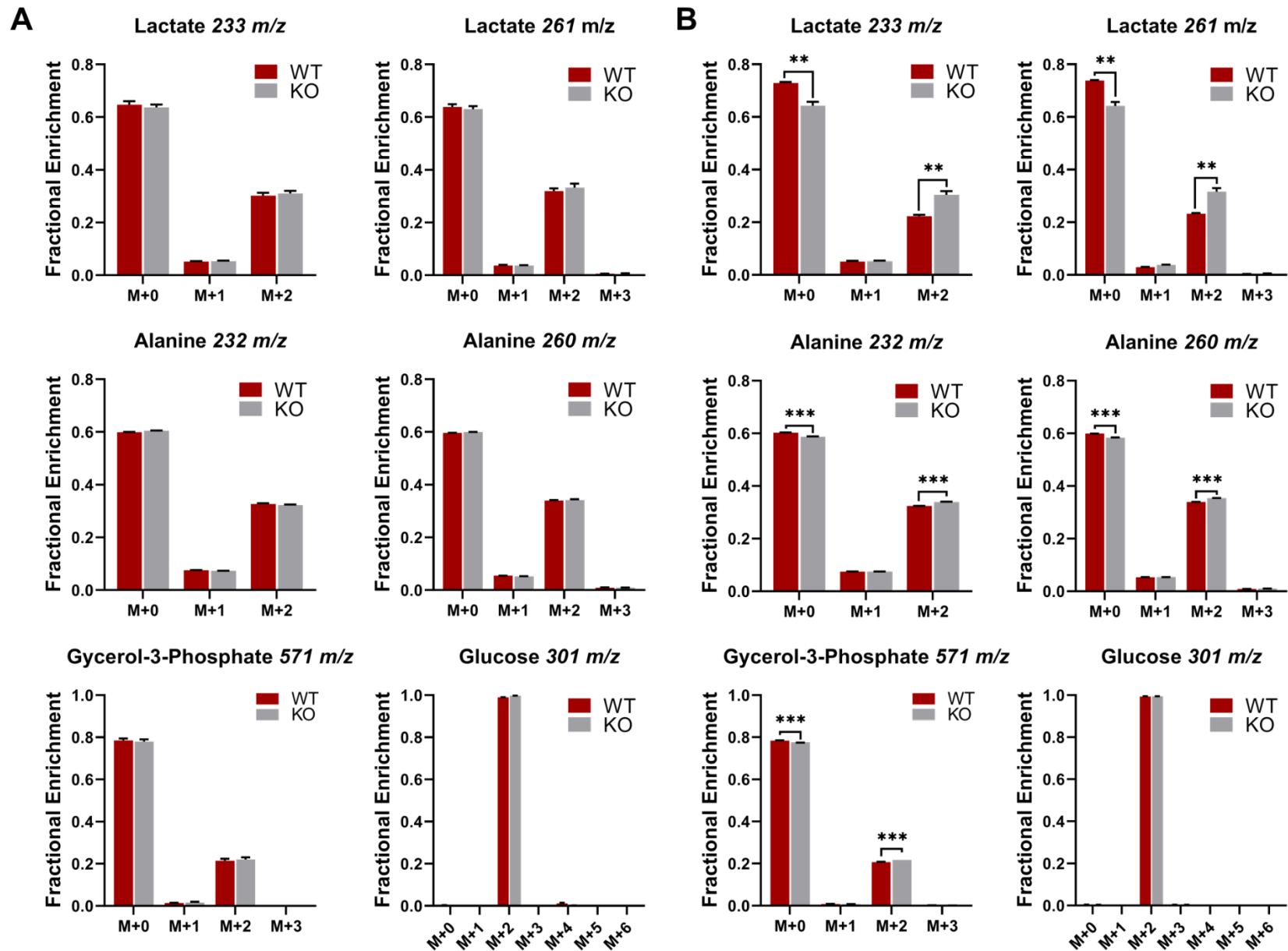
A) APE in glycolytic metabolites reaches steady state within 24h when labelled with 11 mM [U-<sup>13</sup>C<sub>6</sub>]glucose.

B) APE in CAC metabolites continues to increase in enrichment over 72h when labelled with 11 mM [U-<sup>13</sup>C<sub>6</sub>]glucose.

C) APE in CAC metabolites reaches steady state between 12 to 24h when labelled with 2 mM [U-<sup>13</sup>C<sub>5</sub>]glutamine.

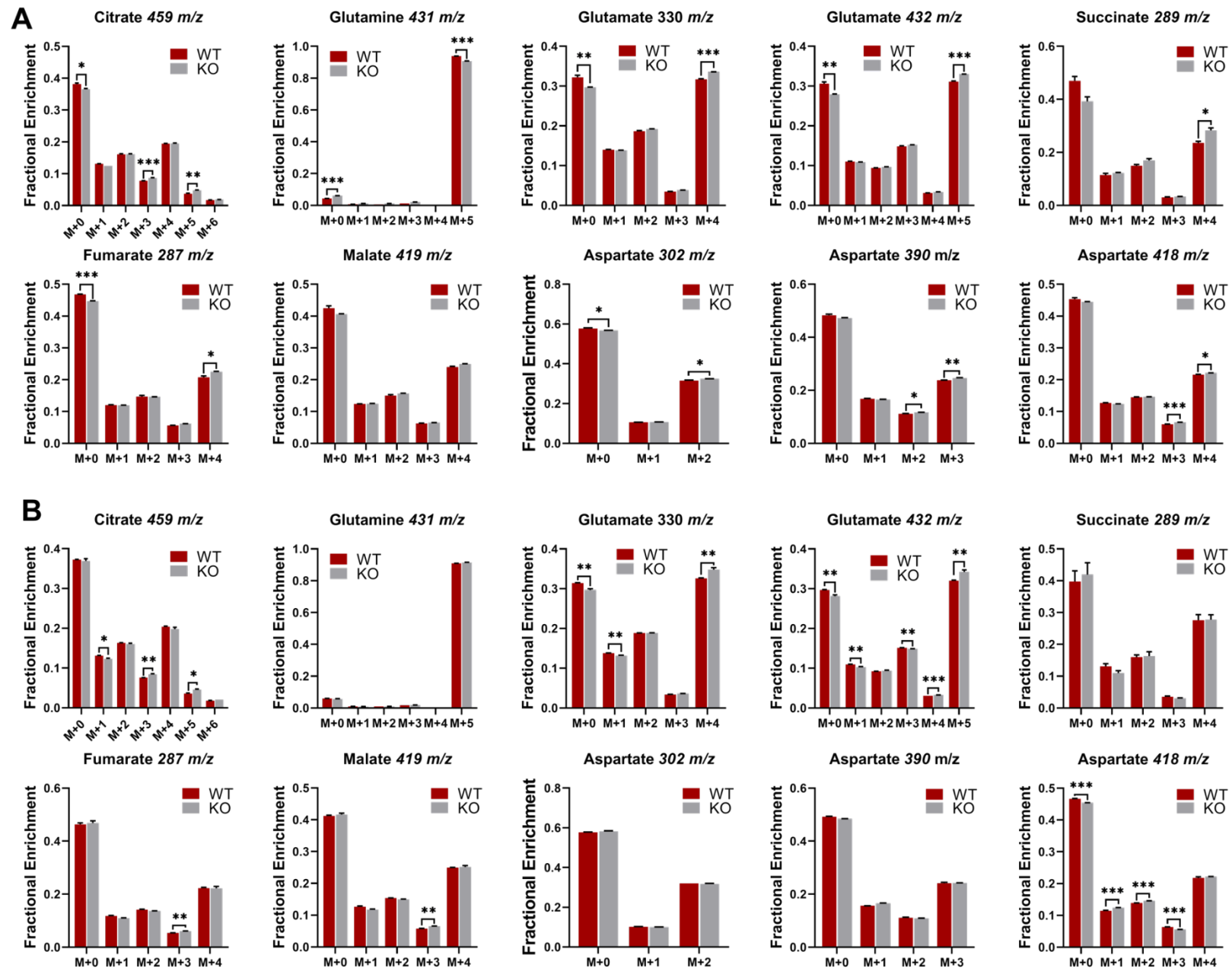
**A****Absolute Extracellular Fluxes - 5 mM Glucose****B****Absolute Extracellular Fluxes - 11 mM Glucose****Figure 3A.4: Extracellular uptake and excretion rates in *G6pc2* WT and KO  $\beta$ TC3 cells**

Extracellular uptake and excretion measured in *G6pc2* WT and KO  $\beta$ TC3 cells incubated at (A) 5 and (B) 11 mM glucose concentrations. Positive values represent excretion fluxes while negative values indicate net uptake of metabolite. Data represent means $\pm$ SEM, \* $p$ <0.05 (n=3).



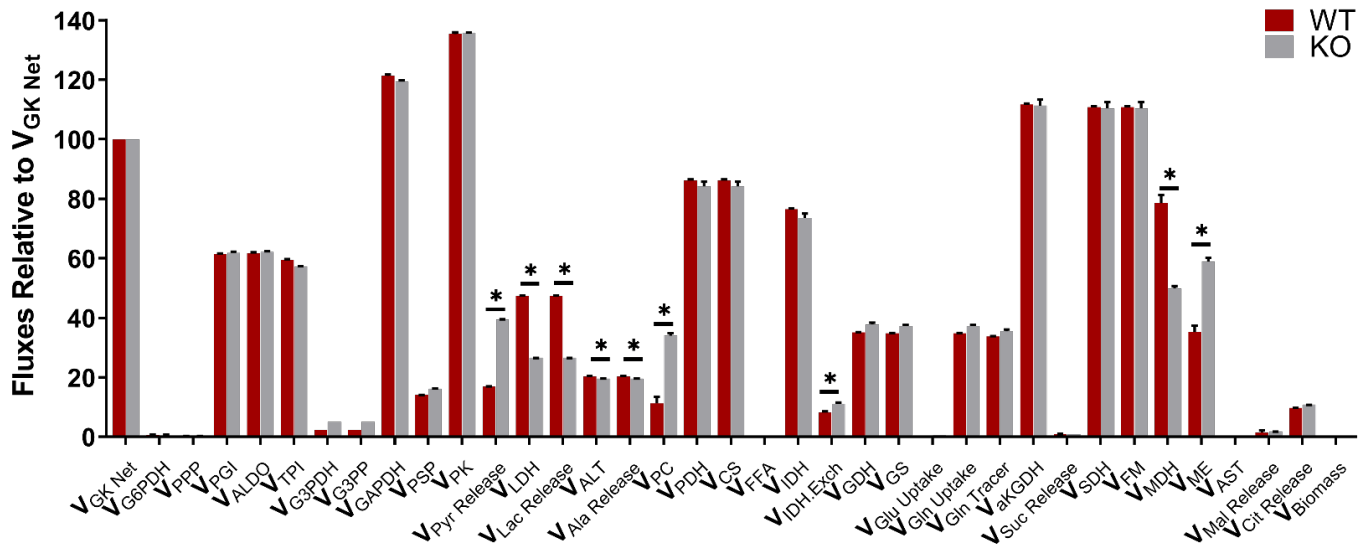
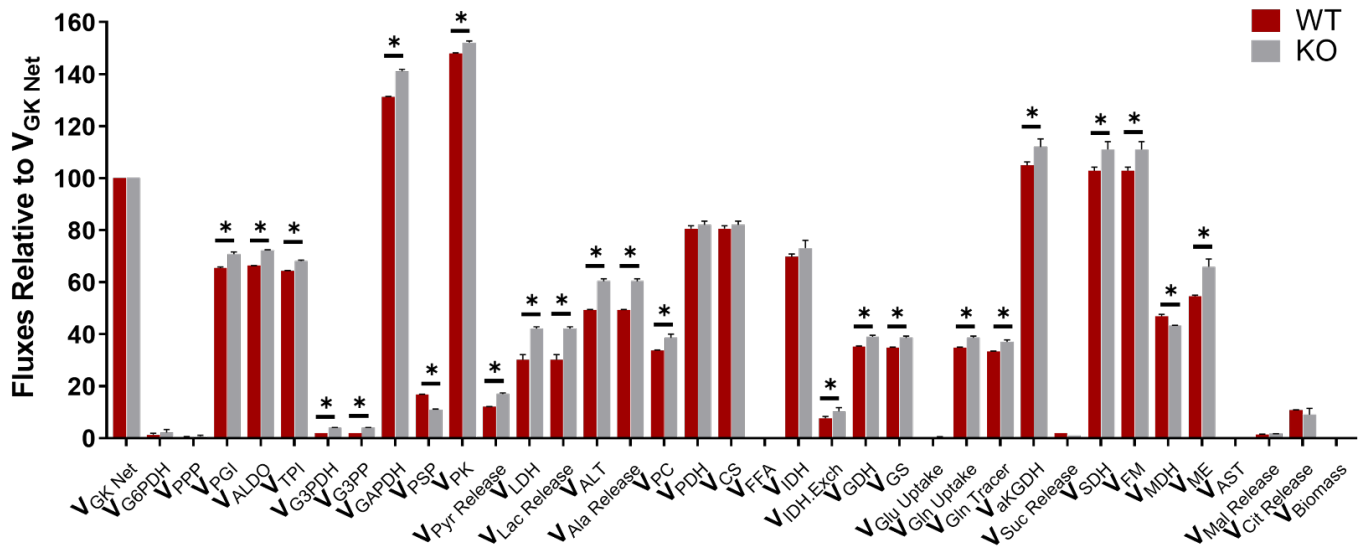
**Figure 3A.5 :Enrichment of glycolytic metabolites in *G6pc2* WT and KO  $\beta$ TC3 cells labeled with [1,2- $^{13}$ C $_2$ ]glucose**  
 Intracellular enrichment in glycolytic metabolites measured in *G6pc2* WT and KO  $\beta$ TC3 cells incubated with (A) 5 and (B) 11 mM [1,2- $^{13}$ C $_2$ ]glucose. Data represent means $\pm$ SEM, \*\*\* $p$ <0.01, \*\* $p$ <0.05 (n=3).



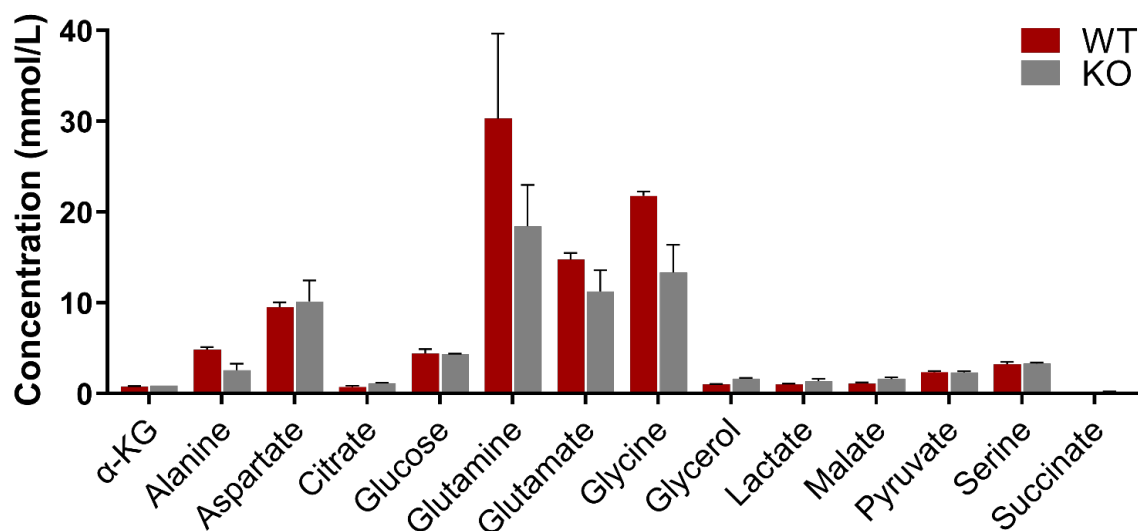
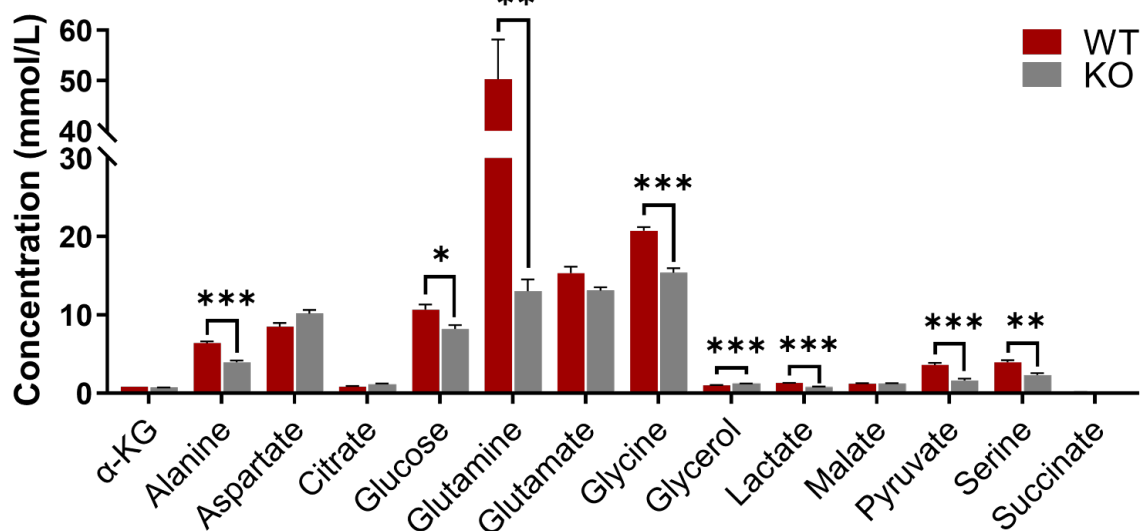


**Figure 3A.6: Enrichment of CAC metabolites in *G6pc2* WT and KO  $\beta$ TC3 cells labeled with 2 mM [U- $^{13}$ C $_5$ ]glutamine**

Intracellular enrichment in CAC metabolites measured in *G6pc2* WT and KO  $\beta$ TC3 cells incubated with (A) 5 and (B) 11 mM glucose. Data represent means $\pm$ SEM, \*\*\* $p$ <0.01, \*\* $p$ <0.05 ( $n$ =3).

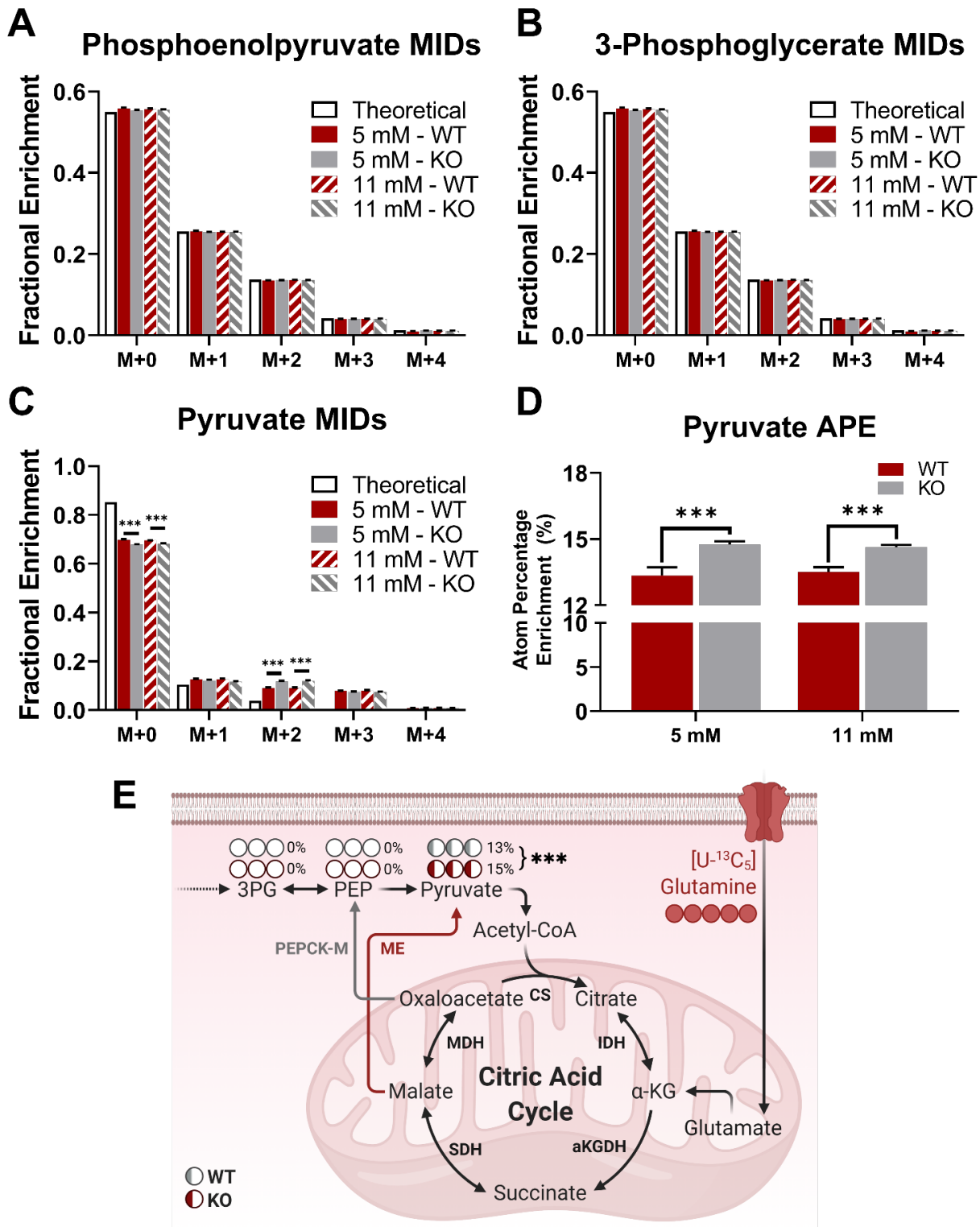
**A****Relative Fluxes in  $\beta$ TC3 Cells at 5 mM Glucose****B****Relative Fluxes in  $\beta$ TC3 Cells at 11 mM Glucose****Figure 3A.7: Metabolic fluxes relative to net glucose uptake in *G6pc2* WT and KO  $\beta$ TC3 cells**

Metabolic fluxes relative to net glucose uptake ( $V_{GK\ Net}$ ) in *G6pc2* WT and KO  $\beta$ TC3 cells at (A) 5 mM and (B) 11 mM glucose concentrations estimated using MFA. Data represent means $\pm$ SEM, \* $p < 0.05$  (n=3)

**A****Intracellular metabolite concentration at 5 mM glucose****B****Intracellular metabolite concentration at 11 mM glucose**

**Figure 3A.8: Intracellular metabolite abundance in *G6pc2* WT and KO  $\beta$ TC3 cells labeled with 2 mM  $[U-^{13}C_5]$ glutamine**

Intracellular metabolite abundance measured in *G6pc2* WT and KO  $\beta$ TC3 cells incubated with (A) 5 and (B) 11 mM glucose. Data represent means $\pm$ SEM, \*\*\* $p$ <0.01, \*\* $p$ <0.05, \* $p$ <0.10 (n=3).



**Figure 3A.9: Enrichment patterns in glycolytic metabolites after incubation with 2 mM  $[U-^{13}C_5]$ glutamine**  
 Intracellular enrichment in (A) phosphoenolpyruvate (PEP) (B) 3-phosphoglycerate (3PG), and (C) pyruvate, uncorrected for background abundance in *G6pc2* WT and KO  $\beta$ TC3 cells at 5 and 11 mM glucose concentrations incubated with 2 mM  $[U-^{13}C_5]$ glutamine for 24h. The theoretical values represent the unlabeled MID for each metabolite. (D) APE of pyruvate at 5 and 11 mM glucose concentrations (E) Schematic showing pathways that can enrich 3PG, PEP and pyruvate when  $[U-^{13}C_5]$ glutamine is used as tracer. Only pyruvate showed isotopic enrichment while PEP and 3PG had negligible  $^{13}C$  incorporation, suggesting that PEPCK-M is inactive at steady state in  $\beta$ TC3 cells. Data represent means $\pm$ SEM, \*\*\* $p$ <0.01 (n=3)

**Table 3A.1: Pancreatic  $\beta$ -cell metabolic reaction network for  $^{13}\text{C}$  MFA. (Related to Fig. 3.4-3.6 and Table 3A.2)**  
 Network maps of  $\beta$ -cell metabolism track carbon atoms through model reactions. Metabolites used to regress fluxes in both compartments are shown in Table 3A.2. Unenriched sources and sinks and “ $\text{CO}_2$ ” are annotated as “.source” and “.sink”, respectively.  $^{13}\text{C}$  isotopes are introduced into model reactions as “.tracer”. Extracellular metabolites are designated as “.ext”.

<b>Glycolysis</b>	
$V_{\text{Gluc.source}}$	Gluc.source (ABCDEF) $\rightarrow$ Gluc (ABCDEF)
$V_{\text{GK}}$	Gluc (ABCDEF) $\rightarrow$ G6P (ABCDEF)
$V_{\text{PGI}}$	G6P (ABCDEF) $\rightarrow$ F6P (ABCDEF)
$V_{\text{ALDO}}$	F6P (ABCDEF) $\rightarrow$ DHAP (CBA) + GAP (DEF)
$V_{\text{TPI}}$	DHAP (ABC) $\leftrightarrow$ GAP (ABC)
$V_{\text{G3PDH}}$	DHAP (ABC) $\rightarrow$ G3P (ABC)
$V_{\text{G3PP}}$	G3P (ABC) $\rightarrow$ Glycerol.ext (ABC)
$V_{\text{GAPDH}}$	GAP (ABC) $\rightarrow$ 3PG (ABC)
$V_{\text{PSP}}$	Ser (ABC) $\rightarrow$ 3PG (ABC)
$V_{\text{PK}}$	3PG (ABC) $\rightarrow$ Pyr (ABC)
$V_{\text{Pyr.exch}}$	Pyr (ABC) $\leftrightarrow$ Pyr.ext (ABC)
$V_{\text{Pyr.release}}$	Pyr.ext (ABC) $\rightarrow$ Pyr.sink (ABC)
$V_{\text{LDH}}$	Pyr (ABC) $\leftrightarrow$ Lac (ABC)
$V_{\text{Lac.exch}}$	Lac (ABC) $\leftrightarrow$ Lac.ext (ABC)
$V_{\text{Lac.release}}$	Lac.ext (ABC) $\rightarrow$ Lac.sink (ABC)
$V_{\text{ALT}}$	Pyr (ABC) $\leftrightarrow$ Ala (ABC)
$V_{\text{Ala.exch}}$	Ala (ABC) $\leftrightarrow$ Ala.ext (ABC)
$V_{\text{Ala.release}}$	Ala.ext (ABC) $\rightarrow$ Ala.sink (ABC)
$V_{\text{PC}}$	Pyr (ABC) + $\text{CO}_2$ (D) $\rightarrow$ Oac (ABCD)
$V_{\text{PDH}}$	Pyr (ABC) $\rightarrow$ AcCoA (BC) + $\text{CO}_2$ (A)
<b>Pentose Phosphate Pathway</b>	
$V_{\text{G6PDH}}$	G6P (ABCDEF) $\rightarrow$ P5P (BCDEF) + $\text{CO}_2$ (A)
$V_{\text{TK1}}$	S7P (ABCDEFGF) + GAP (HIJ) $\leftrightarrow$ F6P (ABCHIJ) + E4P (DEFG)
$V_{\text{PPP}}$	P5P (ABCDE) + P5P (FGHIJ) $\leftrightarrow$ S7P (ABFGHIJ) + GAP (CDE)
$V_{\text{TK2}}$	P5P (ABCDE) + E4P (FGHI) $\leftrightarrow$ F6P (ABFGHI) + GAP (CDE)
<b>Citric Acid Cycle</b>	
$V_{\text{CS}}$	Oac (ABCD) + AcCoA (EF) $\rightarrow$ Cit (DCBFEA)
$V_{\text{Fat.entry}}$	FA (AB) $\rightarrow$ AcCoA (AB)
$V_{\text{ICHD}}$	Cit (ABCDEF) $\leftrightarrow$ $\alpha$ -kg (ABCDE) + $\text{CO}_2$ (F)
$V_{\text{GDH}}$	Glu (ABCDE) $\leftrightarrow$ $\alpha$ -kg (ABCDE)

$V_{GS}$	Gln (ABCDE) $\leftrightarrow$ Glu (ABCDE)
$V_{Glu.entry}$	Glu.ext (ABCDE) $\leftrightarrow$ Glu (ABCDE)
$V_{Glu.source}$	Glu.source (ABCDE) $\rightarrow$ Glu.ext (ABCDE)
$V_{Gln.source}$	Gln.source (ABCDE) $\rightarrow$ Gln.ext (ABCDE)
$V_{Gln.entry}$	Gln.ext (ABCDE) $\rightarrow$ Gln (ABCDE)
$V_{\alpha KGDH}$	$\alpha$ -kg (ABCDE) $\rightarrow$ Suc (BCDE) + CO <sub>2</sub> (A)
$V_{Suc.release}$	Suc (ABCD) $\rightarrow$ Suc.ext (ABCD)
$V_{SDH}$	Suc (ABCD) $\leftrightarrow$ Fum (ABCD)
$V_{FM}$	Fum (ABCD) $\leftrightarrow$ Mal (ABCD)
$V_{MDH}$	Mal (ABCD) $\leftrightarrow$ Oac (ABCD)
$V_{ME}$	Mal (ABCD) $\leftrightarrow$ Pyr (ABC) + CO <sub>2</sub> (D)
$V_{AST}$	Oac (ABCD) $\leftrightarrow$ Asp (ABCD)
$V_{Asp.exch}$	Asp (ABCD) $\leftrightarrow$ Asp.ext (ABCD)
$V_{Asp.source}$	Asp.source (ABCD) $\rightarrow$ Asp.ext (ABCD)
$V_{Mal.release}$	Mal $\rightarrow$ Mal.sink
$V_{Cit.release}$	Cit $\rightarrow$ Cit.sink
<b>Isotope uptake, CO<sub>2</sub> recycling and biomass equation</b>	
$V_{Gluc.tracer}$	Gluc.tracer (ABCDEF) $\rightarrow$ Gluc (ABCDEF)
$V_{Gln.tracer}$	Gln.tracer (ABCDE) $\rightarrow$ Gln.ext (ABCDE)
$V_{CO2.source}$	CO <sub>2</sub> .source (A) $\rightarrow$ CO <sub>2</sub> (A)
$V_{CO2.sink}$	CO <sub>2</sub> (A) $\rightarrow$ CO <sub>2</sub> .sink (A)
$V_{Biomass}$	1389*G6P $\rightarrow$ Biomass

**Table 3A.2: GC-MS fragment ions of measured metabolites regressed using the metabolic model for MFA. (Related to Fig. 3.4-3.6, S3, 3A.5-3A.7 and Table 3A.1)**

Metabolite	<i>m/z</i>	Derivative Formula	Carbons					
			C1	C2	C3			
3-Phosphoglycerate	585	C <sub>23</sub> H <sub>54</sub> O <sub>7</sub> Si <sub>4</sub> P	C1	C2	C3			
Alanine	260	C <sub>11</sub> H <sub>26</sub> O <sub>2</sub> NSi <sub>2</sub>	C1	C2	C3			
Alanine	232	C <sub>10</sub> H <sub>26</sub> ONSi <sub>2</sub>		C2	C3			
Aspartate	302	C <sub>14</sub> H <sub>32</sub> O <sub>2</sub> NSi <sub>2</sub>	C1	C2				
Aspartate	390	C <sub>17</sub> H <sub>40</sub> O <sub>3</sub> NSi <sub>3</sub>		C2	C3	C4		
Aspartate	418	C <sub>18</sub> H <sub>40</sub> O <sub>4</sub> NSi <sub>3</sub>	C1	C2	C3	C4		
Citrate	459	C <sub>20</sub> H <sub>39</sub> O <sub>6</sub> Si <sub>3</sub>	C1	C2	C3	C4	C5	C6
Fumarate	287	C <sub>12</sub> H <sub>23</sub> O <sub>4</sub> Si <sub>2</sub>	C1	C2	C3	C4		
Glucose	301	C <sub>14</sub> H <sub>21</sub> O <sub>7</sub>	C1	C2	C3	C4	C5	C6
Glutamate	432	C <sub>19</sub> H <sub>42</sub> O <sub>4</sub> NSi <sub>3</sub>		C2	C3	C4	C5	
Glutamate	330	C <sub>16</sub> H <sub>36</sub> O <sub>2</sub> NSi <sub>2</sub>	C1	C2	C3	C4	C5	
Glutamine	431	C <sub>19</sub> H <sub>43</sub> O <sub>3</sub> N <sub>2</sub> Si <sub>3</sub>	C1	C2	C3	C4	C5	
Glycerol	377	C <sub>17</sub> H <sub>41</sub> O <sub>3</sub> Si <sub>3</sub>	C1	C2	C3			
Glycerol-3-Phosphate	571	C <sub>20</sub> H <sub>51</sub> O <sub>6</sub> Si <sub>4</sub> P	C1	C2	C3			
Lactate	261	C <sub>11</sub> H <sub>25</sub> O <sub>3</sub> Si <sub>2</sub>	C1	C2	C3			
Lactate	233	C <sub>10</sub> H <sub>25</sub> O <sub>2</sub> Si <sub>2</sub>		C2	C3			
Malate	419	C <sub>18</sub> H <sub>39</sub> O <sub>5</sub> Si <sub>3</sub>	C1	C2	C3	C4		
Phosphoenolpyruvate	453	C <sub>17</sub> H <sub>38</sub> O <sub>6</sub> Si <sub>3</sub> P	C1	C2	C3			
Pyruvate	174	C <sub>6</sub> H <sub>12</sub> O <sub>3</sub> NSi	C1	C2	C3			
Serine	390	C <sub>17</sub> H <sub>40</sub> O <sub>3</sub> NSi <sub>3</sub>	C1	C2	C3			
Succinate	289	C <sub>12</sub> H <sub>25</sub> O <sub>4</sub> Si <sub>2</sub>	C1	C2	C3	C4		

#### **4. *In vivo* Estimates of Liver Metabolic Fluxes Assessed by <sup>13</sup>C-Propionate and <sup>13</sup>C-Lactate are Impacted by Tracer Recycling and Equilibrium Assumptions**

*Cell Reports* (2020), 32-5:107986

##### **4.1 Abstract**

Isotope-based assessment of metabolic flux is achieved through a judicious balance of measurements and assumptions. Recent publications debate the validity of key assumptions used to model stable isotope labeling of liver metabolism *in vivo*. Here we examine the controversy surrounding estimates of liver citric acid cycle and gluconeogenesis fluxes using a flexible modeling platform that enables rigorous testing of standard assumptions. Fasted C57Bl/6J mice are infused with either [<sup>13</sup>C<sub>3</sub>]lactate or [<sup>13</sup>C<sub>3</sub>]propionate isotopes, and hepatic fluxes are regressed using models with gradually increasing complexity and relaxed assumptions. We confirm that liver pyruvate cycling fluxes are incongruent between different <sup>13</sup>C tracers in models with conventional assumptions. When models are expanded to include more labeling measurements and fewer constraining assumptions, however, liver pyruvate cycling is significant and inconsistencies in hepatic flux estimates using [<sup>13</sup>C<sub>3</sub>]lactate and [<sup>13</sup>C<sub>3</sub>]propionate isotopes emanate, in part, from peripheral tracer recycling and incomplete isotope equilibration within the citric acid cycle.



## 4.2 Introduction

Hepatic gluconeogenesis and the mitochondrial citric acid cycle (CAC) act in concert to supply the body with glucose when the dietary supply is reduced (e.g., during fasting). Many reactions in these pathways are catalyzed by regulatory enzymes that have been proposed as drug targets for treating insulin resistance, type 2 diabetes, and fatty liver disease. There has been a long-running debate over the nature of liver metabolic adaptations that occur during the progression of these obesity-related conditions. Some groups hypothesize that impairments in mitochondrial metabolism are responsible for accumulation of toxic lipid species that cause insulin resistance and tissue damage in the liver. Others hypothesize that hepatic lipid overload causes elevations in CAC and anaplerotic fluxes that drive excess gluconeogenesis and accumulation of toxic free radicals. Because metabolic flux alterations cannot be assessed *in vivo* without the use of isotope tracers, the two competing hypotheses cannot be completely resolved without accurate methods to model and interpret data from *in vivo* isotope labeling experiments (ILEs).

An ILE introduces a stable or radioactive tracer (e.g., containing heavy isotopes such as  $^{13}\text{C}$  or  $^{14}\text{C}$ ) to a live biological system. After the tracer has been sufficiently metabolized through the target biochemical pathways of interest, the isotope enrichment of downstream metabolites is determined experimentally. Because different pathways rearrange the labeled atoms in unique ways, it is often possible to calculate metabolic flux rates from the relative abundance of different isotopically labeled species (i.e., isotopomers) comprising those metabolites. Various approaches have been taken to estimate hepatic pathway fluxes from *in vivo* ILEs. Least-squares regression approaches have been developed to estimate fluxes from metabolite mass isotopomer distributions (MIDs). Other approaches relate positional isotopomer abundances to pathway fluxes through distilled mathematical equations.

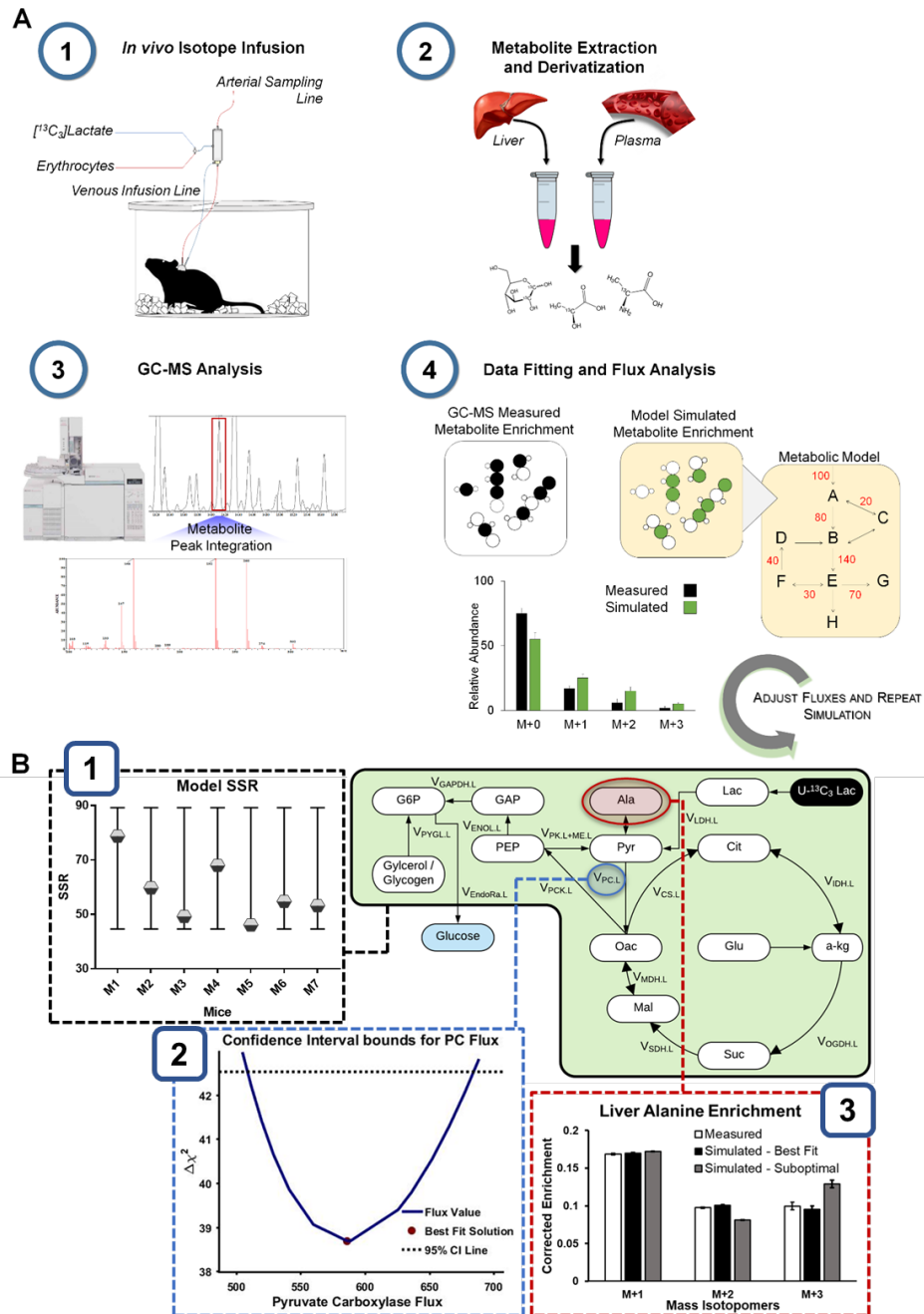
Regardless of the approach, assumptions are implemented to limit the complexity of model-based flux analysis. It is often assumed that primary isotopes equilibrate completely in the liver; also, the release,

circulation, and reuptake of enriched products of liver metabolism are assumed to have a negligible impact on liver metabolic flux estimates. A challenge to these assumptions was illustrated in the classic debate over *in vivo* estimates of the parameter  $y$ , which represents the ratio of liver anaplerosis to citrate synthase flux. In the academic exchange, studies that used isotopic acetate or lactate yielded very different flux ratios. This incompatibility was partially reconciled through evidence that, in contrast to lactate, the extensive extrahepatic metabolism of isotopic acetate generated metabolites which artefactually lowered  $y$  values [62], [208]–[211].

The aforementioned studies underscore the importance of secondary sites of isotope metabolism and generation. We have previously developed a modeling platform for *in vivo* liver metabolic flux analysis (MFA) that has been optimized for application to the conscious mouse [29] (Fig 4.1A). Mice are infused with  $^2\text{H}$  and/or  $^{13}\text{C}$  isotopes, metabolites are analyzed by GC-MS, and fluxes are estimated by least-squares regression of MID measurements using the INCA software [69]. One advantage of INCA is that users can adjust the mathematical model to rapidly test the effects of specific reactions or modeling assumptions on the best-fit solution (Fig 4.1B). Nevertheless, our MFA platform shares some common challenges with other contemporary *in vivo* flux analysis approaches. Specifically, stable isotopes delivered in large quantities may perturb the intrinsic metabolism of the pathways they are intended to assess. Primary isotopes, or their enriched products, may also be metabolized in non-target tissues *in vivo*, and metabolites enriched from their breakdown or exchange may circulate to the liver and further impact flux estimates.

Here we applied INCA to model the formation and effects of secondary tracers on liver flux analysis *in vivo*. These effects were tested in models that treat the liver as a single compartment or as a central hub in a multi-compartment network that accommodates the Cori cycle. Fluxes were regressed in models constrained by more common assumptions (base models) or expanded to rigorously account for incomplete isotope equilibration and additional metabolite measurements (expanded models). Using the aforementioned models, we assessed differences in the utility of [ $^{13}\text{C}_3$ ]propionate ( $^{13}\text{C}_3\text{Prop}$ ) and

$[^{13}\text{C}_3]$ lactate ( $^{13}\text{C}_3\text{Lac}$ ) as tracers for regressing liver metabolic fluxes, with or without  $^2\text{H}$  isotopes, in overnight fasted C57Bl/6J mice.



**Figure 4.1: Metabolic flux analysis (MFA) determines fluxes through model-based regression of isotope labeling measurements.**

(A) MFA workflow. (1) Stable isotopes and replacement erythrocytes are infused intravenously in catheterized mice to enrich liver and plasma metabolites. (2) Plasma and liver tissue harvested at the end of the infusion are extracted and derivatized for GC-MS analysis. (3) Chromatographic peaks corresponding to the metabolites of interest are integrated and processed to obtain mass isotopomer distributions (MIDs). (4) The best-fit solution for all fluxes included in the metabolic model is obtained by minimizing the sum of squared residuals (SSR) between experimentally determined and model-simulated MIDs.

(B) Verification of best-fit solution. (1) The best-fit solution for each mouse is accepted if the minimized SSR is within the expected range of a chi-square cumulative distribution function. (2) Flux uncertainties are assessed by determining the sensitivity of the minimized SSR to variations in each flux value. For example, the points of intersection with the dotted line indicate the boundaries of the 95% confidence interval (CI) of the estimated pyruvate carboxylase (PC) flux. (3) Varying the flux values away from the optimal solution increases the measurement residuals, as shown in the suboptimal case.

## 4.3 Methods

### 4.3.1 *In vivo* Procedures in the Mouse

Indwelling catheters were surgically implanted in the jugular vein and carotid artery ~1wk prior to experimentation for infusing and sampling, respectively, as previously described [212]. *In vivo* studies were performed identically to those described in detail elsewhere in long-term (~19-20hr) fasted mice [29]. Briefly, mice received an intravenous primed, continuous infusion of [6,6-<sup>2</sup>H<sub>2</sub>]glucose (440μmol/kg + 4.4μmol/kg/min), bolus of <sup>2</sup>H<sub>2</sub>O to enrich body water to 4.5% (abbreviated collectively as <sup>2</sup>H), and a primed, continuous infusion of <sup>13</sup>C<sub>3</sub>Prop (1.1mmol/kg + 0.055mmol/kg/min) or <sup>13</sup>C<sub>3</sub>Lac (0.160mmol/kg + 0.040mmol/kg/min) (Cambridge Isotope Laboratories, Tewksbury MA). Isotopes were delivered over a 4hr time course, as previously described. A separate cohort of overnight fasted mice was infused with a primed, continuous infusion of <sup>13</sup>C<sub>3</sub>Lac (0.160mmol/kg + 0.040mmol/kg/min, respectively) for 120min in the absence of <sup>2</sup>H isotopes for relative liver flux estimation. Mice were sacrificed through cervical dislocation and liver tissue was rapidly excised and freeze-clamped in liquid nitrogen at the close of the study; plasma samples and tissues obtained at the end of the study were stored at -80°C prior to analysis.

### 4.3.2 Metabolite Extraction, Derivatization, and GC-MS

Plasma glucose was extracted and derivatized according to protocols developed elsewhere [41]. Following acetone or a biphasic methanol/water/chloroform extraction, polar plasma (~10-50μL) and liver (~30-50mg) metabolites were converted to their methoxamine *tert*-butylsilyl derivatives (TBDMS) using MBTSTFA+1% TBDMCS (ThermoFisher Scientific, Waltham MA). Glucose and other metabolite derivatives were injected in an Agilent 7890A gas chromatograph equipped with an HP-5ms capillary column and 5975C mass spectrometer in scan mode for analysis of isotopic enrichment. Metabolites were identified through comparison to a library of known standards, and the accuracy of MID measurements was

validated through an assessment of unenriched control samples. Post hoc simulations for metabolite MIDs were performed following best-fit flux regression for each mouse.

### 4.3.3 Metabolic Flux Analysis (MFA)

All metabolic models were constructed using the Isotopomer Network Compartmental Analysis (INCA) software package (accessible at <http://mfa.vueinnovations.com/mfa>) [69]; metabolic networks and carbon/hydrogen atom transitions for each modeled reaction are summarized in **Tables 4A.1, 4A.3 and 4A.4**. Flux models were constructed from classical biochemical reactions with consideration to those published previously [75], [111], [213]. Unless otherwise noted, assumptions used for flux analysis were the same as those provided in a previous publication [29]. MIDs for glucose, plasma and liver polar metabolites were introduced into INCA for flux regression. After constraining citrate synthase flux ( $V_{CS,L}$ ) to an arbitrary value of 100, relative fluxes were estimated by minimizing the sum of squared residuals (SSRs) between simulated and experimentally derived MIDs. Measurement uncertainties were estimated based on the root-mean square error of unenriched control samples and/or the standard error of measurement of technical GC-MS replicates. Best-fit flux estimates were obtained from least-squares regression starting from at least 25 random initial values. Goodness of fit was assessed by a chi-square test, and 95% flux confidence intervals were calculated by evaluating the sensitivity of SSRs to variations in flux values [75]. In studies where both  $^{13}\text{C}/^2\text{H}$  isotopes were infused, relative fluxes were converted to absolute fluxes using the known  $[6,6\text{-}^2\text{H}_2]\text{glucose}$  infusion rate and mouse weights. For mice infused with  $^{13}\text{C}/^2\text{H}$  isotopes, glucose-producing flux from glycerol ( $V_{GK,L}$ ) was summed with glycogen ( $V_{PYGL,L}$ ) and presented in hexose units ( $V_{PYGL+GK,L}$ ).

MIDs and NMR positional enrichments were simulated in INCA using the best-fit flux solutions obtained from *in vivo* labeling experiments. Where appropriate, urea and lactate enrichments obtained during the isotopic steady state were included in the liver flux regressions. An increase in the  $^{13}\text{C}$  enrichment of the

CO<sub>2</sub> pool *in vivo* is anticipated to some extent, given the introduction of propionate or lactate isotopes into the CAC. A modeling approach was taken to accommodate the reintroduction of locally synthesized <sup>13</sup>CO<sub>2</sub> in the liver in a previous publication [29]. Here, <sup>13</sup>CO<sub>2</sub>/bicarbonate enrichment was assumed to equilibrate with the carbonyl carbon of urea (retained by the urea-TBMDS m/z 231 ion), since carbamoyl phosphate is formed from HCO<sub>3</sub><sup>-</sup> in hepatic mitochondria. As such, the Urea231 enrichment was used as a proxy for <sup>13</sup>CO<sub>2</sub>, similar to that applied elsewhere [213]. The MIDs of additional metabolites (e.g., Lac261 ion as a measure of lactate enrichment) were included in specific flux regressions as described in *Results* (Table S5). Unless otherwise noted, a two-tailed t-test was used to test for differences with significance at  $p \leq 0.05$ .

#### 4.3.4 Correction of Liver Oxaloacetate Isotopomers to Account for <sup>13</sup>CO<sub>2</sub> Recycling

In the absence of <sup>13</sup>CO<sub>2</sub> recycling, the fully labeled M+4 isotopomer Oac<sub>1111</sub> should exhibit negligible abundance and only the M+3 oxaloacetate isotopomers Oac<sub>1110</sub> and Oac<sub>0111</sub> should be formed from <sup>13</sup>C<sub>3</sub>Lac infusion. Yet, after correcting the aspartate MID for natural isotopic background, significant M+4 enrichment was detected (Figure 4.3E), which stems from carboxylation of M+3 pyruvate with recycled <sup>13</sup>CO<sub>2</sub> (Figure 4.3D). Because <sup>13</sup>CO<sub>2</sub> can lead to production of M+3 oxaloacetate isotopomers other than Oac<sub>1110</sub> and Oac<sub>0111</sub>, the measured MIDs of alanine (a proxy for liver pyruvate) and urea (a proxy for liver CO<sub>2</sub>) were used to mathematically correct the M+3 oxaloacetate isotopomers to account for contributions from <sup>13</sup>CO<sub>2</sub> recycling:

$$Oac_{1234}^{cor}(M+3) = Oac_{1234}(M+3) + \frac{V_{PC}}{V_{\Sigma Ana}} \cdot {}^{13}CO_2 \cdot [Pyr_{123}(M+3) - Pyr_{123}(M+2)]$$

$$Oac_{234}^{cor}(M+3) = Oac_{234}(M+3) - \frac{V_{PC}}{V_{\Sigma Ana}} \cdot {}^{13}CO_2 \cdot Pyr_{23}(M+2),$$

where

$Oac_{1234}(M+3)$  = M+3 abundance of Asp418 fragment ion (derived from carbons 1-4 of oxaloacetate)

$Oac_{234}(M+3)$  = M+3 abundance of Asp390 fragment ion (derived from carbons 2-4 of oxaloacetate)

$Oac_{1234}^{cor}(M + 3) = M+3$  abundance of Asp418 after correction for  $^{13}CO_2$  recycling

$Oac_{234}^{cor}(M + 3) = M+3$  abundance of Asp390 after correction for  $^{13}CO_2$  recycling

$Pyr_{123}(M + 3) = M+3$  abundance of Ala260 fragment ion (derived from carbons 1-3 of pyruvate)

$Pyr_{123}(M + 2) = M+2$  abundance of Ala260

$Pyr_{23}(M + 2) = M+2$  abundance of Ala232 fragment ion (derived from carbons 2-3 of pyruvate)

$^{13}CO_2 = M+1$  abundance of Urea231 fragment ion (derived from liver  $CO_2$ ),

and the ratio of pyruvate carboxylase flux ( $V_{PC}$ ) to total anaplerosis ( $V_{\Sigma Ana}$ ) is determined by:

$$\frac{V_{PC}}{V_{\Sigma Ana}} = \frac{Oac_{1234}(M+4)}{Pyr_{123}(M+3) \cdot ^{13}CO_2}$$

All MIDs were corrected for natural stable isotope abundance prior to applying the above equations.

#### 4.3.5. Calculation of Percent Equilibration in the 4C reactions of the CAC

If oxaloacetate fully equilibrates with rotationally symmetric CAC intermediates (i.e., fumarate and succinate) through reversible exchange, an equal abundance of the M+3 oxaloacetate isotopomers  $Oac_{1110}$  and  $Oac_{0111}$  would be expected (Figure 4.3D). However, incomplete equilibration would cause the abundance of  $Oac_{1110}$  (formed directly from pyruvate carboxylation) to exceed the abundance of  $Oac_{0111}$  (formed from reversible exchange with fumarate). Once the corrected oxaloacetate M+3 abundances were calculated as described above, the abundances of  $Oac_{1110}$  and  $Oac_{0111}$  positional isotopomers formed from  $^{13}C_3Lac$  were determined as follows:

$$Oac_{0111} = Oac_{234}^{cor}(M + 3)$$

$$Oac_{1110} = Oac_{1234}^{cor}(M + 3) - Oac_{234}^{cor}(M + 3).$$

These abundances were then used to assess the percentage isotope equilibration using the equation:

$$\%Equilibration = \left(1 - \frac{Oac_{1110} - Oac_{0111}}{Oac_{1110} + Oac_{0111}}\right) \times 100\%$$

### 4.3.6. Quantification and Statistical Analysis

All data were analyzed using an unpaired student's t-test without assuming a consistent standard deviation between groups. Biological replicates and significance values for each analysis are noted in each figure caption.

## 4.4 Results

### 4.4.1 Secondary Tracer Effects Influence Estimates of Liver Pyruvate Cycling

We previously described a base model of *in vivo* liver metabolism that was applied to regress hepatic CAC and gluconeogenic fluxes from MID measurements of plasma glucose obtained from conscious, unrestrained mice [29]. The model consists of a biochemical network with hydrogen and carbon atom transitions defined for each reaction (Table 4A.1). The model assumes full equilibration of four-carbon (4C) intermediates in the CAC and no re-entry of labeled CO<sub>2</sub> or other secondary tracers. We used the best-fit solutions obtained from our prior studies of four long-term fasted mice infused with <sup>13</sup>C<sub>3</sub>Prop/<sup>2</sup>H tracers to simulate the predicted MIDs of liver lactate (Lac261) and alanine (Ala260) fragment ions (Figure 4.2A). The simulated MIDs qualitatively resembled the measured enrichments of liver lactate and alanine, confirming that the base model is capable of accurately predicting isotope enrichments in other liver-derived metabolites in addition to glucose.

The assumption that secondary tracer effects are minimal is a pragmatic first approximation, as analyzing sources of secondary tracers and deriving equations that account for those measurements *ad hoc* may be impractical in some cases. However, upon further investigation we found that plasma lactate and urea (an indicator of circulating bicarbonate) were enriched significantly above natural isotopic background following 120min of <sup>13</sup>C<sub>3</sub>Prop/<sup>2</sup>H infusion (Fig. 4.2B). Inclusion of these measured lactate and CO<sub>2</sub> enrichments in the model regressions (Fig. 4.2C) increased pyruvate cycling flux estimates ( $V_{PC,L}$ ,  $V_{PCK,L}$ , and  $V_{PK+ME,L}$ ) in the liver (Fig. 4.2D and 4A.1A), similar to the effect of <sup>14</sup>CO<sub>2</sub> recycling in prior studies



using [3-<sup>14</sup>C]lactate in humans [213]. In summary, these findings indicate that recycling of labeled lactate and CO<sub>2</sub> to the liver from the plasma is significant, and it likely impacts *in vivo* estimates of liver pyruvate cycling obtained with <sup>13</sup>C tracers when applying the assumptions implicit to our base model.

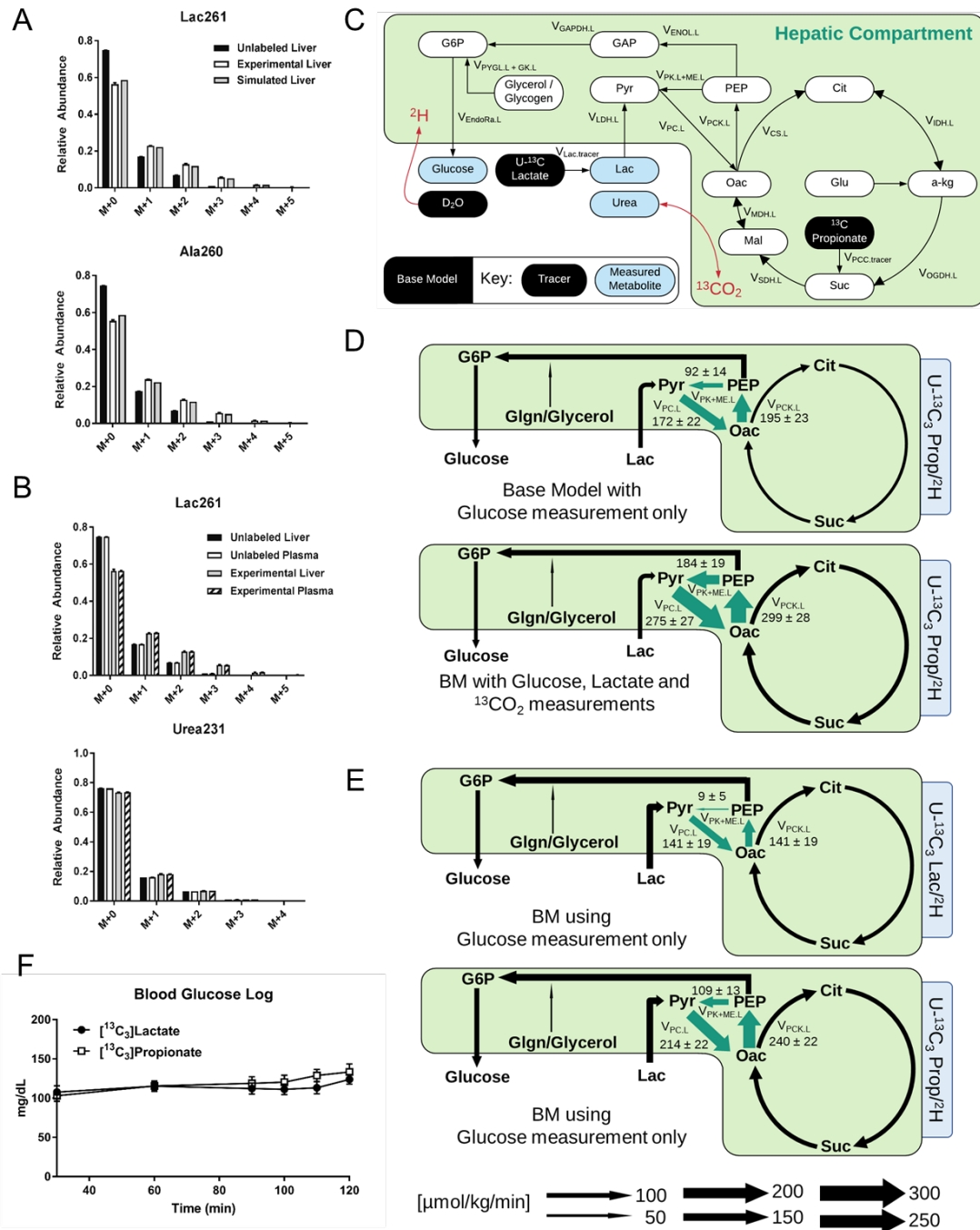
#### **4.4.2 Incongruent Hepatic Flux Estimates are Obtained with Base Models of <sup>13</sup>C<sub>3</sub>Lac/<sup>2</sup>H and <sup>13</sup>C<sub>3</sub>Prop/<sup>2</sup>H Tracers**

Adjustments were made to the base model of liver metabolism to accommodate a study with the infusion of <sup>13</sup>C<sub>3</sub>Lac/<sup>2</sup>H or <sup>13</sup>C<sub>3</sub>Prop/<sup>2</sup>H isotopes (Table 4A.1). The infusion rate for each <sup>13</sup>C isotope was analogous to previous studies [29], [214]. All mice were long-term fasted to induce a gluconeogenic state of the liver. No differences in glucose producing fluxes or blood glucose concentrations were observed between <sup>13</sup>C<sub>3</sub>Lac/<sup>2</sup>H and <sup>13</sup>C<sub>3</sub>Prop/<sup>2</sup>H tracer infusions (Figure 4.2E,F and 4A.1B, 4A.2A). Nevertheless, pyruvate cycle fluxes ( $V_{PC,L}$ ,  $V_{PCK,L}$ ,  $V_{PK+ME,L}$ ) estimated from <sup>13</sup>C<sub>3</sub>Prop/<sup>2</sup>H infusions were higher than those estimated with an analogous model of <sup>13</sup>C<sub>3</sub>Lac/<sup>2</sup>H infusion (Figure 4.2E and 4A.1B, 4A.2A, Table 4A.2). Thus, best-fit pyruvate cycle fluxes obtained from base models were incongruent between <sup>13</sup>C<sub>3</sub>Lac/<sup>2</sup>H and <sup>13</sup>C<sub>3</sub>Prop/<sup>2</sup>H labeling studies.

A similar disparity has been observed in perfused livers [109] and *in vivo* [214]. Others have proposed these discrepancies may result from incomplete randomization of <sup>13</sup>C atoms derived from <sup>13</sup>C-lactate due to its lesser interconversion with symmetric 4C-intermediates in the CAC. This is purported to occur for <sup>13</sup>C tracers that enter the CAC downstream of fumarate (e.g., lactate or alanine), rather than those that enter upstream of succinate (e.g., propionate) [109]. Thus, we next examined the effects of incomplete isotope randomization on estimated flux ratios in our base models.

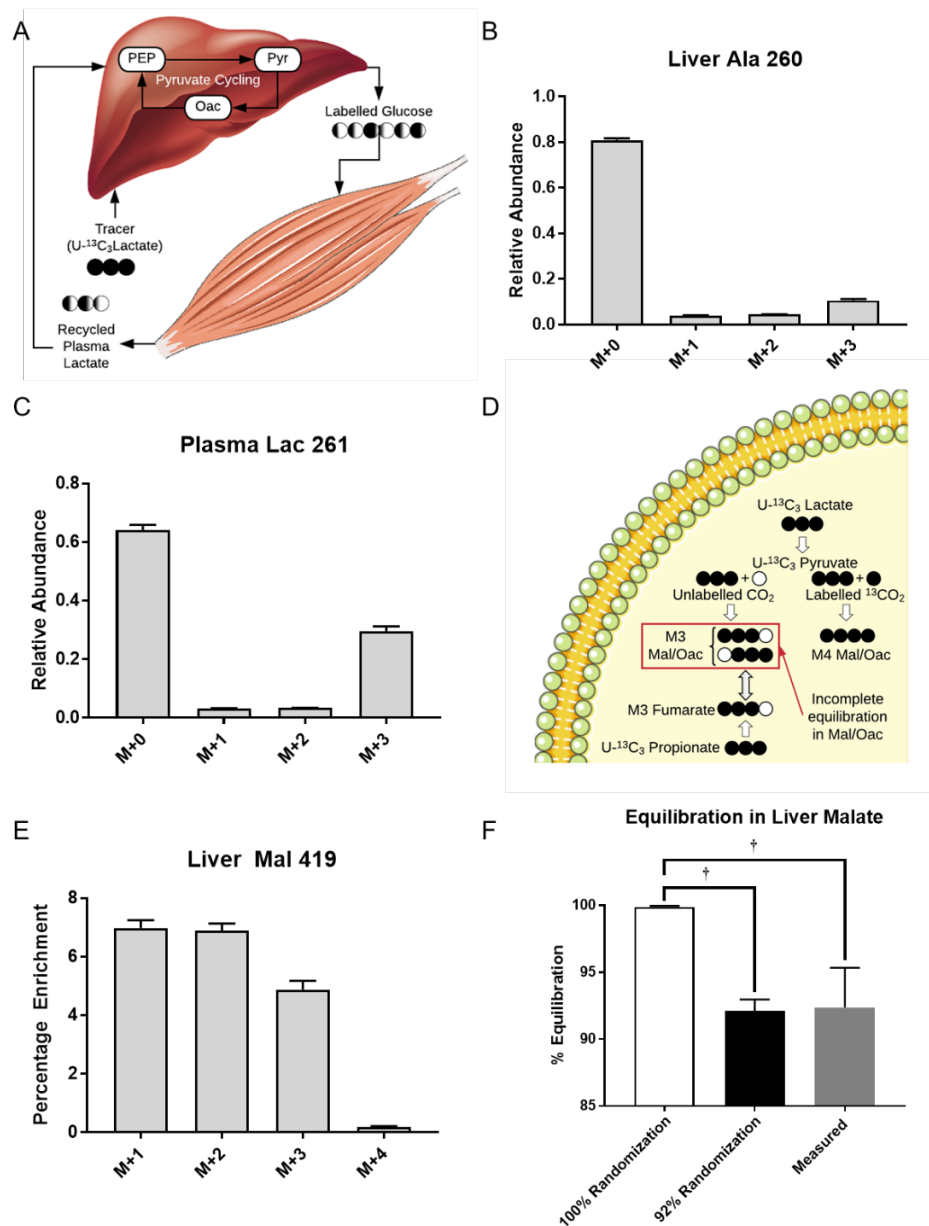
#### **4.4.3 <sup>13</sup>C<sub>3</sub>Lac Infusion without <sup>2</sup>H Tracers Enables Rigorous Testing of Base Model Assumptions**

Because of the aforementioned uncertainties related to (i) the extent of reversibility of 4C reactions of the CAC and (ii) the influence of secondary tracer recycling on liver flux estimates, we designed a study to



**Figure 4.2: Base model shows evidence of secondary tracer effects and provides different estimates of hepatic fluxes for  $^{13}\text{C}_3\text{Lac}^{2}\text{H}$  and  $^{13}\text{C}_3\text{Prop}^{2}\text{H}$  tracers**

- (A) Model simulated and empirically measured (means  $\pm$  SEM,  $n=4$ ) liver metabolite MID for lactate ( $m/z$  261) and alanine ( $m/z$  260) and
- (B) MID of plasma and liver lactate ( $m/z$  261) and urea ( $m/z$  231) obtained at isotopic steady state from long-term fasted C57Bl/6J mice infused with  $^{13}\text{C}_3\text{Prop}^{2}\text{H}$  isotopes contrasted with MID from unlabeled control samples (means  $\pm$  SEM,  $n=4$ )
- (C) Network map of the base model showing infusion of either  $^{13}\text{C}_3\text{Lac}$  or  $^{13}\text{C}_3\text{Prop}$  with  $^2\text{H}_2\text{O}$ . Plasma urea was used as a proxy measurement for  $\text{CO}_2$  enrichment
- (D) Flux estimates obtained from the base model using plasma glucose enrichments alone contrasted with those that included  $^{13}\text{CO}_2$  and plasma lactate measurements in the flux regression. Arrows highlighted in green represent significant changes between flux estimates obtained from the base model using the two measurement sets. Fluxes expressed as means  $\pm$  SEM ( $n=4$ ,  $*p \leq 0.05$ )
- (E) Flux estimates obtained from the base model using plasma glucose enrichments alone in mice infused with either  $^{13}\text{C}_3\text{Lac}^{2}\text{H}$  or  $^{13}\text{C}_3\text{Prop}^{2}\text{H}$  isotopes. Arrows highlighted in green show significant flux changes between the  $^{13}\text{C}_3\text{Lac}^{2}\text{H}$  and  $^{13}\text{C}_3\text{Prop}^{2}\text{H}$  isotope studies using the base model. Fluxes expressed as means  $\pm$  SEM ( $n=6-7$ ,  $*p \leq 0.05$ )
- (F) Blood glucose log (mg/dL) during the infusion of  $^{13}\text{C}_3\text{Lac}^{2}\text{H}$  or  $^{13}\text{C}_3\text{Prop}^{2}\text{H}$  isotopes in 19-20hr fasted C57Bl/6J mice (means  $\pm$  SEM,  $n=6-7$ )



specifically address these assumptions by infusing mice with  $^{13}\text{C}_3\text{Lac}$  only (Fig. 4A.1A and 4.3A), without interference from  $^2\text{H}$  tracers. Our measurement set was expanded to include additional plasma and liver metabolites not typically considered in prior *in vivo* flux analyses: lactate and alanine in both liver and plasma compartments, and glutamate, alpha-ketoglutarate, aspartate, and urea extracted from liver tissue. The infusion of  $^{13}\text{C}_3\text{Lac}$  significantly increased the enrichment of circulating and hepatic metabolites (Fig. 4A.3). We observed significant M+1 and M+2 enrichments of liver alanine (Fig. 4A.3B) and plasma lactate (Fig. 4A.3C) after correcting the MIDs for natural background abundance of stable isotopes. The presence of these mass isotopomers reflects contributions from both liver pyruvate cycling and extrahepatic Cori cycling. The abundance of recycled M+1 and M+2 isotopomers relative to the uncycled M+3 isotopomer is higher in liver alanine than in plasma lactate, indicating that intrahepatic pyruvate cycling occurs after lactate is extracted from plasma. The presence of M+1 and M+2 isotopomers in plasma lactate also provides some evidence that tracer recycling occurs outside the liver, and the contribution from Cori cycling should be considered when making quantitative estimates of liver pyruvate cycle fluxes.

Next, we examined measurements of liver oxaloacetate labeling to assess the randomization of M+3 species that traverse the 4C reactions of the CAC (Fig. 4.3D). The measured M+3 and M+4 abundances of the Asp418 fragment ion (Fig. 4.3E), which is biosynthetically derived from oxaloacetate, and the M+3 abundance of Asp390 (Fig. 4A.3A), which is derived from carbons 2-4 of oxaloacetate, were used to calculate the fractional abundances of  $\text{Oac}_{1110}$  and  $\text{Oac}_{0111}$  isotopomers (see *Methods*). After accounting for  $^{13}\text{CO}_2$  recycling, randomization in the oxaloacetate pool was determined to be ~90% with  $^{13}\text{C}_3\text{Lac}$  as a tracer (Fig. 4.3F). A similar calculation can be performed with predicted Ala and Asp MIDs simulated from the base model of liver metabolism: a model that accounts for  $^{13}\text{CO}_2$  recycling and assumes 90%, but not 100%, randomization leads to results comparable to those derived from the empirically measured MIDs (Fig. 4.3F). These results suggest that *in vivo* estimates of hepatic metabolism would benefit from relaxing

common assumptions regarding secondary tracer recycling and equilibration of 4C intermediates in the CAC.

#### **4.4.4 Model Expansion to Account for Extrahepatic Metabolism Significantly Alters Pyruvate Cycle and CAC Fluxes**

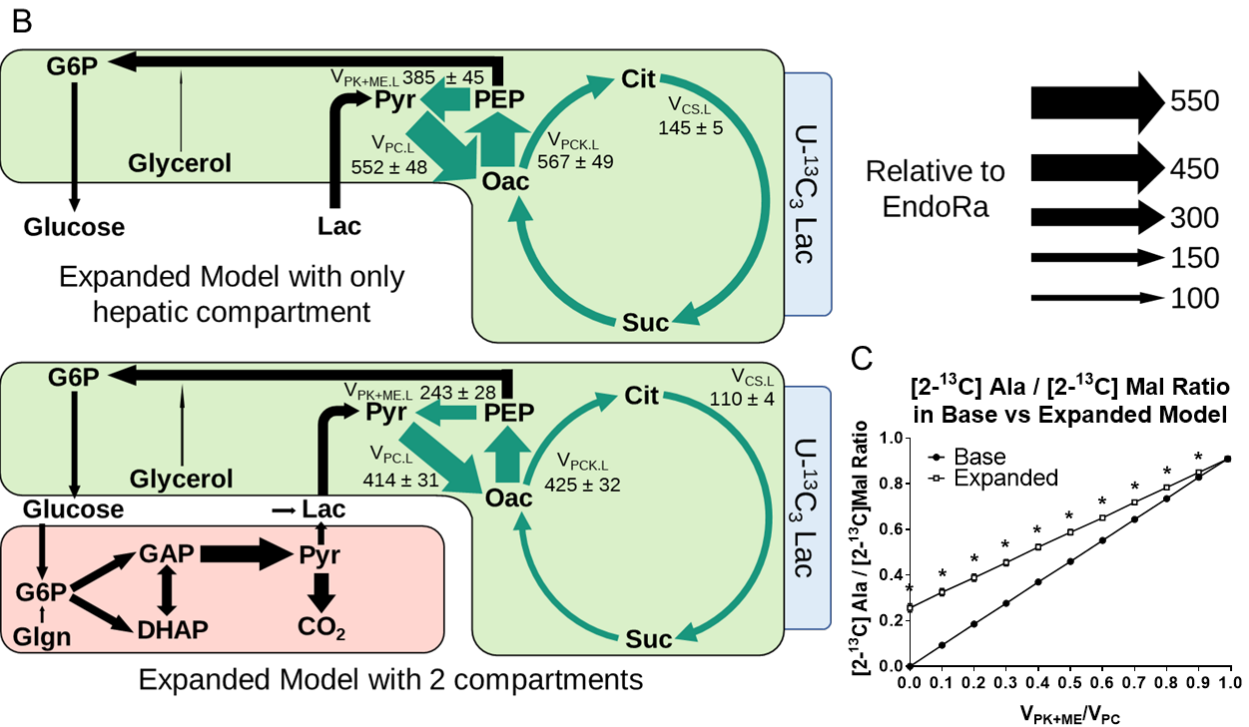
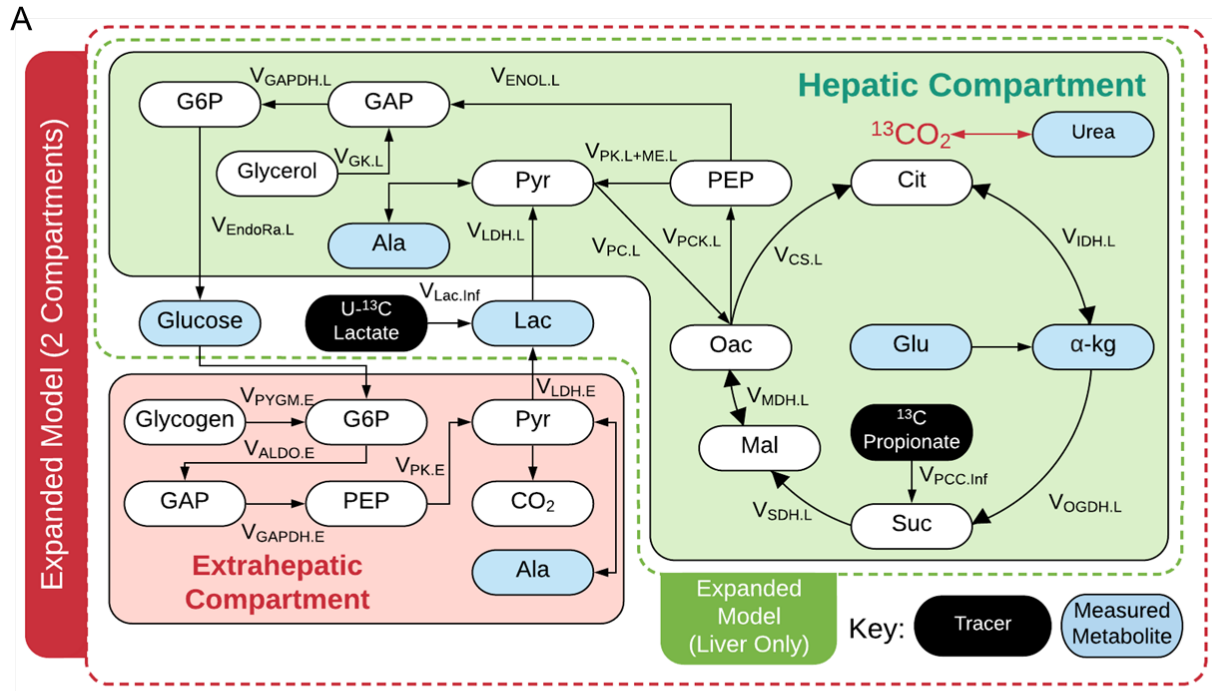
To relax several constraining assumptions of the base model and accommodate a broader set of plasma and tissue measurements, we constructed an expanded model that explicitly accounts for Cori cycling between hepatic and extrahepatic compartments (Fig. 4.4A, Table 4A.3). Liver pyruvate was allowed to reversibly exchange with liver lactate/alanine and glutamate was allowed to reversibly exchange with  $\alpha$ -ketoglutarate. Importantly, the triose phosphate isomerase (TPI) and fumarate hydratase (FH) reactions were no longer assumed to fully equilibrate, but instead the reaction reversibilities were treated as adjustable parameters and determined by model regression of plasma and tissue MIDs. When the expanded model was regressed to data from  $^{13}\text{C}_3\text{Lac}$  infusions, the best-fit flux estimates indicated that the FH reaction was  $\sim 92\%$  equilibrated, matching closely with values determined empirically from analysis of oxaloacetate isotopomer ratios (Fig. 4.3F). Because mice were fasted to deplete liver glycogen prior to isotope infusions, the regressed estimates of glucose production from glycogen were typically  $\sim 1\%$ . Thus,  $V_{\text{PYGLL}}$  was treated as inactive in the subsequent analyses to improve model reproducibility.

We compared best-fit solutions obtained from one-compartment (i.e., liver only) or two-compartment versions of the expanded model when regressed with plasma and liver MIDs obtained from  $^{13}\text{C}_3\text{Lac}$  infusions (Fig. 4.4B and 4A.4). Model expansion did not adversely impact flux precision, as confidence intervals for most fluxes were well constrained in both models (Fig. 4A.5A,B). Liver glucose production and net lactate uptake fluxes were not significantly different between the two models. Gluconeogenesis from PEP accounted for the majority of  $V_{\text{EndoRa}}$ , with a smaller fraction emanating from glycerol, and total liver anaplerotic flux ( $V_{\text{PCK.L}}$ ) was  $\sim 4$ -fold higher than the rate of citrate synthase ( $V_{\text{CS.L}}$ ) in both models

(Fig. 4.4B and 4A.4). In contrast, allowing return of lactate through the Cori cycle reduced liver pyruvate cycling ( $V_{PK+ME,L}$ ,  $V_{PC,L}$ ,  $V_{PCK,L}$ ) and CAC ( $V_{CS,L}$ ) fluxes in the two-compartment model relative to the liver-only model (Fig. 4.4B). Nevertheless, liver pyruvate cycling remained substantial in both models, with ~57% of total anaplerosis returned to pyruvate ( $V_{PK+ME,L}$ ) in the two-compartment model compared to ~68% in the liver-only model (Fig. 4.4B).

Pyruvate decarboxylation by the pyruvate dehydrogenase (PDH) complex is generally assumed to be low in long-term fasted conditions. Albeit less precise, fluxes regressed using either one- or two-compartment expanded models with an active PDH reaction were consistent with low levels of pyruvate decarboxylation ( $V_{PDH,L}$  was ~5% the rate of total pyruvate flux into the CAC) (Fig. 4A.6). Estimates of liver glutamate anaplerosis were particularly sensitive to changing model assumptions about PDH activity, as increased glutamate entry effectively offset reductions in  $V_{CS,L}$  so that estimates of  $V_{MDH,L}$  were unchanged when PDH was active (Fig. 4A.4 and 4A.6). Other liver fluxes were not significantly altered by inclusion of PDH in the reaction network. Importantly, the effects of Cori cycling to reduce pyruvate cycle and CAC fluxes were replicated in models with an active PDH complex ( $V_{PDH,L}$ ) (Fig. 4A.6). In summary, estimates of liver pyruvate cycling and CAC-associated fluxes were sensitive to changing model assumptions regarding secondary tracer recycling and equilibration in the CAC. On the other hand, glucose-producing fluxes were robust to changes in these same model assumptions.

Finally, we examined whether an alternative approach for assessing liver pyruvate cycling would be similarly impacted by assumptions related to secondary tracer recycling. Perry et al. (2016) have previously described a method for estimating liver pyruvate cycling that relies on the measured ratio of [2-<sup>13</sup>C]alanine to [2-<sup>13</sup>C]malate enrichments following infusion with [3-<sup>13</sup>C]lactate. We simulated steady-state <sup>13</sup>C enrichments at the C2 positions of malate and alanine derived from [3-<sup>13</sup>C]lactate based on best-fit flux solutions obtained from either the one- or two-compartment expanded model.



**Figure 4.4: Expansion of base model in mice infused with <sup>13</sup>C<sub>3</sub>Lac only**

(A) Network diagram showing the expanded model with an extrahepatic compartment to facilitate descriptions of Cori cycling in <sup>13</sup>C<sub>3</sub>Lac tracer experiments. A broader set of plasma and tissue measurements was used to constrain the model (Table S3)

(B) Comparison of expanded model flux results with either one compartment (liver only) or two compartments showing relative flux estimates in 19-20hr fasted, C57Bl/6J mice infused with <sup>13</sup>C<sub>3</sub>Lac. Fluxes are normalized to total glucose production ( $V_{\text{EndoRa}}=100$ ). Fluxes highlighted in green show significant changes between the two models. Data are presented as means  $\pm$  SEM ( $n=7$ );  $p \leq 0.05$

(C) [2-<sup>13</sup>C]alanine/[2-<sup>13</sup>C]malate ratio predicted for varying liver  $V_{PK+ME,L}/V_{PC,L}$  ratios in a simulated study using [3-<sup>13</sup>C]lactate. Simulations were performed using the best-fit solutions obtained from a liver-only or two-compartment expanded model regressed to fit the <sup>13</sup>C<sub>3</sub>Lac measurements. Data are presented as means  $\pm$  SEM ( $n=7$ ); \* $p \leq 0.01$  determined using unpaired t-test without assuming consistent SD.

Both models simulated  $[2-^{13}\text{C}]\text{Ala}/[2-^{13}\text{C}]\text{Mal}$  ratios that varied linearly with liver  $V_{\text{PK+ME}}/V_{\text{PC}}$  flux, but the two-compartment model predicted higher isotopomer ratios compared to the liver-only model (Fig. 4.4C). The divergence between the models was most substantial at the lower range of  $V_{\text{PK+ME}}/V_{\text{PC}}$  flux, where the two-compartment model predicted a non-zero  $[2-^{13}\text{C}]\text{Ala}/[2-^{13}\text{C}]\text{Mal}$  ratio even in the absence of liver pyruvate cycling due to contributions from extrahepatic sources of  $[2-^{13}\text{C}]\text{Ala}$ . This incongruity provides evidence that secondary tracer effects are also embedded in liver flux estimates obtained from other stable isotope approaches, since these estimates do not differentiate between pyruvate cycling within the liver or in an extrahepatic compartment.

#### 4.4.5 Expanded Two-Compartment Models Provide Consistent Hepatic Flux Estimates Using $^{13}\text{C}_3\text{Prop}/^2\text{H}$ and $^{13}\text{C}_3\text{Lac}/^2\text{H}$ Tracers *In Vivo*

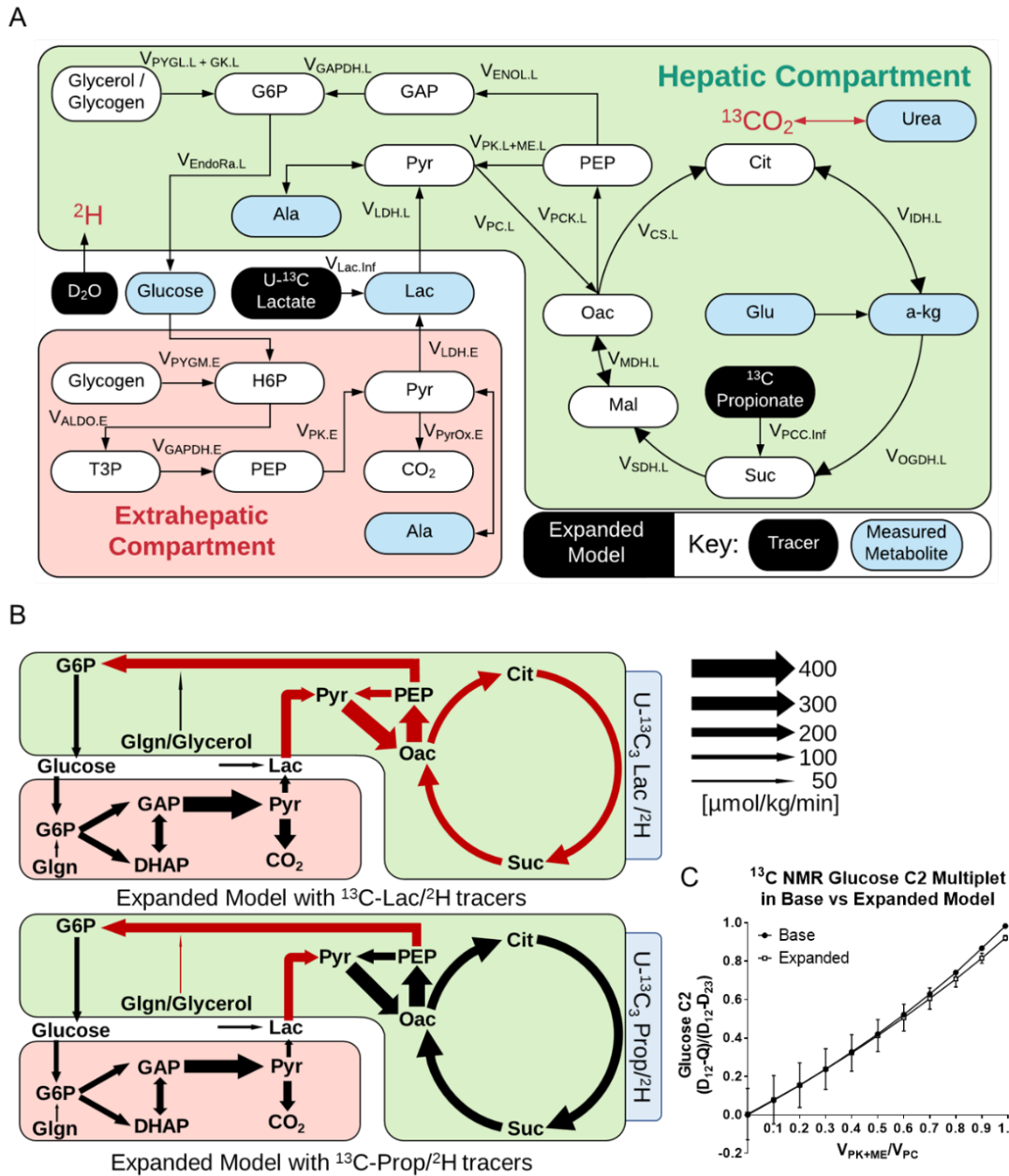
Plasma and liver tissues extracted from mice in prior  $^{13}\text{C}_3\text{Prop}/^2\text{H}$  and  $^{13}\text{C}_3\text{Lac}/^2\text{H}$  studies (assessed with base models in Fig. 4.2D-E) were re-analyzed to yield a similar set of metabolite MIDs as shown in Fig. 4A.3. Expanded models for the exchange of both  $^{13}\text{C}/^{12}\text{C}$  and  $^2\text{H}/^1\text{H}$  atoms were constructed to accommodate measurements from  $^{13}\text{C}_3\text{Lac}/^2\text{H}$  and  $^{13}\text{C}_3\text{Prop}/^2\text{H}$  experiments (Fig. 4.5A and Table 4A.4). These models were similar to the expanded  $^{13}\text{C}$ -only model of Fig. 4.4A with the following modifications: (i) hydrogen atom transitions were included, (ii) reactions to account for infusion of  $^2\text{H}$  and  $^{13}\text{C}_3\text{Prop}$  tracers were added, (iii) glycogenolysis was assumed active, and (iv) glutamate anaplerosis was assumed inactive. The latter assumption was necessary as glutamate MID measurements were not attainable from samples collected in  $^{13}\text{C}_3\text{Lac}/^2\text{H}$  and  $^{13}\text{C}_3\text{Prop}/^2\text{H}$  experiments, making the  $V_{\text{Glu,source}}$  flux unidentifiable. Hepatic flux estimates obtained from  $^{13}\text{C}_3\text{Lac}/^2\text{H}$  and  $^{13}\text{C}_3\text{Prop}/^2\text{H}$  infusions were similar when regressed with expanded models:  $V_{\text{EndoRa}}$  and  $V_{\text{EnolL}}$  were comparable (Fig. 4.5B and 4A.7), and pyruvate cycle and CAC fluxes were not significantly different (Table 4A.2). Thus, expanded models that allow secondary tracer recycling and



data-driven estimation of *in vivo* reaction reversibility provide congruent liver flux estimates with  $^{13}\text{C}_3\text{Prop}/^2\text{H}$  or  $^{13}\text{C}_3\text{Lac}/^2\text{H}$ .

To investigate the impacts of model expansion, we compared flux estimates from expanded versus base models using the same tracer datasets. There were no significant differences between fluxes estimated by the expanded and base  $^{13}\text{C}_3\text{Prop}/^2\text{H}$  models. However, the expanded  $^{13}\text{C}_3\text{Lac}/^2\text{H}$  model showed a significant elevation in hepatic pyruvate cycling ( $V_{\text{PK+ME,L}}$ ,  $V_{\text{PC,L}}$ ,  $V_{\text{PCK,L}}$ ) and CAC ( $V_{\text{CS,L}}$ ) fluxes compared to the base  $^{13}\text{C}_3\text{Lac}/^2\text{H}$  model (Table 4A.2). Thus, model expansion had a more pronounced impact on flux estimates obtained from  $^{13}\text{C}_3\text{Lac}/^2\text{H}$  studies than  $^{13}\text{C}_3\text{Prop}/^2\text{H}$  studies.

Finally, we used our expanded model of  $^{13}\text{C}_3\text{Prop}/^2\text{H}$  experiments to assess a  $^{13}\text{C}$  NMR approach for estimating liver metabolic fluxes using this same combination of tracers. Jin et al. (2005) have previously described a method for estimating liver pyruvate cycling that relies on the measured ratio of (D12–Q)/(D12–D23) multiplets obtained from the C2 resonance of plasma glucose. We adapted our base and expanded models to simulate these multiplet signals [65] using best-fit flux solutions obtained from our  $^{13}\text{C}_3\text{Prop}/^2\text{H}$  infusions. Both models simulated C2 multiplet ratios that varied roughly in proportion to liver  $V_{\text{PK+ME}}/V_{\text{PC}}$  flux, with only slight divergence at higher levels of pyruvate cycling flux (Fig. 4.5C). The agreement between the two models can be explained by the approximately offsetting effects of  $^{13}\text{CO}_2$  recycling and Cori cycling on the simulated C2 multiplet ratio.  $^{13}\text{CO}_2$  recycling tends to elevate the quartet (Q) signal while Cori cycling tends to decrease it, thus making the (D12–Q)/(D12–D23) ratio fairly insensitive to model expansion. This empirical finding is not a theoretically generalizable result, however, and may depend on the tracer infusion rate, the physiological state of the animals, as well as other methodological parameters.



**Figure 4.5: Comparison of  $^{13}\text{C}_3\text{Lac}/^2\text{H}$  and  $^{13}\text{C}_3\text{Prop}/^2\text{H}$  isotopes for hepatic flux estimation using expanded models of metabolism**

(A) Network map showing expanded model with  $^{13}\text{C}_3\text{Prop}/^2\text{H}$  or  $^{13}\text{C}_3\text{Lac}/^2\text{H}$  isotopes and highlighting measured metabolites

(B) Comparison of two-compartment expanded models regressed to either  $^{13}\text{C}_3\text{Prop}/^2\text{H}$  or  $^{13}\text{C}_3\text{Lac}/^2\text{H}$  labeling measurements. Absolute flux estimates are shown for 19-20hr fasted, C57Bl/6J mice. Data are presented as means  $\pm$  SEM ( $\mu\text{mol}/\text{kg}/\text{min}$ ,  $n=5$ )

(C) Glucose-C2  $^{13}\text{C}$ -NMR ( $\text{D}_{12}\text{-Q}/\text{D}_{12}\text{-D}_{23}$ ) multiplet ratio predicted for varying liver  $V_{\text{PK+ME/L}}/V_{\text{PC.L}}$  ratios using different models of the [ $^{13}\text{C}_3$ ]propionate tracer experiment. Simulations were performed using the best-fit solutions obtained from the base model (Figure 2D) or two-compartment expanded model (Figure 5B) regressed to  $^{13}\text{C}_3\text{Prop}/^2\text{H}$  measurements. Data are presented as means  $\pm$  SEM ( $n=4$  for base model,  $n=7$  for expanded model)

## 4.5 Discussion

Isotope-based flux analysis is the gold standard for measurements of *in vivo* metabolism and has provided important insights into whole-body fuel utilization, cancer metabolism, insulin resistance and fatty liver disease [107], [109], [163], [215]–[217]. Thus, the use of MFA to model and interpret data from *in vivo* ILEs is only expected to increase. During an effort to improve the robustness of our own MFA platform for assessing *in vivo* liver metabolism, we noted isotope-specific inconsistencies similar to previous observations that have given rise to a contentious debate in the literature [109], [218], [219]. Studies with  $^{13}\text{C}$ -propionate administered to human fatty liver patients or high-fat fed mice have reported dramatic elevations in liver CAC and anaplerotic fluxes compared to controls [99], [107]. In contrast, studies with  $^{13}\text{C}$ -acetate have reported no increases in CAC or anaplerotic fluxes in fatty liver patients [220]. However, the mathematical model used to estimate fluxes in the latter study neglected liver pyruvate kinase (PK) activity and therefore did not account for the possibility of liver pyruvate cycling, which is needed to explain the labeling patterns typically observed with  $^{13}\text{C}$  NMR analysis of plasma samples obtained from  $^{13}\text{C}$ -propionate tracer studies [221].

The omission of PK flux in models of liver metabolism is supported by arguments that “futile” pyruvate cycling is not energetically feasible, that inhibition of PK by glucagon during fasting should prevent pyruvate cycling, and that some experiments with  $^{13}\text{C}$ -lactate tracers indicate that liver pyruvate cycling is negligible [219]. One explanation for the divergent results of prior studies is that elevated rates of liver anaplerosis and pyruvate cycling reported in some cases may have been an artefact of  $^{13}\text{C}$ -propionate administration [214]. Yet, large estimates for hepatic PK flux have been measured in fasted conditions across species with radioactive and stable isotopes [62], [111], [209], [213]. One might expect liver flux analysis in perfusion or *in vitro* to clarify discrepancies in PK flux estimates. However, removal of the liver from the physiological milieu can rapidly alter PK activity [222], [223]. Liver PK activity is also responsive to endocrine hormone regulation. This was shown using  $[3\text{-}^{13}\text{C}]\text{lactate}$  to assess metabolic fluxes in

perfused livers from 48hr fasted rats in the presence or absence of glucagon [223].  $V_{PK}$  was ~50% the rate of  $V_{PCK}$  in control livers, which was reduced to ~20% during the perfusion of glucagon [223]. The aforementioned work is one publication among several to yield sizeable estimates of  $V_{PK+ME}/V_{PCK}$  and  $V_{PK+ME}/V_{CS}$  in the liver [209], [213], [224]; it is noteworthy that no research in these cited publications used isotopic propionate to estimate liver fluxes.

Because of the significance of pyruvate cycling in the interpretation of ILEs and the importance of PK in regulating liver glycolysis and gluconeogenesis, we sought to examine the incongruent findings of prior studies by testing specific modeling assumptions and assessing different combinations of isotope tracers and measurements that have been previously used to estimate liver metabolic fluxes *in vivo*. We confirmed that assumptions about extrahepatic tracer recycling and equilibration of 4C CAC intermediates can significantly alter estimates of pyruvate cycle fluxes. These assumptions may be sensitive to hormonal and nutritional status and to whether the primary tracer enters “upstream” or “downstream” of oxaloacetate. It is noteworthy that multi-compartment models with expanded metabolite labeling measurements and fewer simplifying assumptions still indicated significant liver pyruvate cycling.

Previous work suggests that extrahepatic tissues may not process isotopic propionate and lactate equivalently [211]. This has been shown in the perfused heart where the provision of propionate can influence oxidative metabolism [154]. Nevertheless, liver flux estimates using both isotopes achieved reasonable agreement when broader *in vivo* physiology was modeled. Liver  $V_{PK+ME}$  flux was reduced, but not eliminated, by the *in vivo* operation of the Cori cycle in models that accounted for extrahepatic metabolism. Total anaplerosis was consistently observed to be higher than the rate of citrate synthase, regardless of the isotope used in the study. Estimates of the  $V_{PCK}/V_{CS}$  ratio reported here are within the range previously observed across modeling platforms and species using various isotopes [62], [99], [100], [106], [209], [213], [218], [224]. These observations, perhaps, help to resolve some of the recent concerns expressed by others on the incompatibility of  $^{13}C$ -labeled propionate or lactate for the measurement of

hepatic fluxes. Our results also underscore the importance of model design and optimal isotope selection for the accuracy and precision of MFA [24].

No differences in plasma glucose concentration, endogenous glucose production, or gluconeogenesis were observed in mice infused with either  $^{13}\text{C}_3\text{Prop}$  or  $^{13}\text{C}_3\text{Lac}$ , consistent with other recently published data [29], [109]. The substrate actions of propionate on hepatic metabolism, however, are unclear. Others have reported that propionate increases glucose production and plasma glucose concentrations in rats [218]. Conversely, administration of propionate with lactate in perfused liver has been shown to inhibit glucose production [225]. Similar limitations may also be important in the use of  $^{13}\text{C}_3\text{Lac}$ , as circulating lactate acts as a major carbon shuttle between and within numerous tissues in the body [163], and recycled lactate significantly contributes to gluconeogenesis during fasting [165]. In fact, infusion of  $[\text{U-}^{13}\text{C}_6]\text{glucose}$  and the generation of enriched lactate from extrahepatic tissues may serve as an experimental tracer strategy for estimating endogenous glucose production and gluconeogenesis [75], [110]. In consideration of these data, we developed expanded models where liver and extrahepatic metabolism were treated as separate compartments bridged by a plasma compartment, and plasma lactate was allowed to equilibrate with extrahepatic pyruvate/alanine.

Affirmative claims regarding the ability of these expanded models to resolve specific peripheral fluxes are cautioned as the extrahepatic compartment was not designed to encompass the gamut of metabolism present outside the liver. For example, gluconeogenic fluxes from extrahepatic tissues (e.g., kidney) were assumed to have a marginal influence on plasma glucose enrichment. This assumption was validated, in part, by the acceptable agreement between plasma glucose and liver metabolite enrichments obtained when both were simultaneously regressed using expanded models. It is also plausible that other enriched plasma metabolites not measured here could influence flux solutions. Though the liver displays some functional heterogeneity, liver metabolites were modeled as steady-state components of a single gluconeogenic compartment. This is a limited but reasonable assumption for hepatocytes; but not likely to be true for nonparenchymal cells

of the liver which could not be separated from tissue extracts. It is important to also consider that our results are specific to a discrete set of well controlled, *in vivo* conditions; the experimental strategy and results presented here should not necessarily be extrapolated to other designs (e.g., involving significant variations in nutrient load). A carotid artery catheter was surgically implanted to avoid mouse handling during plasma sample collection. It is not known whether other sampling procedures might impact the endocrine state of the mouse and interfere with flux estimates.

Model-based regression approaches are needed to account for the complexities of *in vivo* stable isotope experiments and to rigorously test assumptions used in the calculation of metabolic fluxes. The availability of flexible modeling tools [e.g., INCA [69], Metran [70], 13CFLUX2 [78]] now make this increasingly possible. Comprehensive isotopomer modeling and integrative flux analysis methodologies have the potential to reconcile apparently divergent results and identify flux estimates that are sensitive to methodological differences or, conversely, are robust to a variety of study designs and assumptions. The INCA software is generalizable to tracers with any combination of labeled atoms, and we can readily construct models that take differences in tracers or administration route into account. Furthermore, INCA can model transient labeling experiments that result from a step input of labeled tracer [69]. As a result, we expect that the findings of the current study are applicable to a wide range of experimental systems used in metabolism research, and the models can be adapted to other possible study designs.

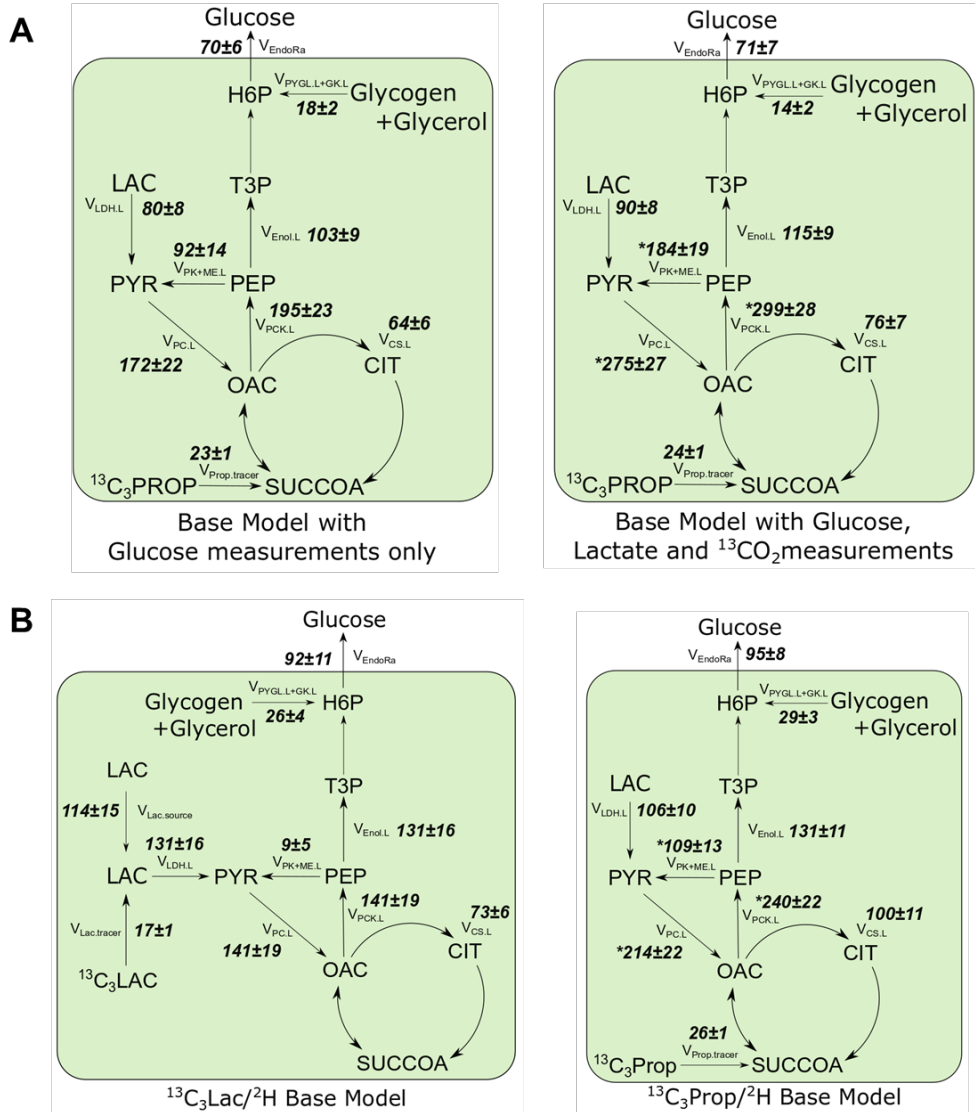
Here, we demonstrate the significance of secondary tracer effects and incomplete isotope equilibration on flux estimates obtained from *in vivo* ILEs, which can impact a variety of flux modeling approaches. When we expanded our base model by adding several liver-specific metabolite measurements while relaxing assumptions related to isotopic equilibrium and tracer recycling, our results indicate that significant liver pyruvate cycling persists under fasting conditions. Furthermore, we did not find evidence that exogenous propionate administration had a significant effect on glucose-producing or pyruvate cycling fluxes. Although estimates of liver pyruvate cycling were influenced by Cori cycle activity, accounting for

extrahepatic metabolism in an expanded multi-compartment MFA model did not abolish liver pyruvate cycle flux. One potential way to further examine the role and importance of pyruvate cycling in the liver would be to utilize liver-specific, genetic or pharmacological inhibition of the PK enzyme.

#### **4.6 Acknowledgements**

We thank Vanderbilt's Mouse Metabolic Phenotyping Center (MMPC) for their assistance in some *in vivo* studies described here. The authors have no conflicts of interest. This research was supported by NIH grants R01 DK106348 and U01 CA235508, the Integrated Training in Engineering and Diabetes (T32) Kirschstein NRSA Fellowship, and Vanderbilt's MMPC (NIH grant U24 DK059637).

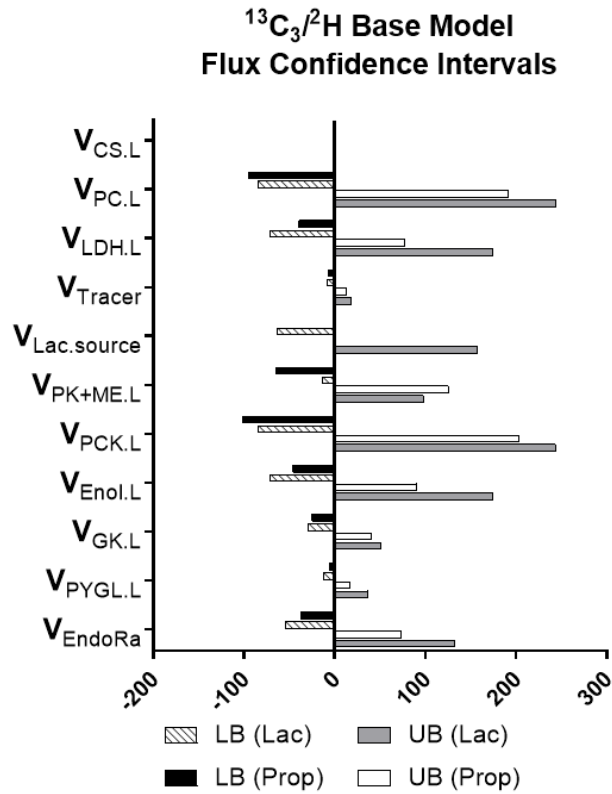
#### 4.7 Appendix: Supplemental figures and tables



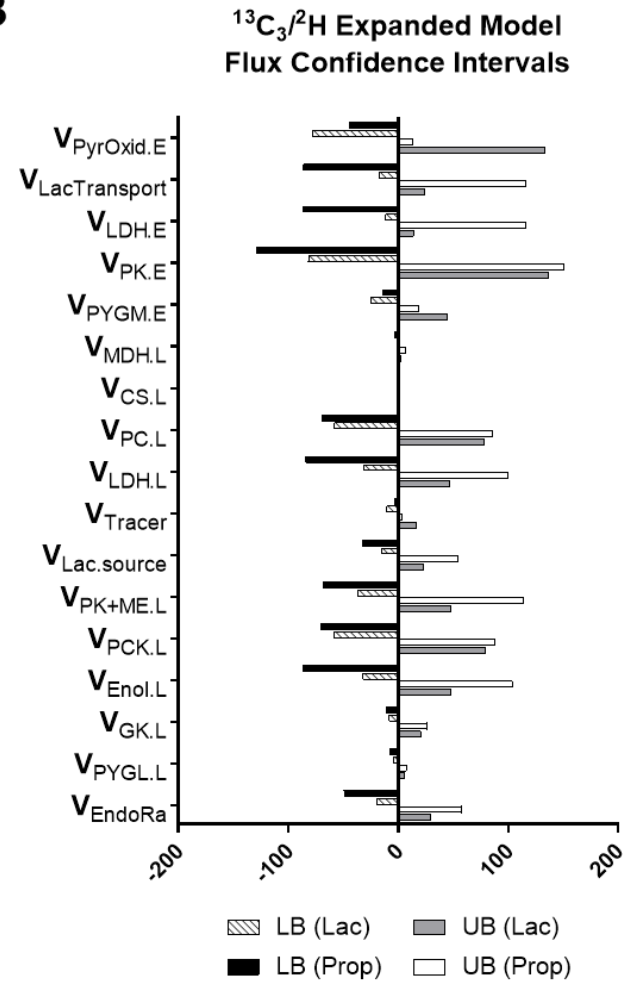
**Figure 4A.1: Regression of base model to specific measurement sets. Related to Figures 4.2, 4A.2, and Table 4A.1**  
 (A) Flux estimates obtained from the base model using plasma glucose MIDAs alone contrasted with those that included  $^{13}\text{CO}_2$  and plasma lactate measurements in the flux regression. Data are presented as means ( $\mu\text{mol}/\text{kg}/\text{min}$ )  $\pm$  SEM, ( $n=4$ ) \* $p < 0.05$  vs. base model with glucose measurements only  
 (B) Base model flux estimates from mice infused with  $^{13}\text{C}_3\text{Lac}/^2\text{H}$  or  $^{13}\text{C}_3\text{Prop}/^2\text{H}$  isotopes. Data are presented as means ( $\mu\text{mol}/\text{kg}/\text{min}$ )  $\pm$  SEM ( $n=6-7$ ) \* $p < 0.05$  vs.  $^{13}\text{C}_3\text{Lac}/^2\text{H}$  base model



**A**



**B**



**Figure 4A.2: Confidence interval widths in dual tracer models. Related to Figures 4.2 and 4.5**

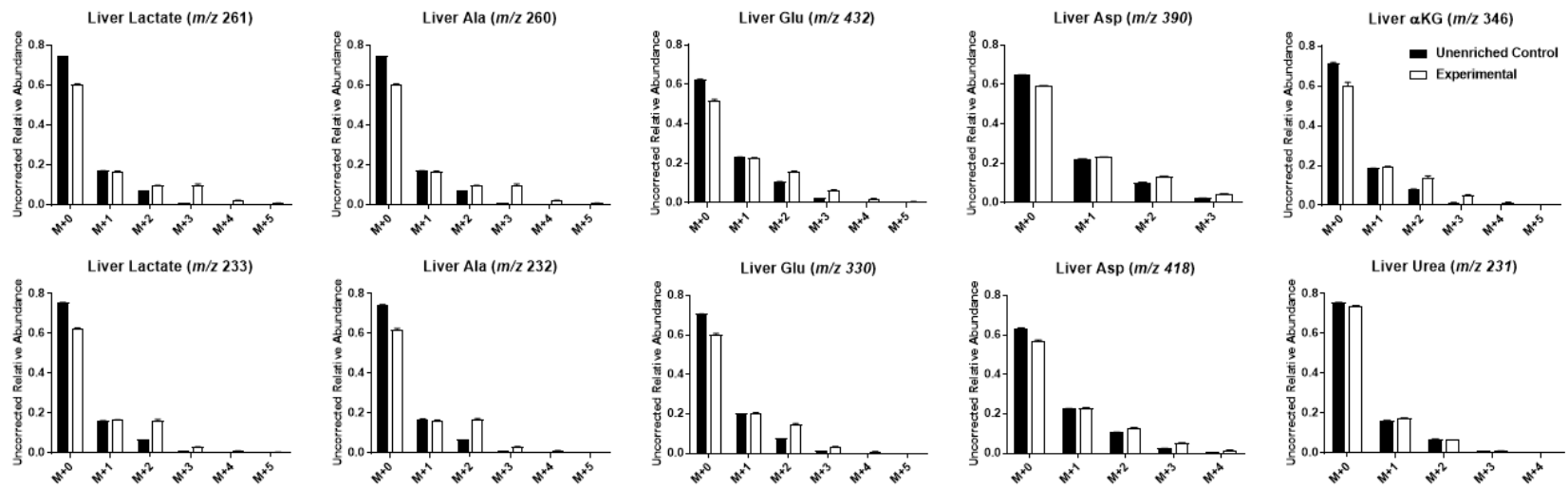
95% confidence intervals were calculated for relative hepatic and extrahepatic fluxes in INCA.

(A)  $^{13}\text{C}_3\text{Lac}/^2\text{H}$  (SSR Ave:  $19.9 \pm 3.5$ , Expected Range: 11-36.8 DOF: 22) and  $^{13}\text{C}_3\text{Prop}/^2\text{H}$  Base Models (SSR Ave:  $32.5 \pm 5.4$ , Expected Range: 11-36.8 DOF: 22).  $V_{\text{Tracer}}$  represents the flux  $V_{\text{Lac.tracer}}$  or  $V_{\text{Prop.tracer}}$  in the liver compartment, depending on the experiment

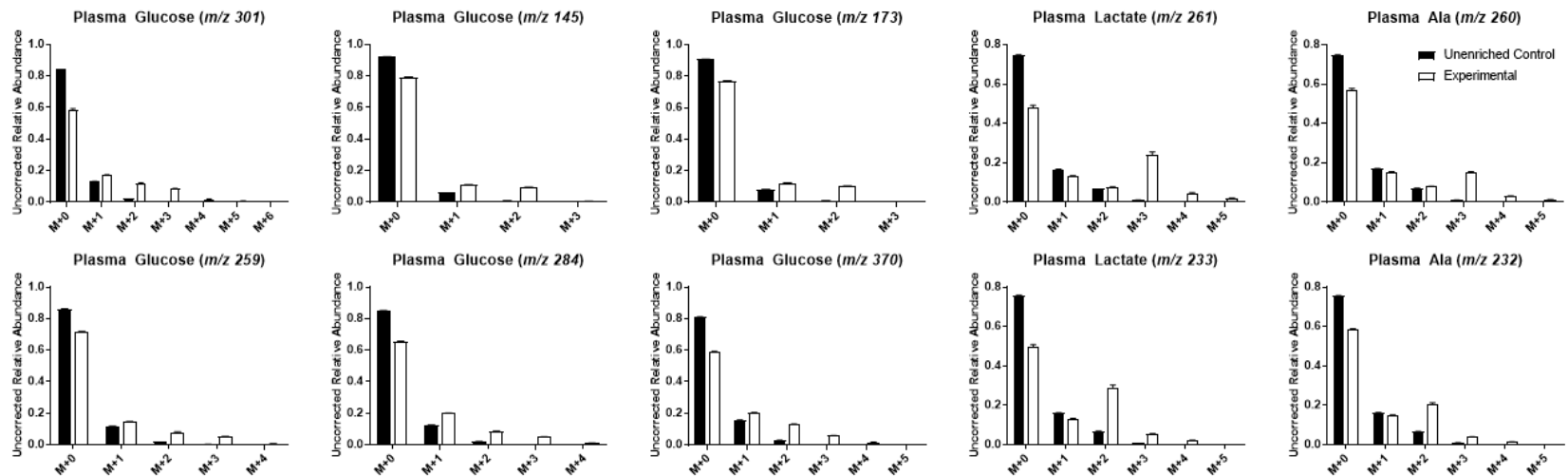
(B)  $^{13}\text{C}_3\text{Lac}/^2\text{H}$  (SSR Ave:  $78.4 \pm 8.3$ , Expected Range: 49.6-96.2, DOF: 72) and  $^{13}\text{C}_3\text{Prop}/^2\text{H}$  Expanded Models (SSR Ave:  $70.9 \pm 8.1$ , Expected Range: 49.6-96.2, DOF: 72).  $V_{\text{Tracer}}$  represents the flux  $V_{\text{Lac.inf}}$  in blood plasma or the flux of  $V_{\text{Prop.inf}}$  in the liver compartment, depending on the experiment

Upper and lower bounds are presented as the mean differences (x-axis) from the relative flux estimates ( $n=5-7$ ). Ranges are expressed relative to  $V_{\text{CS.L}}=100$ . The Expected Range of the SSR is calculated from the 95% confidence limits of a chi-square cumulative distribution function with the indicated degrees of freedom (DOF)

**A**



**B**

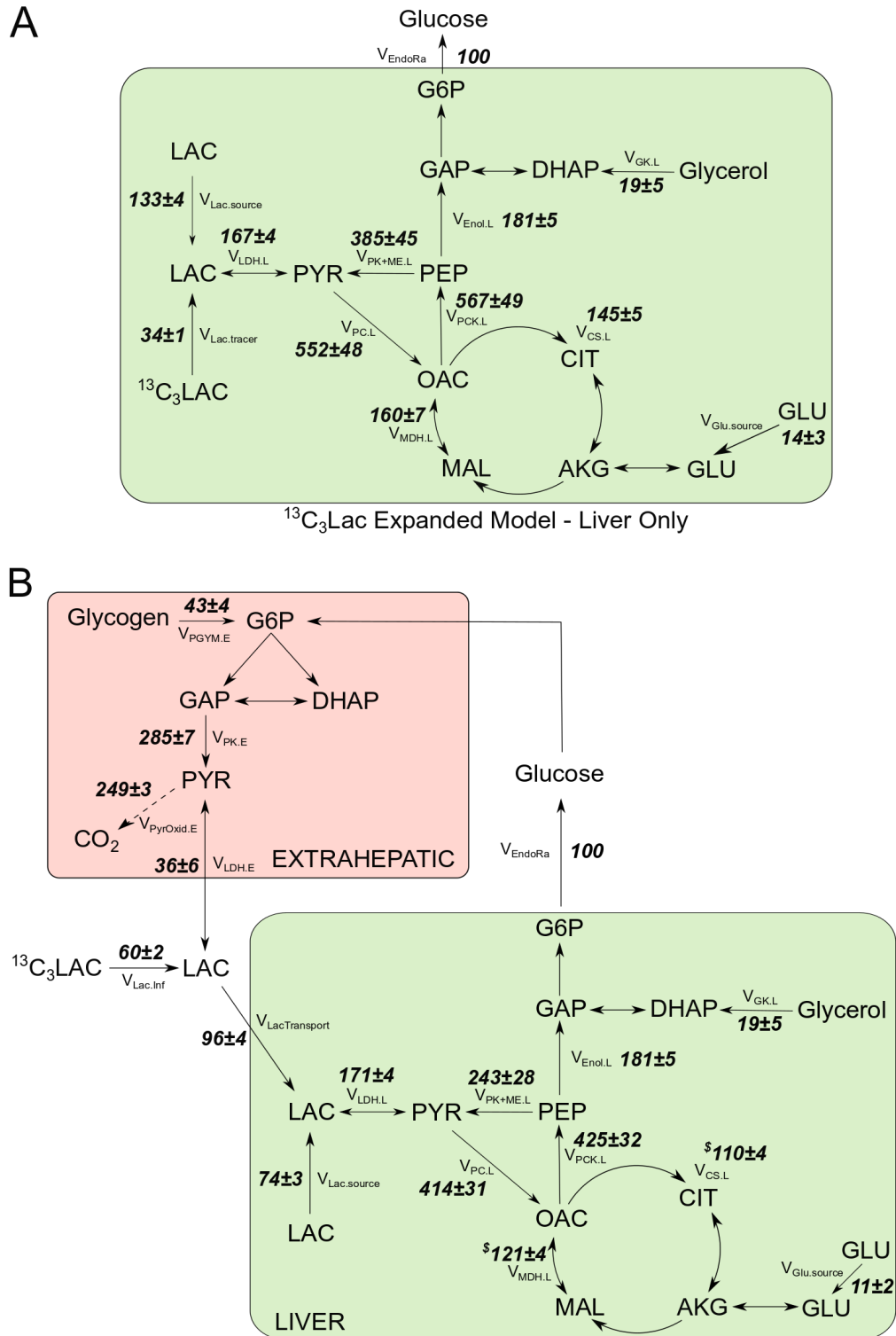


**Figure 4A.3: Mass isotopomer measurements for plasma and liver metabolites. Related to Figures 3, 4, S4, S5, S6, and Tables S3 and S5.**

(A) Liver lactate (m/z 261, 233), alanine (m/z 260, 232), glutamate (m/z 432, 330), aspartate (m/z 418, 390),  $\alpha$ -ketoglutarate (m/z 346), and urea (m/z 231) derivative measurements

(B) Plasma glucose (m/z 301,145,173, 259, 284, 370), alanine, (m/z 260, 232) and lactate (m/z 261, 233) derivative measurements

Enriched mass isotopomer distributions were determined using GC-MS for metabolites extracted from liver and plasma harvested at the close of the experimental period from 19-20hr fasted C57Bl/6J mice infused with  $^{13}\text{C}_3\text{Lac}$ . Unenriched samples were obtained from control C57Bl/6 mice for metabolite identification and measurement error determination. Data are presented as means  $\pm$  SEM (n=7)

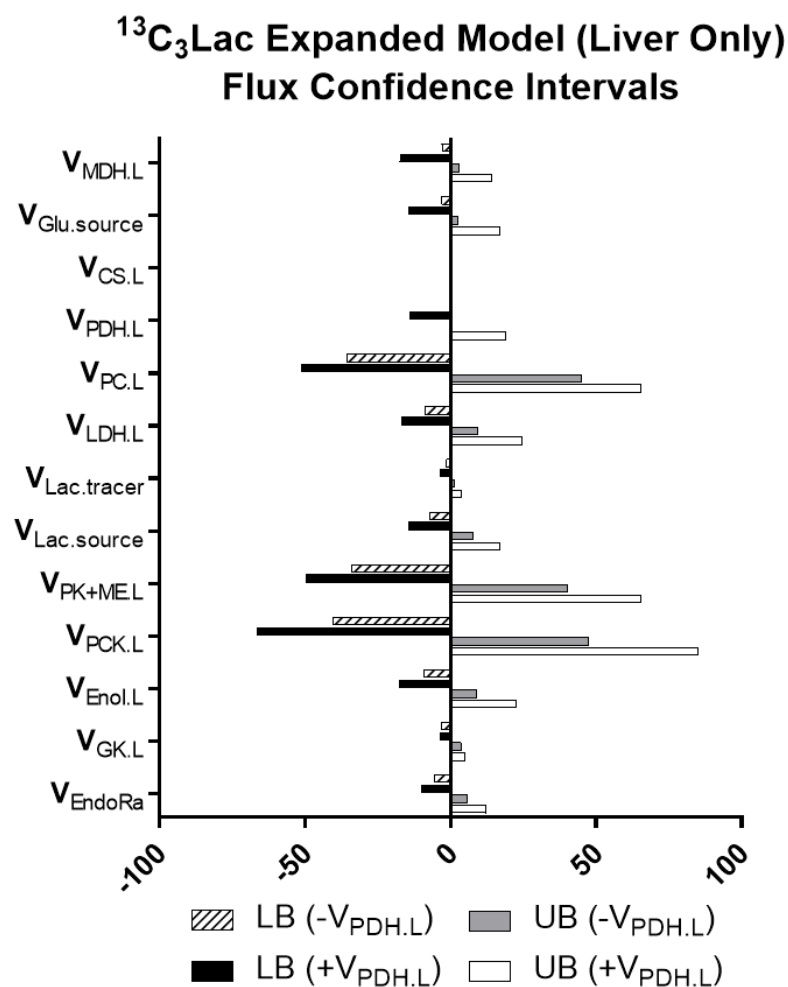


**Figure 4A.4: Expansion of models in mice infused with  $^{13}\text{C}_3\text{Lac}$ . Related to Figures 4, S3, S5 and Tables S3 and S5**

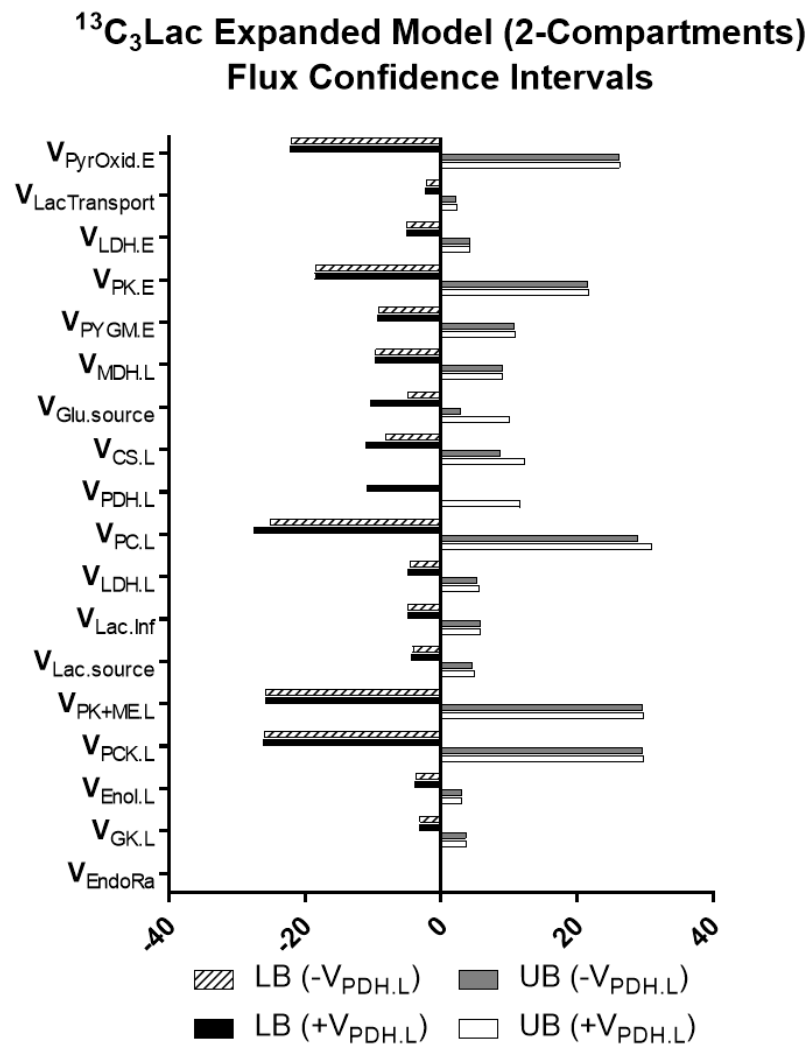
- (A) Relative flux estimates from expanded model (liver only) using plasma and liver tissue measurements  
 (B) Relative flux estimates from the same mice presented in (A) regressed using an expanded model including an extrahepatic compartment to facilitate descriptions of Cori cycling; mice were infused with  $^{13}\text{C}_3\text{Lac}$  only.

Data are presented as means  $\pm$  SEM (n=7) \*p<0.05 vs.  $^{13}\text{C}_3\text{Lac}$  expanded model – liver only

A



B

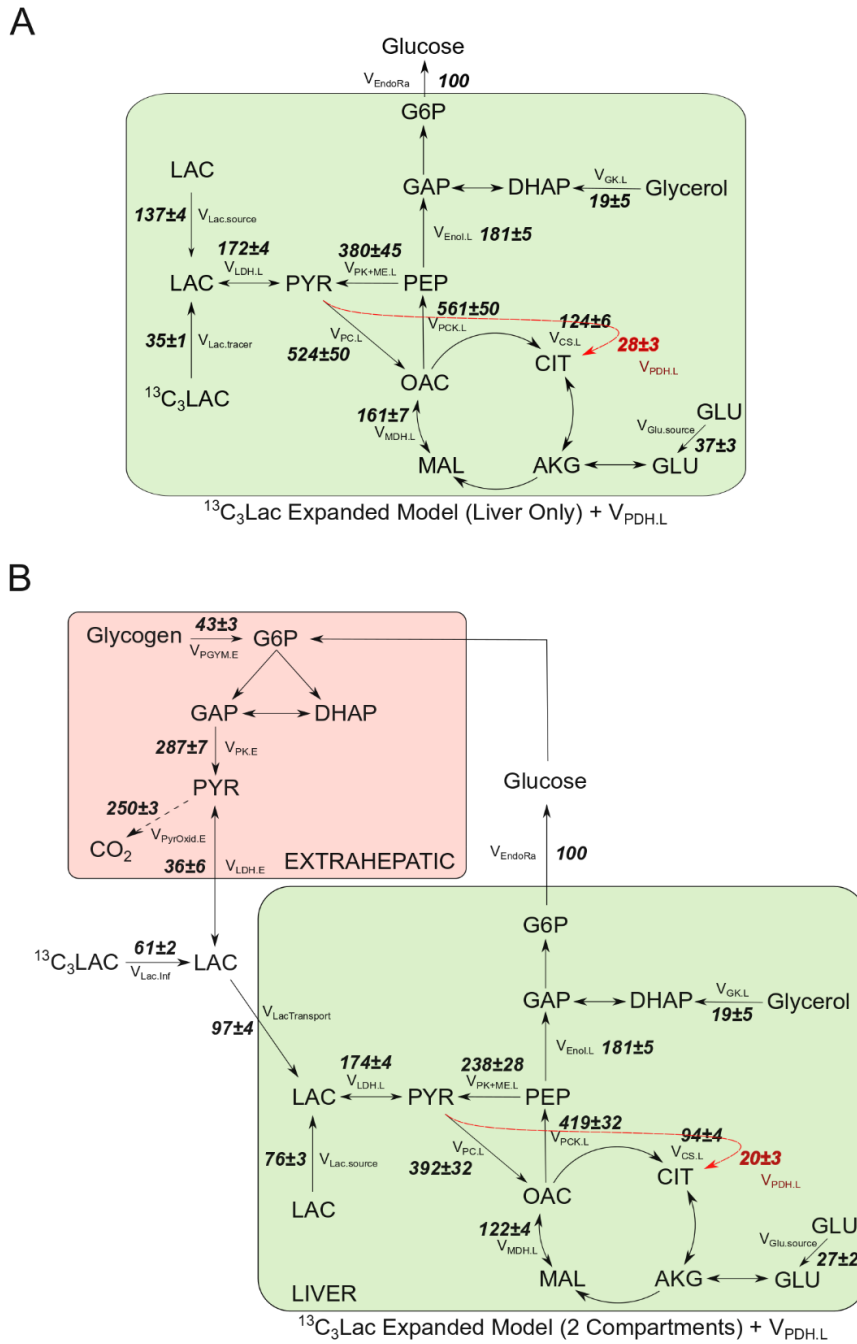


**Figure 4A.5: Confidence interval widths in  $^{13}\text{C}_3\text{Lac}$  studies. Related to Figures 4.4, 4A.4 and 4A.6**

(A)  $^{13}\text{C}_3\text{Lac}$  expanded model – Liver Only for networks without PDH (SSR Ave:  $65.1 \pm 8.9$ , Expected Range: 44.6-89.2, DOF: 65) or with PDH ( $+V_{\text{PDH.L}}$ ) (SSR Ave:  $53.9 \pm 6.0$ , Expected Range 43.8-88, DOF: 64)

(B)  $^{13}\text{C}_3\text{Lac}$  expanded model with two compartments for networks without PDH (SSR Ave:  $80.7 \pm 9.6$ , Expected Range: 63.1-114.7, DOF: 87) or with PDH ( $+V_{\text{PDH.L}}$ ) (SSR Ave:  $68.4 \pm 6.6$ , Expected Range: 62.2-113.5, DOF: 86)

Upper and lower bounds are presented as the mean differences (x-axis) from relative flux estimates ( $n=5-7$ ). Ranges are expressed relative to  $V_{\text{CS.L}}=100$ . The Expected Range of the SSR is calculated from the 95% confidence limits of a chi-square cumulative distribution function with the indicated degrees of freedom (DOF)

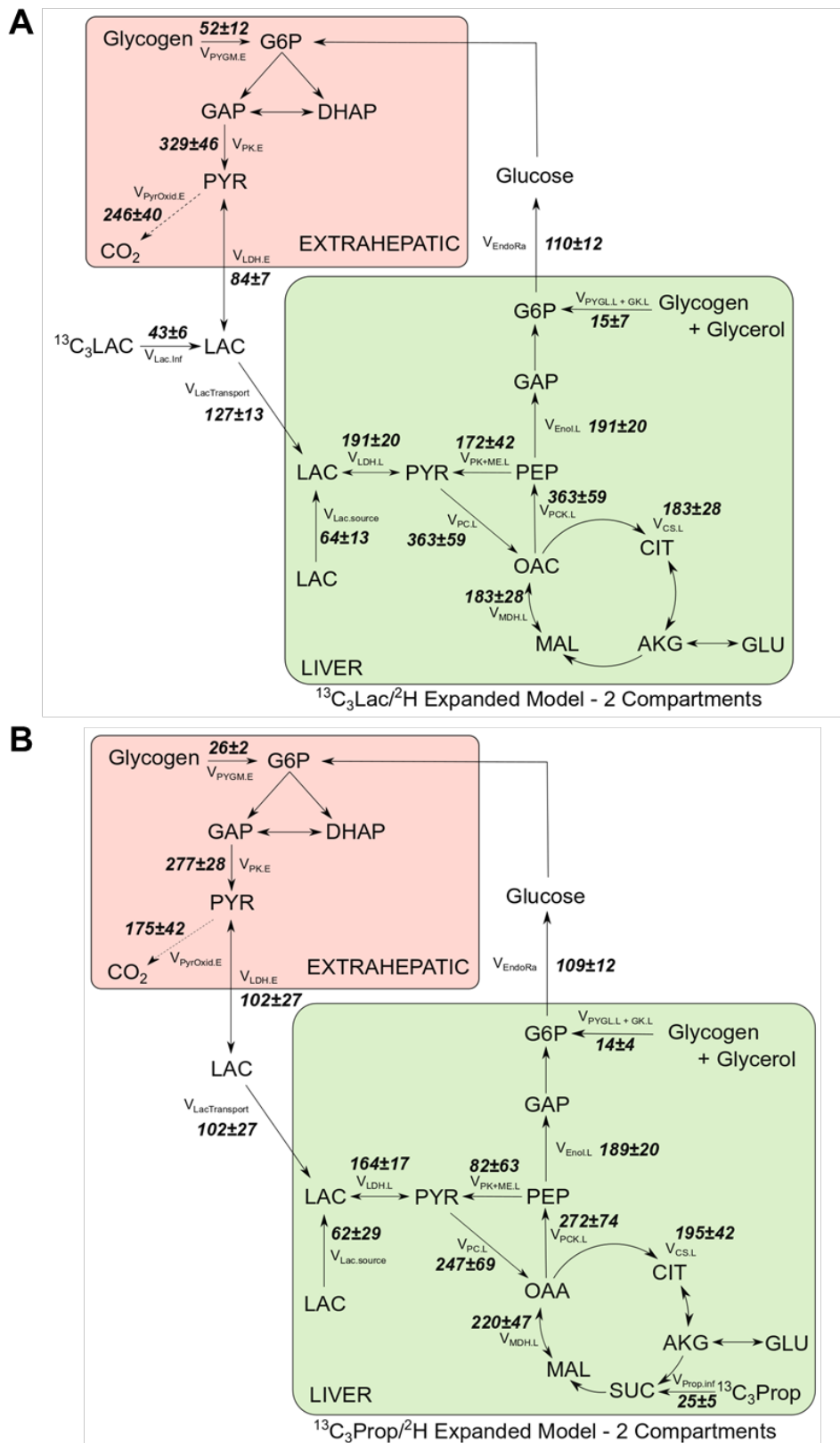


**Figure 4A. 6: Testing the assumption of low  $V_{\text{PDH.L}}$  flux during fasting with  $^{13}\text{C}_3\text{Lac}$ . Related to Figure 4.4B, 4A.3, 4A.5, and Tables 4A.3 and 4A.5**

(A) Relative flux estimates from expanded model (liver only) using plasma and liver tissue measurements and an active pyruvate dehydrogenase complex (+ $V_{\text{PDH.L}}$ ) in the liver

(B) Relative flux estimates from the same mice presented in (A) using a two-compartment expanded model with an active pyruvate dehydrogenase complex (+ $V_{\text{PDH.L}}$ ) in the liver

Data are presented as means  $\pm$  SEM ( $n=7$ )



**Figure 4A.7: Comparison of <sup>13</sup>C<sub>3</sub>Lac/<sup>2</sup>H and <sup>13</sup>C<sub>3</sub>Prop/<sup>2</sup>H isotopes for hepatic flux estimates using expanded models of metabolism. Related to Figures 4.5, 4A.2, and Tables 4A.2 and 4A.4**

(A) Expanded model (two compartments) showing absolute flux estimates in 19-20hr fasted, C57Bl/6J mice infused with <sup>13</sup>C<sub>3</sub>Lac/<sup>2</sup>H or

(B) <sup>13</sup>C<sub>3</sub>Prop/<sup>2</sup>H isotopes

Data are presented as means  $\pm$  SEM ( $\mu$ mol/kg/min, n=5)

**Table 4A.1: Base reaction network for  $^2\text{H}/^{13}\text{C}$  MFA. Related to Figures 4.2D, 4.2E and 4A.1.**

The base model of liver metabolism tracks carbon (uppercase) and hydrogen (lowercase) atoms through the specified enzymatic reactions. Fluxes are regressed from plasma measurements of glucose MIDAs using either  $^{13}\text{C}_3\text{Lac}/^2\text{H}$  or  $^{13}\text{C}_3\text{Prop}/^2\text{H}$  isotopes. Unenriched sources and sinks are denoted “.source” and “.sink”, respectively.  $^2\text{H}$  and  $^{13}\text{C}$  isotopes are introduced into model reactions as “.tracer” sources. Compartments are denoted by “.P” for plasma and “.L” for liver. Liver is the default compartment if no compartment is designated for a metabolite. Simulations were performed post hoc from fluxes regressed to experimental labeling data. Unless otherwise noted here, reaction network and model assumptions have been described elsewhere [14]

Flux	Base Model Reaction Network
<b><i>Liver Compartment: Glucose Synthesizing and Oxidative Metabolic Reactions</i></b>	
$V_{\text{Glc.inf}}$	Glucose.inf (AaBbCcDdEeFfg) $\rightarrow$ Glucose.P (AaBbCcDdEeFfg)
$V_{\text{EndoRa}}$	H6P (AaBbCcDdEeFfg) $\rightarrow$ Glucose.P (AaBbCcDdEeFfg)
$V_{\text{PYGL.L}}$	Glycogen (AaBbCcDdEeFfg) + H (h) $\rightarrow$ H6P (AaBbCcDdEeFfg) + H (b)
$V_{\text{Aldo.L}}$	T3P (ChBcAab) + T3P (DdEeFfg) + H (i) $\rightarrow$ H6P (AbBiCcDdEeFfg) + H (h) + H (a)
$V_{\text{GAPDH.L}}$	BPG (ABbCcd) + H (e) + H (f) $\rightarrow$ T3P (AfBeCcd) + H (b)
$V_{\text{GK.L}}$	Glycerol (AaeBbCcd) + H (f) $\rightarrow$ T3P (AeBfCcd) + H (a) + H (b)
$V_{\text{EnoL.L}}$	PEP (ABCcd) + H (b) $\rightarrow$ BPG (ABbCcd)
$V_{\text{PK+ME.L}}$	PEP (ABCab) + H (c) $\rightarrow$ Pyr (ABCabc)
$V_{\text{LDH.L}}$	Lac (ABbCcde) $\rightarrow$ Pyr (ABCcde) + H (b)
$V_{\text{Lac.source}}$	Lac.source (ABaCbcd) $\rightarrow$ Lac (ABaCbcd)
$V_{\text{PC.L}}$	Pyr (ABCcde) + CO <sub>2</sub> (D) + H (f) + H (g) $\rightarrow$ 0.5*Oac (ABCfgD) + 0.5*Oac (DCBfgA) + H (c)
$V_{\text{PCK.L}}$	Oac (ABCabD) $\rightarrow$ PEP (ABCab) + CO <sub>2</sub> (D)
$V_{\text{CS.L}}$	Oac (ABCcdD) + AcCoA (EFfgh) $\rightarrow$ Cit (DCcdBFfgEA) + H (h)
$V_{\text{IDH.L}}$	Cit (ABabCDcdEF) + H (e) $\rightarrow$ Akg (ABCeaDcdE) + H (b) + CO <sub>2</sub> (F)
$V_{\text{OGDH.L}}$	Akg (ABCabDcdE) $\rightarrow$ SucCoA (BCabDcdE) + CO <sub>2</sub> (A)
$V_{\text{SDH.L}}$	SucCoA (ABabCcdD) + H (e) + H (f) $\rightarrow$ 0.5*Oac (ABCefD) + 0.5*Oac (DCBefA) + H (a) + H (g)
$V_{\text{PCC.L}}$	PropCoA (ABabCcde) + CO <sub>2</sub> (D) $\rightarrow$ SucCoA (ACcdBabD) + H (e)
$V_{\text{Bicarb.source}}$	Bicarb.source (A) $\rightarrow$ CO <sub>2</sub> (A)
$V_{\text{Bicarb.sink}}$	CO <sub>2</sub> (A) $\rightarrow$ Bicarb.sink (A)
$V_{\text{H.inf}}$	H.inf (a) $\rightarrow$ H (a)
$V_{\text{H.sink}}$	H $\rightarrow$ H.sink
<b><i><math>^{13}\text{C}</math>-Isotope Infusate Reactions</i></b>	
$V_{\text{Lac.tracer}}$	Lac.tracer (ABaCbcd) $\rightarrow$ Lac (ABaCbcd)
$V_{\text{Prop.tracer}}$	Prop.tracer (ABabCcde) $\rightarrow$ PropCoA (ABabCcde)

**Table 4A.2: Comparison of selected flux estimates between base and expanded models of  $^{13}\text{C}/^2\text{H}$  studies. Related to Figures 4.2 and 4.5, 4A.1 and 4A.7.**

<sup>a</sup> denotes fluxes that are significantly different between the  $^{13}\text{C}_3\text{Lac}/^2\text{H}$  and  $^{13}\text{C}_3\text{Prop}/^2\text{H}$  Base Models. <sup>b</sup> denotes fluxes that are significantly different between the  $^{13}\text{C}_3\text{Lac}/^2\text{H}$  Base and  $^{13}\text{C}_3\text{Lac}/^2\text{H}$  Expanded Models. Data presented as means ( $\mu\text{mol}/\text{kg}/\text{min}$ )  $\pm$  SEM ( $p \leq 0.05$ ,  $n=5-7$ )

<b>Flux Reaction</b>	<b>Base Model <math>^{13}\text{C}_3\text{Lac}/^2\text{H}</math></b>	<b>Base Model <math>^{13}\text{C}_3\text{Prop}/^2\text{H}</math></b>	<b>Expanded Model <math>^{13}\text{C}_3\text{Lac}/^2\text{H}</math></b>	<b>Expanded Model <math>^{13}\text{C}_3\text{Prop}/^2\text{H}</math></b>
$V_{\text{CS.L}}$	$73 \pm 6$	$100 \pm 11$	$183 \pm 28^b$	$195 \pm 42$
$V_{\text{Enol.L}}$	$131 \pm 16$	$131 \pm 11$	$191 \pm 20$	$189 \pm 20$
$V_{\text{PYGL+GK.L}}$	$26 \pm 4$	$29 \pm 3$	$15 \pm 7$	$14 \pm 4$
$V_{\text{LDH.L}}$	$131 \pm 16$	$106 \pm 10$	$191 \pm 20$	$164 \pm 17$
$V_{\text{PC.L}}$	$141 \pm 19$	$214 \pm 22^a$	$363 \pm 59^b$	$247 \pm 69$
$V_{\text{PCK.L}}$	$141 \pm 19$	$240 \pm 22^a$	$363 \pm 59^b$	$272 \pm 74$
$V_{\text{PK+ME.L}}$	$9 \pm 5$	$109 \pm 13^a$	$172 \pm 42^b$	$82 \pm 63$



**Table 4A.3: Expanded reaction network for <sup>13</sup>C MFA. Related to Figures 4.4, 4A.4 and 4A.6. (Table and caption continues to next page)**

<b>Flux</b>	<b>Expanded Model Reaction Network (<sup>13</sup>C transitions only)</b>
<b><i>Liver Compartment: Glucose Synthesizing and Oxidative Metabolic Reactions</i></b>	
$V_{\text{EndoRa}}$	G6P (ABCDEF) → Glucose.P (ABCDEF)
$V_{\text{Aldo.L}}$	DHAP (ABC) + GAP (DEF) → G6P (CBADEF)
$V_{\text{TPI.L}}$	DHAP (ABC) ↔ GAP (ABC)
$V_{\text{GAPDH.L}}$	BPG (ABC) → GAP (ABC)
$V_{\text{GK.L}}$	Glycerol (ABC) → DHAP (ABC)
$V_{\text{Enol.L}}$	PEP (ABC) → BPG (ABC)
$V_{\text{PK+ME.L}}$	PEP (ABC) → Pyr (ABC)
$V_{\text{LDH.L}}$	Lac (ABC) ↔ Pyr (ABC)
$V_{\text{Lac.source}}$	Lac.source (ABC) → Lac (ABC)
$V_{\text{ALT.L}}$	Ala (ABC) ↔ Pyr (ABC)
$V_{\text{PC.L}}$	Pyr (ABC) + CO <sub>2</sub> (D) → Oac (ABCD)
$V_{\text{PCK.L}}$	Oac (ABCD) → PEP (ABC) + CO <sub>2</sub> (D)
$V_{\text{PDH.L}}$	Pyr (ABC) → AcCoA (BC) + CO <sub>2</sub> (A)
$V_{\beta\text{Oxid.L}}$	Fat (AB) → AcCoA (AB)
$V_{\text{CS.L}}$	Oac (ABCD) + AcCoA (EF) → Cit (DCBFEA)
$V_{\text{IDH.L}}$	Cit (ABCDEF) ↔ Akg (ABCDE) + CO <sub>2</sub> (F)
$V_{\text{GDH.L}}$	Glu (ABCDE) ↔ Akg (ABCDE)
$V_{\text{Glu.source}}$	Glu.source (ABCDE) → Glu (ABCDE)
$V_{\text{OGDH.L}}$	Akg (ABCDE) → SucCoA (BCDE) + CO <sub>2</sub> (A)
$V_{\text{SCS.L}}$	SucCoA (ABCD) → Suc* (ABCD)
$V_{\text{SDH.L}}$	Suc* (ABCD) ↔ Fum* (ABCD)
$V_{\text{FH.L}}$	Fum* (ABCD) ↔ Mal (ABCD)
$V_{\text{MDH.L}}$	Mal (ABCD) ↔ Oac (ABCD)
$V_{\text{Bicarb source}}$	Bicarb.source (A) → CO <sub>2</sub> (A)
$V_{\text{Bicarb sink}}$	CO <sub>2</sub> (A) → Bicarb.sink (A)
<b><i><sup>13</sup>C-Isotope Infusate Reactions</i></b>	
$V_{\text{Lac.tracer}}$	Lac.inf (ABC) → Lac (ABC)
$V_{\text{Lac.inf}}$	Lac.inf (ABC) → Lac.P (ABC)

**Table 4A.3: Expanded reaction network for <sup>13</sup>C MFA. Related to Figures 4.4, 4A.4 and 4A.6.**

Expanded model of liver metabolism for tracking only carbon atoms through the specified enzymatic reactions. Fluxes are regressed from liver and plasma measurements for mice infused with <sup>13</sup>C<sub>3</sub>Lac. Unenriched sources and sinks are denoted “.source” and “.sink”, respectively. Infused <sup>13</sup>C isotopes are introduced into model reactions as “.tracer” sources in liver-only models or “.inf” sources for two-compartment models. (Note that these two types of tracer input fluxes are not expected to be equivalent in the case of <sup>13</sup>C<sub>3</sub>Lac administration, since V<sub>Lac.tracer</sub> represents liver-specific uptake of the tracer while V<sub>Lac.inf</sub> represents infusion of tracer into the plasma compartment.) Compartments are denoted by “.P” for plasma, “.E” for extrahepatic, and “.L” for liver. Liver is the default compartment if no compartment is designated for a metabolite. The two-compartment model includes reactions for the liver, <sup>13</sup>C-bicarbonate recycling, and Cori cycle reactions. \*denotes that the carbons of succinate and fumarate are symmetric.

<i>Extrahepatic Compartment: Glycolytic, and Cori Cycle Reactions</i>	
V <sub>HK.E</sub>	Glucose.P (ABCDEF) → G6P.E (ABCDEF)
V <sub>PYGM.E</sub>	Glycogen.E (ABCDEF) → G6P.E (ABCDEF)
V <sub>Aldo.E</sub>	G6P.E (ABCDEF) → GAP.E (CBA) + DHAP.E (DEF)
V <sub>TPI.E</sub>	GAP.E (ABC) ↔ DHAP.E (ABC)
V <sub>GAPDH.E</sub>	GAP.E (ABC) → BPG.E (ABC)
V <sub>Enol.E</sub>	BPG.E (ABC) → PEP.E (ABC)
V <sub>PK.E</sub>	PEP.E (ABC) → Pyr.E (ABC)
V <sub>PyrOxid.E</sub>	Pyr.E (ABC) → CO <sub>2</sub> (A) + CO <sub>2</sub> (B) + CO <sub>2</sub> (C)
V <sub>LDH.E</sub>	Pyr.E (ABC) ↔ Lac.P (ABC)
V <sub>LacTransport</sub>	Lac.P (ABC) → Lac (ABC)

**Table 4A.4: Expanded reaction network for  $^2\text{H}/^{13}\text{C}$  MFA. Related to Figures 4.5 and 4A.7. (Table and caption continues to next page)**

<b>Flux</b>	<b>Expanded Model Reaction Network (<math>^2\text{H}/^{13}\text{C}</math> transitions)</b>
<b>Expanded Liver Compartment: Glucose Synthesizing and Oxidative Metabolic Reactions</b>	
$V_{\text{Glc.inf}}$	Glucose.inf (AaBbCcDdEeFfg) $\rightarrow$ Glucose.P (AaBbCcDdEeFfg)
$V_{\text{EndoRa}}$	G6P (AaBbCcDdEeFfg) $\rightarrow$ Glucose.P (AaBbCcDdEeFfg)
$V_{\text{PYGL.L}}$	Glycogen (AaBbCcDdEeFfg) + H (h) $\rightarrow$ G6P (AaBbCcDdEeFfg) + H (b)
$V_{\text{Aldo.L}}$	DHAP (AabBCcd) + GAP (DeEfFgh) + H (i) $\rightarrow$ G6P (CdBiAaDeEfFgh) + H (b) + H (c)
$V_{\text{TPI.L}}$	DHAP (AabBCcd) + H (e) $\leftrightarrow$ GAP (AbBeCcd) + H (a)
$V_{\text{GAPDH.L}}$	BPG (ABbCcd) + H (a) $\rightarrow$ GAP (AaBbCcd)
$V_{\text{GK.L}}$	Glycerol (AabBeCcd) $\rightarrow$ DHAP (AabBCcd) + H (e)
$V_{\text{Enol.L}}$	PEP (ABCcd) + H (b) $\rightarrow$ BPG (ABbCcd)
$V_{\text{PK+ME.L}}$	PEP (ABCab) + H (c) $\rightarrow$ Pyr (ABCabc)
$V_{\text{LDH.L}}$	Lac (ABbCcde) $\leftrightarrow$ Pyr (ABCcde) + H (b)
$V_{\text{Lac.source}}$	Lac.source (ABbCcde) $\rightarrow$ Lac (ABbCcde)
$V_{\text{ALT.L}}$	Ala (ABbCcde) + H (f) $\leftrightarrow$ Pyr (ABCcdf) + H (b) + H (e)
$V_{\text{PC.L}}$	Pyr (ABCcde) + CO <sub>2</sub> (D) $\rightarrow$ Oac (ABCcdD) + H (e)
$V_{\text{PCK.L}}$	Oac (ABCabD) $\rightarrow$ PEP (ABCab) + CO <sub>2</sub> (D)
$V_{\text{CS.L}}$	Oac (ABCcdD) + AcCoA (EFfgh) $\rightarrow$ Cit (DCcdBFfgEA) + H (h)
$V_{\text{IDH.L}}$	Cit (ABabCDcdEF) + H (e) $\leftrightarrow$ Akg (ABCeaDcdE) + H (b) + CO <sub>2</sub> (F)
$V_{\text{GDH.L}}$	Glu (ABeCabDcdE) $\leftrightarrow$ Akg (ABCabDcdE) + H (e)
$V_{\text{OGDH.L}}$	Akg (ABCabDcdE) $\rightarrow$ SucCoA (BCabDcdE) + CO <sub>2</sub> (A)
$V_{\text{SCS.L}}$	SucCoA (ABabCcdD) $\rightarrow$ Suc* (ABabCcdD)
$V_{\text{PCC.L}}$	PropCoA (ABabCcde) + CO <sub>2</sub> (D) $\rightarrow$ SucCoA (ACcdBabD) + H (e)
$V_{\text{SDH.L}}$	Suc* (ABabCcdD) $\leftrightarrow$ Fum* (ABaCdD) + H (b) + H (c)
$V_{\text{FH.L}}$	Fum* (ABaCbD) + H (c) $\leftrightarrow$ Mal (ABaCcbD)
$V_{\text{MDH.L}}$	Mal (ABaCbcD) $\leftrightarrow$ Oac (ABCbcD) + H (a)
$V_{\text{Bicarb.source}}$	Bicarb.source (A) $\rightarrow$ CO <sub>2</sub> (A)
$V_{\text{Bicarb.sink}}$	CO <sub>2</sub> (A) $\rightarrow$ Bicarb.sink (A)
$V_{\text{H.inf}}$	H.inf (a) $\rightarrow$ H (a)
$V_{\text{H.sink}}$	H $\rightarrow$ H.sink

**Table 4A.4: Expanded reaction network for  $^2\text{H}/^{13}\text{C}$  MFA. Related to Figures 4.5 and 4A.7.**

Expanded model of liver metabolism for tracking both carbon (uppercase) and hydrogen (lowercase) atoms through the specified enzymatic reactions. Fluxes are regressed from liver and plasma measurements using either  $^{13}\text{C}_3\text{Lac}/^2\text{H}$  or  $^{13}\text{C}_3\text{Prop}/^2\text{H}$  isotopes. See Tables S1 and S3 for nomenclature

<i><math>^{13}\text{C}</math>-Isotope Infusate Reactions</i>	
$V_{\text{Lac.inf}}$	Lac.inf (ABbCcde) $\rightarrow$ Lac.P (ABbCcde)
$V_{\text{Prop.inf}}$	Prop.inf (ABabCcde) $\rightarrow$ PropCoA (ABabCcde)
<i>Expanded Extrahepatic Compartment: Glycolytic, and Cori Cycle Reactions</i>	
$V_{\text{HK.E}}$	Glucose.P (AaBbCcDdEeFfg) $\rightarrow$ G6P.E (AaBbCcDdEeFfg)
$V_{\text{PYGM.E}}$	Glycogen.E (AaBbCcDdEeFfg) + H (h) $\rightarrow$ G6P.E (AaBhCcDdEeFfg) + H (b)
$V_{\text{Aldo.E}}$	G6P.E (CdBiAaDeEfFgh) + H (b) + H (c) $\rightarrow$ DHAP.E (AabBCcd) + GAP.E (DeEfFgh) + H (i)
$V_{\text{TPI.E}}$	DHAP.E (AabBCcd) + H (e) $\leftrightarrow$ GAP.E (AbBeCcd) + H (a)
$V_{\text{GAPDH.E}}$	GAP.E (AaBbCcd) $\rightarrow$ BPG.E (ABbCcd) + H (a)
$V_{\text{Enol.E}}$	BPG.E (ABbCcd) $\rightarrow$ PEP.E (ABCcd) + H (b)
$V_{\text{PK.E}}$	PEP.E (ABCab) + H (c) $\rightarrow$ Pyr.E (ABCabc)
$V_{\text{ALT.E}}$	Ala.E (ABbCcde) + H (f) $\leftrightarrow$ Pyr.E (ABCcdf) + H (b) + H (e)
$V_{\text{PyrOxid.E}}$	Pyr.E (ABCcde) $\rightarrow$ H (c) + H (d) + H (e) + CO <sub>2</sub> (A) + CO <sub>2</sub> (B) + CO <sub>2</sub> (C)
$V_{\text{LDH.E}}$	Pyr.E (ABCcde) + H (b) $\leftrightarrow$ Lac.P (ABbCcde)
$V_{\text{LacTransport}}$	Lac.P (ABbCcde) $\rightarrow$ Lac (ABbCcde)

**Table 4A.5: Measured GC-MS fragment ions. Related to all Figures**

<b>Metabolite</b>	<b>m/z</b>	<b>Formula</b>	<b>Carbons</b>
Alanine	260	C <sub>11</sub> H <sub>26</sub> O <sub>2</sub> NSi <sub>2</sub>	1 2 3
Alanine	232	C <sub>10</sub> H <sub>26</sub> ONSi <sub>2</sub>	2 3
Aspartate	390	C <sub>17</sub> H <sub>40</sub> O <sub>3</sub> NSi <sub>3</sub>	2 3 4
Aspartate	418	C <sub>18</sub> H <sub>40</sub> O <sub>4</sub> NSi <sub>3</sub>	1 2 3 4
α-Ketoglutarate	346	C <sub>14</sub> H <sub>28</sub> O <sub>5</sub> NSi <sub>2</sub>	1 2 3 4 5
Glutamate	432	C <sub>19</sub> H <sub>42</sub> O <sub>4</sub> NSi <sub>3</sub>	1 2 3 4 5
Glutamate	330	C <sub>16</sub> H <sub>36</sub> O <sub>2</sub> NSi <sub>2</sub>	2 3 4 5
Glucose	370	C <sub>17</sub> H <sub>24</sub> O <sub>8</sub> N	1 2 3 4 5
Glucose	301	C <sub>14</sub> H <sub>21</sub> O <sub>7</sub>	1 2 3 4 5 6
Glucose	284	C <sub>13</sub> H <sub>18</sub> O <sub>6</sub> N	1 2 3 4
Glucose	259	C <sub>12</sub> H <sub>19</sub> O <sub>6</sub>	4 5 6
Glucose	173	C <sub>8</sub> H <sub>13</sub> O <sub>4</sub>	5 6
Glucose	145	C <sub>6</sub> H <sub>11</sub> O <sub>3</sub> N	1 2
Lactate	261	C <sub>11</sub> H <sub>25</sub> O <sub>3</sub> Si <sub>2</sub>	1 2 3
Lactate	233	C <sub>10</sub> H <sub>25</sub> O <sub>2</sub> Si <sub>2</sub>	2 3
Urea	231	C <sub>9</sub> H <sub>23</sub> N <sub>2</sub> OSi <sub>2</sub>	1

## **5. Multi-tissue $^2\text{H}/^{13}\text{C}$ flux analysis reveals reciprocal upregulation of renal gluconeogenesis in hepatic PEPCK-C knockout mice**

*JCI Insights* (2021), 6(11)

### **5.1 Abstract**

The liver is the major source of glucose production during fasting under normal physiological conditions. However, the kidney may also contribute to maintaining glucose homeostasis in certain circumstances. To test the ability of the kidney to compensate for impaired hepatic glucose production *in vivo*, we developed a novel stable isotope approach to simultaneously quantify gluconeogenic and oxidative metabolic fluxes in the liver and kidney. Hepatic gluconeogenesis from phosphoenolpyruvate was disrupted via liver-specific knockout of cytosolic PEPCK (KO).  $^2\text{H}/^{13}\text{C}$  isotopes were infused in fasted KO and wild-type (WT) littermate mice, and fluxes were estimated from isotopic measurements of tissue and plasma metabolites using a multi-compartment metabolic model. Hepatic gluconeogenesis and glucose production were reduced in KO mice, yet whole-body glucose production and arterial glucose were unaffected. Glucose homeostasis was maintained by a compensatory rise in renal glucose production and gluconeogenesis. Renal oxidative metabolic fluxes of KO mice increased to sustain the energetic and metabolic demands of elevated gluconeogenesis. These results show the reciprocity of the liver and kidney in maintaining glucose homeostasis by coordinated regulation of gluconeogenic flux through PEPCK-C. Combining stable isotopes with mathematical modeling provides a versatile platform to assess multi-tissue metabolism in various genetic, (patho)physiological, and pharmacological settings.

## 5.2 Introduction

Biochemical methods to quantify gene transcript, enzyme, and metabolite levels are widely used to assess metabolic pathway regulation. Though informative and even vital in some contexts, static measurements of biomolecule abundance may not be reliable indicators of the movement of substrates through a metabolic pathway (i.e., metabolic flux). For example, cytosolic phosphoenolpyruvate carboxykinase (PEPCK-C) decarboxylates and phosphorylates oxaloacetate to form phosphoenolpyruvate (PEP), yet PEPCK-C expression does not solely determine the rate of hepatic gluconeogenesis [2]. Burgess et al. have shown that PEPCK-C expression can vary widely while exerting limited control over gluconeogenic flux in perfused livers [2]. Similarly, knockout of PEPCK-C from the liver (KO) increases the mRNA of several enzymes of the hepatic citric acid cycle (CAC) [226]; however, flux through the CAC is expected to be minimal under these conditions [2], [227].

Isotopic tracer techniques have been developed to address the limitations of static metabolite and enzyme measurements in order to more accurately quantify metabolic flux. In general, these methods introduce a stable isotope to a live biological system; metabolic fluxes are then determined by analyzing the isotopic enrichment of metabolites in that system using mathematical models [172], [228]. Recent studies have applied metabolic flux analysis (MFA) to better understand nutrient production and utilization in normal and pathologic physiology [48], [164], [166], [167], [217]. Several groups have focused on quantifying liver gluconeogenic and oxidative metabolism using stable isotopes, including our own prior contributions to assess *in vivo* fluxes in conscious, catheterized mice and rats [29], [48], [65], [110], [229], [230].

It may be reasonable and necessary to assume the kidney has a minor role in endogenous glucose production in some conditions, as no methods exist to disambiguate the hepatic and renal contributions to glucose production in conscious mice. As a result, the functional interaction between the liver and kidneys in controlling metabolic fluxes is largely understudied. For example, gluconeogenesis from PEP is severely

impaired in perfused livers isolated from KO mice [2], [227], but rates of whole-body glucose production and gluconeogenesis are sufficient to maintain fasting euglycemia [101], [226]. The authors note that two other potential sites of gluconeogenesis—the intestines and kidney—may compensate for the absence of hepatic PEPCK-C [101]. Studies testing the significance of intestinal gluconeogenesis have been debated [231]–[233]; a recent study by Potts et. al [234] showed that PEPCK-C in the small intestine supports nutrient processing of lipids and amino acids but is not necessary to maintain normal rates of glucose production during fasting. The kidney cortex expresses all gluconeogenic enzymes, including PEPCK, FBPase, and G6PC1 and may significantly contribute to glucose production in certain contexts [235]–[237].

Here we developed an isotopic flux modeling approach to simultaneously quantify gluconeogenic and oxidative metabolic fluxes in the liver and kidneys. This technique was then applied to WT and KO mice to test the hypothesis that renal gluconeogenic and oxidative metabolism compensates for deficiencies in hepatic gluconeogenesis in KO mice. Metabolic fluxes were estimated from the enrichment of plasma, liver, and kidney metabolites of WT and KO mice infused with  $^2\text{H}/^{13}\text{C}$  isotopes. The results show that the kidneys have significant gluconeogenic potential upon loss of hepatic PEPCK-C. A 30-fold rise in renal gluconeogenesis was accompanied by an upregulation in the expression of both PEPCK-C and mitochondrial PEPCK (PEPCK-M) isozymes in the kidney. Furthermore, renal CAC fluxes were accelerated to sustain the energetic and metabolic demands of glucose production. More broadly, our novel multi-compartment model provides a versatile platform to simultaneously assess *in vivo* hepatic and renal metabolism in a variety of experimental systems.

## 5.3 Methods

### 5.3.1 *In vivo* Procedures in the Mouse

Approximately one week prior to experimentation, jugular vein and carotid artery catheters were surgically implanted in 15-week-old PEPCK-C WT and KO mice for infusing and sampling, respectively [212]. In



vivo infusion studies were performed in long-term (~18h) fasted mice, similar to those described in detail elsewhere [29]. Briefly, mice received a bolus of  $^2\text{H}_2\text{O}$  to enrich body water at 4.5% and a primed (440 $\mu\text{mol/kg}$ ), continuous (4.4 $\mu\text{mol/kg/min}$ ) infusion of [6,6- $^2\text{H}_2$ ]glucose (abbreviated collectively as  $^2\text{H}$ ) for 4 hrs. A primed (1.1 $\text{mmol/kg}$ ), continuous (0.055 $\text{mmol/kg/min}$ ) infusion of [ $^{13}\text{C}_3$ ]propionate (Cambridge Isotope Laboratories, Tewksbury MA) was administered for ~2hrs prior to plasma sampling and tissue excision. Liver and kidney tissue were rapidly excised and freeze-clamped in liquid nitrogen at the close of the study. Plasma samples and tissues obtained at the end of the study were stored at  $-80^\circ\text{C}$  prior to analysis.

### 5.3.2 Gene Expression Analysis

RNA was isolated from ~40 mg of powdered kidneys using TRizol reagent (Invitrogen, Cat# 15596026) and RNeasy Mini Kit (Qiagen, Cat# 74104), according to manufacturer protocols. cDNA was synthesized using the iScript cDNA synthesis kit (Bio-Rad, Cat# 1708891) and diluted tenfold with DI water. cDNA was then combined with target primers (defined below) (Integrated DNA Technologies) and iQ SYBR Green Supermix (Bio-Rad, Hercules, CA) and analyzed on a CFX96 Real-Time PCR System (Bio-Rad, Hercules, CA). Transcripts were quantified using the  $2^{-\Delta\Delta\text{Ct}}$  method [176] and normalized to the WT group, with *Ppia* as an internal reference. Primer sequences were as follows: *Pck1*, forward 5'-CTGCATAACGGTCTGGACTTC, reverse 5'-CAGCAACTGCCCCGTACTCC; *Pck2*, forward 5'-ATGGCTGCTATGTACCTCCC, reverse 5'-GCGCCACAAAGTCTCGAAC; *Gcgr*, forward 5'-TGCACTGCACCCGAAACTAC, reverse 5'-CATCGCCAATCTTCTGGCTGT; *G6pc*, forward 5'-CGACTCGCTATCTCCAAGTGA, reverse 5'-GTTGAACCAGTCTCCGACCA; *Ppargc1a*, forward 5'-TATGGAGTGACATAGAGTGTGCT, reverse 5'-CCACTTCAATCCACCCAGAAAG. All abundances were normalized to *Ppia*: forward 5'-GGCCGATGACGAGCCC, reverse 5'-TGTCTTTGGAACCTTGTCTGCAA.

### 5.3.3 Western Blotting

Protein was extracted from approximately 30 mg of frozen livers and kidneys with CelLytic MT mammalian tissue lysis/extraction reagent supplemented with protease inhibitor cocktail, and PMSF (Cat No. C3228, Millipore Sigma). Samples were centrifuged at 16,000 g and 4°C for 20 min, and the resulting supernatants constituted the total protein extracts. Protein concentrations were determined by a BCA assay kit (Pierce™ BCA Protein Assay Kit, Cat No. 23225, Thermo Fisher Scientific). Samples were added in concentrations of 30 µg/lane for SDS-PAGE Western blotting using NuPAGE 10% Bis-Tris Mini Gels. Total protein on the membrane was quantified using Revert 700 Total Protein Stain (Cat No. 926-11016, LI-COR Biotechnology). Membranes were probed with antibodies against Pck1 (1:1000 dilution, Cat No. 10004943, Cayman Chemicals, RRID: AB\_10141789) and Pck2 (1:1000 dilution, Cat No. 6924, Cell Signaling Technology, RRID: AB\_10836185). All western blots were imaged using the LI-COR Odyssey Fc imaging system, and signal was quantified using the LI-COR Image Studio software.

### 5.3.4 Glucagon Measurement

Plasma glucagon was determined by the Vanderbilt University Mouse Metabolic Phenotyping Center Hormone Assay and Analytical Resources Core using an ELISA assay kit (Cat No. 10-1271-01, Mercodia Inc).

### 5.3.5 Metabolite Extraction, Derivatization, and GC-MS

Plasma glucose was extracted using cold acetone to precipitate protein. Samples were air dried at 60°C for 30 minutes followed by immediate derivatization. Tissue metabolites were isolated from 30-50 mg of liver and powdered kidney using a biphasic methanol/water/chloroform extraction. The polar layer of the extract was isolated using a fine-tipped pipette and air-dried overnight for storage at -80 °C prior to derivatization. Plasma glucose samples were converted into three separate derivatives of di-*O*-isopropylidene, methyloxime pentapropionate, or aldonitrile pentapropionate according to protocols described elsewhere

[41]. Polar metabolites from tissue extracts were converted to their methoxime *tert*-butylsilyl derivatives (TBDMS) using MtBSTFA+1% TBDMCS (Cat No. 1-270144-200, Regis Technologies). Derivatized samples were injected onto a HP-5ms column (Cat No. 19091S-433, Agilent Technologies) in an Agilent 7890A gas chromatograph paired with an Agilent 5975C mass spectrometer. Data were acquired in scan mode, and metabolites were identified through comparison of mass spectra using a previously generated standard library. In some cases, multiple fragments of the same metabolite were used for flux analysis (Table S2). Combining data from multiple fragments can improve the precision of flux estimates by providing increased information on the position of isotope labeling within a parent molecule. For example, the three glucose derivatives described above yield a total of six independent GC-MS fragment ions (301, 145, 173, 259, 284, and 370 m/z), which each contain a unique subset of carbon and hydrogen atoms derived from the parent glucose molecule (Table S2). The accuracy of mass isotopomer distribution (MID) measurements was validated through comparison of the theoretical and experimental values of unenriched control samples.

### 5.3.6 $^2\text{H}/^{13}\text{C}$ Metabolic Flux Analysis (MFA)

The complete metabolic network and the carbon/hydrogen transitions used in the multi-compartment liver-kidney model can be found in Table S1. Metabolic equations were constructed from classical biochemical reactions and previously defined networks [29], [48]. Glycerol-3-phosphate was included as a measurement to help resolve gluconeogenic flux from glycerol and to quantify the extent of equilibration between DHAP and GAP in the triose phosphate isomerase reaction. Fumarate and malate measurements were also introduced, enabling the model to estimate the extent of equilibration within the four-carbon branch of the CAC [48]. Despite deletion of PEPCK-C in the livers of KO mice, the hepatic  $V_{\text{PEPCK}}$  reaction was included in the model to account for potential contributions from PEPCK-M and/or residual PEPCK-C expression in liver. The renal flux model was similar to that of the liver except with respect to glycogen. Since the

renal cortex does not synthesize appreciable amounts of glycogen [235], [237], glycogen synthase and phosphorylase reactions were omitted from the renal compartment.

MFA was performed by minimizing the sum of squared residuals (SSR) between model-simulated and experimental metabolite labeling measurements. The Isotopomer Network Compartmental Analysis (INCA) software package [69] was used to develop metabolic models and regress all fluxes. Plasma glucose and polar liver and kidney metabolite MIDs were provided as measurements into INCA. The error in these measurements was set to either the root-mean square error of unenriched control samples or the standard error of measurement of technical GC-MS replicates, whichever was greater. Best-fit metabolic flux solutions were determined for each animal by least-squares regression of the experimental measurements to the isotopomer network model. To ensure that a global solution was obtained, flux estimations were repeated a minimum of 100 times from randomized initial guesses. A chi-square test was used to assess goodness-of-fit, and a sensitivity analysis was performed to determine 95% confidence intervals associated with the calculated flux values. Initially, fluxes were estimated relative to the combined glucose production flux from liver and kidneys ( $V_{\text{Gluc.Prod}}$ ) constrained to an arbitrary value of 100. Relative fluxes were converted to absolute fluxes using the [6,6- $^2\text{H}_2$ ]-glucose infusion rate and mouse weights.

### 5.3.7 Statistical Analysis

Data were analyzed using an unpaired 2-tailed Student's t-test without assuming a consistent standard deviation between groups. Results with a p-value <0.05 were considered significant.

### 5.3.8 Study approval

All protocols were approved by the Vanderbilt Institutional Animal Care and Use Committee. Mice with a liver-specific deletion of cytosolic PEPCCK (*Pck1*) driven by the albumin-*cre* transgene (*Pck1*<sup>lox/lox</sup>Alb-*cre*) and wild-type littermates (*Pck1*<sup>lox/lox</sup>) were used [226]. Male mice were studied to facilitate comparison to

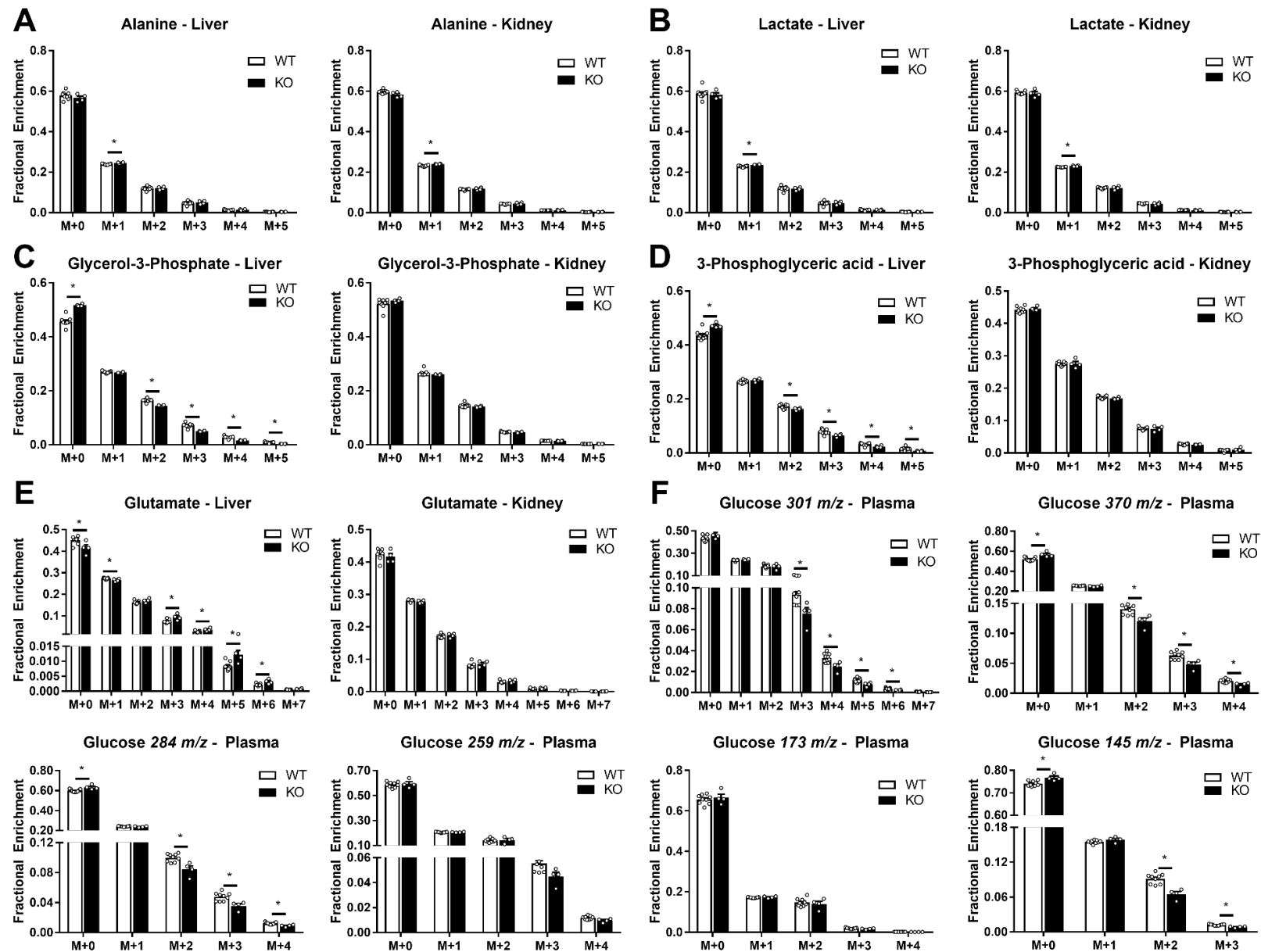
previous studies on Pck1 KO mice. Mice were maintained on a 12-h light-dark cycle with *ad libitum* access to water and a standard rodent chow diet (LabDiet 5001, PMI Nutrition International).

## 5.4 Results

### 5.4.1 Development of a novel liver-kidney multi-compartment model to quantify glucose-producing fluxes *in vivo*

To better understand the renal contribution to gluconeogenesis in the absence of hepatic PEPCK-C, a range of metabolites were isolated from the plasma, liver, and kidney of WT and KO mice obtained at the end of an infusion of  $^2\text{H}_2\text{O}$ ,  $[6,6\text{-}^2\text{H}_2]\text{glucose}$ , and  $[^{13}\text{C}_3]\text{propionate}$ . The mass isotopomer distribution (MID) of liver glutamate showed significantly higher enrichment in KO mice compared to WT mice, indicating that the livers of KO mice were able to extract the administered  $^2\text{H}/^{13}\text{C}$  isotopes from plasma (Fig. 5.1E). In contrast, metabolites measured above the PEPCK node, such as glycerol-3-phosphate (Fig. 5.1C) and 3-phosphoglyceric acid (Fig. 5.1D), exhibited an inverse trend with lower enrichments observed in the livers of KO mice. Arterial glucose enrichment in KO mice (Fig. 5.1F) was also lower than in WT mice, suggesting higher contributions from unlabeled sources to plasma glucose production in KO mice. To assess hepatic and renal contributions in maintaining euglycemia in the absence of liver PEPCK-C, we developed a novel metabolic model (Table 5A.1) to determine fluxes from MIDs of metabolites extracted from the plasma, liver, and kidneys (Fig. 5.1).

Our previously developed liver metabolic reaction network [29] was expanded to include a kidney compartment with reactions of glucose production and oxidative metabolism (Fig. 5.2A, Table 5A.1, also see *Methods*). The resulting liver-kidney flux model was used to regress MIDs of measured metabolites (Fig. 5.1 and Table 5A.2) and to obtain a best-fit solution for all fluxes in the metabolic network [69] (Fig. 5A.1-5A.3). The precision of hepatic and renal fluxes was determined by calculating 95% confidence intervals for each estimated flux (Fig. 5A.4). The multi-compartment flux model yielded acceptable



**Figure 5.1. Mass isotopomer distributions (MIDs) of liver, kidney, and plasma metabolites.**

**A.** alanine **B.** lactate **C.** glycerol-3-phosphate **D.** 3-phosphoglyceric acid and **E.** glutamate and **F.** plasma glucose fragments from WT (n=7) and KO (n=4) mice. Differences between group means were assessed by a 2-tailed *t* test (\* denotes  $P < 0.05$ ). Data are means $\pm$ SEM and are not corrected for natural isotope abundance.

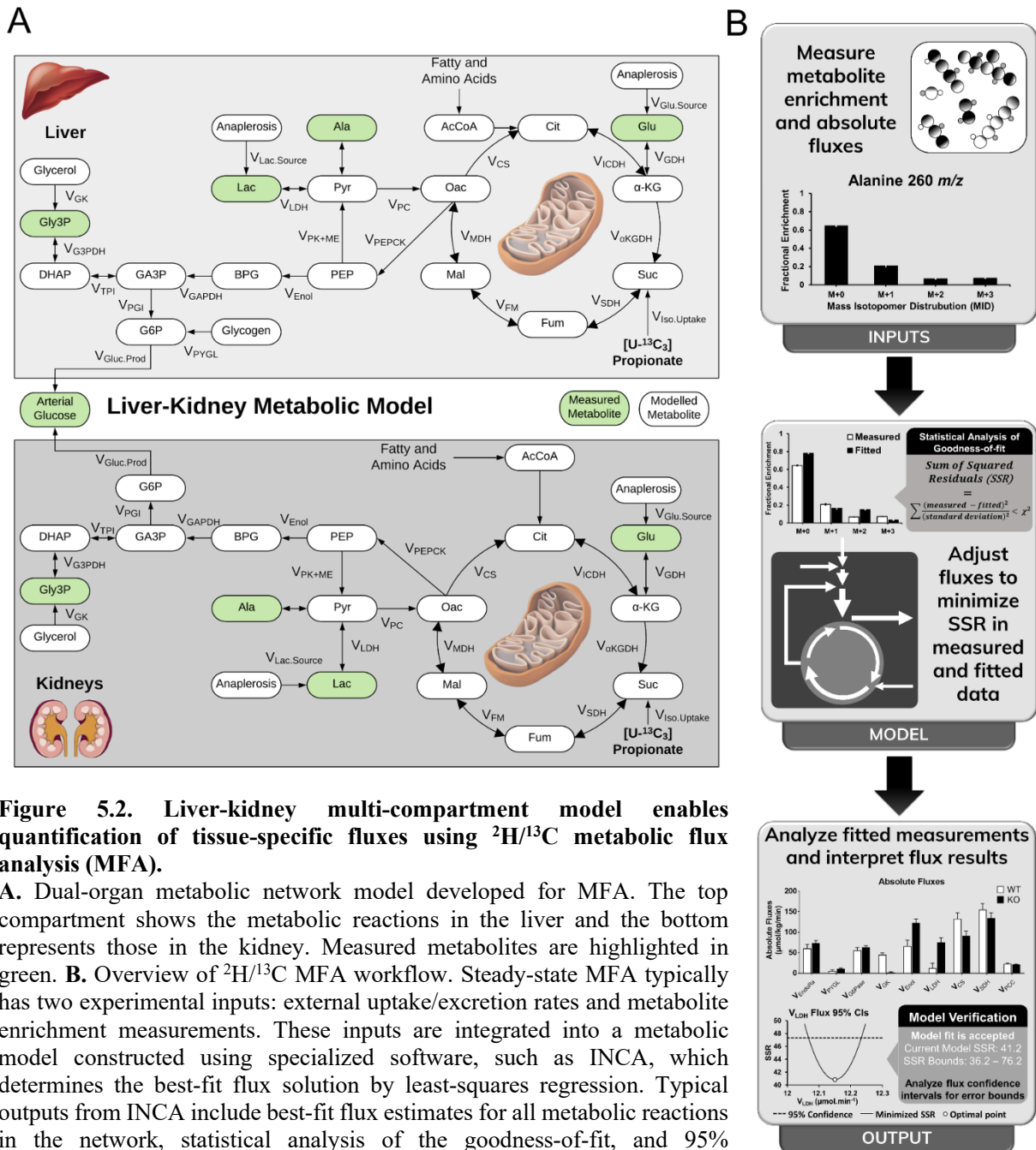
statistical fits with an average SSR of  $56 \pm 10$  and  $89 \pm 8$  for WT and KO groups, respectively. The goodness-of-fit was verified by comparing the SSR values to the expected range of the chi-square cumulative distribution function (95% confidence interval range of 55–108). The MFA approach is summarized in Fig. 5.2B with further details available in *Methods*.

#### **5.4.2 Liver PEPCK-C KO mice exhibit significant renal gluconeogenesis compared to WT**

##### **littermates**

Fluxes estimated in KO mice using the liver-kidney model indicate diminished CAC activity and glucose production by the liver compared to WT mice (Fig. 5.3A), consistent with previous results obtained in perfused livers[2], [227]. Hepatic glucose production decreased from 70 to 25  $\mu\text{mol} \cdot \text{kg}^{-1} \cdot \text{min}^{-1}$  in KO mice, and pyruvate cycling and enolase flux were diminished. The majority of glucose produced from KO livers came from glycogen (~40%) and gluconeogenesis from glycerol (~30%) (Fig. 5.3A), consistent with a significant decrease in enrichment measured in plasma glucose MIDs (Fig. 5.1F). Furthermore, anaplerotic fluxes from glutamate ( $V_{\text{Glu.source}}$ ) and pyruvate ( $V_{\text{PC}}$ ) were significantly decreased, consistent with the reduction in total cataplerotic flux ( $V_{\text{PEPCK}}$ ) in livers of KO mice (Fig. 5.3A). The increased enrichment of CAC intermediates and decreased enrichment of glycolytic metabolites in the liver—such as 3-phosphoglycerate—reflected the limited flux of labeled carbon exiting the hepatic CAC of KO mice (Fig. 5.1C-E).

The kidney compensated for the absence of hepatic PEPCK-C by increasing glucose production to maintain euglycemia (Fig. 5.3B). Renal glucose production was increased from 2 to 34  $\mu\text{mol} \cdot \text{kg}^{-1} \cdot \text{min}^{-1}$  through an acceleration in gluconeogenic fluxes from both glycerol and PEP. Oxidative, CAC flux also increased to sustain the energetic demands of gluconeogenesis. Cataplerotic and anaplerotic fluxes through PEPCK and pyruvate carboxylase (PC) were significantly higher in the kidneys of KO mice. Similar to WT hepatic metabolism, a large proportion (~75%) of renal cataplerosis was returned to the CAC through pyruvate kinase (and malic enzyme) flux in KO mice. To supply gluconeogenic precursors, increases in net



**Figure 5.2. Liver-kidney multi-compartment model enables quantification of tissue-specific fluxes using  $^2\text{H}/^{13}\text{C}$  metabolic flux analysis (MFA).**

**A.** Dual-organ metabolic network model developed for MFA. The top compartment shows the metabolic reactions in the liver and the bottom represents those in the kidney. Measured metabolites are highlighted in green. **B.** Overview of  $^2\text{H}/^{13}\text{C}$  MFA workflow. Steady-state MFA typically has two experimental inputs: external uptake/excretion rates and metabolite enrichment measurements. These inputs are integrated into a metabolic model constructed using specialized software, such as INCA, which determines the best-fit flux solution by least-squares regression. Typical outputs from INCA include best-fit flux estimates for all metabolic reactions in the network, statistical analysis of the goodness-of-fit, and 95% confidence intervals for the estimated fluxes.

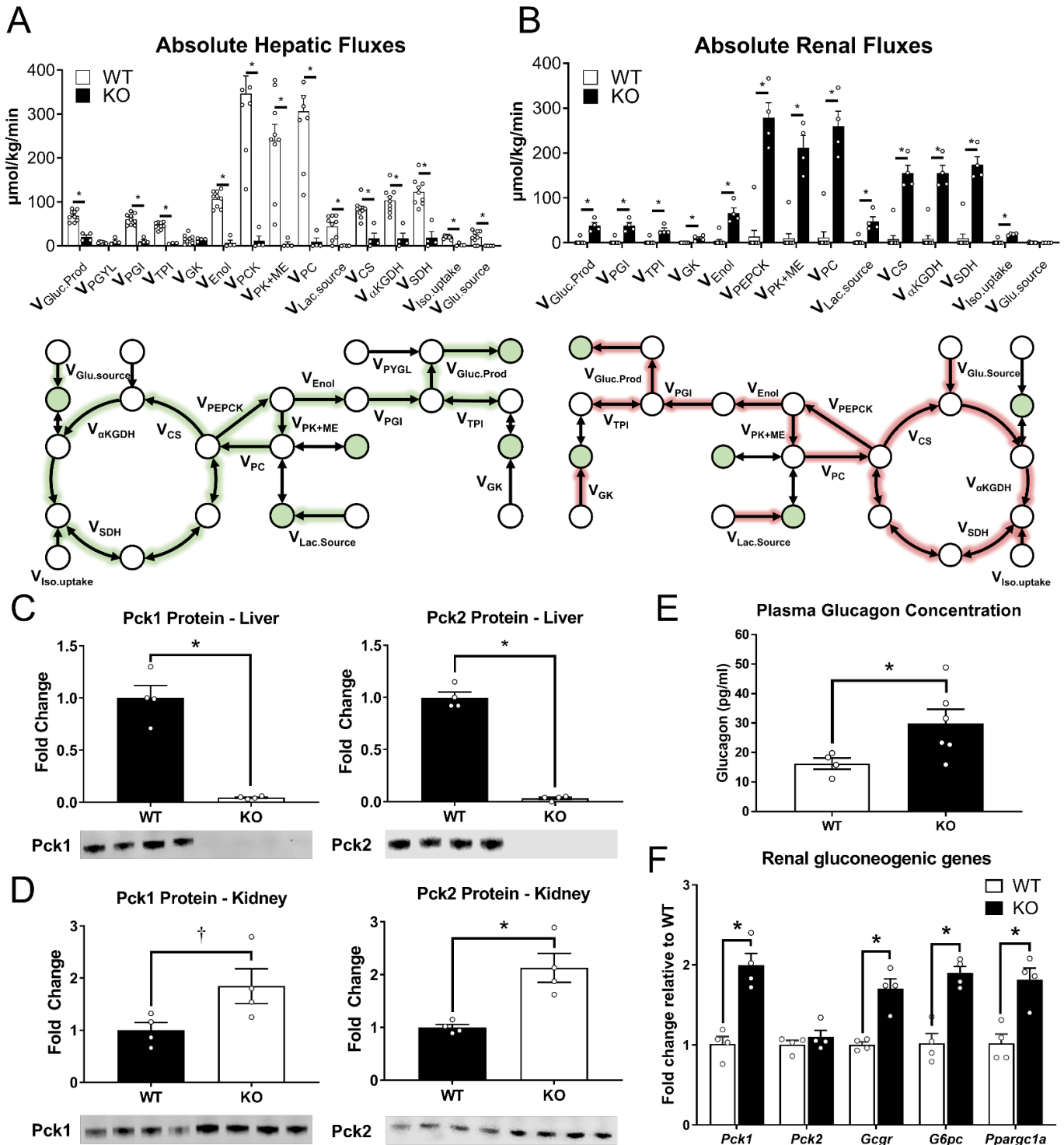
anaplerotic fluxes from both propionate and lactate were observed in the kidneys of KO mice. A limited amount of net anaplerosis to the CAC from glutamine/glutamate was observed in kidneys, although significant exchange flux was detected between glutamate and  $\alpha$ -ketoglutarate ( $\alpha$ -KG) (Table 5A.3). Given



that KO mice exhibited an increase in renal gluconeogenic flux from PEP, we hypothesized that expression of PEPCK also increased in the kidneys of KO mice. In the absence of hepatic PEPCK-C (Fig. 5.3C), we observed a ~2-fold increase in PEPCK-C and PEPCK-M (*Pck2*) expression in the kidney (Fig. 5.3D). These results are consistent with increased renal glucose production, gluconeogenesis, and PEPCK flux. Interestingly, immunoblots showed negligible protein expression of both liver PEPCK isoforms in KO mice (Fig. 5.3C). *G6pc1* knockout in the liver increases renal gluconeogenic gene expression and circulating glucagon concentrations, leading to the hypothesis that glucagon-mediated changes in gene expression facilitate an increase in renal gluconeogenic flux [238]. Based on these prior findings, we measured plasma glucagon concentrations (Fig. 5.3E) and renal gluconeogenic genes regulated by glucagon receptor signaling (Fig. 5.3F). Indeed, plasma glucagon levels were elevated in KO mice alongside increased kidney expression of the glucagon receptor (*Gcgr*), gluconeogenic enzymes (*Pck1*, *G6pc1*) and mitochondrial metabolic transcription factor (*Ppargc1a*). Taken together, these data indicate that loss of cytosolic PEPCK in the liver leads to extrahepatic compensation from the kidneys in order to maintain euglycemia *in vivo*, potentially through increased glucagon action on the kidney.

#### **5.4.3 Results from the dual organ liver-kidney model are consistent with whole-body flux estimates and previous NMR-based $^2\text{H}/^{13}\text{C}$ studies**

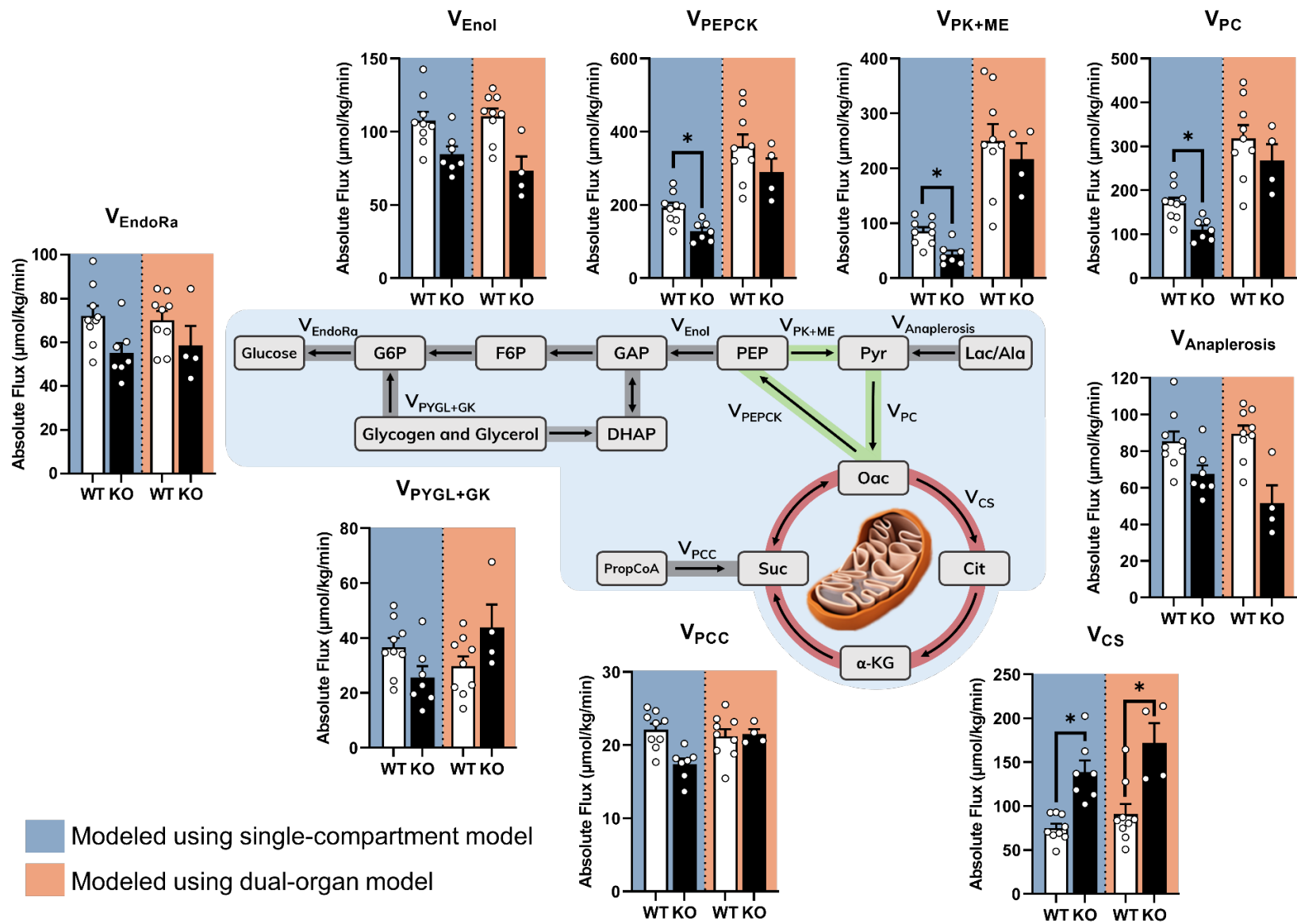
To further validate our results, we applied our previously developed MFA approach [29] to estimate whole-body gluconeogenic fluxes in WT and KO mice using only the measured plasma glucose MIDs (Fig. 5.1F). The flux results obtained from our whole-body gluconeogenic model showed a ~86% increase in citric acid cycle activity and ~33% decrease in pyruvate cycling in KO mice with no significant changes in endogenous glucose production (Fig. 5.4), consistent with results from prior NMR-based  $^2\text{H}/^{13}\text{C}$  studies [101]. Next, we compared these whole-body flux estimates with results from the multi-compartment liver-kidney model. Since the whole-body flux model does not distinguish between hepatic and renal gluconeogenic



**Figure 5.3: Liver PEPCK-C KO mice exhibit significant renal gluconeogenesis compared to WT littermates.**

**A.** Absolute hepatic fluxes for WT (n=7) and KO (n=4) mice, analyzed by a 2-tailed t test where \*  $P < 0.05$ . The map represents the hepatic compartment shown in Fig. 2B, Table S1. Measured metabolic nodes are shown in green (also see Table S2, S3). Arrows with green highlighting represent fluxes that are reduced in the livers from KO mice compared to WT littermates. **B.** Absolute renal fluxes for WT (n=7) and KO (n=4) mice, analyzed by a 2-tailed t test where \*  $P < 0.05$ . The map represents the renal compartment shown in Fig. 2B, Table S1. Measured metabolic nodes are shown in green (also see Table S2, S3). Arrows with red highlighting represent fluxes that are increased in the kidneys from KO mice compared to WT littermates. **C.** Pck1 and Pck2 fold change in the **C.** liver and **D.** kidney of KO (n=4) relative to WT (n=4) mice. Differences between group means were assessed by a 2-tailed t test (\* denotes  $P < 0.05$ , † denotes  $P < 0.10$ ). Protein expression was normalized to total protein content in each lane. **E.** Plasma glucagon concentration after ~20h of fasting in WT (n=4) and KO (n=6) mice, analyzed by a 2-tailed t test where \*  $P < 0.05$ . **F.** Fold change in gene expression in kidneys of KO (n=4) relative to WT (n=4) mice, analyzed by a 2-tailed t test where \*  $P < 0.05$ .

contributions, we combined the liver and kidney flux estimates from our dual organ model to obtain equivalent flux estimates. Summation of hepatic and renal fluxes showed strong agreement with whole-body flux estimates (Fig. 5.4). Endogenous glucose production ( $V_{\text{EndoRa}}$ ), propionate uptake ( $V_{\text{PCC}}$ ), total anaplerosis ( $V_{\text{Anaplerosis}}$ ), net gluconeogenesis ( $V_{\text{Enol}}$ ) and contributions from glycerol and glycogen ( $V_{\text{PYGL+GK}}$ ) were comparable between the two metabolic models. Though not significant, the opposing trend in  $V_{\text{PYGL+GK}}$  observed between the two models may result from an improvement in the resolution of glycerol fluxes with the integration of glycerol-3-phosphate MID measurements. While the single-compartment model showed a decrease in  $V_{\text{PEPCK}}$ ,  $V_{\text{PK+ME}}$ , and  $V_{\text{PC}}$ , combined flux estimates from the dual-organ model showed no statistical differences in pyruvate cycling between WT and KO mice. This distinction likely stems from the use of tissue-specific alanine and lactate MID measurements in the dual-organ model, providing additional constraints to improve the resolution of pyruvate cycle fluxes. The combined magnitude of hepatic and renal fluxes were in general agreement with whole-body flux estimates (Fig. 5.4) and with those measured by other groups [101].

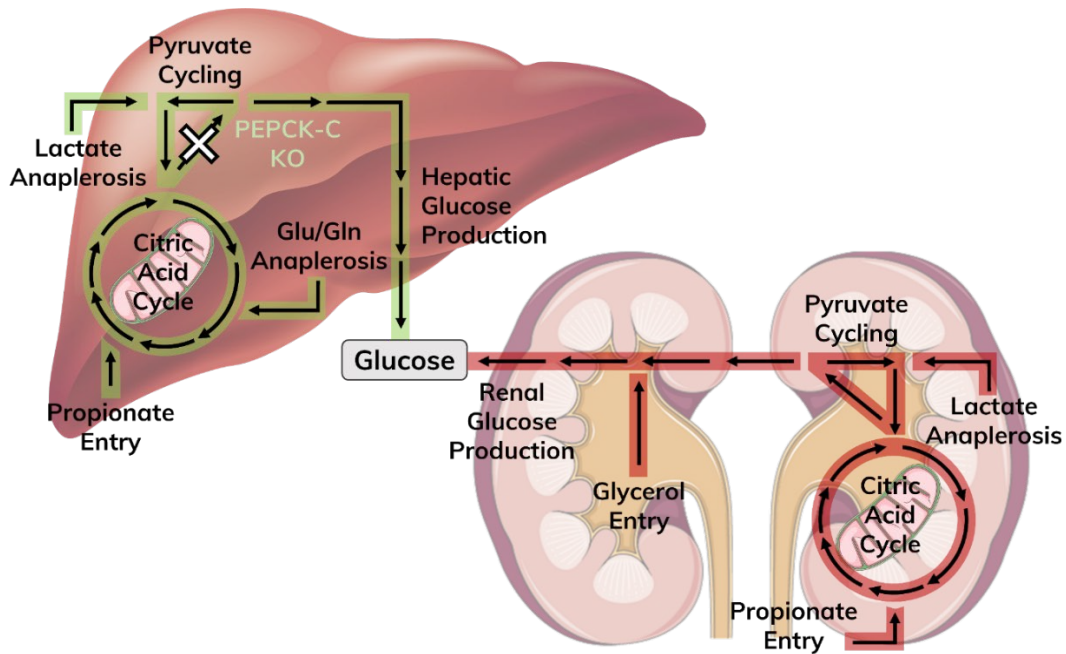


**Figure 5.4: Comparison of flux estimates between the dual-organ model and a previously developed single-compartment model.**

Results from our previously developed single-compartment model [29], which estimates fluxes using plasma glucose enrichments only (blue), were compared to the sum of hepatic and renal fluxes estimated using the dual organ model developed here (orange). Flux values are reported in  $\mu\text{mol/kg/min}$  (mean  $\pm$  SEM) for WT and KO mice ( $n \geq 4$ ), analyzed by a 2-tailed t test where \*  $P < 0.05$ . Pathways highlighted in green indicate a significant flux reduction in KO mice, whereas pathways highlighted in red indicate a significant flux increase in KO mice compared to WT littermates using the single-compartment model.

## 5.5 Discussion

Prior studies have assessed the effects of liver PEPCK-C inhibition on hepatic gluconeogenic and intermediary metabolism *in vivo* or in perfused livers. However, no studies have introduced methods that separate the hepatic and renal contributions to gluconeogenic and oxidative metabolic fluxes *in vivo*. Here, we present a novel mathematical modeling approach that quantifies the metabolic contributions of the liver and kidneys to maintain glucose homeostasis. Similar to results shown in perfused livers [2], [227], KO mice diminished hepatic gluconeogenesis, CAC activity, anaplerosis, and pyruvate cycling *in vivo*. The present study quantifies a previously undefined interaction whereby the kidneys of KO mice exhibited marked upregulation in gluconeogenic flux, anaplerosis/cataplerosis, and oxidative metabolism (Fig. 5.5). These changes in renal fluxes correlated with an increase in the expression of downstream targets of glucagon signaling.



**Figure 5.5: Metabolic pathways affected by knockout of hepatic PEPCK-C.**

Results from our novel liver-kidney metabolic model show that loss of hepatic PEPCK-C diminishes gluconeogenesis, CAC activity, anaplerosis, and pyruvate cycling in the liver. Increases in renal gluconeogenesis, CAC activity and anaplerosis help maintain euglycemia during fasting. Pathways highlighted in green indicate a significant flux reduction in the livers of KO mice, whereas pathways highlighted in red indicate a significant flux increase in the kidneys of KO mice compared to WT littermates.

Fluxes calculated from the enrichment of plasma glucose alone have shown that whole-body glucose production is generally unaffected while gluconeogenesis is modestly reduced by the loss of hepatic PEPCK-C [101]. Not only do we confirm those previous results, but we also characterize the metabolic flux compensation that occurs in the kidney to maintain euglycemia during inhibition of hepatic gluconeogenesis. Consistent with She et al., we observed a trend toward decreased  $V_{\text{EndoRa}}$  in KO mice, suggesting the kidneys may not fully compensate for the loss of hepatic gluconeogenic capacity. The results here provide additional evidence that plasma glucose enrichment is reflective of liver metabolism under ordinary fasting conditions. Generally speaking, hepatic fluxes in WT mice estimated with the liver-kidney model are qualitatively similar to those determined from a single-compartment model of whole-body glucose metabolism (Fig. 5.4). For example, total cataplerosis ( $V_{\text{PCK}}$ ) exceeds CAC-derived gluconeogenesis ( $V_{\text{Enol}}$ ), with surplus PEP returning to the CAC through pyruvate cycling ( $V_{\text{PK+ME}}$ ) in both models. CAC activity is also similar in magnitude to glucose production. Thus, approximations of hepatic metabolism from glucose enrichment alone may be reasonable in WT mice when more comprehensive techniques are unavailable or impractical.

When modeling both *in vivo* liver and kidney metabolism, removal of hepatic PEPCK-C diminishes liver gluconeogenesis, cataplerosis, anaplerosis, and CAC metabolism. These results are consistent with the fundamental coupling of energy-consuming, biosynthetic reactions and energy-producing reactions in the liver. Fluxes that deliver substrates for both oxidation and glucose synthesis are lowered when the liver is incapable of performing gluconeogenesis from the CAC. In fact, Berglund et al. have shown that fasting and glucagon administration lose their effects on the energy state of the liver when PEPCK-C is removed [239]. PC and PEPCK are the prominent anaplerotic and cataplerotic nodes controlling the net flow of substrates in and out of the CAC and thereby regulate the initial steps of gluconeogenesis. PEPCK-C removal decreased hepatic pyruvate cycling, as  $V_{\text{PEPCK}}$ ,  $V_{\text{PK+ME}}$ , and  $V_{\text{PC}}$  were diminished *in vivo*. It was

recently shown that loss of PC from the liver significantly decreases the expression of PEPCK, reflecting a codependent coupling of gene expression and metabolite flux [110]. In some conditions, cataplerotic activity of PEPCK promotes anaplerotic entry of carbon via glutaminolysis and uptake of glutamine [240]. Our results show that the inverse relationship exists whereby loss of PEPCK-C decreases hepatic anaplerosis from all sources, including from sources that flux to  $\alpha$ -KG (e.g. glutamate).

Until now, studies have relied on gene/enzyme expression or static metabolite assays to probe the impact of impaired hepatic gluconeogenesis on renal metabolic fluxes. Our study builds upon previous work [226], [238], [241] by quantifying the specific hepatic and renal flux contributions to glucose production in KO mice. Not only did the expression of gluconeogenic enzymes increase, but, more importantly, the rate of metabolic flux through renal gluconeogenesis and the CAC increased upon loss of liver PEPCK-C. Comparable to fluxes observed in WT livers, we observed significantly higher  $V_{\text{PEPCK}}$ ,  $V_{\text{PC}}$ , and CAC fluxes in the kidneys of KO mice. These data are consistent with previous studies showing a reliance on renal glucose production during the anhepatic phase of liver transplantation in humans [242]. A recent *in vivo* isotope labeling study reported increased enrichment of metabolites and expression of gluconeogenic genes in the kidney after knockout of hepatic PC, a major anaplerotic enzyme in the liver [110]. It stands to reason that metabolite MIDs from that study [110] would be a rich data source to simultaneously regress renal and hepatic fluxes using the model developed here.

Cytosolic and mitochondrial PEPCK exhibit similar catalytic properties [243], yet PEPCK-M may only account for up to 5% of the total hepatic PEPCK activity in mice and rats [244], [245]. It has also been reported that PEPCK-M requires the presence of PEPCK-C to substantially affect CAC activity and gluconeogenesis in perfused livers [246]. The analyses presented here are consistent with these results, as the loss of PEPCK-C inhibited gluconeogenesis from PEP and significantly lowered PEPCK-M expression. This effect is similar to the relationship between Pdk1 and Pdk2 isozymes in the liver, where ablation of Pdk1 has a destabilizing effect on the protein levels of Pdk2 [247]. In contrast, the expression of genes that

mediate gluconeogenesis and oxidative metabolism in the kidney was increased as a result of hepatic PEPCK-C deletion. Some of these changes in gene expression may emanate, in part, through increased glucagon signaling in the kidney [238]; the influence of other potential regulators (e.g., glucocorticoids, acidosis, etc.) [238], [241] was not evaluated here. Interestingly, we observed increased renal expression of Pck2 protein but not *Pck2* mRNA in KO mice. Unlike PEPCK-C, it is less certain whether glucoregulatory hormones like glucagon and insulin influence PEPCK-M expression, which has generally been described as constitutive in nature [243], [248], [249]. The results presented here suggest that renal PEPCK-M expression is post-transcriptionally upregulated upon the loss of hepatic PEPCK-C.

Recent work from others has helped characterize the contribution of glucose and other circulating metabolites to the CAC in multiple organs [164], [167]. Though our work captures some of systemic fluxes, it focuses more heavily on characterizing intermediary metabolism within the liver and the kidneys. We expect this novel approach to be leveraged to rigorously investigate liver-kidney interactions in models of diabetes, obesity, fatty liver disease, and steatohepatitis. One advantage of our methodology is that it does not depend on measurements of renal arterial-venous differences, which require additional surgical expertise and may introduce some analytical imprecision [231]. Thus, this technology may provide new avenues to better understand the reciprocal or even pathophysiological relationship between the liver and kidneys in various contexts.

As detailed in *Results*, the dual-organ model relies upon assumptions that introduce some inherent limitations:

The model does not account for additional sources of glucose synthesis other than the liver and kidney. While some studies indicate that glucose production by the small intestine is marginal in certain conditions [231], [234], our results do not strictly exclude the possibility of increased intestinal gluconeogenesis during a chronic deficiency in hepatic glucose production, as suggested elsewhere [241]. If the intestines were to



generate a significant amount of plasma glucose and exhibit a unique gluconeogenic metabolism, we would anticipate a significant lack-of-fit between simulated and measured isotopomers. Yet, statistically acceptable fits were obtained for all data sets in our study. That said, it is possible that the intestines have an undetectable (e.g., redundant) influence on whole-body adaptations to impaired hepatic gluconeogenesis that cannot be distinguished from kidney or liver contributions based on our available measurements.

No other study has quantified *in vivo* renal glucose production and other associated metabolic fluxes in conscious, unrestrained mice. Thus, renal flux estimates reported here do not benefit from measurements obtained through arteriovenous balance and radio isotope-dilution methods and may not be reflective of cross-species differences [235], [250]–[253].

The dual-organ model estimated significantly different renal fluxes between WT and KO groups, yet a comparison of uncorrected MIDs showed similar enrichments for many kidney metabolites in WT and KO mice. This may be explained by the fact that MIDs are a composite of  $^2\text{H}$  and  $^{13}\text{C}$  enrichment and, as a result, a basic analysis of individual isotopomer patterns will not provide the resolution of a model-based flux regression. Furthermore, isotope incorporation into measured metabolite pools can result from a combination of net flux as well as reversible/cyclic exchange flux of the tracer. Hence, many pools become enriched with isotope due to metabolite turnover in the absence of net flux through a pathway. The modeling software used in these studies (INCA) provides a platform to rigorously test various modes of isotope incorporation while accounting for mass balance constraints on all pathway intermediates, thus enabling the detection of non-obvious changes in metabolic flux that could be overlooked by direct inspection of the mass isotopomer data [69]. As a result, most fluxes were reasonably well resolved in both liver and kidney compartments.

The MFA approach used here relies on measuring a validated panel of labeled metabolites (Table 5A.2) that is sufficient to precisely quantify gluconeogenic and oxidative fluxes in our metabolic models. This

targeted approach was not designed to assess global changes in adjacent or overlapping metabolic pathways, which might be revealed through an untargeted metabolomics analysis of tissue and plasma extracts.

Lastly, a unique facet of our experimental system is the ability to measure plasma glucose enrichment over time and verify steady state conditions over a similar isotope-infusion time course [29]. However, end-point measurements of tissue metabolites can be obtained only in a terminal sample and, therefore, steady-state assumptions for liver and kidney metabolites cannot be confirmed.

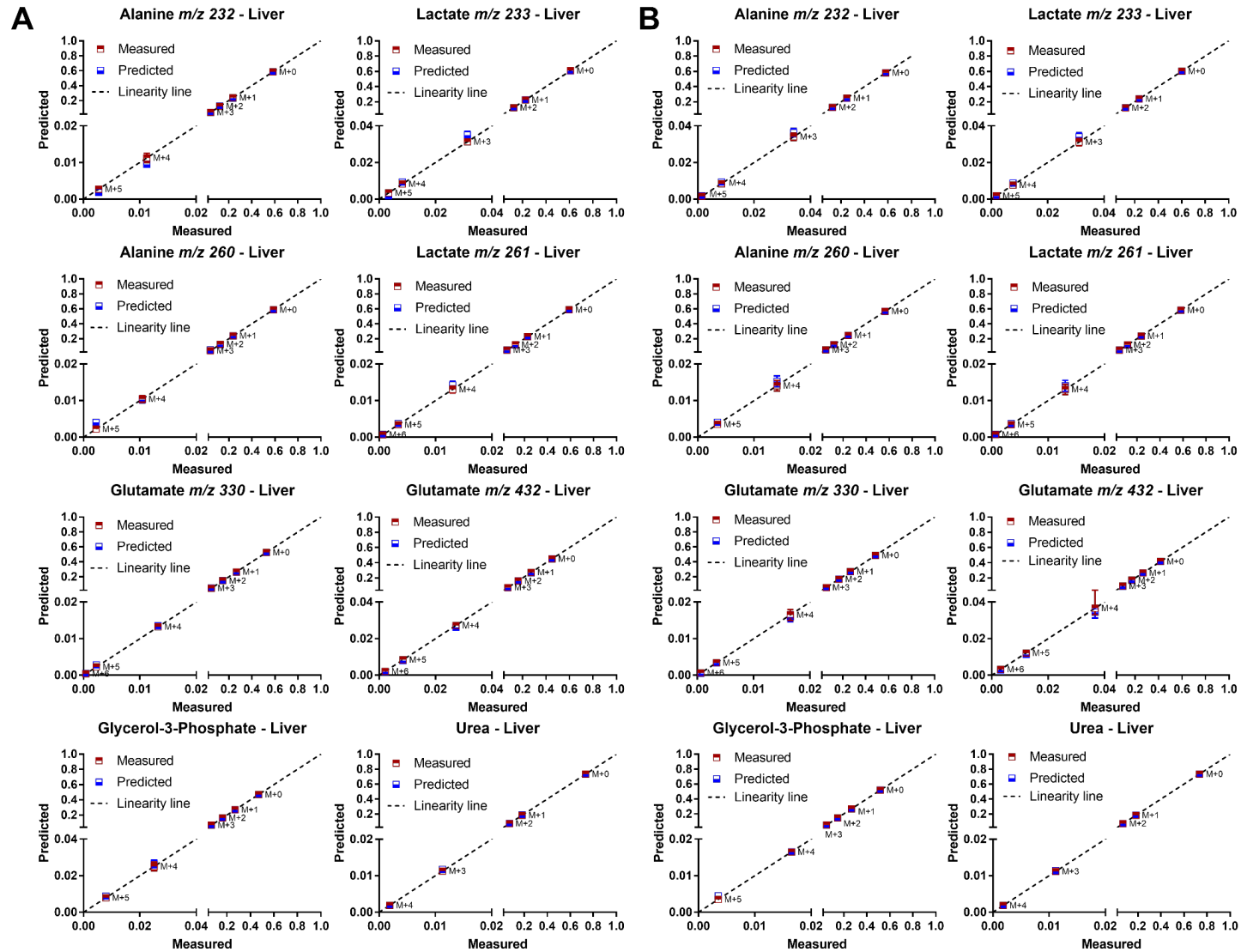
In summary, this study describes the development and application of a novel liver-kidney metabolic model that can be used to simultaneously assess intermediary metabolism in the liver and kidneys of individual mice, based on measurements of isotope enrichment in tissue and plasma metabolites. Our flux model shows that isotopic tracing and metabolic flux analysis are extensible tools that can aid in shaping our understanding of *in vivo* mammalian metabolism. Applying our dual-organ model, we show that mice lacking hepatic PEPCK-C maintain euglycemia by upregulating renal glucose production and oxidative metabolism. Loss of hepatic PEPCK-C diminishes gluconeogenesis, CAC activity, anaplerosis, and pyruvate cycling in the liver. Compensatory increases in expression of both PEPCK isozymes in the kidneys facilitates increased gluconeogenesis and cataplerosis from the CAC. Although hepatic PEPCK-C knockout has been extensively studied, its cross-regulatory effects on renal metabolism have not been rigorously defined. The integration of numerous measurements of metabolite enrichment from the plasma, liver, and kidney into a comprehensive liver-kidney metabolic model provides a platform to simultaneously evaluate hepatic and renal metabolism *in vivo* in other genetic, (patho)physiological, or pharmacological contexts.

## 5.6 Acknowledgements

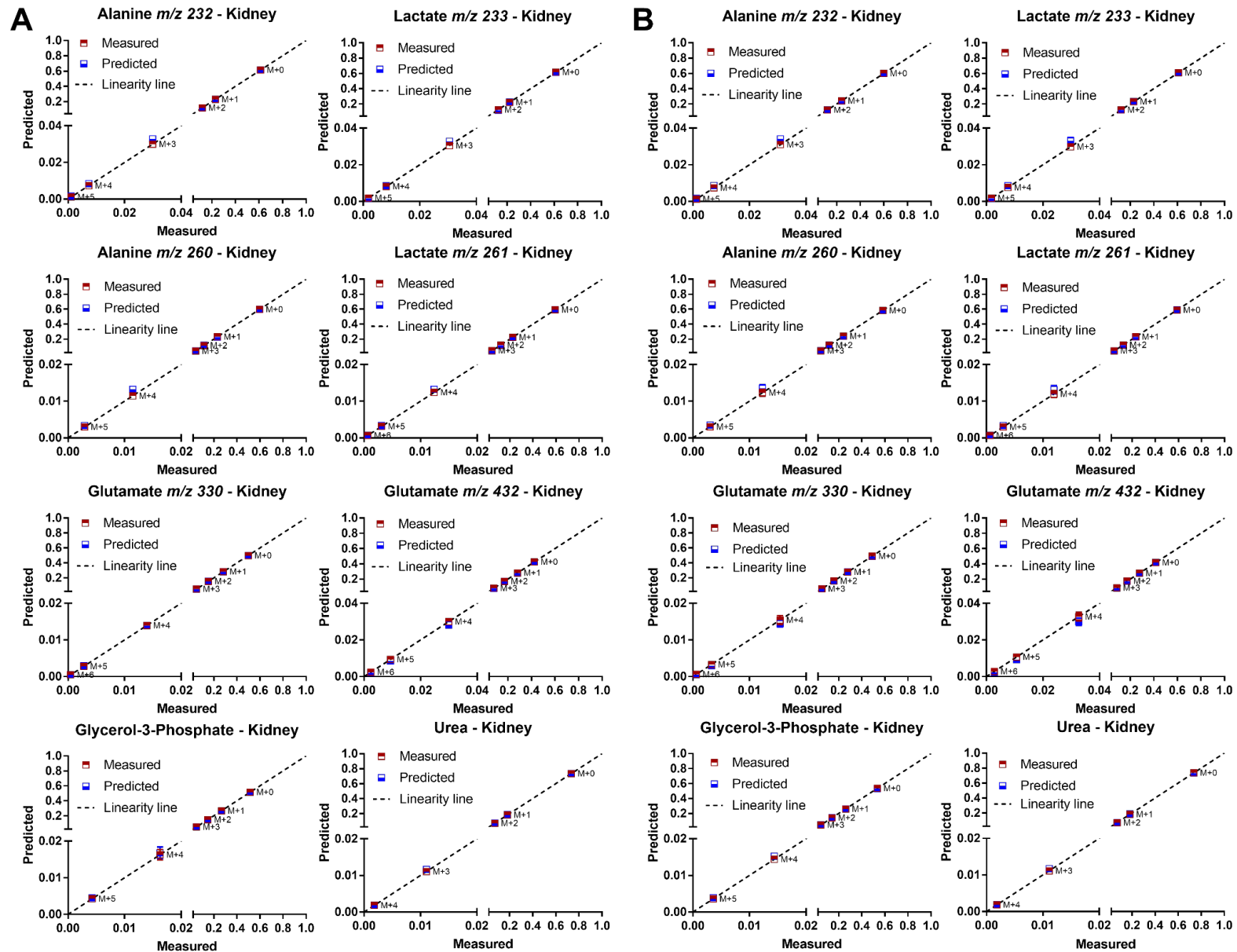
We thank the Vanderbilt University Mouse Metabolic Phenotyping Center (MMPC) for assistance with some *in vivo* studies described here. We thank Freyja D. James for performing surgical catheterization of mice. We also thank Martha Wall for assisting with genotyping some mice. We would like to thank Susan

Hajizadeh in the Vanderbilt University Mouse Metabolic Phenotyping Center Hormone and Analytical Core for measuring glucagon. This research was supported by NIH grants R01 DK106348 and U01 CA235508, the Integrated Training in Engineering and Diabetes NIH training grant (T32 DK101003), and the Vanderbilt MMPC (NIH grant U24 DK059637).

## 5.7 Appendix: Supplemental figures and tables

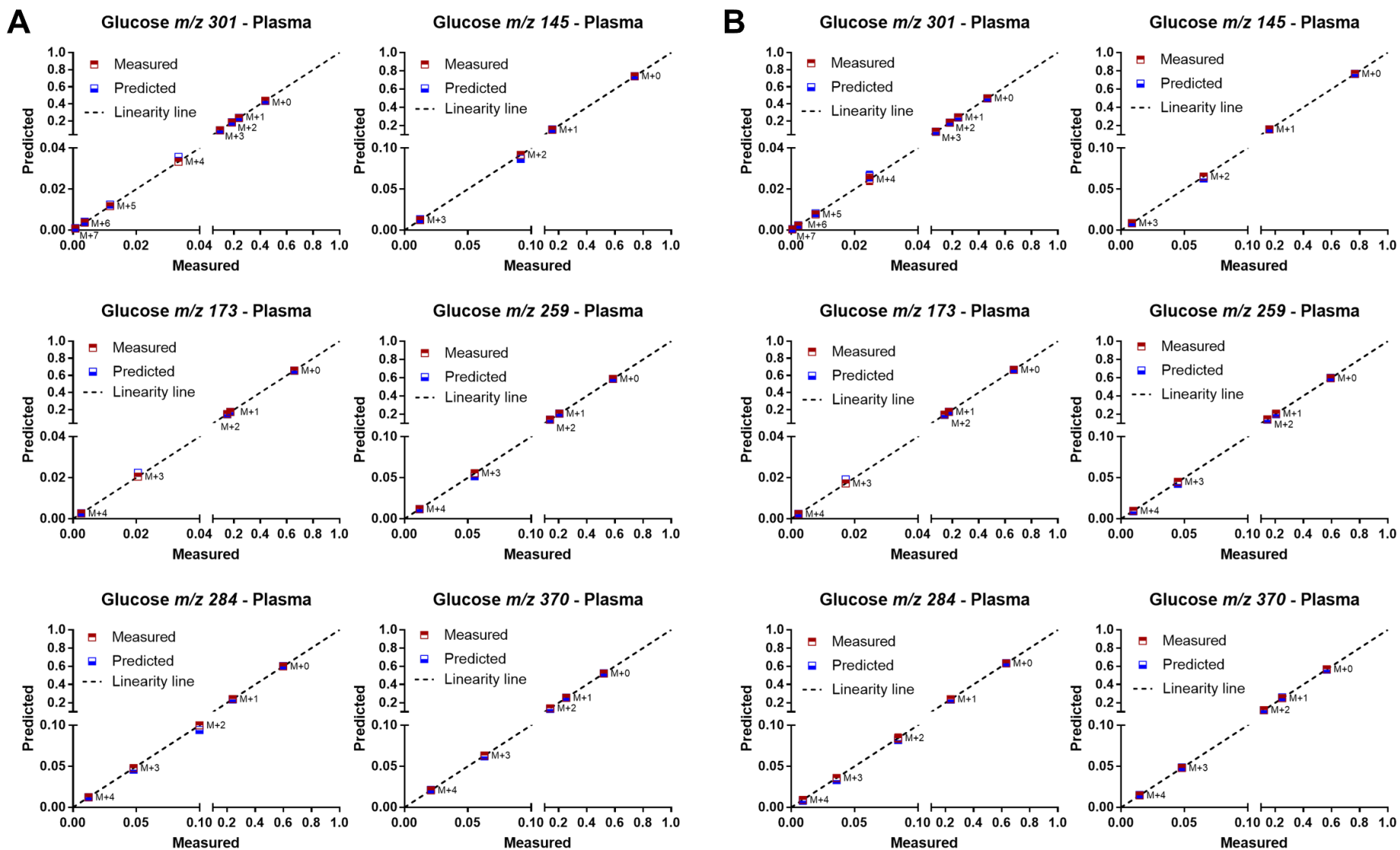


**Figure 5A.1: Measured and predicted fractional enrichments of liver metabolites for WT and KO mice.** Linearity analysis of measured and predicted liver metabolite MID values for **A.** WT (n=7) and **B.** KO (n=4) mice. Values on the x and y axes (means±SEM) represent the uncorrected measured and predicted fractional enrichments, respectively.



**Figure 5A.2: Measured and predicted fractional enrichments of kidney metabolites for WT and KO mice.**

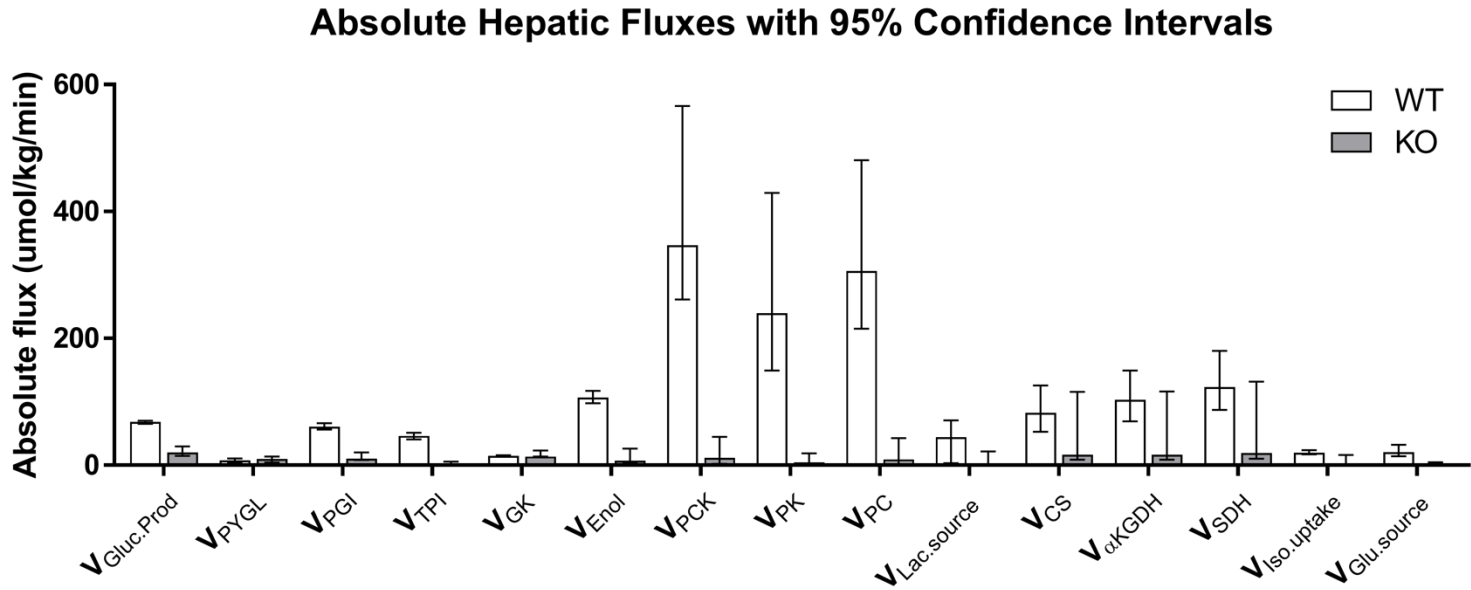
Linearity analysis of measured and predicted kidney metabolite MID<sub>s</sub> for **A**. WT (n=7) and **B**. KO (n=4) mice. Values on the x and y axes (means±SEM) represent the uncorrected measured and predicted fractional enrichments, respectively.



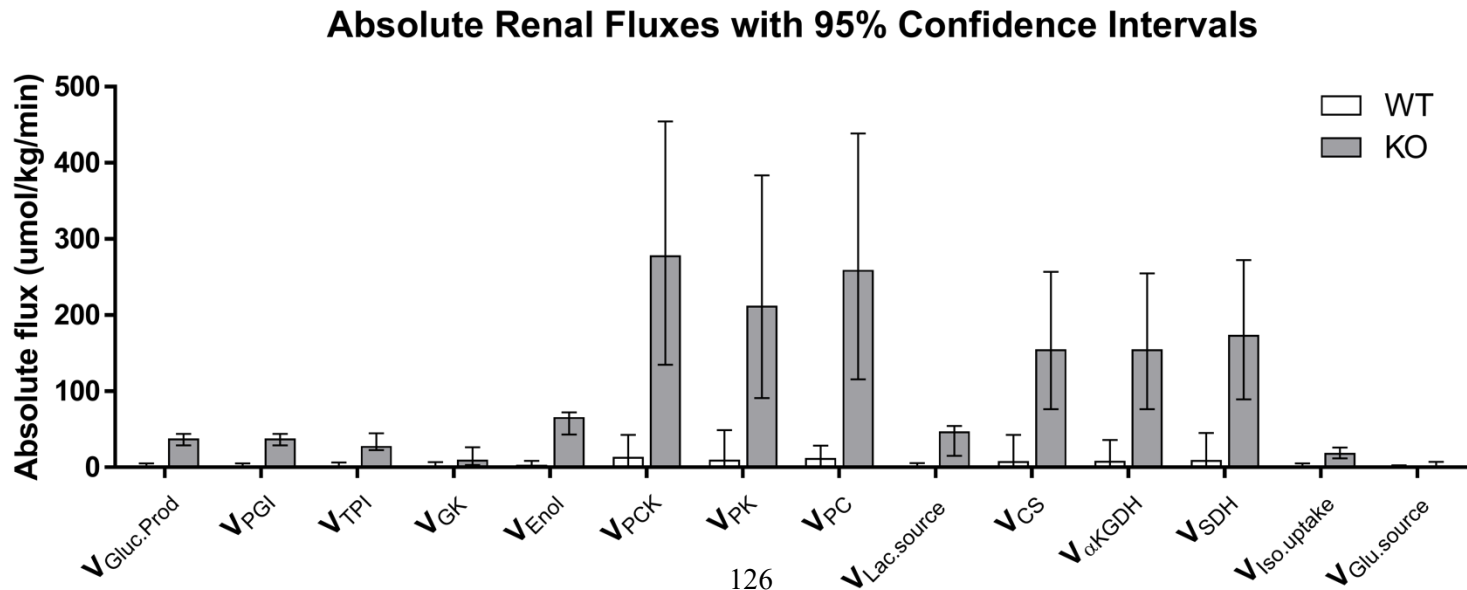
**Figure 5A.3: Measured and predicted fractional enrichments of plasma glucose for WT and KO mice.**

Linearity analysis of measured and predicted plasma glucose MIDs for **A.** WT (n=7) and **B.** KO (n=4) mice. Values on the x and y axes (means±SEM) represent the uncorrected measured and predicted fractional enrichments, respectively.

A



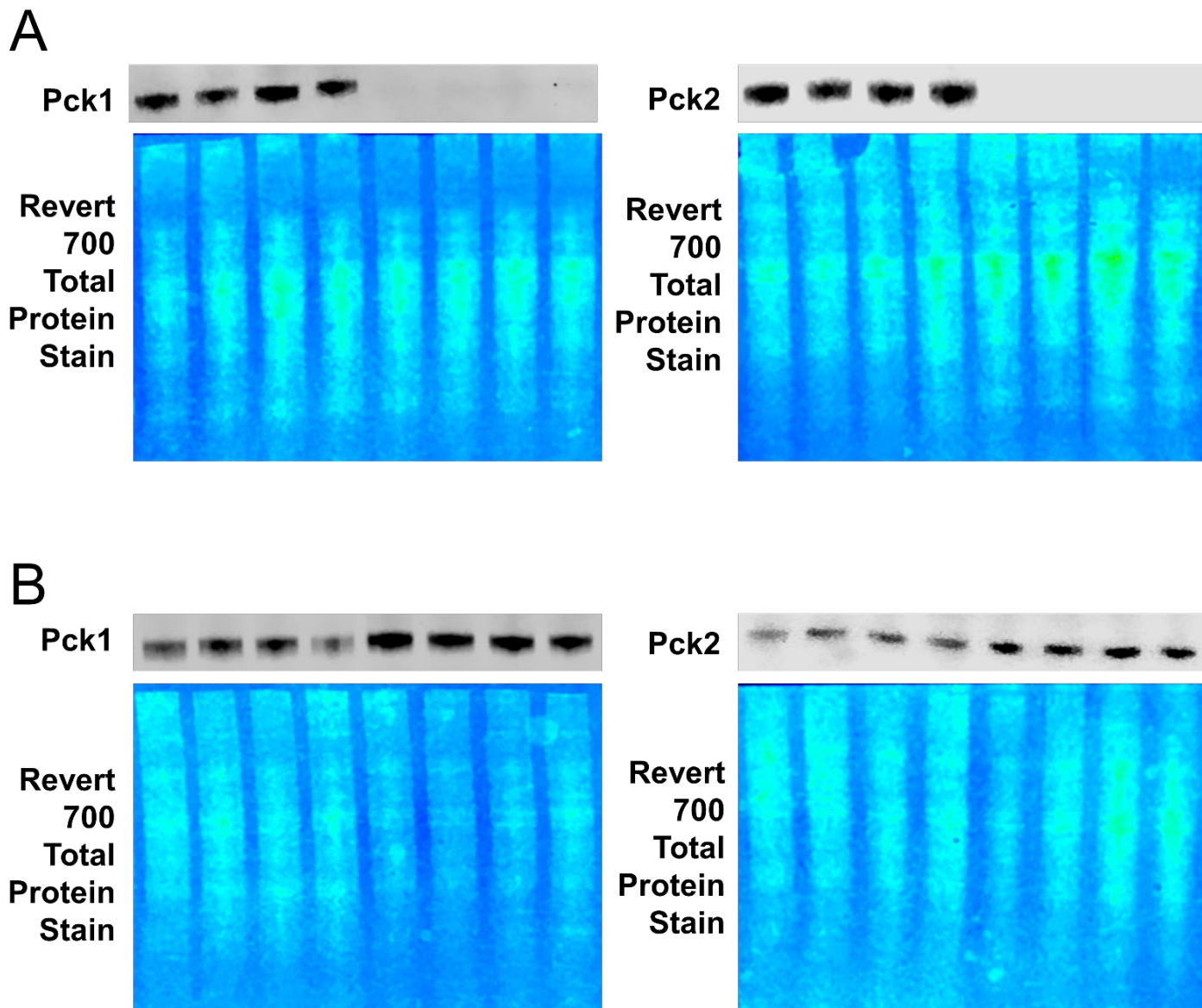
B



126

**Figure 5A.4: Mean hepatic and renal fluxes with 95% confidence intervals represented as error bars.**

Absolute **A.** hepatic and **B.** renal fluxes for WT (n=7) and KO (n=4) mice



**Figure 5A.5: Protein expression of Pck1 (PEPCK-C) and Pck2 (PEPCK-M) in the liver and kidney.** Total protein stain used to determine fold changes in protein expression of Pck1 and Pck2 in the **A.** liver and **B.** kidney of KO (n=4) and WT (n=4) mice.



**Table 5A.1: Dual organ metabolic reaction network for <sup>2</sup>H/<sup>13</sup>C MFA.**

Network maps of liver and kidney metabolism track carbon (uppercase) and hydrogen (lowercase) atoms through model reactions. Metabolites used to regress fluxes in both compartments are shown in Table S2. Metabolites in the liver, kidney, and plasma compartments are denoted as “.L”, “.K”, and “.P,” respectively. Unenriched sources and sinks for “H” and “CO<sub>2</sub>” are annotated as “.source” and “.sink”, respectively. <sup>2</sup>H and <sup>13</sup>C isotopes are introduced into model reactions as “iso.uptake”. The Dummy metabolite and reaction V<sub>Fixed</sub> were used to constrain the relative glucose production rate to 100.

<i>Hepatic Compartment</i>	
Flux	Reaction Network
V <sub>GlucProd.L</sub>	G6P.L (AaBbCcDdEeFfg) → Gluc.P (AaBbCcDdEeFfg) + Dummy
V <sub>PYGL.L</sub>	Glycogen.L (AaBbCcDdEeFfg) + H (q) → G6P.L (AaBqCcDdEeFfg) + H (b)
V <sub>PGI.L</sub>	F16BP.L (CcdBAaDeEfFgh) + H (q) → G6P.L (CcBqAaDeEfFgh) + H (d)
V <sub>Ald.L</sub>	DHAP.L (AabBCcd) + GAP.L (DeEfFgh) → F16BP.L (CcdBAaDeEfFgh) + H (b)
V <sub>TPI.L</sub>	DHAP.L (AaqBCcd) + H (z) ↔ GAP.L (AqBzCcd) + H (a)
V <sub>G3PDHL.L</sub>	G3P.L (AabBcCde) ↔ DHAP.L (AabBCde) + H I
V <sub>GK.L</sub>	Glycerol.L (AabBcCde) → G3P.L (AabBcCde)
V <sub>GAPDHL.L</sub>	BPG.L (AbbCcd) + H (a) → GAP.L (AaBbCcd)
V <sub>EnoL.L</sub>	PEP.L (ABCcd) + H (b) → BPG.L (AbbCcd)
V <sub>PCK.L</sub>	Oac.L (ABCabD) → PEP.L (ABCab) + CO <sub>2</sub> .L (D)
V <sub>PK+ME.L</sub>	PEP.L (ABCab) + H I → Pyr.L (ABCabc)
V <sub>PC.L</sub>	Pyr.L (ABCcde) + CO <sub>2</sub> .L (D) → Oac.L (ABCcdD) + H I
V <sub>LDHL.L</sub>	Lac.L (AbbCcde) ↔ Pyr.L (ABCcde) + H (b)
V <sub>Lac Source.L</sub>	Lac.Source (AbbCcde) → Lac.L (AbbCcde)
V <sub>CS.L</sub>	Oac.L (ABCcdD) + AcCoA.L (Effgh) → Cit.L (DccdBFfgEA) + H (h)
V <sub>ICDH.L</sub>	Cit.L (AbabCDcdEF) + H I ↔ α-KG.L (ABCeaDcdE) + H (b) + CO <sub>2</sub> .L (F)
V <sub>aKGDHL.L</sub>	α-KG.L (ABCabDcdE) → SucCoA.L (BcabDcdE) + CO <sub>2</sub> .L (A)
V <sub>SCS.L</sub>	SucCoA.L (AbabCcdD) → Suc.L (AbabCcdD)
V <sub>SDHL.L</sub>	Suc.L (AbabCcdD) ↔ Fum.L (AbaCdD) + H (b) + H (c)
V <sub>FM.L</sub>	Fum.L (AbaCbD) + H I ↔ Mal.L (AbaCcbD)
V <sub>MDHL.L</sub>	Mal.L (AbaCbcD) ↔ Oac.L (ABCbcD) + H (a)
V <sub>CO2 Source.L</sub>	BicarbL.source (A) → CO <sub>2</sub> .L (A)
V <sub>CO2 Sink.L</sub>	CO <sub>2</sub> .L (A) → BicarbL.sink (A)
V <sub>Iso.uptake.L</sub>	PropCoA.inf (AbabCcde) → PropCoA.L (AbabCcde)
V <sub>PCC.L</sub>	PropCoA.L (AbabCcde) + CO <sub>2</sub> .L (D) → SucCoA.L (AccdBabD) + H I
V <sub>ALT.L</sub>	Ala.L (AbbCcde) + H (f) ↔ Pyr.L (ABCcdf) + H (b) + H I
V <sub>GDHL.L</sub>	Glu.L (AbeCabDcdE) ↔ α-KG.L (ABCabDcdE) + H I
V <sub>Glu Source.L</sub>	Glu.Source (AbeCabDcdE) → Glu.L (AbeCabDcdE)
<i>Renal Compartment</i>	
Flux	Reaction Network

$V_{\text{GlucProd.K}}$	$\text{G6P.K (AaBbCcDdEeFfg)} \rightarrow \text{Gluc.P (AaBbCcDdEeFfg)} + \text{Dummy}$
$V_{\text{PGL.K}}$	$\text{F16BP.K (CcdBAaDeEffgh)} + \text{H (q)} \rightarrow \text{G6P.K (CcBqAaDeEffgh)} + \text{H (d)}$
$V_{\text{Ald.K}}$	$\text{DHAP.K (AabBCcd)} + \text{GAP.K (DeEffgh)} \rightarrow \text{F16BP.K (CcdBAaDeEffgh)} + \text{H (b)}$
$V_{\text{TPI.K}}$	$\text{DHAP.K (AaqBCcd)} + \text{H (z)} \leftrightarrow \text{GAP.K (AqBzCcd)} + \text{H (a)}$
$V_{\text{GAPDH.K}}$	$\text{BPG.K (AbbCcd)} + \text{H (a)} \rightarrow \text{GAP.K (AaBbCcd)}$
$V_{\text{G3PDH.K}}$	$\text{G3P.K (AabBcCde)} \leftrightarrow \text{DHAP.K (AabBCde)} + \text{H I}$
$V_{\text{GK.K}}$	$\text{Glycerol.K (AabBcCde)} \rightarrow \text{G3P.K (AabBcCde)}$
$V_{\text{Enol.K}}$	$\text{PEP.K (ABCcd)} + \text{H (b)} \rightarrow \text{BPG.K (AbbCcd)}$
$V_{\text{PCK.K}}$	$\text{Oac.K (ABCabD)} \rightarrow \text{PEP.K (ABCab)} + \text{CO2.K (D)}$
$V_{\text{PK+ME.K}}$	$\text{PEP.K (ABCab)} + \text{H I} \rightarrow \text{Pyr.K (ABCabc)}$
$V_{\text{PC.K}}$	$\text{Pyr.K (ABCcde)} + \text{CO2.K (D)} \rightarrow \text{Oac.K (ABCcdD)} + \text{H I}$
$V_{\text{LDH.K}}$	$\text{Lac.K (AbbCcde)} \leftrightarrow \text{Pyr.K (ABCcde)} + \text{H (b)}$
$V_{\text{Lac Source.K}}$	$\text{Lac.Source (AbbCcde)} \rightarrow \text{Lac.K (AbbCcde)}$
$V_{\text{CS.K}}$	$\text{Oac.K (ABCcdD)} + \text{AcCoA.K (Effgh)} \rightarrow \text{Cit.K (DccdBFfgEA)} + \text{H (h)}$
$V_{\text{ICDH.K}}$	$\text{Cit.K (AbabCDcdEF)} + \text{H I} \leftrightarrow \alpha\text{-KG.K (ABCeaDcdE)} + \text{H (b)} + \text{CO2.K (F)}$
$V_{\text{aKGDH.K}}$	$\alpha\text{-KG.K (ABCabDcdE)} \rightarrow \text{SucCoA.K (BcabDcdE)} + \text{CO2.K (A)}$
$V_{\text{SCS.K}}$	$\text{SucCoA.K (AbabCcdD)} \rightarrow \text{Suc.K (AbabCcdD)}$
$V_{\text{SDH.K}}$	$\text{Suc.K (AbabCcdD)} \leftrightarrow \text{Fum.K (AbaCdD)} + \text{H (b)} + \text{H (c)}$
$V_{\text{FM.K}}$	$\text{Fum.K (AbaCbD)} + \text{H I} \leftrightarrow \text{Mal.K (AbaCcbD)}$
$V_{\text{MDH.K}}$	$\text{Mal.K (AbaCbcD)} \leftrightarrow \text{Oac.K (ABCbcD)} + \text{H (a)}$
$V_{\text{CO2 Source.K}}$	$\text{BicarbK.source (A)} \rightarrow \text{CO2.K (A)}$
$V_{\text{CO2 Sink.K}}$	$\text{CO2.K (A)} \rightarrow \text{BicarbL.sink (A)}$
$V_{\text{Iso.uptake.K}}$	$\text{PropCoA.inf (AbabCcde)} \rightarrow \text{PropCoA.K (AbabCcde)}$
$V_{\text{PCC.K}}$	$\text{PropCoA.K (AbabCcde)} + \text{CO2.K (D)} \rightarrow \text{SucCoA.K (AccdBabD)} + \text{H I}$
$V_{\text{ALT.K}}$	$\text{Ala.K (AbbCcde)} + \text{H (f)} \leftrightarrow \text{Pyr.K (ABCcdf)} + \text{H (b)} + \text{H I}$
$V_{\text{GDH.K}}$	$\text{Glu.K (AbeCabDcdE)} \leftrightarrow \alpha\text{-KG.K (ABCabDcdE)} + \text{H I}$
$V_{\text{Glu Source.K}}$	$\text{Glu.Source (AbeCabDcdE)} \rightarrow \text{Glu.K (AbeCabDcdE)}$
<b>Transport Reactions</b>	
$V_{66\text{Gluc}}$	$\text{Gluc.inf (AaBbCcDdEeFfg)} \rightarrow \text{Gluc.P (AaBbCcDdEeFfg)}$
$V_{\text{Hinf}}$	$\text{H.inf (a)} \rightarrow \text{H (a)}$
$V_{\text{Hsink}}$	$\text{H} \rightarrow \text{Sink}$
$V_{\text{Fixed}}$	$\text{Dummy} \rightarrow \text{Sink}$

**Table 5A.2: GC-MS fragment ions of measured metabolites regressed using the metabolic model for MFA.**

H<sub>R</sub> and H<sub>S</sub> refer to diastereotopic hydrogens attached to each carbon. Hydrogens marked with an asterisk (H\*) are modeled as equivalent.

Metabolite	m/z	Derivative Formula	Carbons and Hydrogens												
			C1	C2	H1	C3	H2*	H3*	H4*						
Alanine	260	C <sub>11</sub> H <sub>26</sub> O <sub>2</sub> Nsi <sub>2</sub>	C1	C2	H1	C3	H2*	H3*	H4*						
Alanine	232	C <sub>10</sub> H <sub>26</sub> ONSi <sub>2</sub>		C2	H1	C3	H2*	H3*	H4*						
Glutamate	432	C <sub>19</sub> H <sub>42</sub> O <sub>4</sub> Nsi <sub>3</sub>	C1	C2	H1	C3	H2 <sub>R</sub>	H3 <sub>S</sub>	C4	H4 <sub>R</sub>	H5 <sub>S</sub>	C5			
Glutamate	330	C <sub>16</sub> H <sub>36</sub> O <sub>2</sub> Nsi <sub>2</sub>		C2	H1	C3	H2 <sub>R</sub>	H3 <sub>S</sub>	C4	H4 <sub>R</sub>	H5 <sub>S</sub>	C5			
Glycerol-3-Phosphate	571	C <sub>20</sub> H <sub>51</sub> O <sub>6</sub> Si <sub>4</sub> P	C1	H1 <sub>R</sub>	H2 <sub>S</sub>	C2	H3	C3	H4 <sub>R</sub>	H5 <sub>S</sub>					
Glucose	370	C <sub>17</sub> H <sub>24</sub> O <sub>8</sub> N	C1		C2	H2	C3	H3	C4	H4	C5	H5			
Glucose	301	C <sub>14</sub> H <sub>21</sub> O <sub>7</sub>	C1	H1	C2	H2	C3	H3	C4	H4	C5	H5	C6	H6 <sub>R</sub> H7 <sub>S</sub>	
Glucose	284	C <sub>13</sub> H <sub>18</sub> O <sub>6</sub> N	C1		C2	H2	C3	H3	C4	H4					
Glucose	259	C <sub>12</sub> H <sub>19</sub> O <sub>6</sub>							C4	H4	C5	H5	C6	H6 <sub>R</sub> H7 <sub>S</sub>	
Glucose	173	C <sub>8</sub> H <sub>13</sub> O <sub>4</sub>									C5	H5	C6	H6 <sub>R</sub> H7 <sub>S</sub>	
Glucose	145	C <sub>6</sub> H <sub>11</sub> O <sub>3</sub> N	C1	H1	C2	H2									
Lactate	261	C <sub>11</sub> H <sub>25</sub> O <sub>3</sub> Si <sub>2</sub>	C1	C2	H1	C3	H2*	H3*	H4*						
Lactate	233	C <sub>10</sub> H <sub>25</sub> O <sub>2</sub> Si <sub>2</sub>		C2	H1	C3	H2*	H3*	H4*						
Urea	231	C <sub>13</sub> H <sub>32</sub> N <sub>2</sub> Osi <sub>2</sub>	C1												

**Table 5A.3: Metabolic fluxes in the liver and kidneys of WT and KO mice (Related to Fig. 5.3)**

Absolute fluxes (mean  $\pm$  SEM) in the hepatic and renal compartment of WT (n=7) and KO (n=4) mice. Exchange fluxes have been normalized to a scale of 0–100 by dividing each exchange flux ( $V_{\text{exch}}$ ) by the sum  $V_{\text{exch}}+V_{\text{Gluc.Prod}}$ , where  $V_{\text{Gluc.Prod}}$  is the combined glucose production flux from liver and kidneys. Significant flux differences between WT and KO mice are marked with an asterisk, analyzed by a 2-tailed  $t$  test where  $* P < 0.05$ .

	WT	KO
<b>Liver Compartment</b>		
$V_{\text{GlucProd.L}}^*$	69 $\pm$ 5	21 $\pm$ 5
$V_{\text{PYGL.L}}$	8 $\pm$ 1	10 $\pm$ 4
$V_{\text{PGL.L}}^*$	61 $\pm$ 5	11 $\pm$ 4
$V_{\text{Ald.L}}^*$	61 $\pm$ 5	11 $\pm$ 4
$V_{\text{TPLL}}^*$	47 $\pm$ 3	4 $\pm$ 3
$V_{\text{TPLL exchange}}$	78 $\pm$ 7	100 $\pm$ 1
$V_{\text{G3PDH.L}}^*$	15 $\pm$ 4	14 $\pm$ 2
$V_{\text{G3PDH.L exchange}}$	12 $\pm$ 3	32 $\pm$ 23
$V_{\text{GK.L}}$	15 $\pm$ 4	14 $\pm$ 2
$V_{\text{GAPDH.L}}^*$	107 $\pm$ 7	8 $\pm$ 6
$V_{\text{Enol.L}}^*$	107 $\pm$ 7	8 $\pm$ 6
$V_{\text{PCK.L}}^*$	347 $\pm$ 40	12 $\pm$ 11
$V_{\text{PK+ME.L}}^*$	240 $\pm$ 37	5 $\pm$ 5
$V_{\text{PC.L}}^*$	307 $\pm$ 37	10 $\pm$ 9
$V_{\text{LDH.L}}^*$	45 $\pm$ 9	1 $\pm$ 1
$V_{\text{LDH.L exchange}}^*$	54 $\pm$ 10	3 $\pm$ 2
$V_{\text{Lac Source.L}}^*$	45 $\pm$ 9	1 $\pm$ 1
$V_{\text{CS.L}}^*$	83 $\pm$ 8	17 $\pm$ 12
$V_{\text{ICDH.L}}^*$	83 $\pm$ 8	17 $\pm$ 12
$V_{\text{ICDH.L exchange}}^*$	100 $\pm$ 1	26 $\pm$ 25
$V_{\text{aKGDH.L}}^*$	104 $\pm$ 10	17 $\pm$ 12
$V_{\text{SCS.L}}^*$	124 $\pm$ 11	20 $\pm$ 14
$V_{\text{SDH.L}}^*$	124 $\pm$ 11	20 $\pm$ 14
$V_{\text{SDH.L exchange}}$	12 $\pm$ 9	27 $\pm$ 25

$V_{FM.L}^*$	$124 \pm 11$	$20 \pm 14$
$V_{Fum.L} \text{ exchange}$	$83 \pm 11$	$44 \pm 22$
	<b>WT</b>	<b>KO</b>
$V_{MDH.L}^*$	$124 \pm 11$	$20 \pm 14$
$V_{MDH.L} \text{ exchange}^*$	$87 \pm 5$	$25 \pm 25$
$V_{CO2 \text{ Source.L}}^*$	$591 \pm 87$	$132 \pm 62$
$V_{CO2 \text{ Sink.L}}^*$	$798 \pm 93$	$166 \pm 85$
$V_{Iso.uptake.L}^*$	$20 \pm 2$	$3 \pm 2$
$V_{PCC.L}^*$	$20 \pm 2$	$3 \pm 2$
$V_{ALT.L}^*$	$23 \pm 10$	$5 \pm 5$
$V_{ALT.L} \text{ exchange}$	$46 \pm 13$	$76 \pm 25$
$V_{GDH.L}^*$	$23 \pm 10$	$1 \pm 1$
$V_{GDH.L} \text{ exchange}^*$	$100 \pm 1$	$25 \pm 25$
$V_{Glu \text{ Source.L}}^*$	$21 \pm 5$	$1 \pm 1$
<b>Renal Compartment</b>		
$V_{GlucProd.K}^*$	$2 \pm 2$	$39 \pm 7$
$V_{PGL.K}^*$	$2 \pm 2$	$39 \pm 7$
$V_{Ald.K}^*$	$2 \pm 2$	$39 \pm 7$
$V_{TPI.K}^*$	$2 \pm 2$	$29 \pm 5$
$V_{TPI.K} \text{ exchange}$	$58 \pm 16$	$33 \pm 10$
$V_{GAPDH.K}^*$	$4 \pm 4$	$67 \pm 12$
$V_{G3PDH.K}^*$	$1 \pm 1$	$11 \pm 3$
$V_{G3PDH.K} \text{ exchange}$	$1 \pm 1$	$2 \pm 1$
$V_{GK.K}^*$	$1 \pm 1$	$11 \pm 3$
$V_{Enol.K}^*$	$4 \pm 4$	$67 \pm 12$
$V_{PCK.K}^*$	$14 \pm 14$	$279 \pm 34$
$V_{PK+ME.K}^*$	$11 \pm 11$	$213 \pm 27$
$V_{PC.K}^*$	$13 \pm 13$	$260 \pm 34$
$V_{LDH.K}^*$	$3 \pm 3$	$48 \pm 11$
$V_{LDH.K} \text{ exchange}^*$	$3 \pm 3$	$50 \pm 6$

$V_{\text{Lac Source.K}}^*$	$3 \pm 3$	$48 \pm 11$
$V_{\text{CS.K}}^*$	$9 \pm 9$	$156 \pm 18$
$V_{\text{ICDH.K}}^*$	$9 \pm 9$	$156 \pm 18$
	<b>WT</b>	<b>KO</b>
$V_{\text{ICDH.K exchange}}$	$100 \pm 1$	$50 \pm 27$
$V_{\text{aKGDH.K}}^*$	$9 \pm 9$	$156 \pm 18$
$V_{\text{SCS.K}}^*$	$10 \pm 10$	$175 \pm 18$
$V_{\text{SDH.K}}^*$	$10 \pm 10$	$175 \pm 18$
$V_{\text{SDH.K exchange}}$	$1 \pm 1$	$1 \pm 1$
$V_{\text{FM.K}}^*$	$10 \pm 10$	$175 \pm 18$
$V_{\text{Fum.K exchange}}$	$93 \pm 7$	$100 \pm 1$
$V_{\text{MDH.K}}^*$	$10 \pm 10$	$175 \pm 18$
$V_{\text{MDH.K exchange}}^*$	$12 \pm 12$	$96 \pm 3$
$V_{\text{CO2 Source.K}}^*$	$87 \pm 87$	$1019 \pm 284$
$V_{\text{CO2 Sink.K}}^*$	$104 \pm 104$	$1329 \pm 309$
$V_{\text{Iso.uptake.K}}^*$	$2 \pm 2$	$20 \pm 2$
$V_{\text{PCC.K}}^*$	$2 \pm 2$	$20 \pm 2$
$V_{\text{ALT.K}}$	$1 \pm 1$	$1 \pm 1$
$V_{\text{ALT.K exchange}}$	$1 \pm 1$	$1 \pm 1$
$V_{\text{GDH.K}}$	$1 \pm 1$	$1 \pm 1$
$V_{\text{GDH.K exchange}}^*$	$16 \pm 11$	$76 \pm 25$
$V_{\text{Glu Source.K}}$	$1 \pm 1$	$1 \pm 1$

## 6. Simultaneous *in vivo* multi-organ fluxomics in obese mice

### 6.1 Abstract

Metabolic flux control is distributed across several distinct tissues and organ systems. The use of isotope-based metabolic flux analysis (MFA) has enabled the quantification of metabolic fluxes *in vivo*. Research groups capable of performing *in vivo* MFA have primarily confined their focus to intermediary metabolism in a single organ which helps to reduce analytical complexity. As a result, the crosstalk of metabolic fluxes across multiple organ systems in normal and pathophysiology has largely been understudied. Here we present an *in vivo*, MFA-based approach to simultaneously quantify metabolic fluxes in the liver, heart, and skeletal muscle in a single mouse. This method was scaled to several cohorts of mice to examine the metabolic dysfunction in obesity. Diet-induced obesity caused an increase in gluconeogenesis and endogenous glucose production from the liver and was accompanied by a >1.9-fold elevation in cardiac glycolytic and mitochondrial flux whereas citric acid cycle activity in the skeletal muscle was significantly reduced. Despite a ~2-fold increase in myocardial glucose oxidation, fatty acid oxidation genes were also elevated. These findings challenge the “glucose-fatty acid cycle” showing that fuel selection and flux differs between cardiac and skeletal muscle under obesity. Furthermore, using multivariate multi-omics analysis we identified regulatory and clinical biomarkers of obesity in each tissue. Our results here demonstrate that the metabolic syndrome has wide ranging effects on fluxes in each organ. We anticipate our multi-tissue metabolic model to have significant applications in better characterizing non-communicable diseases, (patho)physiology, and drug metabolism.

## 6.2 Introduction

Metabolism is vital for cellular function where enzymes break down nutrients to provide the chemical energy and material resources required for organisms to grow and survive. Understanding changes in metabolic regulation under both normal and pathological conditions is essential for developing interventions to prevent, diagnose, and treat metabolic diseases. It is preferential to study metabolic control *in vivo*, since the body is a complex, cross-regulatory environment aimed at maintaining homeostasis [254]. Gene and protein abundances, although helpful, often do not directly correlate with pathway fluxes because metabolic enzymes are tightly regulated by several factors such as allosteric feedback, post-translational modifications, and substrate availability [2], [228]. Furthermore, metabolic fluxes cannot be determined solely from static measurements of metabolite pool sizes [17]. In contrast, metabolic flux analysis (MFA) can provide functional readouts of *in vivo* metabolic pathway activity, offering an ultimate representation of the cellular phenotype of each tissue [255].

Assessment of *in vivo* metabolic fluxes has largely focused on the liver since it is a metabolic hub of the body. Decades of work by various groups has led to generation of refined *in vivo* methods for assessing gluconeogenesis, glycogenolysis, anaplerosis, citric acid cycle (CAC), lipid biosynthesis, fat oxidation, and ketogenesis fluxes in the liver [68], [256]. However, understanding *in vivo* metabolism of multiple organs using isotopic tracers presents inherent challenges due to organ crosstalk, systemic circulation of isotopes and multiple overlapping pathways. Recently, by taking advantage of the advances in computational and analytical technologies, several groups have attempted to quantify the systemic fluxes of circulating metabolites, focusing on the major nutrient sources that serve as the primary fuel to specific tissues and the TCA cycle [163], [164], [166], [167]. Some have begun to develop techniques to simultaneously quantify metabolic fluxes in multiple tissues [257], however to our knowledge, no study has simultaneously quantified intermediary metabolism within glycolytic and gluconeogenic tissues in a single mouse.



Quantification of intermediary metabolism can help decipher the energy demands on various pathways required for the functioning of a particular organ. For example, cardiac tissue heavily relies on oxidative phosphorylation where the mitochondria account for ~35% of the heart's volume [258] while skeletal muscle is more glycolytic and the mitochondria only occupy 4-15% of the tissue volume [259]. Similarly, during exercise, glucose uptake increases linearly with increasing  $V_{O_{2,max}}$  in the skeletal muscle whereas the myocardial glucose uptake rates do not scale linearly [260]. More importantly, while extensive research has been conducted to assess of hepatic metabolism, limited methods exist to quantify metabolic fluxes in the skeletal muscle and the heart *in vivo* [161], [261]–[264]. Advancements in magnetic resonance spectroscopy have enabled the quantification of small number of fluxes such as pyruvate dehydrogenase in the heart and the muscle [151], [152], but *in vivo* assessment of intermediary metabolism in skeletal and cardiac largely remains challenging.

Here we developed an isotopic flux modeling approach to simultaneously quantify gluconeogenic and glycolytic fluxes in the liver, heart, gastrocnemius, and vastus *in vivo*. The methodology was applied to three cohorts of mice (WT Chow, KO Chow and KO WD) in which adiposity and metabolic disease were progressively increased. Fluxes were assessed from the enrichment of plasma and tissue metabolites infused with radio and stable isotopes. Our results show an 8-fold increase in hepatic pyruvate cycling and a 50% increase in endogenous glucose production (EGP) as a consequence of hyperphagia and western diet feeding. More importantly, we saw a ~2.3 and ~1.9 fold increase in the glycolytic and CAC flux in the heart, respectively, despite an elevation in fatty acid oxidation genes in obese mice. Conversely, skeletal muscle showed a >50% decrease in CAC flux with reductions in glucose oxidation and CAC activity. Additionally, integrative multi-omics analysis of transcriptomics, metabolomics and fluxomics data identified tissue specific biomarkers that underly the progression of obesity in animals. More broadly, our modeling platform can be scaled to numerous conditions where changes in metabolism across organ systems may be relevant.

## 6.3 Methods

### 6.3.1 Experimental model and subject details

All protocols and procedures were approved by the Vanderbilt Institutional Animal Care and Use Committee. All studies were performed on ~16-week-old, male C57Bl/6 mice (Wild-type [WT]) or MC4R deficient mice (Knockout [KO]), based on the same parental background; parental breeders were generously provided by the Roger D. Cone laboratory [265]. Mice were maintained on a 12-h light-dark cycle with *ad libitum* access to water and a standard rodent chow diet (5L0D, 29% protein, 58% carbohydrates, 13% fat by caloric contribution; LabDiet, St. Louis, MO) for 8 weeks. At 8 weeks of age, a small cohort of mice were switched to WD (D12079B, 17% protein, 43% carbohydrates, and 40% fat by caloric contribution; Research Diets Inc., New Brunswick, NJ) while others were kept on chow diet for another 8 weeks. Overall, 3 groups were utilized for these studies: WT mice on chow (WT Chow), KO mice on chow (KO chow) and KO mice on western diet for 8 weeks (KO WD).

### 6.3.2 *In vivo* procedures in the mouse

One week prior to conducting isotope infusion studies, 15-week-old mice were surgicized with dual, jugular vein and carotid artery, catheters for simultaneous infusion and sampling of blood, respectively [212]. *In vivo* studies were performed by infusing a cocktail of tracers in overnight fasted mice (~16h) through a jugular vein catheter over a total time course of 180min. Mice were primed (1.5  $\mu\text{Ci}$ ) and then intravenously infused with a continuous (0.075  $\mu\text{Ci}/\text{min}$ ) dose of [ $3\text{-}^3\text{H}$ ]glucose for 180min. 60min after the start of the [ $3\text{-}^3\text{H}$ ]glucose infusion, a primed (0.200 mmol/kg), continuous (0.050 mmol/kg/min) infusion of [ $^{13}\text{C}_3$ ]lactate was administered for 120min. Lastly, a 12  $\mu\text{Ci}$  bolus of [ $^{14}\text{C}$ ] 2-deoxyglucose was given 25min before the end of each infusion. Blood samples were collected from an carotid artery catheter just prior to [ $^{13}\text{C}_3$ ]lactate infusion, and then at 2, 5, 10, 15, and 25min after the bolus of [ $^{14}\text{C}$ ] 2-deoxyglucose. After the final blood sample, mice were rapidly euthanized and excised tissues were snap frozen in liquid nitrogen for further analysis.

This protocol enabled the measurement of rates for endogenous glucose production, tissue-specific glucose uptake, and the stable, isotopic enrichment of plasma and tissue metabolites from a single, unstressed mouse. Throughout the study, blood glucose levels were monitored using an Accu-Check glucometer (Roche Diagnostics, Indianapolis, IN) and hematocrit was maintained through an infusion of donor erythrocytes (suspended in 10U/mL heparinized-saline). Additionally, age-matched mice from each group were maintained similarly—except without surgery or isotope tracer infusions—for body composition and gene expression analysis following an overnight fast (~19h). Mice were placed in a restrainer prior to obtain plasma (isolated from blood obtained from the cut tail) and tissues were rapidly obtained and snap frozen in liquid nitrogen post euthanasia. All plasma and tissues samples obtained at the end of the study were stored at -80°C until processed for further analysis.

### **6.3.3 Metabolite extraction, derivatization, and GC-MS**

Plasma and tissue metabolites were extracted and derivatized as described elsewhere [48]. Briefly, plasma glucose was extracted using cold acetone to precipitate protein. Samples were air dried followed by immediate derivatization into three separate derivatives of di-O-isopropylidene, methyloxime pentapropionate or aldonitrile pentapropionate according to protocols described elsewhere [41]. Polar metabolites were isolated from 40  $\mu$ L of plasma or 30-50 mg of liver, heart, gastrocnemius, and vastus tissues using a biphasic methanol/water/chloroform extraction. The polar layer of the extract was isolated using a fine-tipped pipette and air-dried overnight for storage at -80 °C prior to derivatization. Ten  $\mu$ L of 5-mM norvaline was spiked as an internal standard for metabolite quantification. Metabolites were then converted to their methyloxime tert-butyldimethylsilyl (Mox-TBDMS) derivatives using MtBSTFA+1% TBDMCS (Cat No. 1-270144-200, Regis Technologies). Derivatized samples were analyzed by GC-MS. Sample volumes of 1  $\mu$ L were injected in a 5:1 split in an Agilent 7890A gas chromatography system equipped with two HP-5 ms (15 m x 0.25 mm x 0.25  $\mu$ m; Agilent J&W Scientific) capillary columns and interfaced with an Agilent 5977C mass spectrometer. Previously defined temperature programs for Mox-

TBDMS [172] and glucose derivatives [29] were used for data collection. Derivative peaks were integrated using a custom MATLAB function [143] to obtain mass isotopomer distributions (MIDs) for the metabolite fragment ions shown in Table S2. Measurement uncertainty was assessed by calculating the root-mean-square deviation between the MID of unlabeled standards and the theoretical MID computed from the known abundances of naturally occurring isotopes.

#### **6.3.4 Multi-tissue metabolic flux analysis (MFA)**

The complete metabolic network and the carbon/hydrogen transitions used in the multi-compartment flux model can be found in Table S1. Metabolic equations were constructed from classical biochemical reactions and previously defined networks [24], [29], [48]. The hepatic and extrahepatic compartments are identical to those shown in our previous work [48]. Cardiac fluxes, including important sources and sinks of carbon, were modeled based on prior findings [15], [50], [153]. Myocardial glycogen breakdown was neglected in the model since the glycogen breakdown during fasting is non-existent and the glycogen pool is miniscule in the heart (<2% of total cell volume) [266], [267]. Given that the skeletal muscle consumes fats and stored glycogen under fasting [268], [269], entry of unlabeled carbon source representing inflow of glycerol and glycogen were added to the compartment as  $V_{PYGM+GK}$ . Major sources of efflux for the skeletal muscles were modelled as lactate and glutamate, two metabolites connected with anaerobic respiration and ammonia clearance, respectively. It is important to note that the hepatic and extrahepatic compartments were allowed to communicate with the cardiac and skeletal muscle compartments via glucose, lactate, and alanine. However, in order to better constrain the model, only the metabolite enrichment and isotopomer information was allowed to exchange between the compartments (Fig. 6.1A, Table 6A.1). Metabolite fragments used for each compartment have been shown in Table 6A.2.

MFA was performed by minimizing the sum of squared residuals (SSR) between model-simulated and experimental metabolite labeling measurements. The Isotopomer Network Compartmental Analysis

(INCA) software package [69] was used to develop metabolic models and regress all fluxes. Plasma, liver, heart, gastrocnemius, and vastus metabolite MIDs were provided as measurements into INCA. The error in these measurements was set to either the root-mean square error of unenriched control samples or the standard error of measurement of technical GC-MS replicates, whichever was greater. Best-fit metabolic flux solutions were determined for each animal by least-squares regression of the experimental measurements to the isotopomer network model. To ensure that a global solution was obtained, flux estimations were repeated a minimum of 100 times from randomized initial guesses. A chi-square test was used to assess goodness-of-fit, and a sensitivity analysis was performed to determine 95% confidence intervals associated with the calculated flux values. Initially, fluxes in the hepatic and extrahepatic compartments were estimated relative to liver citrate synthase flux by constraining the  $V_{CS,L}$  to an arbitrary value of 100. Relative cardiac and skeletal muscle fluxes were estimated by setting the glucose uptake flux ( $V_{GK}$ ) to 100. Endogenous glucose production (EndoRa), determined by subtracting the [3-<sup>3</sup>H] glucose infusion rate from the glucose turnover rate [270], was used to convert relative hepatic and extrahepatic fluxes to absolute rates. Similarly, relative cardiac and skeletal muscle fluxes were converted into absolute rates using  $R_g$ , an index of tissue-specific glucose uptake, determined from [<sup>14</sup>C]2-DG administration as shown previously [271].

### 6.3.5 Multi-omics analysis

For multivariate analysis, transcriptomics, metabolomics and fluxomics datasets for each compartment were z-score normalized and imported into the MetaboAnalyst software [272]. To find variables that best discriminate the WT chow, KO chow and KO WD groups in each tissue, we performed several supervised and unsupervised clustering analyses. Since the number of measurements far outnumbered the number of samples, we first performed a sparse partial least-squares discriminate analysis (sPLS-DA) with lasso penalization to determine the top 10 biomarkers that best separate the groups. Next, using disease severity as the correlation variable, we used the pattern finder tool in MetaboAnalyst to identify the top 25 variables

that correlate with increasing obesity. Lastly, we generated a hierarchical clustering heatmap, an unsupervised clustering method, to select the top 10 significantly altered metabolites in each tissue.

### **6.3.6 Gene expression analysis**

RNA was isolated from ~30 mg of liver, heart, gastrocnemius, and vastus using Trizol reagent (Cat. No. 15596026, Invitrogen), according to manufacturer protocols. To eliminate phenolic impurities carried over from the Trizol extraction, we further processed the samples using a Rneasy mini kit (Qiagen, Hilden, Germany). RNA yield from each sample was determined using a NanoDrop ND-100 spectrophotometer (Thermo Scientific, Wilmington, DE) and RNA integrity was determined using a 2100 Bioanalyzer (Agilent Technologies, Santa Clara, CA). RNA transcript abundance for each tissue was analyzed using the NanoString nCounter mRNA custom codeset panel, according to manufacturer protocols. Briefly, hybridization reactions were set up by adding 10  $\mu$ L of hybridization buffer, 5  $\mu$ L of TagSet Master mix, 5  $\mu$ L of Extension TagSet, 1  $\mu$ L of 30x working probe A pool, 1  $\mu$ L of 30x working probe B pool, 3  $\mu$ L of Dnase/Rnase free water and 5  $\mu$ L of RNA Sample (20 ng/ $\mu$ L), for a total volume of 30  $\mu$ L to each sample tube. The samples were hybridized at 67 °C for 16 hours. The hybridized samples were then analyzed using the FLEX system's nCounter Prep Station and the cartridge was scanned using a nCounter Digital Analyzer to generate RCC files. Raw counts were normalized with the nSolver software (4.0) package using the geometric mean of both positive control probes and housekeeping probes. Lastly, logarithmic fold change, relative to the WT chow group, was calculated using the normalized data obtained from nSolver.

### **6.3.7 Quantification of tissue and plasma metabolites and assessment of redox markers**

All plasma and tissue metabolites were extract as defined above (See *Metabolite Extraction, Derivatization, and GC-MS*). Absolute quantification of metabolite amount was performed by running calibration standards along with extracted samples. Plasma and tissue metabolite amount was normalized to the plasma volume and tissue weight, respectively. For analysis of ammonium, 300  $\mu$ L sample was diluted by dH<sub>2</sub>O to 1.5 mL

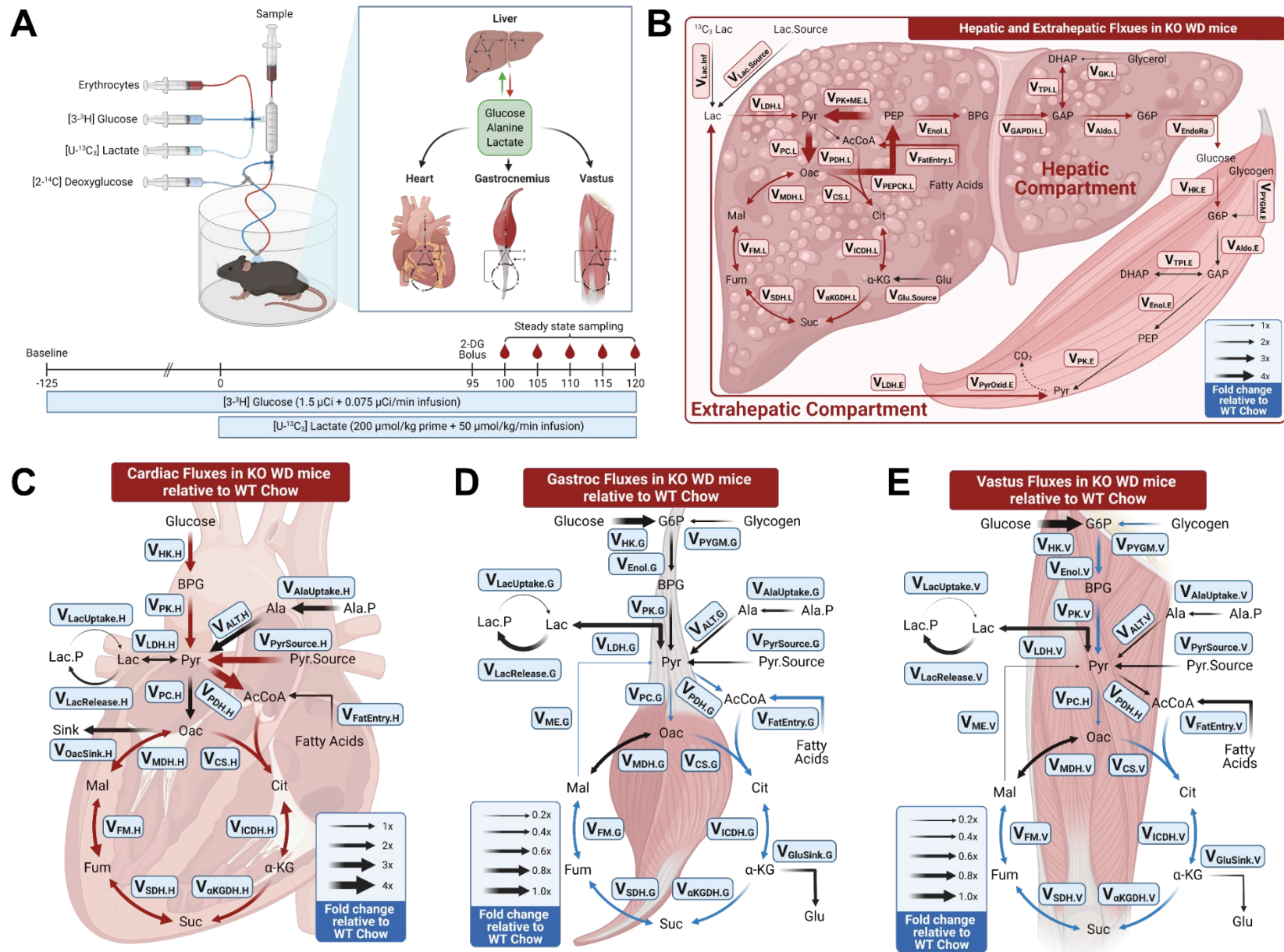
and then analyzed using an Ammonia Gas Sensing Electrode (Cat. No. 9512BNWP, Thermo Fisher Scientific, MA, USA) according to the manual. Cytosolic and mitochondrial redox state for each tissue were estimated using enzymatic equilibrium relations described elsewhere [175]. The cytosolic NADH/NAD<sup>+</sup> was estimated from lactate dehydrogenase equilibrium (i.e. cNADH/NAD<sup>+</sup> = [Lactate]/[Pyruvate] x 1/K<sub>LDH</sub>; where K<sub>LDH</sub> = 1.11 x 10<sup>-4</sup>). Similarly, cytosolic NADPH/NADP<sup>+</sup> was estimated from malate dehydrogenase equilibrium (cNADPH/NADP<sup>+</sup> = [Malate]/[Pyruvate][CO<sub>2</sub>] x K<sub>MDH</sub>; where K<sub>MDH</sub> = 34.4 x 10<sup>3</sup> uM). Lastly, mitochondrial NADPH/NADP<sup>+</sup> was estimated from glutamate dehydrogenase equilibrium (mNADPH/NADP<sup>+</sup>=[Glutamate]/[α-ketoglutarate][NH<sub>4</sub><sup>+</sup>] x K<sub>GDH</sub>; where K<sub>GDH</sub>=2.49 x 10<sup>-3</sup> mM) [175].

### **6.3.8 Liver histology, plasma analyses and body composition measurements**

Liver histology was conducted as previously described [217]. Briefly, liver tissues were fixed in formalin, routinely processed, embedded in paraffin, and cut into sections. Hematoxylin and eosin (H&E) stained sections of liver from each mouse were evaluated for evidence of NAFLD by a board-certified veterinary pathologist in masked fashion. Scoring of nonalcoholic steatohepatitis was based on previous published criteria [273]. Plasma glucose concentrations were determined using an Accu-Chek glucometer (Roche, Risch-Rotkreuz, Switzerland). Body composition was assessed using a Bruker Minispec benchtop pulsed NMR (7T) system (model mq7.5) (Bruker, Billerica, MA). Insulin was measured with radioimmunoassay RI-13K (MilliporeSigma, Burlington, MA).

### **6.3.9 Statistical Analysis**

Unless otherwise specified, data are presented as means ± SEM. Differences between groups were tested using ANOVA and Tukey multiple comparisons post hoc analysis. Analysis of histological scoring was performed using Kruskal-Wallis ANOVA with a Dunn's multiple comparisons test for post hoc analysis.



**Figure 6.1: Hepatic, cardiac and skeletal muscle fluxes reveal organ specific metabolic signatures of obesity**

(A) Overview of isotope infusion protocol. Fold change in absolute fluxes assessed in the (B) liver, (C) heart, (D) Gastrocnemius, (E) Vastus tissues of KO WD (n=6) mice relative to WT Chow (n=8) controls. The map represents the metabolic network shown in Table S1. Red and blue arrows represent fluxes that are significantly increased and decreased in the KO WD mice compared to lean WT chow mice, respectively.



## 6.4 Results

### 6.4.1 Simultaneous flux assessment of hepatic, cardiac and skeletal muscle reveals organ-specific metabolic signatures of obesity

To assess the metabolic effects of hyperphagia and western-diet feeding on the body, we studied ~19h fasted, 16-week-old WT and KO mice. To disambiguate the effect of hyperphagia from western diet feeding, lean mice (WT chow) were compared to hyperphagic (KO chow) and hyperphagic and diet-induced obese (KO WD) mice. Hyperphagia and western diet feeding led to a significant increase in body weight and fat mass for the KO animals (Fig. 6A.1A-D). Consistent with these changes in body composition, we also saw impairment in glucose tolerance (Fig. 6A.1E-F) and increased fasting plasma glucose and insulin levels. Additionally, estimation of HOMA-IR using these two parameters suggesting lower insulin sensitivity in both KO cohorts (Fig. 6A.1I). To quantify metabolic fluxes, a cocktail of stable and radio isotopes was infused to via indwelling dual-catheters implanted in the jugular vein and carotid artery. Endogenous glucose production ( $V_{\text{EndoRa}}$ ) or the peripheral glucose disposal ( $R_d$ ), assessed using tritiated glucose ( $3\text{-}^3\text{H-glucose}$ ), was significantly higher in the KO chow and WD mice (Fig. 6A.1J). In line with increased  $V_{\text{EndoRa}}$  and higher plasma insulin levels (Fig. 6A.1H), use of  $2\text{-}^{14}\text{C}$  deoxyglucose (2-DG) as an index for tissue specific glucose uptake rates showed an increase in glucose uptake by the cardiac and skeletal muscle (Fig. 6A.1K-M).

To assess tissue-specific intermediary fluxes, a range of metabolites were isolated from the plasma, liver, heart, gastrocnemius, and vastus tissues at the end of a primed, continuous infusion of  $^{13}\text{C}_3$  lactate in each mouse (Fig. 6.1A). Taking advantage of Cori cycling and the systemic circulation of  $^{13}\text{C}$  isotopes, we expanded our previously developed 2-compartment model [48] to a multi-organ metabolic model. In addition to assessing hepatic and extrahepatic fluxes, we also estimated glycolytic and mitochondrial metabolism *in vivo* within the heart, gastrocnemius and vastus (Fig. 6A.1). To assess cardiac and skeletal

muscle metabolism, tissue specific metabolic models were constructed and mass isotopomer distributions (MIDs) from glucose, lactate, and alanine in the extrahepatic compartment were allowed to irreversibly exchange with each glycolytic tissue (for details, see *Methods*). Simultaneous estimation of metabolic fluxes revealed tissue specific alterations due to progressive adiposity.

Consistent with previous reports [99], [107], [217], western diet feeding layered with hyperphagia had significant effects on hepatic fluxes compared to lean controls. Western diet feeding led to a significant increase in pyruvate cycling fluxes ( $V_{PEPCK,L}$ ,  $V_{PK,L}$ ,  $V_{PC,L}$ ) (Fig. 6.1B) accompanied by a doubling of both, CAC activity and acetyl-CoA oxidation in the CAC (Fig. 6.1B). Increased anaplerosis and cataplerosis through pyruvate carboxylase (PC) and phosphoenolpyruvate carboxykinase (PEPCK), two rate limiting enzymes of gluconeogenesis [2], [110], caused a  $\sim 1.7$  and  $\sim 1.5$  fold increase in hepatic gluconeogenesis ( $V_{Enol,L}$ ) and fasting endogenous glucose production ( $V_{EndoRa}$ ) in KO WD mice, respectively (Fig. 6A.1B, 6A.1J). Additionally, the extrahepatic compartment showed an 56% increase in glucose uptake ( $V_{HK,E}$ ) and a 78% increase in lactate production ( $V_{LDH,E}$ ). This is consistent with increased  $R_g$  measured in the heart, gastrocnemius and vastus muscles (Fig. 6A.1K-M). Compared to lean mice, KO chow-fed mice had limited but still significant effects on hepatic fluxes (Fig. 6A.2A). Increased food consumption in KO chow mice (Fig. 6A.1B) coincided with a 4-fold increase in hepatic PDH activity ( $V_{PDH,L}$ ) and  $\sim 50\%$  increase in both hepatic gluconeogenesis and endogenous glucose production (Fig. 6A.2A). Similar to the KO WD group, extrahepatic glucose uptake ( $V_{HK,E}$ ) was also elevated by 1.5-fold in the KO chow cohort (Fig. 6A.2A).

In line with the increased production of hepatic glucose in KO WD mice, assessment of cardiac fluxes showed a  $\sim 2.3$ -fold elevation in the hexose kinase flux ( $V_{HK,E}$ ) (Fig. 6.1C, 6A.1K). Consistent with this increase, we also saw a  $\sim 2.3x$  and  $1.9x$  increase in glycolytic ( $V_{PK,H}$ ) and CAC ( $V_{CS,H}$ ) activity, respectively. Additionally, anaplerosis from pyruvate ( $V_{PyrSource,H}$ ) supported an increase in cardiac pyruvate dehydrogenase ( $V_{PDH,H}$ ) and CAC flux. Despite an increase in endogenous glucose production, KO chow mice did not exhibit any differences in cardiac metabolism compared to WT chow mice (Fig. 6A.2B).

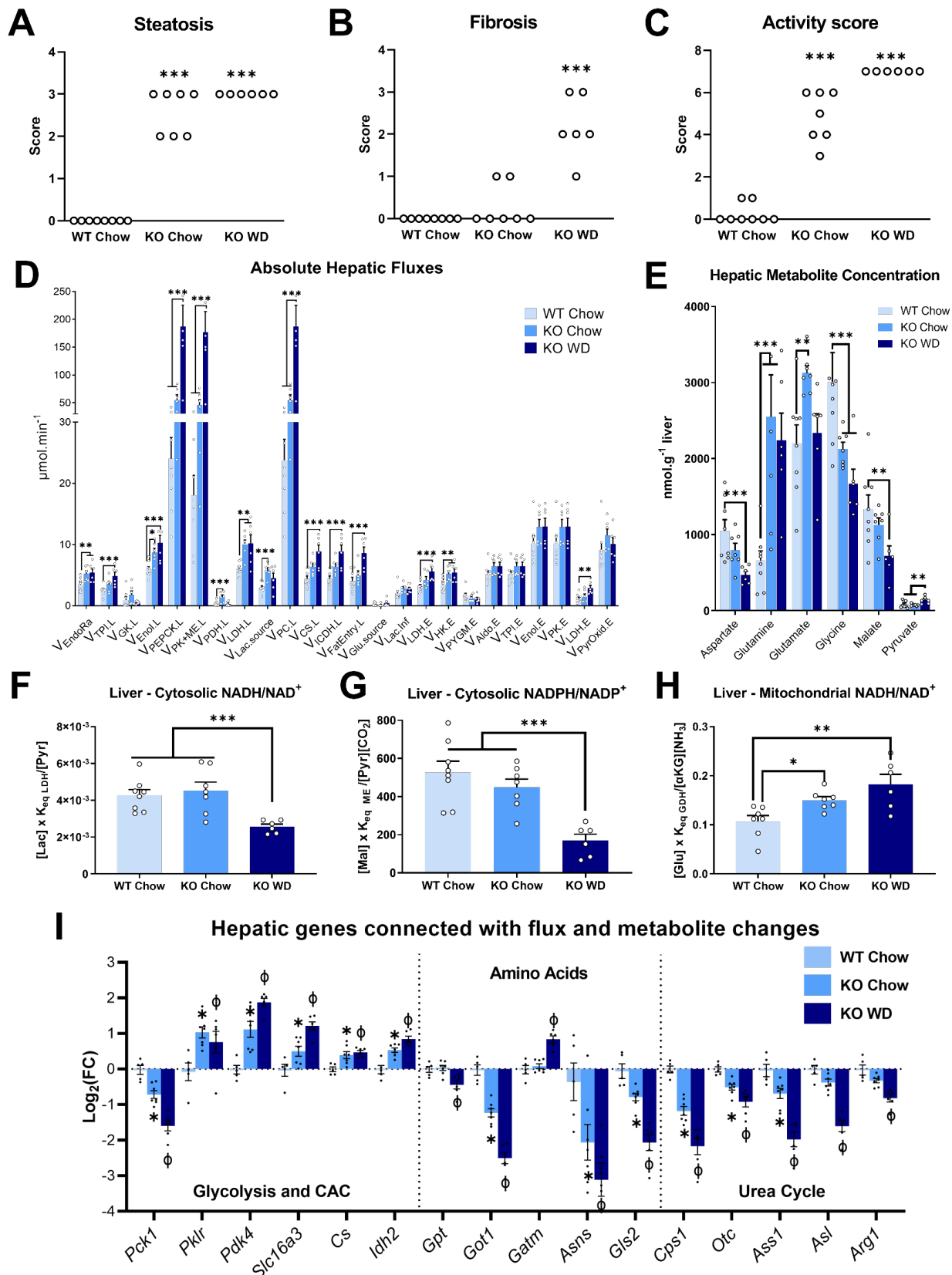
In contrast to myocardial metabolism, flux estimation in the skeletal muscle of KO WD mice showed significantly lower oxidative fluxes despite a modest increase in glucose uptake (Fig. 6.1D-E, 6A.2C-D). The gastrocnemius skeletal muscle showed a 2-fold decrease in CAC flux along with a 73% decrease in anaplerotic flux through PC ( $V_{PC,G}$ ) in KO WD mice compared to WT Chow littermates. Consistent with this decreased CAC activity, acetyl-CoA entry through PDH ( $V_{PDH,G}$ ) and other sources ( $V_{FatEntry,G}$ ) was also reduced by 64% and 48% respectively (Fig. 6.1D). Decreased anaplerosis through PC was accompanied with an 88% decrease in malic enzyme activity (Fig. 6.1D). Similar to gastrocnemius, KO WD mice had decreased oxidative flux through the vastus skeletal muscle, with a 4-fold and 1.8-fold decrease in  $V_{PC,V}$  and  $V_{CS,V}$ , respectively (Fig. 6.1E). We also measured a 38% decrease in glycolytic flux to the CAC ( $V_{PK,V}$ ) (Fig. 6.1E). KO chow mice showed similar perturbations in skeletal muscle metabolic fluxes to those seen in the KO WD cohort when compared to littermate lean controls (Fig. 6A.2C-D). Gastrocnemius from KO chow animals showed reductions in  $V_{PYGM,G}$  (65%),  $V_{PC,G}$  (73%),  $V_{CS,G}$  (55%),  $V_{FatEntry,G}$  (47%),  $V_{ME,G}$  (88%), and  $V_{MDH,G}$  (37%) (Figure S2C). Similar to KO WD mice, vastus from KO chow mice showed a decrease in glycolysis (45%), pyruvate anaplerosis (61%) and CAC activity (36%) (Figure 6A.2D). Overall, these results show that that our innovative approach can simultaneously quantify the distinct changes in metabolic flux that occur across multiple organs in response increasing metabolic disease.

#### **6.4.2 Genetic, metabolite and redox changes during the hepatic response to increasing steatosis and fibrosis**

Histology data from the livers of the three cohorts of mice showed an increase in steatosis (Fig. 6.2A), hepatocellular ballooning (Fig. 6A.3B), lobular inflammation (Fig. 6A.3C), and fibrosis (Fig. 6.2B), resulting in an overall elevation in the non-alcoholic steatohepatitis (NASH) activity score (Fig. 6.2C). Increased activity score and a rise in pyruvate cycling and gluconeogenic fluxes (Fig. 6.2D) in obese subjects is consistent with previous findings [107], [109], [217]. The increase seen in the hepatic pyruvate cycling fluxes of KO WD mice compared with lean controls (Fig. 6.2D) coincided with several metabolite

changes measured in the livers of these mice (Fig. 6.2E). A 2-fold decrease in aspartate and malate and a ~2-fold increase in pyruvate concentration (Fig. 6.2E) corresponded to increased flux through  $V_{PC}$ ,  $V_{PEPCK}$  and pyruvate kinase and malic enzyme ( $V_{PK+ME}$ ). Contrary to previous data [109], our results showed that under the pathophysiological conditions of obesity and non-alcoholic fatty liver disease (NAFLD), cytosolic NAD(P)H:NAD(P) is decreased in the liver yielding a more oxidized cytoplasm (Fig. 6.2F,G). However, similar to the findings of Satapati et. al, we did see a 40% and 80% increase in mitochondrial NADH:NAD<sup>+</sup> of KO chow and KO WD livers, respectively (Fig. 6.2H). These results are consistent with newer findings showing that NAFLD and NASH development primarily alters the hepatic mitochondrial redox potential due to the production of a majority of ROS species in that specific cell compartment [274], [275].

In addition to measuring metabolite changes, we also measured the mRNA expression of 72 hepatic genes (Fig. 6.2I, 6A.3D, 6A.4). Our results showed an increase in CAC genes (*Cs* and *Idh2*) (Fig. 6.2I, 6A.4) in the KO chow and KO WD groups, consistent with increased gluconeogenesis and CAC flux. Interestingly, *Pck1* expression inversely correlated with our flux results, perhaps to compensate for increased  $V_{PEPCK}$  in the KO WD group. Expression of *Pklr* and *Pdk4*, the genes encoding liver pyruvate kinase and pyruvate dehydrogenase kinase, corresponded with increased  $V_{PK,L}$  and decreased  $V_{PDH,L}$ , respectively. Compared to WT chow controls, measurement of other glycolytic and mitochondrial metabolites showed a 3.5 and 4-fold increase in hepatic glutamine levels and a 30% and 44% decrease in hepatic glycine levels of KO chow and KO WD mice, respectively (Fig. 6.2E, 6A.3C). Expression of *Asns* and *Gls2*, genes connected with glutamine hydrolysis and mitochondrial uptake, were severely reduced (Fig. 6.2I).

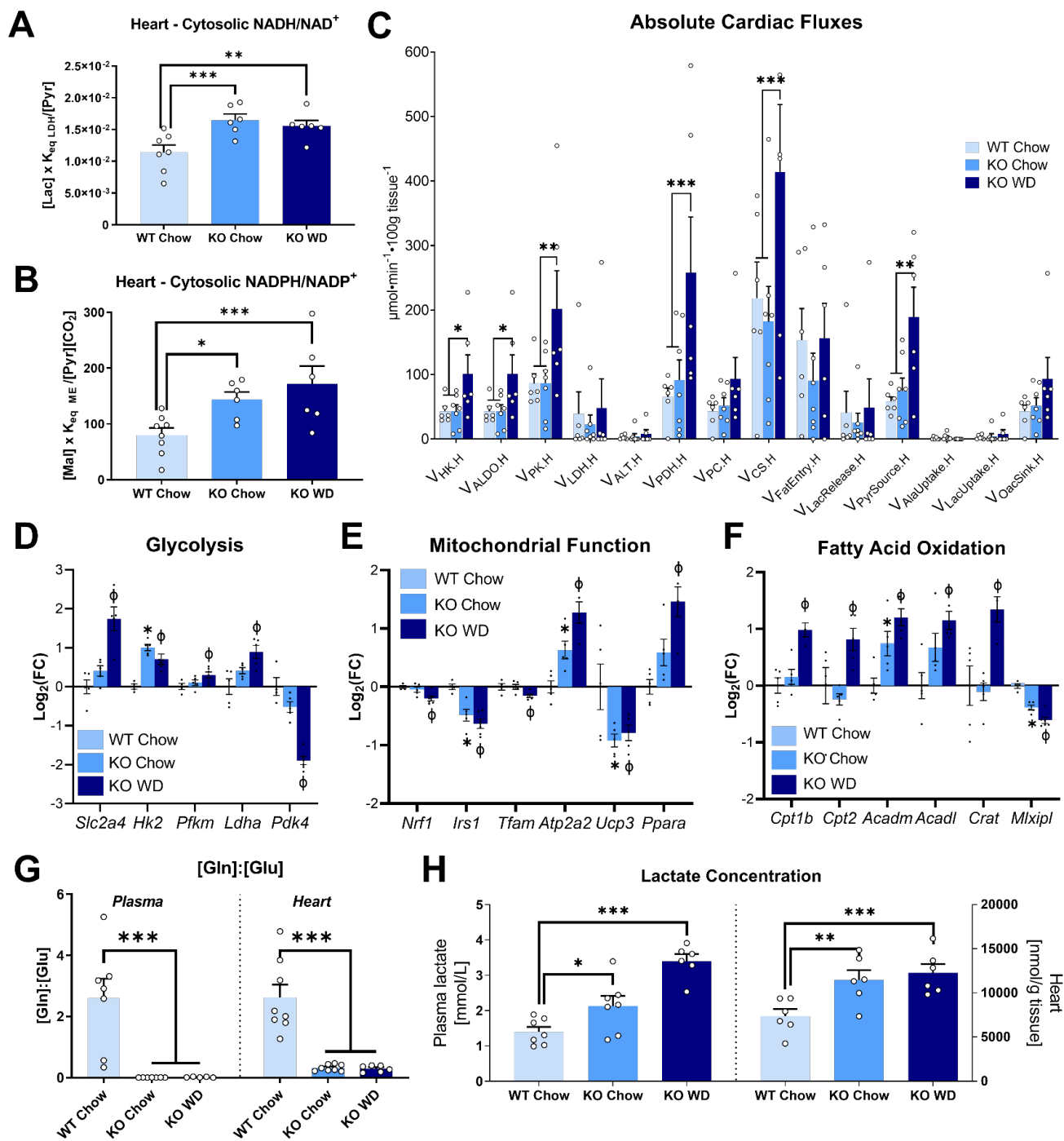


**Figure 6.2: Genetic, metabolite and redox changes support increased hepatic flux measured in obesogenic mice**  
 Scoring of (A) steatosis, (B) fibrosis, and (C) activity in the livers of WT Chow (n=8), KO Chow (n=7) and KO WD mice (n=6) (\*\**P*<0.01). Assessment of (D) absolute hepatic fluxes (E) hepatic metabolite concentration, and (F-G) cytosolic and mitochondrial redox markers in the three cohorts of mice (\**P*<0.10, \*\**P*<0.05, \*\*\**P*<0.01). (I) mRNA expression of genes connected with glycolysis, CAC, amino acid, and urea cycle metabolism in the liver. (\**P*<0.05 for WT chow vs. KO Chow,  $\Phi$  *P*<0.05 for WT chow vs. KO WD).

Despite these genetic changes in glutamine metabolism, glutamate anaplerosis into the CAC was not affected at the flux level (Fig. 6.2D). This is perhaps due to hepatic glutamine's connection with other metabolic pathways such as the urea cycle [276]. Indeed, measurement of urea cycle genes showed significant reduction in ureagenesis (Fig. 6.2I), corresponding with changes seen by others under the conditions of NAFLD and NASH [277], [278]. Overall, these results show that hepatic fluxes estimated by our metabolic model are in agreement with genetic and metabolomic changes caused by obesity and the development of NAFLD and NASH.

### **6.4.3 Myocardial oxidative glucose metabolism is elevated despite an upregulation in fatty acid oxidation**

To characterize static indices of metabolism in the heart, we measured glycolytic and CAC metabolites and mRNA levels of 60 genes associated with those pathways (Fig. 6A.S5). Assessment of cytosolic NADH:NAD<sup>+</sup> and NADPH:NADP<sup>+</sup> ratios using cardiac metabolite concentrations (see *Methods* for details) revealed a more reduced cytosol in KO WD hearts (Fig. 6.3A-B), indicative of increased glycolysis [279]. Indeed, measurement of cardiac fluxes showed an increase in glycolytic ( $V_{PK,H}$ ) and CAC ( $V_{CS,H}$ ) activity (Fig. 6.3C), potentially leading to higher cytosolic NADH and NADPH production. Measurement of mRNA expression of rate limiting glycolytic enzymes showed significant upregulation in *Hk2* and *Pfkfb3* along with an increase gene expression of the muscle glucose transporter, *Glut4* (Fig. 6.3D). The increase seen in PDH flux ( $V_{PDH,H}$ ) corresponded with decreased *Pdk4* expression, an inhibitor of PDH (Fig. 6.3D). Similarly, transcription factors regulating mitochondrial oxidation, namely *Atp2a2* and *Ppara*, were also elevated consistent with increased CAC flux in KO WD mice (Fig. 6.3E). Despite an increase in glucose oxidation via PDH, acetyl-CoA entry into the CAC ( $V_{FatEntry,H}$ ) was unchanged, suggesting impairment in acetyl-CoA oxidation by the CAC (Fig. 6.3C). Genes connected with fatty acid oxidation (*Cpt1b*, *Cpt2*, *Acadm* and *Acadl*) were significantly elevated in the KO WD group, suggesting enzymes required for cardiac



**Figure 6.3: Myocardial oxidative glucose metabolism is elevated despite an upregulation in fatty acid oxidation under obesity**

(A-B) Cytosolic redox state and (C) absolute metabolic fluxes in the hearts of WT Chow (n=8), KO Chow (n=7) and KO WD mice (n=6) (\*  $P < 0.10$ , \*\*  $P < 0.05$ , \*\*\*  $P < 0.01$ ). mRNA expression of genes regulating (D) glycolysis (E) mitochondrial function and (F) fatty acid oxidation in the heart (\*  $P < 0.05$  for WT chow vs. KO Chow,  $\Phi$   $P < 0.05$  for WT chow vs. KO WD). Plasma and cardiac (G) glutamine to glutamate ratios and (H) lactate concentrations in the three groups of mice (\*  $P < 0.10$ , \*\*  $P < 0.05$ , \*\*\*  $P < 0.01$ ).

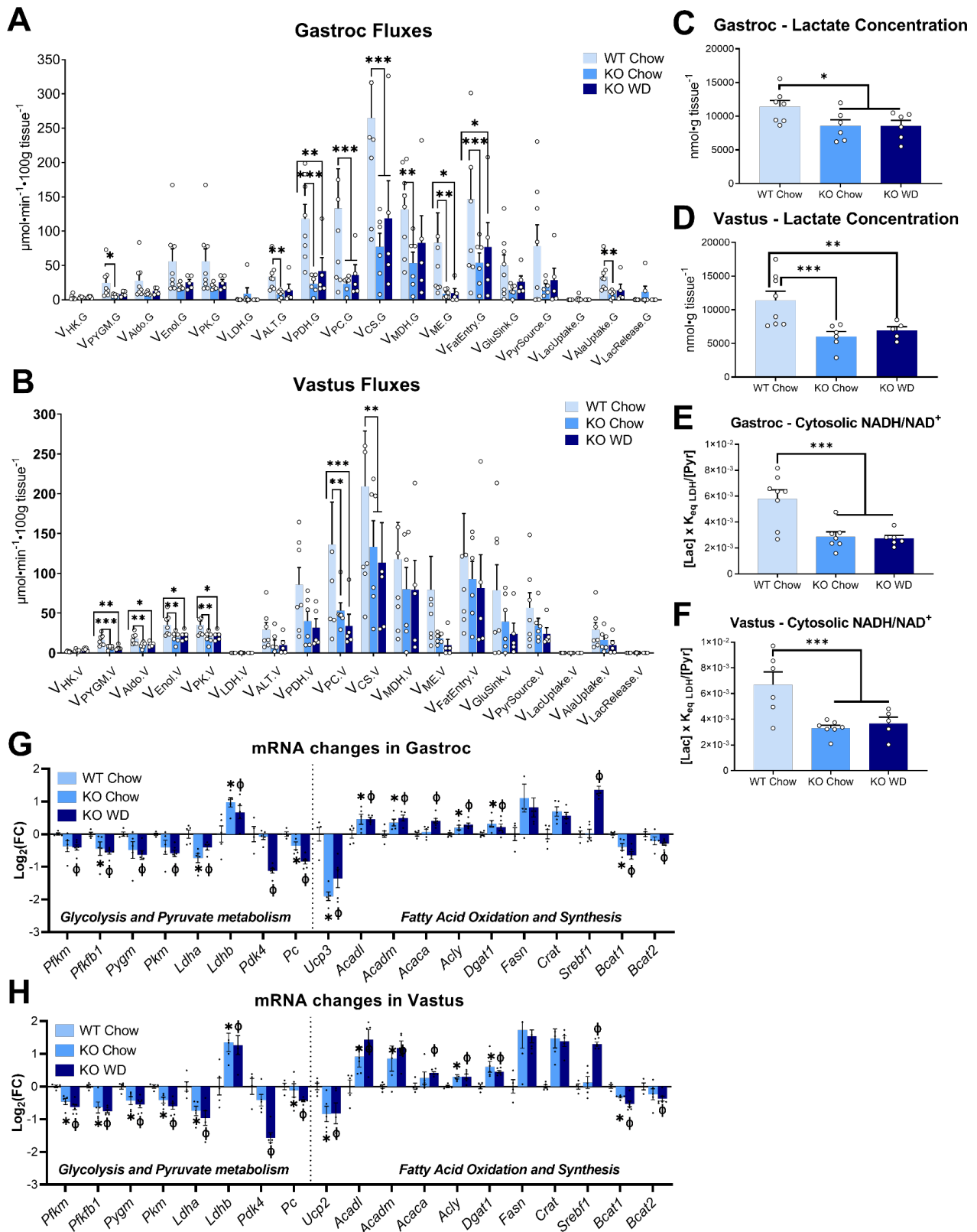
$\beta$ -oxidation were elevated (Fig. 6.3F). Interestingly, measurement of *Crat*, a mitochondrial matrix enzyme whose activity negatively correlates with intramuscular lipid intermediates [280], [281], also showed severe upregulation (Fig. 6.3D). These findings suggest that obesity leads to increased myocardial glucose oxidation without increasing acetyl-CoA oxidation in the CAC from other sources (e.g. fatty acids). These results challenge the existing notion that obesity leads increased myocardial fatty acid oxidation and reduced entry and oxidation of glucose, better known as the Randle cycle [282]. Interestingly, *Irs1* expression was also downregulated (Fig. 6.3E), potentially to compensate for the increased glucose uptake caused by high plasma insulin levels (Fig. 6A.1H). Additionally, genes involved in mitochondrial biogenesis (*Nrf1* and *Tfam*) were slightly but significantly repressed (Fig. 6.3E).

Plasma and heart metabolites showed congruence between the two compartments. We saw a severe reduction in plasma and heart glutamine to glutamate ratio (Fig. 6.3G) in both KO chow and KO WD groups, a signature of cardiometabolic disease and insulin resistance [283]–[285]. Elevation in plasma lactate, a biomarker of metabolic health [286], coincided with a similar rise in cardiac lactate concentration in obese mice compared to WT chow controls (Fig. 6.3H). This is consistent with the increase and decrease measured in *Ldha* and *Ucp3* genetic expression, respectively (Fig. 6.3D, 6.3E). These data suggest that plasma lactate, glutamine and glutamate are biomarkers of cardiometabolic dysfunction.

#### **6.4.4 Reduced skeletal muscle mitochondrial fluxes are associated with dysregulation of multiple metabolic pathways**

Estimation of skeletal muscle metabolic fluxes showed significant downregulation through oxidative pathways in both KO chow and KO WD mice (Fig. 6.4A-B, 1D-E). Reduction in pyruvate anaplerosis through  $V_{PC}$  flux was associated with a reduction in the muscle lactate pool size (Fig. 6.4C-D, 6A.6B, 6A.7B), suggesting a more oxidized cytosol. Indeed assessment of NADH:NAD<sup>+</sup> in both gastrocnemius and vastus skeletal muscle showed a significantly oxidized cytosol for both KO chow and KO WD mice, relative to lean WT chow controls (Fig. 6.4E-F).





**Figure 6.4: Obese mice have reduced mitochondrial flux in the skeletal muscle along with dysregulation of multiple metabolic pathways**

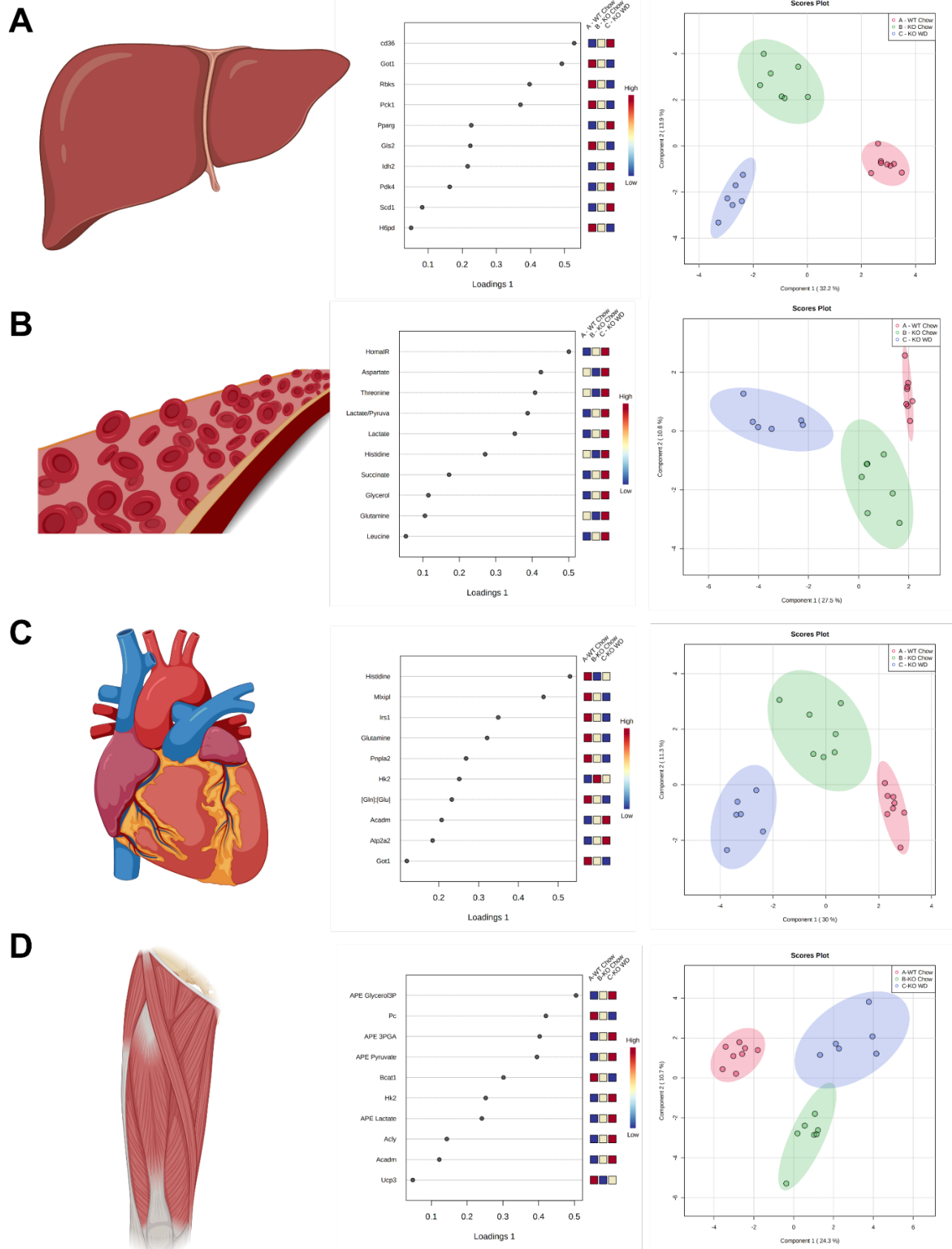
Absolute fluxes estimated in the (A) gastrocnemius and (B) vastus skeletal muscles of WT Chow (n=8), KO Chow (n=7) and KO WD mice (n=6) (\* $P < 0.10$ , \*\* $P < 0.05$ , \*\*\* $P < 0.01$ ). (C-F) (C-D) Lactate concentration and (E-F) cytosolic NADH:NAD<sup>+</sup> ratio, assessed using metabolite concentration, in the gastrocnemius and vastus tissues (\* $P < 0.10$ , \*\* $P < 0.05$ , \*\*\* $P < 0.01$ ). Log fold change in mRNA expression of genes regulating glycolysis, pyruvate metabolism and fatty acid metabolism in (G) gastrocnemius and (H) vastus muscles (\* $P < 0.05$  for WT chow vs. KO Chow, φ $P < 0.05$  for WT chow vs. KO WD).

Quantification of mRNA expression of *Ldha* and *Ldhb* showed a decrease and an increase, respectively in the KO chow and KO WD groups, possibly to generate more pyruvate for anaplerosis (Fig. 6.4F-G, 6A.6C, 6A.7C).

Interestingly, despite a slight but significant increase in glucose uptake rate, glycerol and glycogen flux ( $V_{PYGL+GK.V}$ ), was reduced along with a decrease in glycolysis in the vastus muscle ( $V_{PK.V}$ ) (Fig. 6.4B). In agreement with this result, glycolytic genes (*Pfkm*, *Pfkfb1*, *Pkm*) were downregulated in both skeletal muscles along with a reduction in *Pygm* (Fig. 6.4F-G, 6A.6A, 6A.6C, 6A.7A, 6A.7C). While flux through this pathway was significantly limited in vastus, we measured downregulation of another pathway in the gastrocnemius of KO chow and KO WD mice. Acetyl-CoA entry into the CAC ( $V_{FatEntry.G}$ ) and anaplerosis through various sources (pyruvate, lactate and glutamate) was significantly reduced in gastrocnemius muscle of obese mice (Fig. 6.4A). Consistent with this lower AcCoA flux into the CAC, we measured an upregulation of genes connected with fatty acid oxidation and carnitine production (Fig. 6.4F-G, 6A.6A, 6A.6C, 6A.7A, 6A.7C). Additionally, branch chain amino acids (BCAA) genes, *Bcat1* and *Bcat2*, were significantly reduced in both skeletal muscles (Fig. 6.4F-G, 6A.6C, 6A.7C) along with a rise in plasma BCAA for the KO chow and KO WD mice (Fig. 6A.4E). These results show that obesity leads to severe reduction in glycolytic and mitochondrial fluxes in the skeletal muscle and are a result of perturbations in multiple metabolic pathways i.e., glycogen and glycerol oxidation, fatty acid oxidation and anaplerosis of the CAC.

#### **6.4.5 Multi-omics analysis reveals tissue specific biomarkers for obesity**

To better understand the pleotropic effects of obesity, we combined the transcriptomics, metabolomics and fluxomics datasets for each tissue type and plasma to identify the top 10 variables that help distinguish the three cohorts of mice. To perform this multi-omics analysis, exploratory statistical features in Metaboanalyst 5.0 [272] were used to identify the top 10 variables associated with increasing levels of



**Figure 6.5: Multi-omics analysis reveals tissue specific biomarkers for obesity**

Top 10 loadings that help separate the WT Chow (n=8), KO Chow (n=7) and KO WD mice (n=6) in sparse partial least square analysis score plots for the (A) liver (B) plasma (C) heart and (D) vastus compartments.

obesity in each tissue. Additionally, we performed several types of multivariate analysis to cross-check and verify the robustness of our results (see *Methods* for details). Our results from sPLS-DA analysis of the hepatic dataset showed distinct clustering of the three groups, with identification of genes regulating lipid metabolism (*Cd36*, *Pparg*, *Scd1*), oxidative pentose phosphate pathway (*Rbks*, *H6pd*), CAC (*Idh2*), glutamine (*Gls2*), alanine (*Got1*), and pyruvate metabolism (*Pdk4*, *Pck1*) as biomarkers of hepatic injury and obesity (Fig. 6.5A). Similarly, correlation analysis – using progressive levels of obesity (WT chow → KO chow → KO WD) as a feature of interest – showed similar top 25 features (Fig. 6A.8A). Additionally, heat map clustering using Euclidean distance metrics and ANOVA analysis also identified the exact same top 10 variables that best separate the three groups (Fig. 6A.8B). Similar analysis on the plasma metabolites and fluxes showed Homa-IR as the top biomarker that best separates the groups followed by several other plasma metabolites including plasma lactate, glutamine, and the BCAA, leucine. Interestingly, correlation analysis identified similar variables along with several extrahepatic fluxes such as  $V_{LDH,E}$ ,  $V_{HK,E}$  and  $V_{PYGM,E}$  (Fig. 6.5C). Lastly, heatmap clustering using ANOVA showed results consistent with the sPLS-DA analysis (Fig. 6.5D).

Identification of cardiac biomarkers of obesity using sPLS-DA analysis showed reduction in histidine and glutamine concentrations as well as a decrease in *Mlxipl* and *Irs1* gene expression as top variables that help separate the experimental groups (Fig. 6.5E, F). Other cardiac factors of interest included oxidative metabolism genes (*Hk2*, *Acadm*, *Atp2a2*) and our previously identified cardiometabolic dysfunction biomarker, Gln to Glu concentration ratio (Fig. 6.3G). Correlation analysis identified additional metabolic indicators of obesity such as cardiac enrichment of glutamine and increased *Crat* expression (Fig. 6A.8E). Heatmap clustering analysis of the cardiac multi-omics dataset implicated three additional genes, *Slc2a4* (Glut4), *Pdk4* and *Pdhx* as potential biomarkers of obesity (Fig. 6A.8F). The increase in *Slc2a4* expression and a decrease in *Pdk4* in obesogenic mice is consistent with our cardiac flux results (Fig. 6.3C). Lastly, multivariate analysis of multi-omics datasets from gastrocnemius and vastus skeletal muscles identified

similar biomarkers. Sparse PLS-DA analysis (Fig. 6A.9A) showed increasing enrichment in glycerol-3-phosphate, 3-phosphoglyceric acid (3PGA), pyruvate and lactate as a potential identifier of obesity in the gastrocnemius (Fig. 6A.9A). Other genes connected with oxidative metabolism (*Pc*, *Hk2*, *Ucp3*) and impaired fatty acid and BCAA oxidation (*Acly*, *Acadm*, *Acly* and *Bcat1*) were also implicated by sPLS-DA loadings in the gastrocnemius muscle (Fig. 6A.9A). Likewise, sPLS-DA of vastus dataset (Fig. 6.5H) showed G3P and 3PGA enrichments as indicators along with genes connected with glycolysis (*Pygm*, *Pfkm*, *Pfkfb1*, *Pkm*, *Ldha*) and impaired fatty acid and BCAA oxidation (*Crat* and *Bcat1*) (Fig. 6.5G). All of these biomarkers were also identified in heatmap clustering and correlation analysis based on disease progression, both for gastrocnemius (Fig. 6A.9C-D) and vastus (Fig. 6A.8G-H). These various types of multivariate analysis yielding similar biomarkers for each specific compartment validates the robustness of our dataset. Although few flux measurements were identified in this multi-omics analysis as biomarkers of obesity, almost all the metabolites and genes implicated here are associated with the flux changes seen in each tissue. Overall, this exploratory statistical analysis not only provides tissue specific biomarkers for disease progression but identifies potential pathways of interest that may be targeted to modulate flux changes and ameliorate metabolic diseases.

## 6.5 Discussion

Prior studies have investigated the effects of metabolic diseases on metabolic fluxes within specific tissues [99], [109], [217], [287]. But, to our knowledge, no studies have introduced methods that simultaneously assess intermediary metabolic fluxes in several tissues in a single mouse. Here, we present a novel mathematical modeling approach that simultaneously characterizes metabolic fluxes in the liver, heart, gastrocnemius and vastus with the generalizability and scalability to test hypotheses in a number of conditions. Here we investigated the effects of hyperphagia and western diet feeding on hepatic, cardiac and skeletal muscle fluxes in a setting relevant to the study of cardiometabolic disease. Similar to previous findings, livers from obese mice showed an elevation in pyruvate cycling and gluconeogenesis along with

increased endogenous glucose production. Interestingly, we found that despite an increase in glucose uptake, glycolytic and mitochondrial fluxes in the skeletal muscles were severely reduced. However, cardiac metabolism exhibited the opposite trend, showing an increase in oxidative metabolism and CAC activity. These findings show distinct metabolic signatures of each organ in response to obesity.

An altered metabolic response to obesity in cardiac and skeletal muscles has previously been examined and is indicative of varying insulin sensitivity of the different tissues [288]. Patients with non-insulin dependent diabetes mellitus (NIDDM) and insulin-dependent diabetes mellitus (IDDM) but no history of coronary heart disease showed signs of insulin resistance in the skeletal muscle but had no alterations in myocardial glucose uptake under insulin stimulated conditions [288]–[290]. Under obesogenic conditions, metabolic flexibility of utilizing Fas and glucose is impaired [291]. It is widely accepted that under such conditions, reduced cardiac glucose uptake and increased fatty acid oxidation are putative causes of cardiac dysfunction [282], [292]–[294]. However, we saw that in response to 8 weeks of WD feeding, cardiac fluxes connected with glucose oxidation were enhanced while the terminal entry of acetyl-CoA into the CAC ( $V_{\text{FatEntry,H}}$ ) was unchanged, despite an upregulation in fatty acid oxidation genes (Fig. 6.3). These results challenge the notion that in the setting of obesity, when plasma insulin levels are elevated, cardiac glucose uptake rates decrease. This discrepancy is attributed to the methodology implemented to quantify glucose uptake rates in previous studies, which have often been conducted in isolated hearts or cells with glucose as the sole substrate [295]. Recent work, using [ $^{18}\text{F}$ ] 2-fluoro-2-deoxy-D-glucose and PET imaging *in vivo*, supports our findings, and shows that glucose uptake rates are markedly elevated in the hearts of both young and middle-aged mice fed a high-fat, high-cholesterol Western diet [296]. Our study builds upon these findings, by quantifying glucose oxidation rates and showing that PDH and CS flux is significantly increased under obesity (Fig. 6.1C, 6.3C). Additionally, no change in  $V_{\text{FatEntry,H}}$  yet increased expression of acylcarnitine genes such as *Crat* suggests that increased plasma insulin levels do not inhibit lipid trafficking in the heart, thus preventing the accumulation of lipid intermediates in the heart. Several studies support these findings,

showing that myocardial ceramide content is unaltered in obese mice [293], [297] and obese (and T2DM) patients [298]. Overall, these findings have high clinical relevance due to the enormous patient population living with obesity and at substantial risk of cardiovascular disease.

Many studies have used various approaches to study skeletal muscle metabolism in animal models of obesity and diabetes [160], [299], [300]. However, discrepant results have been observed showing that high-fat feeding in rats is associated with no variation [301], [302] or even a higher mitochondrial capacity [303], and that insulin resistance caused by high fat feeding could be related to incomplete intramitochondrial  $\beta$ -oxidation [300]. Our results here show a significant decrease in CAC flux, despite an increase in glucose uptake rate in the gastrocnemius and vastus muscle (Fig. 6.4A,B). The flux of the terminal product of fat oxidation (Acetyl-CoA) into the CAC is modeled in our flux network ( $V_{\text{FatEntry}}$ ), which was significantly reduced in the gastrocnemius; a similar trend was observed in the vastus (Fig. 6.4A,B). Our transcriptomics results also showed a significant elevation in FAO genes, suggesting elevated  $\beta$ -oxidation in the skeletal muscles of obese mice (Fig. 6.4G,H). These results are consistent with previous findings, showing that high-fat feeding increases incomplete FAO in the skeletal muscle unmatched by compensatory increases in the CAC activity in both animals and humans [300], [304], [305].

The “glucose-fatty acid cycle” postulated by Randle indicates that increased fatty acid oxidation would suppress glycolysis and pyruvate oxidation [282]. In agreement with the Randle cycle, we saw elevations in fatty acid genes concomitant with reduction in glycolytic and pyruvate oxidation genes in the skeletal muscle. Interestingly, despite elevated FAO genes,  $V_{\text{FatEntry}}$  was decreased in the gastrocnemius along with a significant decrease in  $V_{\text{PDH}}$ , where the latter has been shown to be potently inhibited by fatty acids [306], [307]. The reduction of PDH and CS flux shown here are consistent with the hypothesis proposed by Koves et al. where excessive yet incomplete  $\beta$ -oxidation results in impaired mitochondrial flux and acetyl carnitine build up [300], [308], [309]. Interestingly, glucose uptake flux was elevated yet glycolytic flux was still significantly lower, mostly due to reductions in glycogen/glycerol flux in obese mice. Skeletal muscle stores

~80% of total body glycogen, where it acts as a major contributor to glycolysis under fasting and exercise [268], [310]. The reduced glycolytic flux seen in vastus skeletal muscle could perhaps be connected with either an impairment in glycogen synthase seen in both obese mice and humans [311]–[313] and/or to the inhibition of glycolytic enzymes by fatty acids [282], [306].

Integrated multi-omics approaches have emerged as an invaluable tool to obtain a better understanding of the complexity and interactions of the biological systems including those predisposing obesity [314]. Using multi-omics analyses, our study identified important biomarkers of hepatic, cardiac, and skeletal muscle metabolism that could further investigated to elucidate the underlying mechanisms or as an indicator of disease severity. For example, increased hepatic *Cd36* gene expression, seen here, has also been reported to be significantly upregulated in NAFLD patients [315] and mediates FA uptake, thus playing a significant role in hepatic steatosis [316]. Though changes in hepatic *Pck1* expression and pyruvate cycling in liver are characteristic of NAFLD/NASH[99], [107], little is known why the latter is elevated under obesogenic conditions and thus require further investigation. A potential cardiometabolic risk factor of obesity identified here is the heart Gln:Glu ratio which resembled strongly with plasma Gln:Glu ratio. Plasma Gln:Glu ratio has been found to be inversely associated with body mass index, blood pressure, circulating triglycerides and insulin resistant-traits in obese humans and rodents [283]–[285]. Thus, the ratio either from the heart or the plasma, may serve as a valuable biomarker of cardiometabolic risk. Identification of *Bcat1* as a classifier for obesity is supported by recent evidence that shows reduced BCAT activity in the muscle leads to impaired lipid metabolism [317] and increased circulating BCAA [318]. Further studies need to be conducted to better understand the role of BCAA in regulating skeletal muscle fluxes. Similarly, plasma multi-omics analysis showed HOMA-IR, a well-establish index of insulin resistance used in type 2 diabetic patients [319], as the lead plasma biomarker of obesity. Additionally, several metabolites including plasma lactate were identified as variables that best separated the three cohorts, consistent with a recent study showing that elevated fasting plasma lactate levels are a metric for assessing the severity of the



metabolic syndrome [286]. Taken together, these tissue specific factors identify important clinical biomarkers and potential molecular targets for obesity-related disease such as NAFLD/NASH.

Advancements in analytical platforms and mathematical modeling have enabled *in vivo* flux analysis studies to become an important tool for studying physiology and metabolic diseases [68]. Using enrichment of plasma metabolites and mathematical equations, recent studies have quantified the fluxes of circulating metabolites and their contribution to the TCA cycle [163], [164], [167]. Albeit impressive, these studies do not provide any insights on intermediary metabolism within each tissue. Additionally, the methodology provided in these studies require experimentalists to set up and solve complicated mathematical equations to quantify these fluxes. Our approach here overcomes both these limitations since it provides tissue specific metabolic models that estimate intermediary tissues fluxes and it utilizes a generalized software package, INCA, which automatically generates and solves all equations, outputting metabolic fluxes for the user. Another intriguing feature of our metabolic flux model is its generalizability and scalability, allowing for the removal or addition of other tissue compartments depending on the rigor of the analysis required. For example, we saw that the results from extrahepatic glycolytic compartment showed increased extrahepatic glucose uptake ( $V_{HK,E}$ ), lower glycogen contributions ( $V_{PYGM,E}$ ) and higher LDH activity ( $V_{LDH,E}$ ) under obese conditions, consistent with certain muscle specific metabolic fluxes (Figure 6.2). Thus, approximations of extrahepatic metabolism from the plasma enrichment alone may be reasonable in studies when more comprehensive techniques are unavailable or impractical. Additionally, our metabolic model is flexible to where additional compartments for tissues (e.g., brown and white adipose tissue) can be developed for assessment of metabolic fluxes. Therefore, the generality of our platform is standout feature of this approach and has much broader implications in studying the effects of drugs and diseases on different tissues and even tumor macro environments.

In summary, we present the development and application of a novel multi-tissue metabolic model can be used to simultaneously assess intermediary metabolism in the liver, heart, gastrocnemius and vastus

muscles within a single mouse based on the isotope enrichment measurements of tissue and plasma metabolites. By making use of technical and computational advancements in systems biology, our flux approach shows that isotopic tracing and metabolic flux analysis can help resolve *in vivo* fluxes that are otherwise non-quantifiable. Applying our multi-tissue model, we show that obesity has organ specific effects on the body and that metabolic diseases NAFLD and NASH do not develop in a vacuum. Our results showed a significant increase in hepatic pyruvate cycling, gluconeogenesis, and glucose production concomitant with severe hepatic steatosis and obesity. Increased plasma insulin levels correlated with increased glucose uptake by cardiac and skeletal muscle, however, intermediary metabolism of the two tissues was contrastingly different in response to obesity. Both skeletal muscles, gastrocnemius, and vastus, showed a decrease in mitochondrial flux which was in turn connected with reduced fatty acid entry into the CAC and a reduction in glycolytic flux. Conversely, the heart showed a significantly higher glycolytic and mitochondrial flux with no changes in fatty acid contributions to the CAC. Additionally, using integrative multi-omics analysis we were able to identify important regulatory and clinical biomarkers of obesity. Overall, the development of this metabolic model provides a flexible platform to simultaneously evaluate *in vivo* fluxes in response to genetic, (patho)physiological and pharmacological interventions.

### **6.5.1 Limitations of the study**

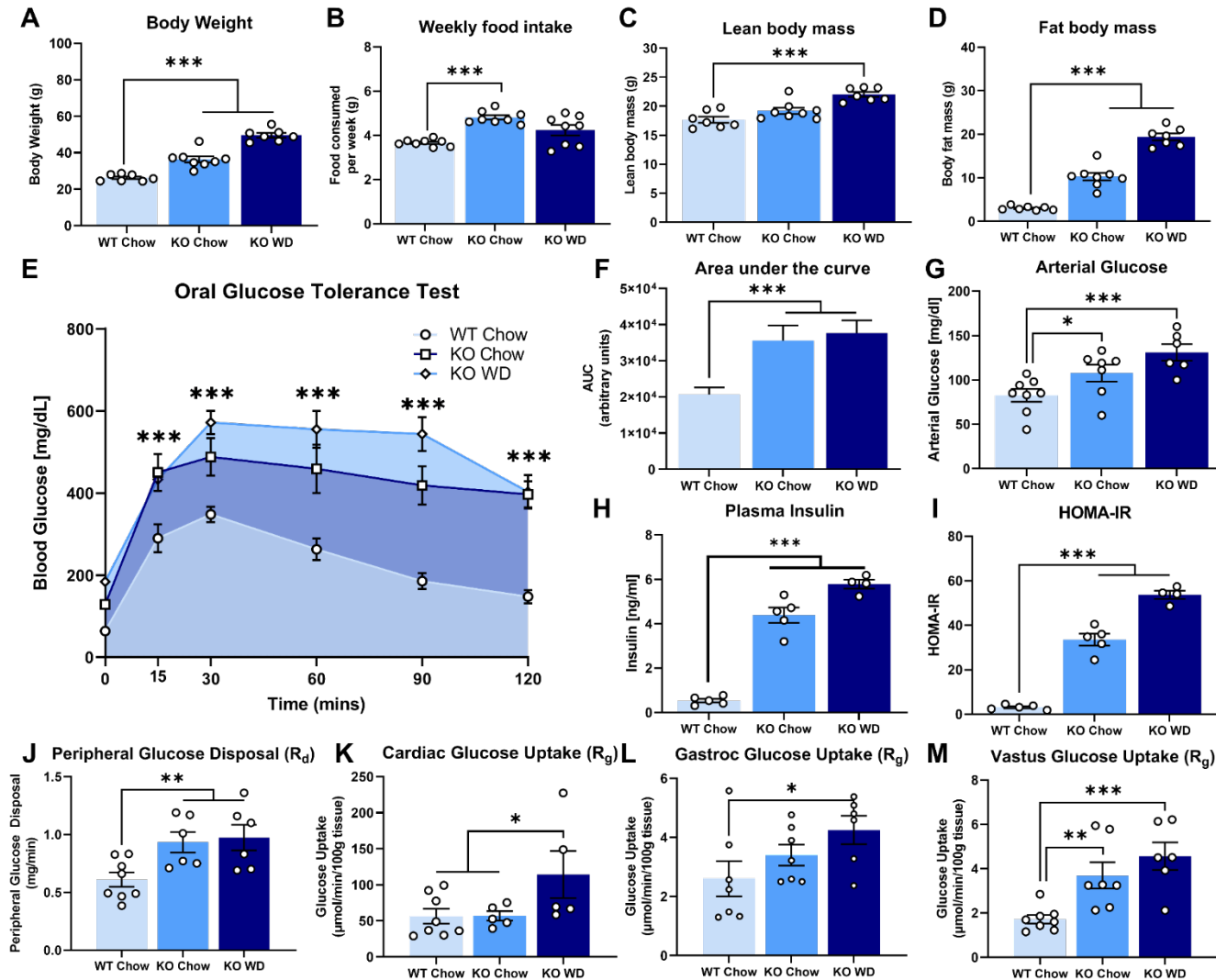
The multi-compartment here relies upon some assumptions that introduce some inherent limitations. The model does not account for additional sources of glucose synthesis other than the liver, though, recent studies suggest a negligible contribution from other tissues to glucose production unless livers gluconeogenic ability is compromised [257]. However, had another tissue generated a significant amount of plasma glucose and a unique underlying metabolism, we would anticipate a significant lack-of-fit between simulated and measured isotopomers. Yet, statistically acceptable fits were obtained for all data sets in our study. That said, the scalability of this flux approach allows for the addition of other gluconeogenic or glycolytic tissues if required. Secondly, the model currently only allows for the exchange

of enrichment information of metabolites between various glycolytic tissues and does not capture absolute circulating fluxes between tissues (see *Methods* for details). Third, our glycolytic metabolic model for the heart and skeletal muscle does not include the oxidative pentose phosphate pathway due to lack of enrichment measurements of phosphate sugars. Although the oxPPP activity is considered to be very low in cardiac [320] and skeletal muscles [321], future studies benefiting from the use of LC-MS/MS will further explore the metabolic effects in this pathway [322]. Lastly, a unique facet of our experimental system is the ability to measure plasma glucose enrichment over time and verify steady state conditions over a similar isotope-infusion time course [29]. However, end-point measurements of tissue metabolites can be obtained only in a terminal sample and, therefore, steady-state assumptions for tissue metabolites cannot be confirmed.

## 6.6 Acknowledgements

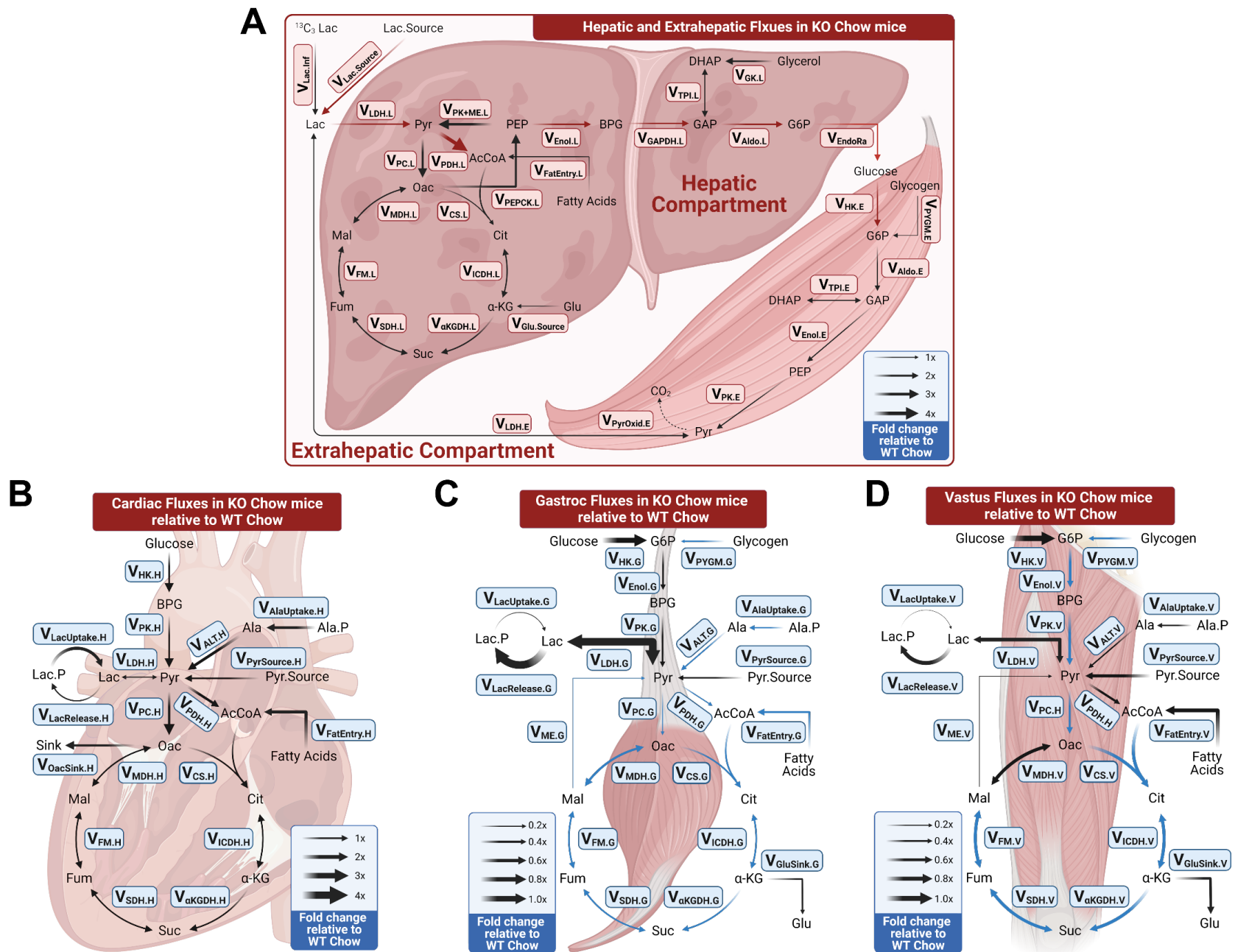
We thank the Vanderbilt University Mouse Metabolic Phenotyping Center (MMPC) for performing surgical catheterization and *in vivo* studies, described here. We would like to thank Susan Hajizadeh in the Vanderbilt University Mouse Metabolic Phenotyping Center Hormone and Analytical Core for measuring insulin. This research was supported by NIH grants R01 DK106348 and U01 CA235508, the Integrated Training in Engineering and Diabetes NIH training grant (T32 DK101003), and the Vanderbilt MMPC (NIH grant U24 DK059637).

## 6.7 Appendix: Supplemental figures and tables



**Figure 6A.1: Hyperphagic mice show phenotypic signatures of obesity along with impaired glucose metabolism**

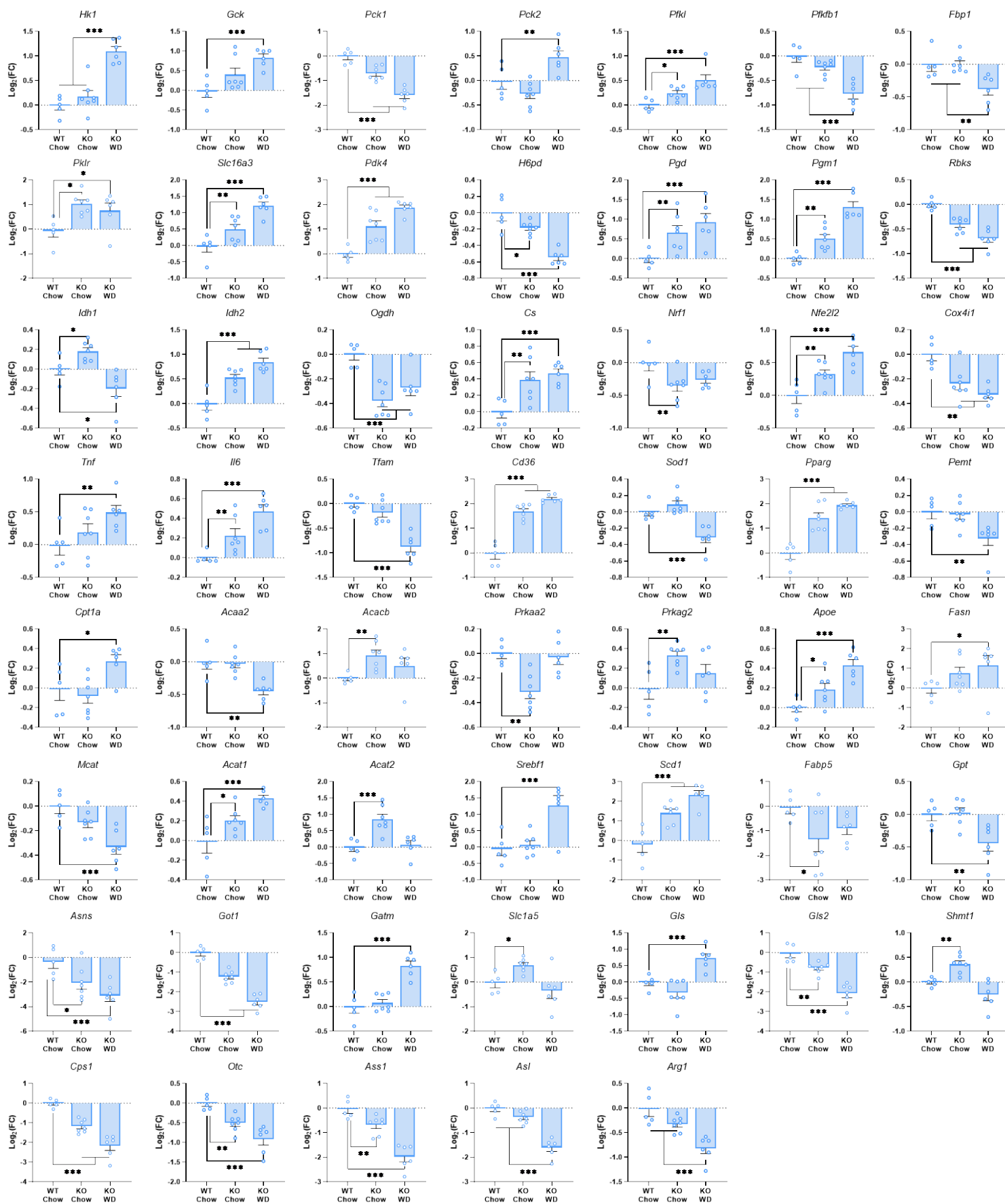
(A) Body weight, (B) weekly food intake, (C) lean and (D) fat body mass, (E) oral glucose tolerance test response and (F) area under the curve, 16h fasting (G) arterial glucose and (H) plasma insulin concentration and (I) HOMA-IR index in WT chow (n=8), KO Chow (n=7) and KO WD (n=6) mice. Assessment of (J) peripheral glucose disposal rate ( $R_d$ ) using [ $3\text{-}^3\text{H}$ ]glucose and tissue specific glucose uptake ( $R_g$ ) measured in the heart, gastrocnemius and vastus using [ $^{14}\text{C}$ ]-2-deoxyglucose in all three groups of mice (\*  $P < 0.1$ , \*\*  $P < 0.05$ , \*\*\*  $P < 0.01$ ).



**Figure 6A.2: Hepatic and skeletal muscle fluxes but not cardiac fluxes are affected by hyperphagia**

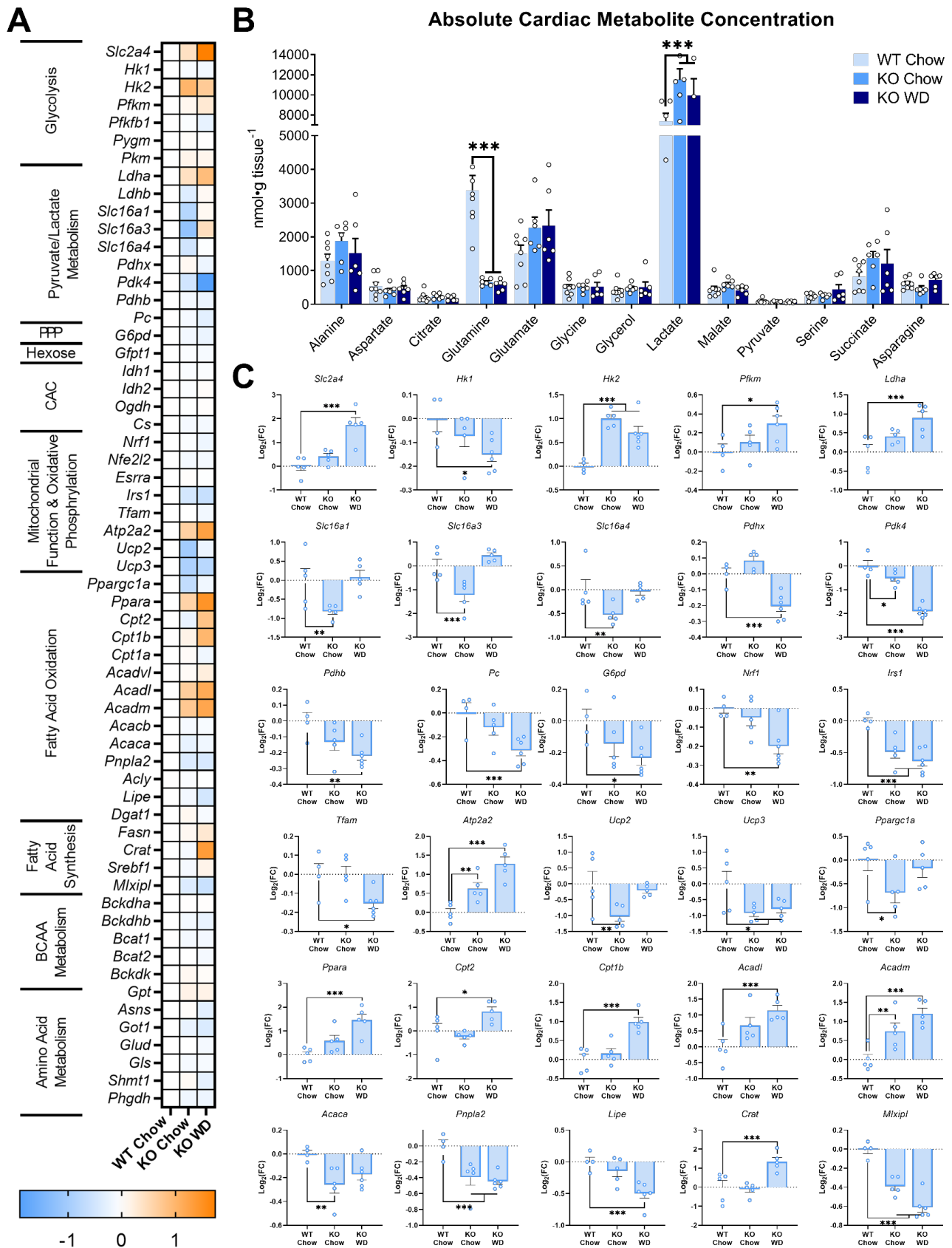
Fold change in absolute fluxes assessed in the (B) liver, (C) heart, (D) gastrocnemius, (E) vastus tissues of KO chow (n=7) mice relative to and WT chow (n=8) lean controls. The map represents the metabolic network shown in Table S1. Red and blue arrows indicate fluxes that are significantly increased and decreased in the KO chow group, compared to lean WT chow mice, respectively.





**Figure 6A.4: Significantly affected genes in the livers of obese mice.**

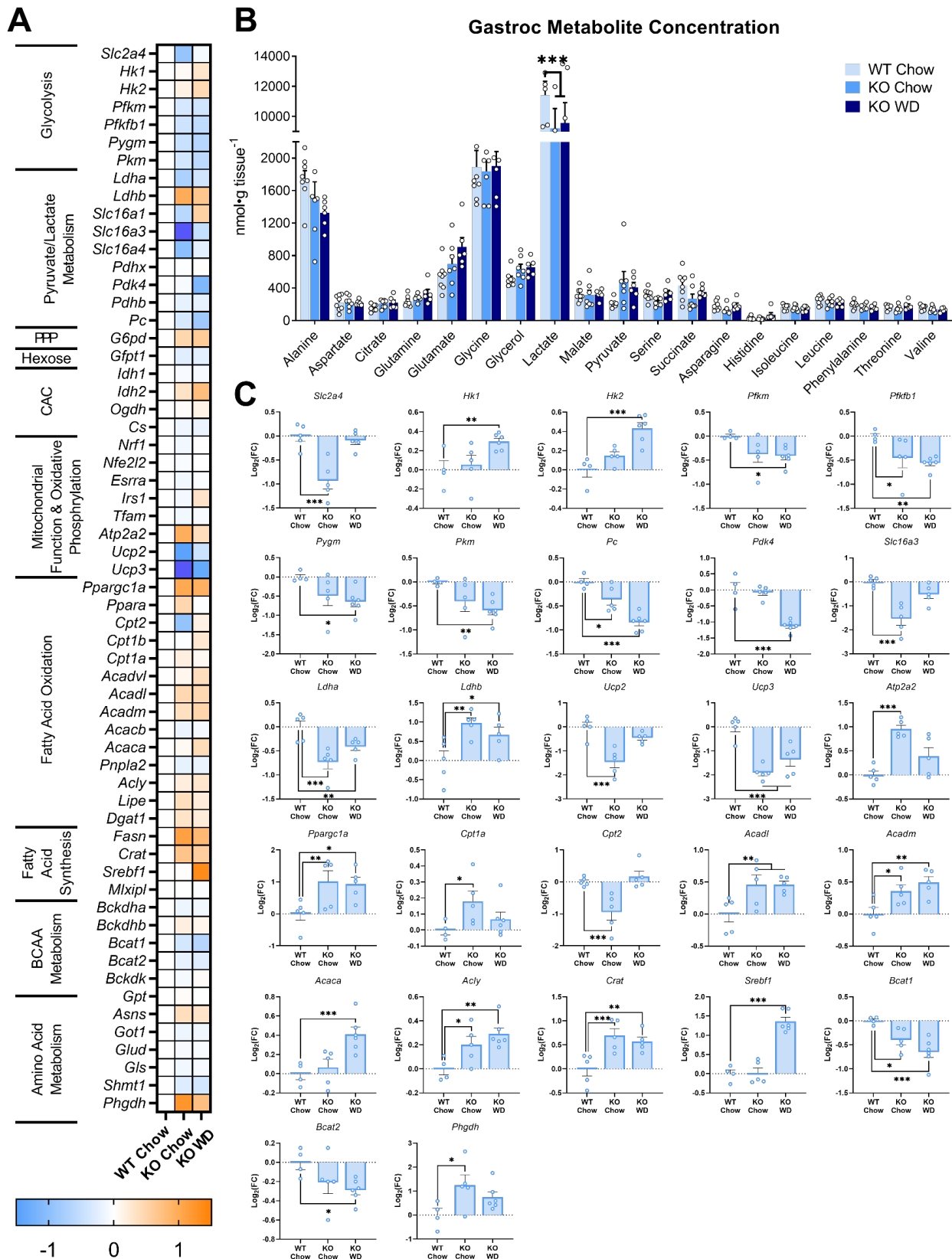
Plots show  $\log_2$  fold change in mRNA expression of significantly affected genes in KO Chow (n=7) and KO WD (n=6) livers relative to livers from WT chow (n=8) mice. (\*  $P < 0.10$ , \*\*  $P < 0.05$ , \*\*\*  $P < 0.01$ )



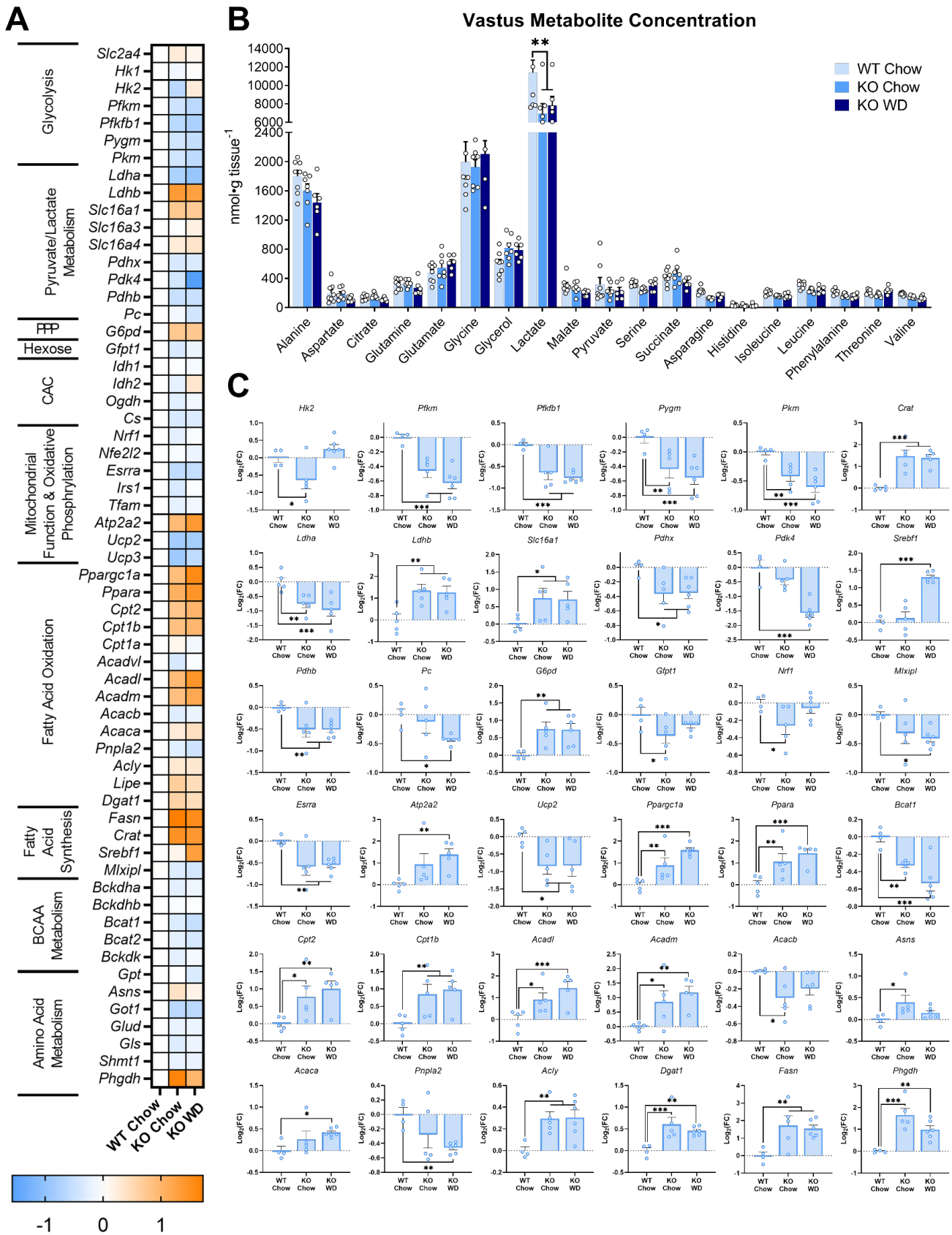
**Figure 6A.5: Genetic and metabolite changes in the cardiac muscle of obese mice**

(A) Heatmap of  $\text{Log}_2$  fold change in the mRNA level of genes regulating various metabolic pathways in KO Chow ( $n=7$ ) and KO WD ( $n=6$ ) hearts relative to hearts from WT chow ( $n=8$ ) mice. (B) Cardiac metabolite concentration in WT Chow ( $n=8$ ), KO Chow ( $n=7$ ) and KO WD mice ( $n=6$ ) (means $\pm$ SEM, \*\*\*  $P<0.01$ ). (C) Plots show  $\text{log}_2$  fold change in mRNA expression of significantly affected genes in the KO Chow ( $n=7$ ) and KO WD ( $n=6$ ) hearts relative to hearts from WT chow ( $n=8$ ) mice. (\*  $P<0.10$ , \*\*  $P<0.05$ , \*\*\*  $P<0.01$ )



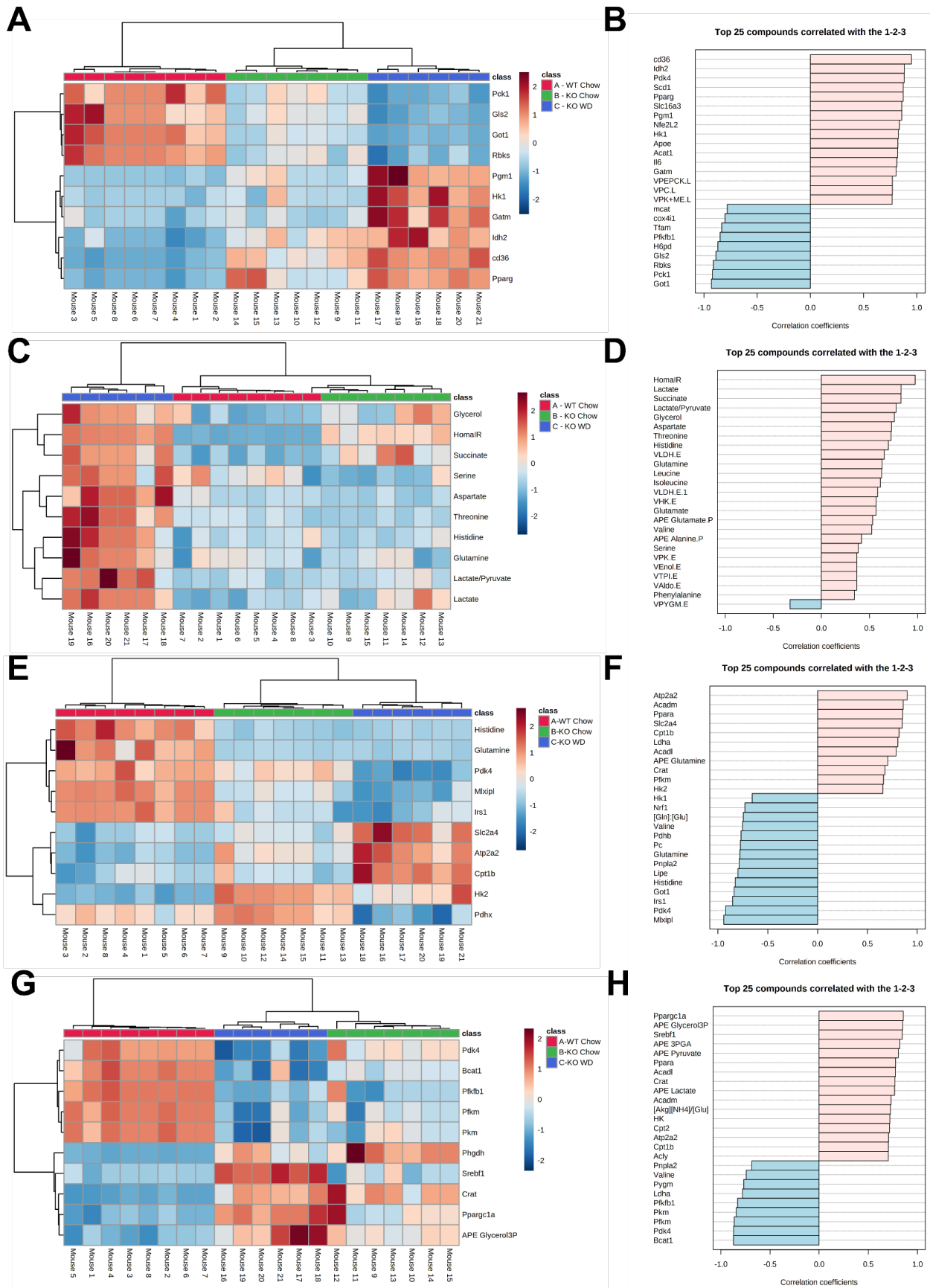


**Figure 6A.6: Genetic and metabolite changes in the gastrocnemius muscle of obese mice**  
 (A) Heatmap of Log<sub>2</sub> fold change in the mRNA level of genes regulating various metabolic pathways in the gastrocnemius muscle of KO Chow (n=7) and KO WD (n=6) relative to the WT chow (n=8) group. (B) Gastrocnemius metabolite concentration in WT Chow (n=8), KO Chow (n=7) and KO WD mice (n=6) (means±SEM, \*\*\*  $P < 0.01$ ). (C) Plots show log<sub>2</sub> fold change in mRNA expression of significantly affected genes in the gastrocnemius muscle of KO Chow (n=7) and KO WD (n=6) relative to the WT chow (n=8) group. (\*  $P < 0.10$ , \*\*  $P < 0.05$ , \*\*\*  $P < 0.01$ )



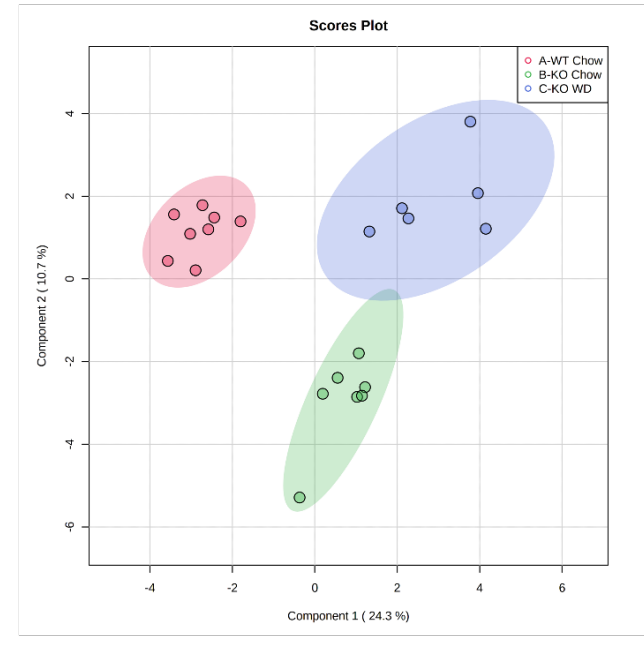
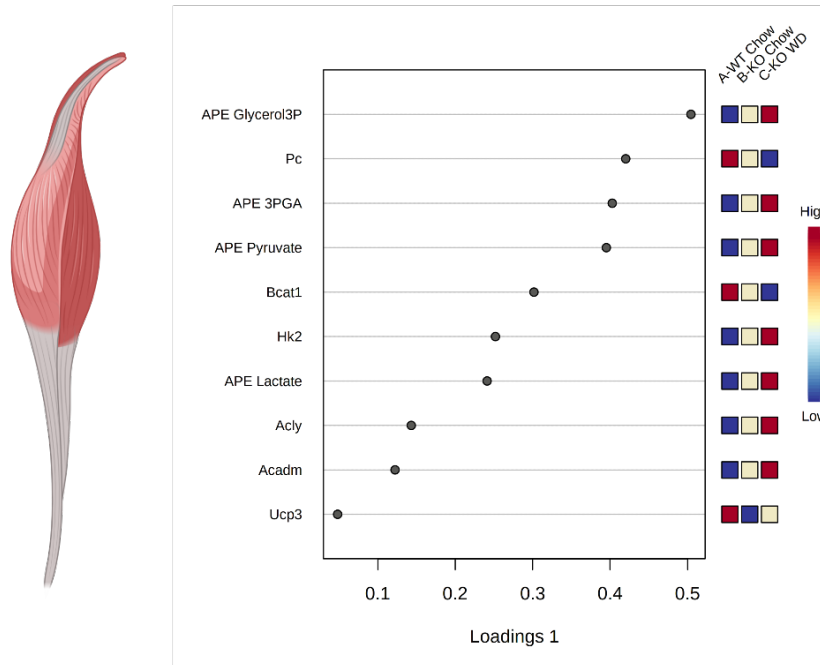
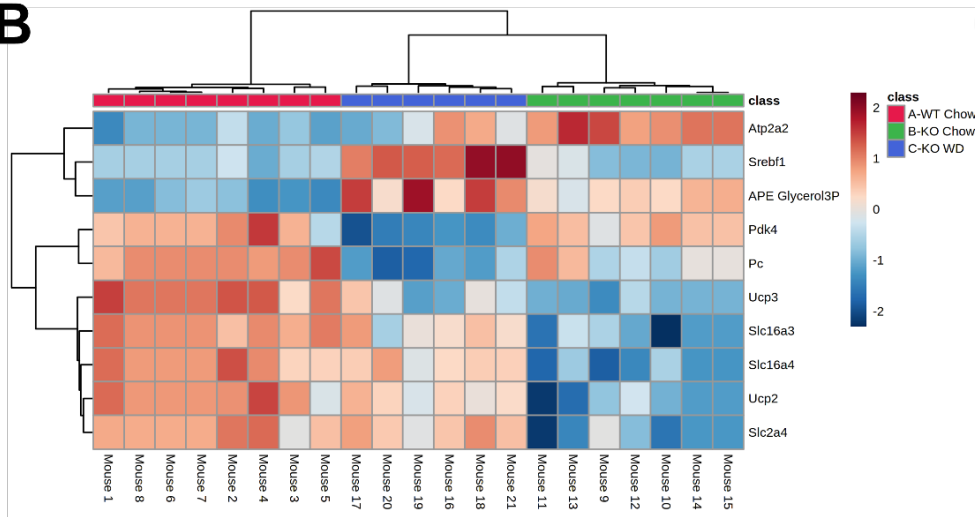
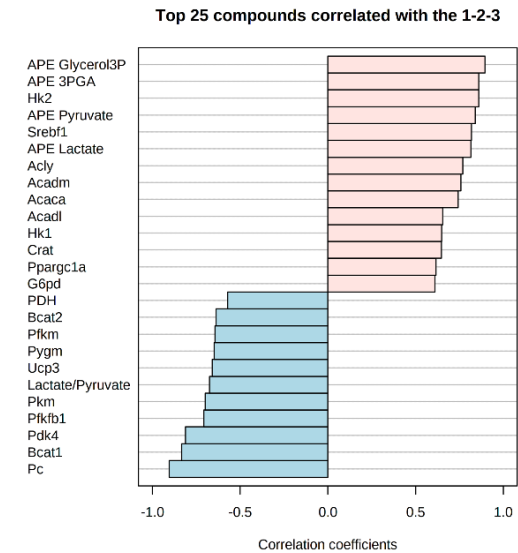
**Figure 6A.7: Genetic and metabolite changes in the vastus muscle of obese mice**

(A) Heatmap of  $\text{Log}_2$  fold change in the mRNA level of genes regulating various metabolic pathways in the vastus muscle of KO Chow ( $n=7$ ) and KO WD ( $n=6$ ) relative to the WT chow ( $n=8$ ) group. (B) Vastus metabolite concentration in WT Chow ( $n=8$ ), KO Chow ( $n=7$ ) and KO WD mice ( $n=6$ ) (means $\pm$ SEM, \*\*\*  $P<0.01$ ). (C) Plots show  $\text{log}_2$  fold change in mRNA expression of significantly affected genes in the vastus muscle of KO Chow ( $n=7$ ) and KO WD ( $n=6$ ) relative to the WT chow ( $n=8$ ) group. (\*  $P<0.10$ , \*\*  $P<0.05$ , \*\*\*  $P<0.01$ )



**Figure 6A.8: Supervised and unsupervised multivariate analysis confirms the robustness of tissue specific biomarkers identified using sPLS-DA analysis**

Factors identified in the (A-B) hepatic, (C-D) extrahepatic, (E-F) cardiac and (G-H) vastus compartment using hierarchical heatmap clustering and correlation analysis with disease progression as the variable of interest.

**A****B****C**

**Figure 6A.9: Multi-omics analysis reveals gastrocnemius specific biomarkers for obesity**

(A) Top 10 loadings that help separate the WT Chow (n=8), KO Chow (n=7) and KO WD mice (n=6) in sparse partial least square analysis score plots for the gastrocnemius tissue. Factors identified in the gastrocnemius compartment using (B) hierarchical heatmap clustering and (C) correlation analysis with disease progression as the variable of interest.

**Table 6A.1: Multi-organ metabolic reaction network for <sup>13</sup>C MFA.**

Network maps of liver, heart, gastrocnemius, and vastus metabolism track carbon atoms through model reactions. Metabolites used to regress fluxes in each compartments are shown in Table S2. Metabolites in the liver, extrahepatic, heart, gastrocnemius and vastus are denoted as “.L”, “.E”, “.H”, “.G”, and “.V” respectively. Unenriched sources and sinks are annotated as “.source” and “.sink”, respectively. [<sup>13</sup>C<sub>3</sub>]lactate is introduced into model reactions as “iso.uptake”.

<b>Flux</b>	<b>Hepatic Compartment</b>	<b>Reaction Network</b>
V <sub>EndoRa</sub>	G6P.L (ABCDEF) → Gluc.E (ABCDEF)	
V <sub>TPI.L</sub>	DHAP.L (ABC) ↔ GAP.L (ABC)	
V <sub>GK.L</sub>	Glycerol.L (ABC) → DHAP.L (ABC)	
V <sub>Enol.L</sub>	PEP.L (ABC) → BPG.L (ABC)	
V <sub>PEPCK.L</sub>	Oac.L (ABCD) → PEP.L (ABC) + CO <sub>2</sub> .L (D)	
V <sub>PK+ME.L</sub>	PEP.L (ABC) → Pyr.L (ABC)	
V <sub>PDH.L</sub>	Pyr.L (ABC) → CO <sub>2</sub> .L (A) + AcCoA.L (BC)	
V <sub>LDH.L</sub>	Lac.L (ABC) ↔ Pyr.L (ABC)	
V <sub>Lac.source</sub>	Lac.source (ABC) → Lac.L (ABC)	
V <sub>PC.L</sub>	Pyr.L (ABC) + CO <sub>2</sub> .L (D) → Oac.L (ABCD)	
V <sub>CS.L</sub>	Oac.L (ABCD) + AcCoA.L (EF) → Cit.L (DCBFEA)	
V <sub>ICDH.L</sub>	Cit.L (ABCDEF) ↔ α-kG.L (ABCDE) + CO <sub>2</sub> .L (F)	
V <sub>GDH.L</sub>	Glu.L (ABCDE) ↔ α-kG.L (ABCDE)	
V <sub>GLS.L</sub>	Glu.L (ABCDE) ↔ Gln.L (ABCDE)	
V <sub>GLN.L</sub>	Gln.E (ABCDE) ↔ Gln.L (ABCDE)	
V <sub>SDH.L</sub>	Suc.L (ABCD) ↔ Fum.L (ABCD)	
V <sub>FM.L</sub>	Fum.L (ABCD) ↔ Mal.L (ABCD)	
V <sub>MDH.L</sub>	Mal.L (ABCD) ↔ Oac.L (ABCD)	
V <sub>FatEntry.L</sub>	Fat.L (AB) → AcCoA.L (AB)	
V <sub>CO<sub>2</sub>.Bal1.L</sub>	BicarbL.source (A) → CO <sub>2</sub> .L (A)	
V <sub>CO<sub>2</sub>.Bal2.L</sub>	CO <sub>2</sub> .L (A) → BicarbL.sink (A)	
	<b>Extrahepatic Compartment</b>	
V <sub>Gln.source</sub>	Gln.source (ABCDE) → Gln.E (ABCDE)	
V <sub>Lac.Inf</sub>	Lac.isotope (ABC) → Lac.E (ABC)	
V <sub>LacTransport.E</sub>	Lac.E (ABC) → Lac.L (ABC)	
V <sub>HK.E</sub>	Gluc.E (ABCDEF) → F6P.E (ABCDEF)	
V <sub>PYGM.E</sub>	Glycogen.E (ABCDEF) → F6P.E (ABCDEF)	
V <sub>Aldo.E</sub>	F6P.E (ABCDEF) → GAP.E (CBA) + DHAP.E (DEF)	
V <sub>TPI.E</sub>	GAP.E (ABC) ↔ DHAP.E (ABC)	
V <sub>Enol.E</sub>	GAP.E (ABC) → PEP.E (ABC)	
V <sub>PK.E</sub>	PEP.E (ABC) → Pyr.E (ABC)	
V <sub>LDH.E</sub>	Pyr.E (ABC) ↔ Lac.E (ABC)	
V <sub>PyrOxid.E</sub>	Pyr.E (ABC) → CO <sub>2</sub> (A) + CO <sub>2</sub> (B) + CO <sub>2</sub> (C)	
	<b>Heart Compartment</b>	





$V_{HK.H}$	Gluc.H (ABCDEF) $\rightarrow$ G6P.H (ABCDEF)
$V_{PGL.H}$	G6P.H (ABCDEF) $\rightarrow$ F6P.H (ABCDEF)
$V_{ALDO.H}$	F6P.H (ABCDEF) $\rightarrow$ DHAP.H (CBA) + GAP.H (DEF)
$V_{G3PDH.H}$	G3P.H (ABC) $\leftrightarrow$ DHAP.H (ABC)
$V_{TPI.H}$	DHAP.H (ABC) $\leftrightarrow$ GAP.H (ABC)
$V_{GAPDH.H}$	GAP.H (ABC) $\rightarrow$ BPG.H (ABC)
$V_{Enol.H}$	BPG.H (ABC) $\rightarrow$ PEP.H (ABC)
$V_{PK.H}$	PEP.H (ABC) $\rightarrow$ Pyr.H (ABC)
$V_{LDH.H}$	Pyr.H (ABC) $\leftrightarrow$ Lac.H (ABC)
$V_{ALT.H}$	Pyr.H (ABC) $\leftrightarrow$ Ala.H (ABC)
$V_{PDH.H}$	Pyr.H (ABC) $\rightarrow$ AcCoA.H (BC) + CO <sub>2</sub> .H (A)
$V_{PC.H}$	Pyr.H (ABC) + CO <sub>2</sub> .H (D) $\rightarrow$ Oac.H (ABCD)
$V_{CS.H}$	Oac.H (ABCD) + AcCoA.H (EF) $\rightarrow$ Cit.H (DCBFEA)
$V_{ICDH.H}$	Cit.H (ABCDEF) $\rightarrow$ $\alpha$ -kg.H (ABCDE) + CO <sub>2</sub> .H (F)
$V_{\alpha KGDH.H}$	$\alpha$ -kg.H (ABCDE) $\rightarrow$ Suc.H (BCDE) + CO <sub>2</sub> .H (A)
$V_{SDH.H}$	Suc.H (ABCD) $\leftrightarrow$ Fum.H (ABCD)
$V_{FM.H}$	Fum.H (ABCD) $\leftrightarrow$ Mal.H (ABCD)
$V_{MDH.H}$	Mal.H (ABCD) $\leftrightarrow$ Oac.H (ABCD)
$V_{FatEntry.H}$	Fat.H (AB) $\rightarrow$ AcCoA.H (AB)
$V_{LacRelease.H}$	Lac.H $\rightarrow$ Lach.sink
$V_{PyrSource.H}$	Pyr.source (ABC) $\rightarrow$ Pyr.H (ABC)
$V_{OacSink.H}$	Oac.H $\rightarrow$ Asp.sink
$V_{CO2.Bal1.H}$	BicarbH.source (A) $\rightarrow$ CO <sub>2</sub> .H (A)
$V_{CO2.Bal2.H}$	CO <sub>2</sub> .H (A) $\rightarrow$ BicarbH.sink (A)
$V_{GlucUptake.H}$	0*Gluc.E (ABCDEF) $\rightarrow$ Gluc.H (ABCDEF)
$V_{LacUptake.H}$	0*Lac.E (ABC) $\rightarrow$ Lac.H (ABC)
$V_{AlaUptake.H}$	0*Pyr.E (ABC) $\rightarrow$ Ala.H (ABC)




















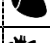












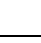








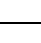
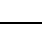










***Gastrocnemius Compartment***

$V_{HK.G}$	Gluc.G (ABCDEF) $\rightarrow$ G6P.G (ABCDEF)
$V_{PGL.G}$	G6P.G (ABCDEF) $\rightarrow$ F6P.G (ABCDEF)
$V_{PYGM.G}$	Glycogen.G (ABCDEF) $\rightarrow$ G6P.G (ABCDEF)
$V_{ALDO.G}$	F6P.G (ABCDEF) $\rightarrow$ DHAP.G (CBA) + GAP.G (DEF)
$V_{TPI.G}$	DHAP.G (ABC) $\leftrightarrow$ GAP.G (ABC)
$V_{GAPDH.G}$	GAP.G (ABC) $\rightarrow$ BPG.G (ABC)
$V_{Enol.G}$	BPG.G (ABC) $\rightarrow$ PEP.G (ABC)
$V_{PK.G}$	PEP.G (ABC) $\rightarrow$ Pyr.G (ABC)
$V_{LDH.G}$	Pyr.G (ABC) $\leftrightarrow$ Lac.G (ABC)
$V_{ALT.G}$	Pyr.G (ABC) $\leftrightarrow$ Ala.G (ABC)
$V_{PDH.G}$	Pyr.G (ABC) $\rightarrow$ AcCoA.G (BC) + CO <sub>2</sub> .G (A)
$V_{PC.G}$	Pyr.G (ABC) + CO <sub>2</sub> .G (D) $\rightarrow$ Oac.G (ABCD)
$V_{CS.G}$	Oac.G (ABCD) + AcCoA.G (EF) $\rightarrow$ Cit.G (DCBFEA)
$V_{ICDH.G}$	Cit.G (ABCDEF) $\rightarrow$ $\alpha$ -kg.G (ABCDE) + CO <sub>2</sub> .G (F)

$V_{\alpha\text{KGDH.G}}$	$\alpha\text{-kg.G (ABCDE)} \rightarrow \text{Suc.G (BCDE)} + \text{CO}_2\text{.G (A)}$
$V_{\text{SDH.G}}$	$\text{Suc.G (ABCD)} \leftrightarrow \text{Fum.G (ABCD)}$
$V_{\text{FM.G}}$	$\text{Fum.G (ABCD)} \leftrightarrow \text{Mal.G (ABCD)}$
$V_{\text{MDH.G}}$	$\text{Mal.G (ABCD)} \leftrightarrow \text{Oac.G (ABCD)}$
$V_{\text{ME.G}}$	$\text{Mal.G (ABCD)} \rightarrow \text{Pyr.G (ABC)} + \text{CO}_2\text{.G (D)}$
$V_{\text{FatEntry.G}}$	$\text{Fat.G (AB)} \rightarrow \text{AcCoA.G (AB)}$
$V_{\text{OacSink.G}}$	$\alpha\text{-kg.G} \rightarrow \text{Glu.sink}$
$V_{\text{LacRelease.G}}$	$\text{Lac.G} \rightarrow \text{Lac.sink}$
$V_{\text{PyrSource.G}}$	$\text{Pyr.source (ABC)} \rightarrow \text{Pyr.G (ABC)}$
$V_{\text{CO}_2\text{.Bal1.G}}$	$\text{BicarbG.source (A)} \rightarrow \text{CO}_2\text{.G (A)}$
$V_{\text{CO}_2\text{.Bal2.G}}$	$\text{CO}_2\text{.G (A)} \rightarrow \text{BicarbG.sink (A)}$
$V_{\text{GlucUptake.G}}$	$0*\text{Gluc.E (ABCDEF)} \rightarrow \text{Gluc.G (ABCDEF)}$
$V_{\text{LacUptake.G}}$	$0*\text{Lac.E (ABC)} \rightarrow \text{Lac.G (ABC)}$
$V_{\text{AlaUptake.G}}$	$0*\text{Pyr.E (ABC)} \rightarrow \text{Ala.G (ABC)}$
<b><i>Vastus Compartment</i></b>	
$V_{\text{HK.V}}$	$\text{Gluc.V (ABCDEF)} \rightarrow \text{G6P.V (ABCDEF)}$
$V_{\text{PGL.V}}$	$\text{G6P.V (ABCDEF)} \rightarrow \text{F6P.V (ABCDEF)}$
$V_{\text{PYGM.V}}$	$\text{Glycogen.V (ABCDEF)} \rightarrow \text{G6P.V (ABCDEF)}$
$V_{\text{ALDO.V}}$	$\text{F6P.V (ABCDEF)} \rightarrow \text{DHAP.V (CBA)} + \text{GAP.V (DEF)}$
$V_{\text{TPI.V}}$	$\text{DHAP.V (ABC)} \leftrightarrow \text{GAP.V (ABC)}$
$V_{\text{GAPDH.V}}$	$\text{GAP.V (ABC)} \rightarrow \text{BPG.V (ABC)}$
$V_{\text{Enol.V}}$	$\text{BPG.V (ABC)} \rightarrow \text{PEP.V (ABC)}$
$V_{\text{PK.V}}$	$\text{PEP.V (ABC)} \rightarrow \text{Pyr.V (ABC)}$
$V_{\text{LDH.V}}$	$\text{Pyr.V (ABC)} \leftrightarrow \text{Lac.V (ABC)}$
$V_{\text{ALT.V}}$	$\text{Pyr.V (ABC)} \leftrightarrow \text{Ala.V (ABC)}$
$V_{\text{PDH.V}}$	$\text{Pyr.V (ABC)} \rightarrow \text{AcCoA.V (BC)} + \text{CO}_2\text{.V (A)}$
$V_{\text{PC.V}}$	$\text{Pyr.V (ABC)} + \text{CO}_2\text{.V (D)} \rightarrow \text{Oac.V (ABCD)}$
$V_{\text{CS.V}}$	$\text{Oac.V (ABCD)} + \text{AcCoA.V (EF)} \rightarrow \text{Cit.V (DCBFEA)}$
$V_{\text{ICDH.V}}$	$\text{Cit.V (ABCDEF)} \rightarrow \alpha\text{-kg.V (ABCDE)} + \text{CO}_2\text{.V (F)}$
$V_{\alpha\text{KGDH.V}}$	$\alpha\text{-kg.V (ABCDE)} \rightarrow \text{Suc.V (BCDE)} + \text{CO}_2\text{.V (A)}$
$V_{\text{SDH.V}}$	$\text{Suc.V (ABCD)} \leftrightarrow \text{Fum.V (ABCD)}$
$V_{\text{FM.V}}$	$\text{Fum.V (ABCD)} \leftrightarrow \text{Mal.V (ABCD)}$
$V_{\text{MDH.V}}$	$\text{Mal.V (ABCD)} \leftrightarrow \text{Oac.V (ABCD)}$
$V_{\text{ME.V}}$	$\text{Mal.V (ABCD)} \rightarrow \text{Pyr.V (ABC)} + \text{CO}_2\text{.V (D)}$
$V_{\text{FatEntry.V}}$	$\text{Fat.V (AB)} \rightarrow \text{AcCoA.V (AB)}$
$V_{\text{OacSink.V}}$	$\alpha\text{-kg.V} \rightarrow \text{Glu.sink}$
$V_{\text{LacRelease.V}}$	$\text{Lac.V} \rightarrow \text{Lac.sink}$
$V_{\text{PyrSource.V}}$	$\text{Pyr.source (ABC)} \rightarrow \text{Pyr.V (ABC)}$
$V_{\text{CO}_2\text{.Bal1.V}}$	$\text{BicarbV.source (A)} \rightarrow \text{CO}_2\text{.V (A)}$
$V_{\text{CO}_2\text{.Bal2.V}}$	$\text{CO}_2\text{.V (A)} \rightarrow \text{BicarbV.sink (A)}$
$V_{\text{GlucUptake.V}}$	$0*\text{Gluc.E (ABCDEF)} \rightarrow \text{Gluc.V (ABCDEF)}$
$V_{\text{LacUptake.V}}$	$0*\text{Lac.E (ABC)} \rightarrow \text{Lac.V (ABC)}$

**Table 6A.2: GC-MS fragment ions of measured metabolites regressed using the multi-tissue metabolic model.**

Metabolite fragment ions measured using a GC-MS and integrated into the metabolic model to constrain fluxes in hepatic () , extrahepatic () , cardiac () and gastrocnemius/vastus skeletal muscle () compartments.

Metabolite	<i>m/z</i>	Derivative Formula	Carbons						Compartment			
			C1	C2	C3							
Alanine	260	C <sub>11</sub> H <sub>26</sub> O <sub>2</sub> NSi <sub>2</sub>	C1	C2	C3							
Alanine	232	C <sub>10</sub> H <sub>26</sub> ONSi <sub>2</sub>		C2	C3							
Aspartate	302	C <sub>14</sub> H <sub>32</sub> O <sub>2</sub> NSi <sub>2</sub>	C1	C2								
Aspartate	390	C <sub>17</sub> H <sub>40</sub> O <sub>3</sub> NSi <sub>3</sub>		C2	C3	C4						
Aspartate	418	C <sub>18</sub> H <sub>40</sub> O <sub>4</sub> NSi <sub>3</sub>	C1	C2	C3	C4						
Citrate	459	C <sub>20</sub> H <sub>39</sub> O <sub>6</sub> Si <sub>3</sub>	C1	C2	C3	C4	C5	C6				
Fumarate	287	C <sub>12</sub> H <sub>23</sub> O <sub>4</sub> Si <sub>2</sub>	C1	C2	C3	C4						
Glucose	370	C <sub>17</sub> H <sub>24</sub> O <sub>8</sub> N	C1	C2	C3	C4	C5					
Glucose	301	C <sub>14</sub> H <sub>21</sub> O <sub>7</sub>	C1	C2	C3	C4	C5	C6				
Glucose	284	C <sub>13</sub> H <sub>18</sub> O <sub>6</sub> N	C1	C2	C3	C4						
Glucose	259	C <sub>12</sub> H <sub>19</sub> O <sub>6</sub>				C4	C5	C6				
Glucose	173	C <sub>8</sub> H <sub>13</sub> O <sub>4</sub>					C5	C6				
Glucose	145	C <sub>6</sub> H <sub>11</sub> O <sub>3</sub> N	C1	C2								
Glutamate	432	C <sub>19</sub> H <sub>42</sub> O <sub>4</sub> NSi <sub>3</sub>		C2	C3	C4	C5					
Glutamate	330	C <sub>16</sub> H <sub>36</sub> O <sub>2</sub> NSi <sub>2</sub>	C1	C2	C3	C4	C5					
Glycerol-3-Phosphate	571	C <sub>20</sub> H <sub>51</sub> O <sub>6</sub> Si <sub>4</sub> P	C1	C2	C3							
Lactate	261	C <sub>11</sub> H <sub>25</sub> O <sub>3</sub> Si <sub>2</sub>	C1	C2	C3							
Lactate	233	C <sub>10</sub> H <sub>25</sub> O <sub>2</sub> Si <sub>2</sub>		C2	C3							
Malate	419	C <sub>18</sub> H <sub>39</sub> O <sub>5</sub> Si <sub>3</sub>	C1	C2	C3	C4						
Pyruvate	174	C <sub>6</sub> H <sub>12</sub> O <sub>3</sub> NSi	C1	C2	C3							
Urea	231	C <sub>13</sub> H <sub>32</sub> N <sub>2</sub> OSi <sub>2</sub>	C1									



## **7. INCA 2.0: a tool for integrated, dynamic modeling of NMR- and MS-based isotopomer measurements and rigorous metabolic flux analysis**

### **7.1 Abstract**

Metabolic flux analysis (MFA) combines experimental measurements and computational modeling to determine biochemical reaction rates in live biological systems. Advancements in analytical instrumentation, such as nuclear magnetic resonance (NMR) spectroscopy and mass spectrometry (MS), have facilitated chemical separation and quantification of isotopically enriched metabolites. However, no software packages currently exist that can integrate isotopomer measurements from both MS and NMR analytical platforms and have flexibility to estimate metabolic fluxes from either isotopic steady-state or dynamic labeling experiments. By applying physiologically relevant cardiac and hepatic metabolic models to assess NMR isotopomer measurements, we herein test and validate new modeling capabilities of our enhanced flux analysis software tool, INCA 2.0. We demonstrate that INCA 2.0 can simulate and regress steady-state  $^{13}\text{C}$  NMR datasets from perfused hearts with accuracy comparable to other established flux assessment tools. Furthermore, by simulating the infusion of three different  $^{13}\text{C}$  acetate tracers, we show that MFA based on dynamic  $^{13}\text{C}$  NMR measurements can more precisely resolve cardiac fluxes compared to isotopically steady-state flux analysis. Finally, we show that estimation of hepatic fluxes using combined  $^{13}\text{C}$  NMR and MS datasets improves the precision of estimated fluxes by up to 50%. Overall, our work here illustrates how the recently added NMR data modeling capabilities of INCA 2.0 can enable entirely new experimental designs that lead to improved flux resolution and can be applied to a wide range of biological systems and measurement time courses.

## 7.2 Introduction

Since their inception and implementation in the 1930s [323], stable isotope tracer studies have provided valuable insights for understanding the metabolic pathways underlying various diseases and disorders, as well as normal physiology. During this time, several metabolic models have been developed to translate isotope enrichment measurements into estimates of metabolic flux [29], [36], [40], [50], [51], [119], [324], [325]. Modern isotope labeling studies integrate numerous metabolite measurements, often enriched with multiple isotope tracers administered simultaneously or in parallel, to assess flux through a network of intersecting metabolic pathways [32], [65], [257], [326]. To fully decipher the flux information encoded in these complex isotope enrichment measurements, sophisticated mathematical models and computational approaches such as metabolic flux analysis (MFA) are typically required [18]. MFA is an integrated experimental and computational workflow that quantifies metabolic fluxes within living cells/tissues by employing models of biochemical reaction networks to regress mass spectrometry (MS) and/or nuclear magnetic resonance (NMR) spectroscopy measurements of isotopic enrichment [18].

NMR spectroscopy and gas/liquid chromatography conjugated to mass spectrometry (GC- or LC-MS) have different data outputs that provide distinct information pertaining to metabolite enrichment patterns. For example,  $^{13}\text{C}$  NMR provides two types of information: (i) relative signal intensity from different  $^{13}\text{C}$ -enriched carbon positions in a molecule and (ii) the relative intensity of the various multiplets within a resonance signal (due to interaction between adjacent  $^{13}\text{C}$  nuclei, also known as  $^{13}\text{C}$ - $^{13}\text{C}$  coupling) [50]. Other modalities such as  $^1\text{H}$ - $^{13}\text{C}$  NMR can be used to quantify the fractional enrichment of  $^{13}\text{C}$  atoms bound to hydrogen at specific molecular positions [327]. Together, this information can be used to determine the position-specific  $^{13}\text{C}$  labelling in a measured metabolite, even when the isotopic enrichment is as low as 0.1%. However,  $^{13}\text{C}$  NMR spectroscopy has two major limitations when applied to measure stable isotope enrichment. First, it does not directly determine the unenriched (i.e., M+0) fraction of the metabolite pool. Second, it has limited sensitivity to detect low-abundance metabolites, e.g., present at

lower than  $\mu\text{mol}$  amounts [34]. This limitation typically restricts the application of  $^{13}\text{C}$  NMR to measurements of highly abundant intracellular metabolites, such as glutamate and aspartate. Conversely, MS platforms such as GC-MS, LC-MS and tandem MS/MS systems have significantly higher sensitivity ( $\sim\text{pmol}$  to  $\text{nmol}$  range) and can precisely determine the total unenriched and enriched fractions of a metabolite pool [34]. However, MS-based systems do not directly provide positional enrichment information unless the metabolite is subjected to extensive chemical degradation or source/collision-induced fragmentation. Instead, MS systems output the relative abundance of chemical species that differ in the number of heavy atoms incorporated (i.e., M+0, M+1, M+2, etc.), which can then be used to determine the mass isotopomer distribution (MID) of a given metabolite [35]. Currently, no analytical platform exists that combines the high sensitivity of MS with the extensive positional enrichment information obtainable from NMR spectroscopy.

Although we cannot directly combine the features of NMR and MS into a single measurement, we can leverage the unique strengths of the two modalities by applying specialized MFA software to estimate metabolic fluxes from integrated MS and NMR datasets. Unfortunately, the majority of flux estimation software packages either support only MS datasets, such as INCA [69], METRAN [20], [70] and OpenFLUX2 [71], or only NMR datasets, such as tcaSIM [76], tcaCALC, and NMR2FLUX [328]. A few MFA tools like `influx_s` [329] and `13CFLUX2` [78] can model isotopic measurements from both analytical platforms, but these software packages can only describe measurements at isotopic equilibrium. Currently, there is not a publicly available software tool that can model integrated NMR and MS datasets obtained from either steady-state or dynamic labeling experiments.

With analytical advancements in both NMR spectroscopy and MS, there is an increasing impetus for quantifying metabolic fluxes to better understand metabolism in systems ranging from cell cultures to *ex vivo* tissues/organs to intact multicellular organisms. Prior studies have individually applied NMR or MS to characterize *in vivo* fluxes of hepatic [29], [48], [101], cardiac [50], [330], and circulatory metabolites

[49], [164], [166], [167]. Additionally, studies assessing microbial [57], [59], [331] and plant [332], [333] metabolism have often involved either NMR- or MS-based analysis of isotope enrichment. To fully harness the advantages of both NMR and MS measurements and to design more sophisticated MFA experiments, we extended our previously developed metabolic modeling software, INCA [69], to enable tracer simulations and flux estimation using combined NMR and MS datasets. Prior versions of INCA were capable of modeling dynamic or steady-state labeling measurements obtained with MS, but not NMR. Our updated software package, INCA 2.0, was compared and validated against current steady-state NMR tracer simulation and flux estimation packages using a perfused heart model. Furthermore, we demonstrate that improved cardiac flux resolution is obtainable from dynamic, rather than steady-state,  $^{13}\text{C}$  NMR datasets. Lastly, we show that combining NMR and GC-MS datasets enables more accurate quantification of hepatic fluxes *in vivo*. Overall, these test cases demonstrate how INCA 2.0 can leverage the data complexity and richness available from different analytical platforms to enhance the precision and flexibility of MFA studies and enable innovative applications of stable isotopes in metabolism research. .

## **7.3 Methods**

### **7.3.1 Animals Care**

Studies involving animals were carried out using protocols approved by the Institutional Animal Care and Use Committees of the University of Florida and University of Texas Southwestern Medical Center [65], [330]. Male C57BL6/J mice and Sprague Dawley rats were maintained on 12-hr/12-hr dark/light cycles, with unrestricted access to standard chow and water unless otherwise noted.

### **7.3.2 Heart perfusions and metabolite extractions**

Heart perfusions and metabolite extractions were performed as previously outlined in Ragavan et al (2017). Briefly, hearts were excised from the thoracic cavity of mice after euthanasia. The cannulated hearts were then perfused with Krebs-Henseleit buffer,  $[1,6-^{13}\text{C}_2]$ glucose,  $[\text{U}-^{13}\text{C}]$  free fatty acids (FAs), and insulin.

After 30 minutes of perfusion, hearts were immediately freeze-clamped and stored at  $-80^{\circ}\text{C}$  for metabolite extraction. Metabolites in the heart were isolated using perchloric acid (PCA) extraction. Powdered heart tissue was mixed with ice-cold PCA, vortexed and then centrifuged. The supernatant was decanted, neutralized and centrifuged to remove insoluble potassium perchlorate and finally lyophilized. Salt-free NMR samples were prepared by dissolving the lyophilized powder in deionized water, centrifuged to remove excess salt and lyophilized again. A total of 9 mouse hearts were perfused, and metabolites were extracted for flux and isotopomer analysis.

### 7.3.3 In vivo stable isotope infusions and sample collection

Stable isotope infusions were carried out as previously described by Deja et al. (2020). Briefly, rats were surgically catharized via the jugular vein and allowed to recover for 4 days. Experiments were carried out in 24-h fasted rats. Prior to tracer infusion, rats were intraperitoneally injected with  $^2\text{H}_2\text{O}$  solution. For the tracer infusions, rats were primed for 10 minutes with  $[\text{U-}^{13}\text{C}_3]\text{propionate}$  and  $[3,4\text{-}^{13}\text{C}_2]\text{glucose}$  followed by an 80-min continuous infusion. At the end of the infusion, rats were anesthetized using isoflurane and blood was collected by cardiac puncture into EDTA-coated tubes. Plasma was separated by centrifugation, aliquoted and stored at  $-80^{\circ}\text{C}$  for further analysis.

### 7.3.3 NMR and GC-MS analysis of plasma glucose

NMR and GC-MS data from *in vivo* isotope infusions were acquired as detailed in Deja et al. (2020). For NMR analysis, plasma glucose was converted to monoacetone glucose (MAG) using a previously described procedure [65], [99], [227].  $^2\text{H}$  and  $^{13}\text{C}$  NMR spectra were recorded using a 14.1-T Varian Inova spectrometer followed by quantification of resonance areas by ACD NMR Processor software. For GC-MS analysis, plasma glucose was extracted and derivatized according to protocols described elsewhere [41]. GC-MS data was collected using an Agilent 7890A GC paired with an Agilent 5975-C mass spectrometer.

Derivatized glucose samples were analyzed using previously defined GC-MS settings [172]. Deuterated body water enrichment was measured as previously described [51].

### **7.3.4 NMR analysis of cardiac tissue extracts**

NMR spectra of tissue extracts were acquired as previously described [330]. Briefly, spectra were measured using a 14.1-T NMR magnet equipped with either a CP-DUL cryoprobe (Bruker Biospin, Billerica, MA) or a home-built superconducting (HTS) probe. Samples were prepared by dissolving the lyophilized powder in  $^2\text{H}_2\text{O}$ -containing sodium phosphate buffer and EDTA. An internal standard (DSS-D6 and  $\text{NaN}_3$  in  $^2\text{H}_2\text{O}$ ) was spiked into the solution. Total sample volumes were either 200  $\mu\text{L}$  (for CP-DUL probe) or 50  $\mu\text{L}$  (for HTS probe).  $^1\text{H}$  spectra and  $^{13}\text{C}$  spectra were then measured with a spectral width of 12 ppm and 240 ppm, respectively. Lastly, ACD NMR Processor was used to extract relative peak areas for glutamate.

### **7.3.5 Tracer simulation and flux estimation using tcaSIM/tcaCALC**

Previously developed NMR software packages, tcaSIM and tcaCALC, were obtained from the National Center for In Vivo Metabolism at the University of Texas-Southwestern. An NMR isotopomer simulation software, tcaSIM, solves numerical equations to predict the steady-state NMR isotopic enrichments of a pre-defined set of central carbon metabolites after  $^{13}\text{C}$  isotope administration [50], [334]. We simulated NMR isotopomer abundances using the MATLAB-based version of tcaSIM [76]. The built-in metabolic network model used by tcaSIM is shown in Fig. 7.1A, and Table 7A.1 shows the selected metabolic parameters used to simulate cardiac isotopomer data. Resonance areas of  $^{13}\text{C}$  glutamate spectra obtained from perfused hearts were used as inputs to the same metabolic model (Fig. 7.1A) and regressed numerically to estimate fluxes using the MS-DOS version of tcaCALC. Complementary to tcaSIM, tcaCALC solves the inverse problem of iteratively determining the metabolic parameters given a set of fractional enrichments and  $^{13}\text{C}$  NMR multiplets [50], [335], [336].

### 7.3.8 EMU modeling of NMR isotopomers in INCA

The INCA software tool was upgraded with capabilities to model NMR-based isotope enrichment measurements as outputs of tracer simulations or inputs of flux estimations [69]. A new version of the software, INCA 2.0, was developed to simulate isotopomer and cumomer fractions in addition to MS-based MID measurements. When properly normalized, these fractions can be used to calculate  $^{13}\text{C}$  NMR multiplet ratios,  $^2\text{H}$  NMR spectra, or  $^1\text{H}$  NMR fractional enrichments. As first described by Antoniewicz et al. (2007), INCA uses linear transformations of EMU (elementary metabolite unit) mass isotopomer abundances to simulate NMR measurements. For example, the C2 isotopomer fractions of glutamate (Glu) were calculated from the transformation:

$$\begin{bmatrix} Glu_{010xx} \\ Glu_{110xx} \\ Glu_{011xx} \\ Glu_{111xx} \end{bmatrix} = \begin{bmatrix} 1 & 1 & 1 & 1 \\ 0 & 0 & 1 & 1 \\ 0 & 1 & 0 & 1 \\ 0 & 0 & 0 & 1 \end{bmatrix}^{-1} \begin{bmatrix} Glu_2^{M+1} \\ Glu_{12}^{M+2} \\ Glu_{23}^{M+2} \\ Glu_{123}^{M+3} \end{bmatrix}$$

where  $Glu_2^{M+1}$  is the M+1 abundance of the EMU comprising C2 of glutamate,  $Glu_{12}^{M+2}$  is the M+2 abundance of the EMU comprising C1 and C2,  $Glu_{23}^{M+2}$  is the M+2 abundance of the EMU comprising C2 and C3, and  $Glu_{123}^{M+3}$  is the M+3 abundance of the EMU comprising C1, C2, and C3. Normalizing the isotopomer fractions by their sum provides a prediction of glutamate C2 isotopomer ratios that are measurable by  $^{13}\text{C}$  NMR:

$$\begin{bmatrix} S \\ D12 \\ D23 \\ Q \end{bmatrix} = \begin{bmatrix} Glu_{010xx} \\ Glu_{110xx} \\ Glu_{011xx} \\ Glu_{111xx} \end{bmatrix} (Glu_{010xx} + Glu_{110xx} + Glu_{011xx} + Glu_{111xx})^{-1}$$

INCA users can specify any combination of isotopomer measurements in order to model NMR fine spectra for tertiary carbon atoms or other long-range  $^{13}\text{C}$ - $^{13}\text{C}$  couplings.

The output signals of  $^1\text{H}$ - $^{13}\text{C}$  NMR and  $^2\text{H}$  NMR are proportional to the fractional enrichments of  $^{13}\text{C}$  and  $^2\text{H}$ , respectively, at each atom position monitored. Consequently, these measurements are readily expressed in terms of cumomers, rather than isotopomers. Since the heaviest cumomer fraction of a selected set of  $n$  labeled atoms is equivalent to the  $M+n$  abundance of the corresponding EMU, it is straightforward to relate cumomer fractions to EMU abundances. For example,  $^2\text{H}$  NMR spectra of glucose (Glc) were calculated from the transformation:

$$\begin{bmatrix} H1 \\ H2 \\ H3 \\ H4 \\ H5 \\ H6R \\ H6S \end{bmatrix} = \begin{bmatrix} Glc_{H1}^{M+1} \\ Glc_{H2}^{M+1} \\ Glc_{H3}^{M+1} \\ Glc_{H4}^{M+1} \\ Glc_{H5}^{M+1} \\ Glc_{H6R}^{M+1} \\ Glc_{H6S}^{M+1} \end{bmatrix} \left( Glc_{H1}^{M+1} + Glc_{H2}^{M+1} + Glc_{H3}^{M+1} + Glc_{H4}^{M+1} + Glc_{H5}^{M+1} + Glc_{H6R}^{M+1} + Glc_{H6S}^{M+1} \right)^{-1}$$

where  $Glc_{H_j}^{M+1}$  represents the  $M+1$  abundance of the EMU comprising the  $j$ -th hydrogen atom of glucose. Note that the  $^2\text{H}$  NMR signals are normalized such that the measurement is represented by a set of cumomer ratios. In contrast,  $^1\text{H}$ - $^{13}\text{C}$  NMR provides fractional enrichment measurements that can be modeled directly as cumomer fractions (i.e., without normalization) as shown below for the C2, C3, and C4 positions of glutamate:

$$\begin{bmatrix} Glu(2) \\ Glu(3) \\ Glu(4) \end{bmatrix} = \begin{bmatrix} Glu_2^{M+1} \\ Glu_3^{M+1} \\ Glu_4^{M+1} \end{bmatrix}$$

where  $Glu_j^{M+1}$  represents the  $M+1$  abundance of the EMU comprising the  $j$ -th carbon atom of glutamate.

### 7.3.7 Metabolic flux analysis (MFA)

MFA was performed by minimizing the sum of squared residuals (SSR) between model-simulated and experimental metabolite labeling measurements. Cardiac glutamate and plasma glucose labeling were



provided as measurements into INCA for perfused hearts and *in vivo* infusion studies, respectively. The error in these measurements was set to either the root-mean square error of unenriched control samples or the standard error of measurement in biological and technical replicates, whichever was greater. Best-fit metabolic flux solutions were determined for each experiment by least-squares regression of the experimental measurements to the isotopomer network model. To ensure that a global solution was obtained, flux estimations were repeated a minimum of 50 times from randomized initial guesses. A chi-square test was used to assess goodness-of-fit, and a sensitivity analysis was performed to determine 95% confidence intervals associated with the calculated flux values.

The complete metabolic network and the carbon transitions used for cardiac metabolism can be found in Table S2. Metabolic equations were constructed from classical biochemical reactions and previously defined networks [50], [153]. For dynamic cardiac tracer simulations, pool size measurements of glycolytic and citric acid cycle metabolites (Table S4) were determined as previously described [330] and from classical literature [35], [337]. Previously published liver metabolic models [29], [65] were used to characterize *in vivo* glucose production, details of which can be found in Deja et. al (2020).

## 7.4 Results

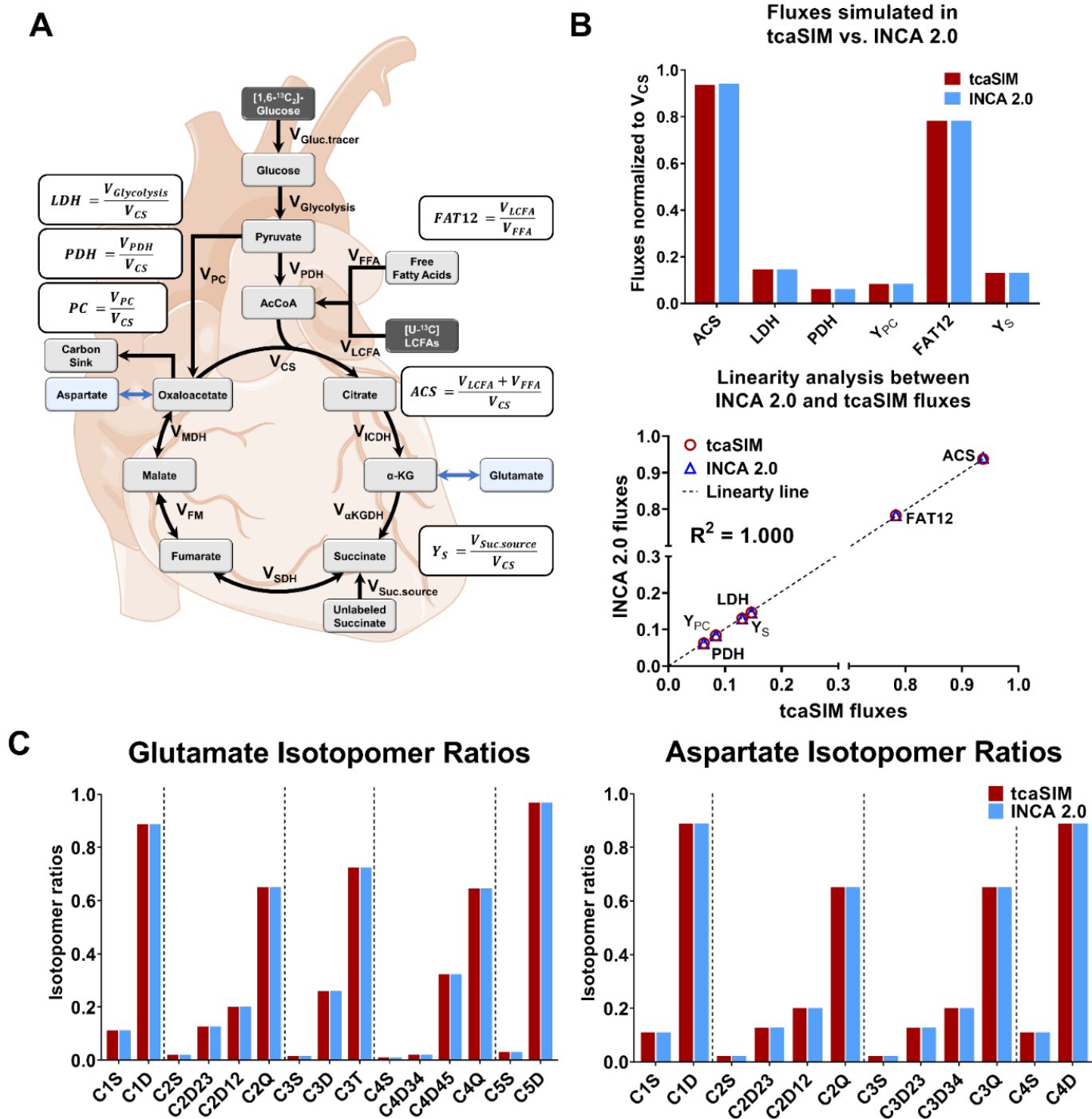
### 7.4.1 INCA 2.0 tracer simulations predict $^{13}\text{C}$ NMR isotopomer ratios consistent with tcaSIM

INCA was previously developed for analysis of MS datasets, but the software has been recently adapted to simulate  $^{13}\text{C}$  NMR multiplet ratios. To test the accuracy of these newly added NMR prediction capabilities, we evaluated INCA against a widely used NMR isotopomer simulation software, tcaSIM. Metabolic parameters in tcaSIM were set to resemble those previously reported in literature (Table 7A.1) [15], [153]. A metabolic model representing heart muscle was constructed within INCA 2.0 (Fig. 7.1A, Table 7A.2, also see *Methods*) and flux values were adjusted to match the metabolic parameters of tcaSIM (Fig. 7.1B, Table 7A.1, 7A.3). Isotopomer ratios were simulated in INCA by setting the citrate synthase flux ( $V_{\text{CS}}$ ) to

100, and formulae were derived to convert the INCA relative flux values to metabolic parameters required by tcaSIM (Fig. 7.1A). Comparison of fluxes simulated in INCA to metabolic parameters set in tcaSIM confirmed that the model and flux values entered in each program were equivalent (Fig. 7.1B,  $R^2 = 1.000$ ). Next, using these identical flux values in both software packages, we simulated all one-bond  $^{13}\text{C}$  NMR isotopomer ratios for glutamate, aspartate and alanine. INCA 2.0 was able to exactly replicate the isotopomer ratios generated by tcaSIM, accurate to 4 decimal places (Fig. 7.1C, 7A.1, Table 7A.S4). These results show that INCA 2.0 can simulate  $^{13}\text{C}$  NMR multiplet ratios that are consistent with the established NMR data modeling program tcaSIM. Unlike tcaSIM, however, the INCA 2.0 metabolic model is fully customizable by the user and can simulate the labeling of any metabolite present in the user-specified reaction network.

#### **7.4.2 Regression of $^{13}\text{C}$ NMR isotopomer ratios in INCA 2.0 estimates cardiac fluxes consistent with tcaCALC**

To verify whether INCA 2.0 can accurately regress NMR datasets to estimate fluxes, we regressed experimental  $^{13}\text{C}$  NMR data from perfused mouse hearts to our previously described cardiac metabolic network (Fig. 7.1A, Table 7A.2). The tcaCALC program, a flux estimation software package widely adopted by the metabolism community, was used to compare flux estimation results with those determined by INCA 2.0. Steady state  $^{13}\text{C}$  NMR isotopomer data were acquired from PCA extracts of perfused hearts incubated in  $[1,6-^{13}\text{C}_2]\text{glucose}$  and  $[\text{U-}^{13}\text{C}_2]\text{LCFA}$ . Glutamate isotopomer ratios were obtained by integration and extraction of relative peak areas from  $^{13}\text{C}$  NMR spectra (see *Methods* for details). These ratios were then provided as measurement inputs to the metabolic network model (Fig. 7.1A), solved numerically using tcaCALC and also regressed in INCA 2.0. Relative flux values from INCA 2.0 were consistent with those estimated by tcaCALC (Fig. 7.2A). Linear regression analysis showed that the regression coefficient ( $R^2$ ) between the two sets of fluxes was 0.9998 (Fig. 7.2B). To test the goodness-of-fit of the solutions obtained from each software package, we compared the model-predicted glutamate



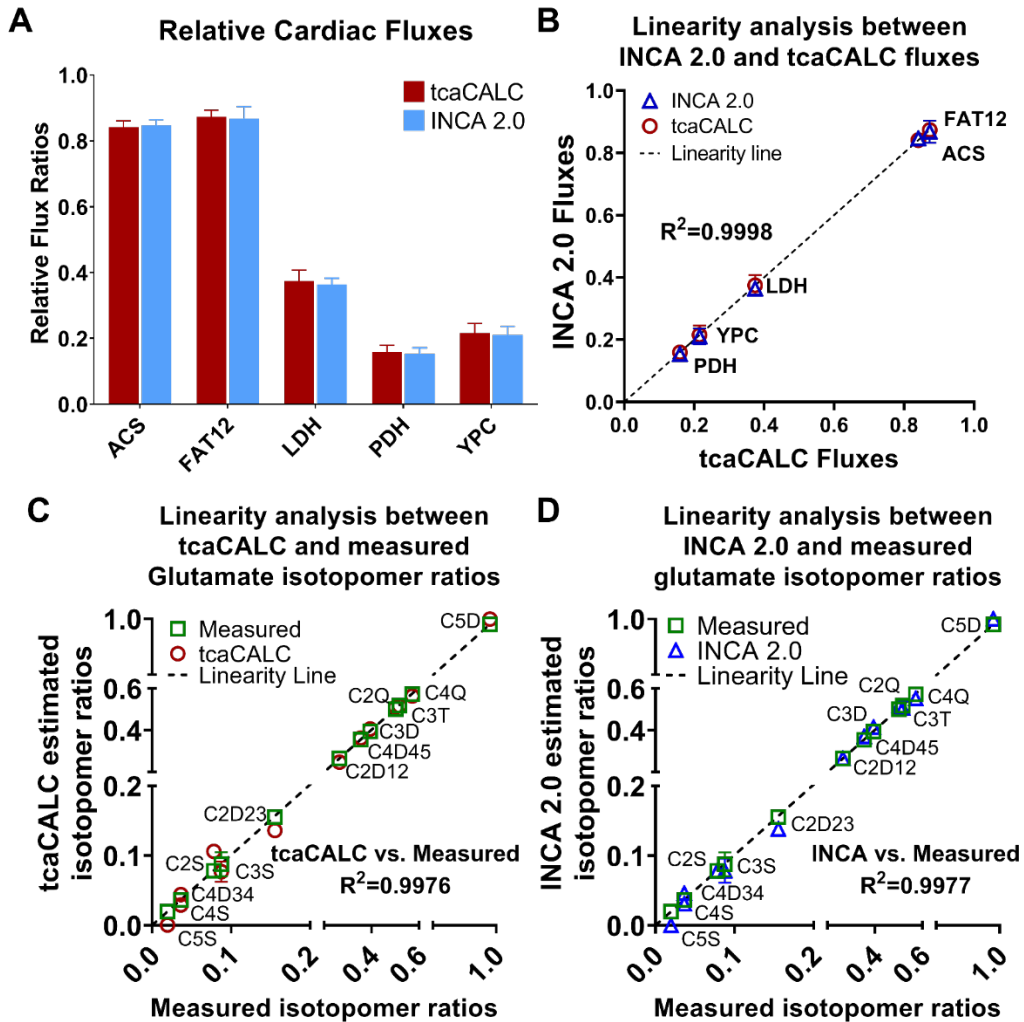
**Figure 7.1 Simulation of  $^{13}\text{C}$  NMR isotopomer ratios using tcaSIM and INCA 2.0**

**A.** Flux map shows the cardiac pathway modeled in INCA and the corresponding metabolic parameters used in tcaSIM

**B.** Comparison of flux parameters fixed in tcaSIM and INCA 2.0. Fluxes set in INCA 2.0 were converted to flux ratios using the formulae shown in Fig. 1A. Linear regression between INCA 2.0 and tcaSIM fluxes computed an ideal coefficient of determination ( $R^2 = 1.000$ )

**C.** tcaSIM and INCA 2.0 predict identical  $^{13}\text{C}$  NMR isotopomer ratios for glutamate and aspartate using an equivalent set of flux parameters. Each set of multiplet ratios is sum-normalized to 1

isotopomers to the experimentally measured values (Fig. 7.2C-D, Fig. 7A.2). The experimentally measured glutamate isotopomers show similar levels of agreement with model-predicted values produced by tcaCALC (Fig. 7.2C,  $R^2=0.9976$ ) and INCA 2.0 (Fig. 7.2D,  $R^2=0.9977$ ). Unlike tcaCALC, which does not report the best-fit SSR value, INCA 2.0 confirms an acceptable fit to the data based on an average SSR of  $3.7\pm 1.1$ . (The expected 95% confidence range is 0–5.0.)



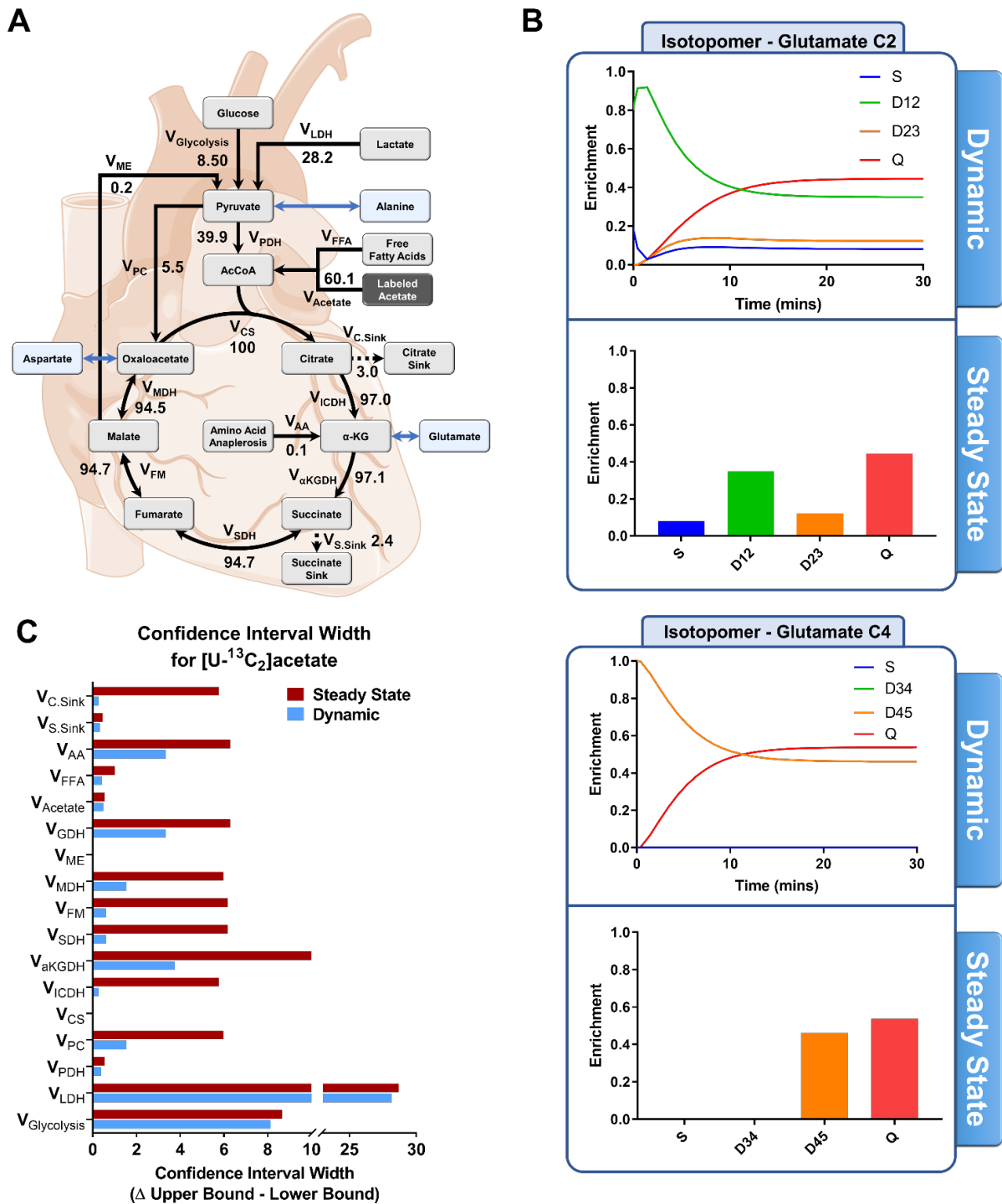
**Figure 7.2: Regression of cardiac fluxes using glutamate isotopomers in tcaCALC and INCA 2.0 shows good agreement when fitting data from [1,6- $^{13}C_2$ ]glucose and [U- $^{13}C$ ]LCFA tracers**

- A. Relative cardiac fluxes estimated using tcaCALC and INCA 2.0 (n=9, means  $\pm$  SEM)
- B. Linearity analysis of cardiac fluxes estimated in INCA 2.0 versus tcaCALC (n=9, means  $\pm$  SEM)
- C. Linearity Analysis of glutamate isotopomer ratios estimated by tcaCALC against measured values obtained from NMR spectra (n=9, means  $\pm$  SEM)
- D. Linearity Analysis of glutamate isotopomer ratios estimated by INCA 2.0 against measured values obtained from NMR spectra (n=9, means  $\pm$  SEM)

Overall, these results indicate that INCA can precisely regress  $^{13}\text{C}$  NMR datasets to estimate fluxes consistent with tcaCALC while providing statistical tests to verify the goodness-of-fit, a feature that is currently lacking in tcaCALC.

### 7.4.3 Flux estimation using dynamic $^{13}\text{C}$ NMR datasets improves cardiac flux precision

One of the unique features of INCA 2.0 is the capability to simulate dynamic isotopomer measurements and regress metabolic fluxes from non-steady-state labeling data using isotopically nonstationary MFA (INST-MFA). To determine whether dynamic NMR isotopomer measurements can improve the precision of flux estimates relative to steady-state measurements, we simulated non-steady state  $^{13}\text{C}$  NMR isotopomer ratios with INCA 2.0 by setting cardiac fluxes to values reported in literature [15], [153]. Since dynamic labeling also depends on the abundance of intermediate metabolites, estimates of metabolite pool sizes were matched with those measured in myocardial cells (Table 7A.5) [330]. Three different  $^{13}\text{C}$  isotopic tracers ([1- $^{13}\text{C}$ ]acetate, [2- $^{13}\text{C}$ ]acetate and [U- $^{13}\text{C}_2$ ]acetate) were simulated under isotopically steady-state and dynamic conditions. Previous studies suggest that  $^{13}\text{C}$ -acetate labelling experiments reach steady state within 30 minutes of heart perfusion [35]. Therefore, dynamic simulations were run from 0 to 30 minutes with a maximum step size of 1 min. Dynamic simulations of [U- $^{13}\text{C}_2$ ]acetate labeling, for example, show that the D12 doublet initially dominates the C2 resonance of glutamate but is partially supplanted by the quartet (Q) signal over time (Fig. 7.3B). Similarly, we observed a gradually decreasing D45 doublet and increasing quartet signal for the C4 isotopomers of glutamate (Fig. 7.3B). This pattern emerged because acetate labelling was initially present on the fourth and fifth carbons of  $\alpha$ -KG, forming a strong D45 doublet. However, as labelled carbon circulated through multiple rounds of the TCA cycle, the symmetry of succinate and re-entry of carbon through oxaloacetate led to the re-distribution of  $^{13}\text{C}$  labelling into other carbon positions of  $\alpha$ -KG, eventually reaching steady state within 30 min (Fig. 7.3B, 7A.3, 7A.8, also see *Supplementary Results*). Note that contributions from natural  $^{13}\text{C}$  abundance were not included in these simulations, although this option can be selected by users when modeling NMR data in INCA 2.0.



**Figure 7.3: INST-MFA of dynamic  $^{13}C$  NMR measurements provides more precise estimation of cardiac fluxes**

- A.** Flux map shows the cardiac fluxes used in INCA 2.0 to simulate steady-state and dynamic isotopomers of glutamate, aspartate and alanine
- B.** Glutamate C2 and C4 isotopomers simulated at steady state and dynamic time points using the flux solution shown in Fig. 7.3A
- C.** Comparison of confidence interval widths from flux solutions obtained using steady-state versus dynamic measurements

Next, using these simulated enrichments, we regressed fluxes and performed parameter continuation to determine 95% confidence intervals for fluxes determined from each metabolic tracer using steady state or transient isotopomer measurements. To ensure a fair comparison, we added an equal number of replicate measurements for the steady state dataset to match the 30 time points simulated for the dynamic dataset. Our results show substantially higher precision (i.e., narrower 95% confidence intervals) for fluxes determined from the dynamic dataset when using [U-<sup>13</sup>C<sub>2</sub>] or [2-<sup>13</sup>C]acetate (Fig. 7.3C, 7A.9). The most striking improvements in the TCA cycle, where formation of complex labeling patterns in glutamate, aspartate and alanine provided increased information to the INST-MFA flux regression. In contrast, since  $V_{\text{Glycolysis}}$  and  $V_{\text{LDH}}$  fluxes are both sources of unlabeled carbon that simply dilute the pyruvate enrichment, no significant improvement in precision was observed for these two flux estimates. Although flux resolution was improved for all three tracers when using dynamic isotopomer measurements, [1-<sup>13</sup>C]acetate showed the least improvement because the steady-state and dynamic enrichment patterns are very similar (Fig. 7A.9). Furthermore, minimal <sup>13</sup>C incorporation and the lack of complicated enrichment patterns with [1-<sup>13</sup>C] acetate administration resulted in poor resolution of the TCA cycle fluxes evident by the extremely wide flux confidence intervals (Fig. 7A.9B). Overall, these results show that INCA 2.0 can accurately simulate and regress dynamic NMR datasets and, furthermore, that INST-MFA of dynamic NMR datasets can estimate fluxes with improved precision compared to steady-state MFA.

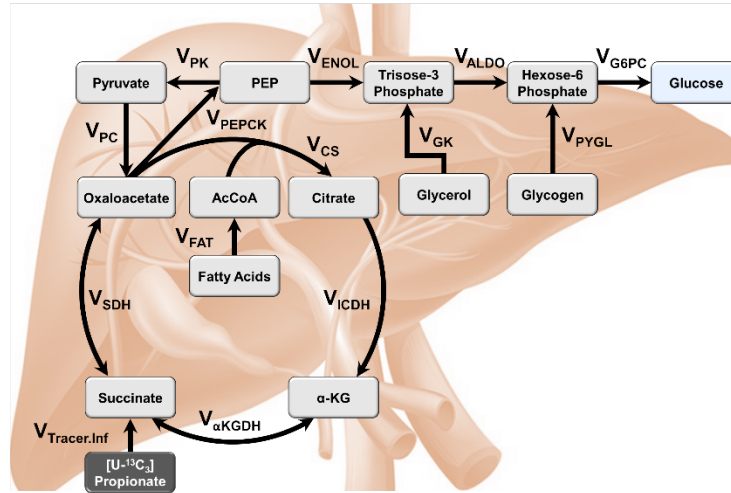
#### **7.4.4 Integration of MS and NMR datasets improves precision of *in vivo* hepatic flux estimates**

With the added functionality to model <sup>13</sup>C and <sup>2</sup>H NMR measurements, we tested whether regression of combined MS and NMR datasets improves the precision of flux estimates. Plasma glucose from *in vivo* <sup>2</sup>H/<sup>13</sup>C infused rats was derivatized and analyzed using GC-MS and NMR approaches. Datasets obtained from each analysis were then entered into INCA and regressed using a hepatic metabolic model (Fig. 7.4A) described previously by Deja et al. (2020) (See *Methods* for details). Regression of glucose enrichment data provided equivalent flux estimates for the GC-MS dataset alone, the NMR dataset alone, and the combined

dataset (Fig. 7.4B, also see *Methods*). Analysis of 95% confidence intervals of flux estimates showed consistent improvements in flux precision when both GC-MS and NMR datasets were regressed simultaneously (Fig. 7.4C). While analysis of the GC-MS dataset requires deconvolution of flux contributions toward several different mass isotopomers, the pyruvate cycling fluxes ( $V_{PEP}$ ,  $V_{PEPCK}$ , and  $V_{PK+ME}$ ) were better resolved by  $^{13}C$  NMR measurements due to their dependence on a distinct D12/Q multiplet ratio at the C2 position of MAG [65]. Additionally, positional information on carbon one, two, five and six allowed for more accurate assessment of the glycerol kinase ( $V_{GK}$ ) flux from the NMR dataset (Fig. 7.4C). However, combining isotope enrichments from both GC-MS and NMR datasets enabled better flux resolution than either dataset alone (Fig. 7.4C). These results show that INCA 2.0 can successfully integrate both NMR and MS datasets to improve the precision of estimated fluxes. Additionally, these results show that GC-MS and NMR datasets provide different and complementary isotope enrichment information, even for the same metabolite (e.g., glucose in this case), which helps to better determine the flux solution. Overall, these results show that the capabilities of INCA 2.0 to simulate and regress NMR datasets open a myriad of possibilities to design more sophisticated isotope labeling experiments and better constrain metabolic fluxes in a variety of biological systems.

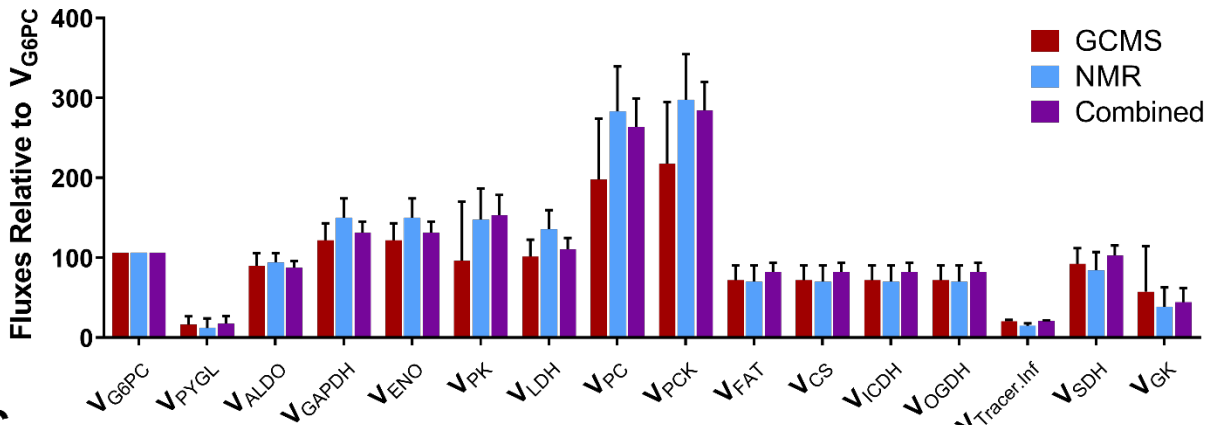


**A**



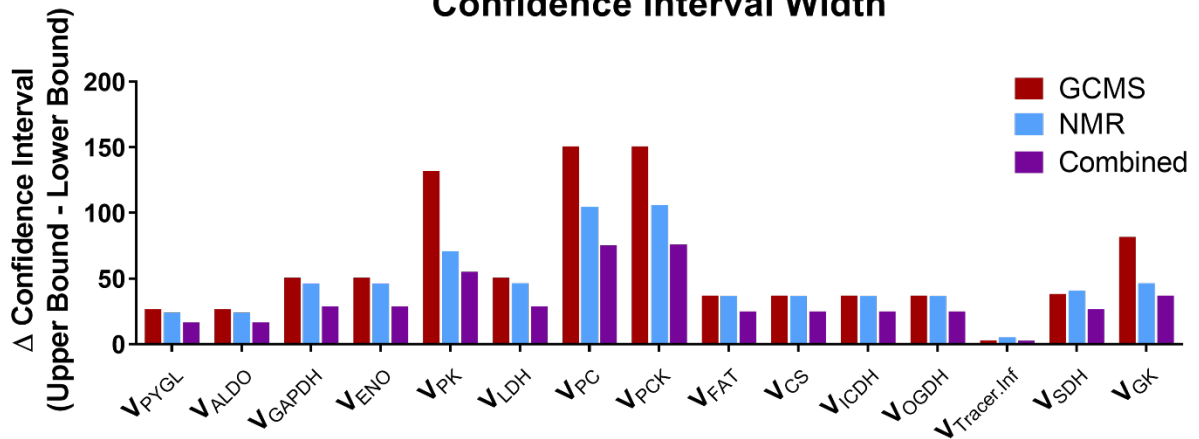
**B**

**Relative Hepatic Fluxes**



**C**

**Confidence Interval Width**



**Figure 7.4: Combining NMR and GC-MS measurements in INCA 2.0 improves precision of in vivo hepatic flux estimates**

**A.** Flux map shows the hepatic pathway modeled in INCA 2.0 using glucose measurements

**B.** Fluxes estimated using glucose enrichment measurements obtained through GC-MS, NMR or both.

Values represent fluxes relative to  $V_{G6PC}$ ; error bars represent 95% confidence intervals

**C.** Differences between the upper and lower bounds of 95% confidence intervals determined from regression of GC-MS, NMR, or combined measurement sets

## 7.5 Discussion

Technological advancements in analytical instrumentation now provide increasingly larger and richer metabolite measurements, which require modern software packages for rigorous data analysis and modeling. Here we examined physiological applications of metabolic flux analysis using our newly expanded software tool, INCA 2.0. Simulation of cardiac  $^{13}\text{C}$  NMR measurements with INCA 2.0 provided equivalent results to tcaSIM, a widely used software for NMR isotopomer simulation and tracer experiment design. Using steady-state  $^{13}\text{C}$  NMR measurements from perfused hearts, we also showed that fluxes estimated in INCA 2.0 were comparable to those calculated using tcaCALC. Finally, we assessed two new categories of tracer experiments that can be modeled in INCA 2.0 but not in other publicly available software tools. First, we found that INST-MFA of cardiac metabolism based on simulated  $^{13}\text{C}$  NMR datasets from three different  $^{13}\text{C}$ -acetate tracers led to improved flux precision when compared to steady-state MFA. Second, we demonstrated that regression of combined NMR and MS measurements in INCA 2.0 provided more precise *in vivo* hepatic flux estimates than either measurement set alone.

Deconvolution of flux contributions from intersecting metabolic pathways often requires sophisticated experimental designs involving multiple isotope tracers and metabolite measurements. Interpretation of the complex datasets obtained from these experiments depends on the availability of powerful yet user-friendly metabolic modeling tools. For example, analytical and computational advancements have enabled the concurrent assessment of glycolytic/gluconeogenic, TCA cycle, and anaplerotic fluxes in liver [29], [101] and cardiac tissues [30]. However, these studies have relied solely on either NMR or MS datasets. A major challenge is to combine information from different analytical platforms in order to delineate isotope enrichment patterns and determine metabolic fluxes with improved precision.

Recent attempts to assess hepatic metabolism non-invasively using plasma metabolites has led to the development of tools such as positional isotopomer NMR tracer analysis (PINTA), which incorporates data

from both MS and NMR platforms [287]. PINTA uses relative positional enrichment measurements from  $^{13}\text{C}$  NMR and total  $^{13}\text{C}$  enrichment measurements from GC-MS to determine *in vivo* citrate synthase and pyruvate carboxylase fluxes in the liver. Albeit impressive in its precision and applicability to human physiology [31], PINTA is limited to characterizing hepatic mitochondrial oxidation. In contrast, INCA provides a software platform that can be used to create models of (steady-state or dynamic) isotope labeling in any metabolic pathway, which can involve any combination of metabolic tracers and measured metabolites. Our additions to INCA further build on these capabilities by leveraging the increased information content of combined NMR and MS datasets to characterize a broad set of intermediary fluxes (Fig. 7.4B) while offering the flexibility to adapt models to describe organ-specific metabolic networks based on user input (Fig. 7.1A). We expect that using INCA 2.0 to integrate datasets from multiple analytical platforms will enable improved flux assessment and empower experimentalists to design more sophisticated and information-rich labeling studies.

An assumption critical to  $^{13}\text{C}$ -MFA is that all metabolites are at metabolic steady state [26]. In fact, most isotope labeling studies of cardiac metabolism have been performed under metabolic and isotopic steady state conditions [15], [34], [35], [330]. While parallel tracer studies with different  $^{13}\text{C}$  tracers can effectively determine cardiac metabolic fluxes, exquisite attention to detail is required to obtain biological and operational reproducibility between multiple tracer experiments. Furthermore, parallel tracer experiments significantly increase the number of biological replicates required for flux assessment [153]. Because of the capability to acquire NMR time-course data non-invasively [338]–[341], INST-MFA of dynamic  $^{13}\text{C}$  labeling studies offers an alternative approach to precisely characterize metabolic fluxes while minimizing the number of parallel labeling experiments and biological replicates. Currently, the primary challenge in analyzing dynamic labeling studies is the lack of computational software available to model such datasets. Using INCA 2.0, we show that dynamic  $^{13}\text{C}$  NMR datasets can be used to constrain models of cardiac metabolism and provide significant improvements in flux precision compared to steady-state measurements

(Fig. 7.3). These advancements create an opportunity to design dynamic labeling studies that can leverage the improved information content of time-course measurements to precisely determine fluxes with fewer experiments.

Development of user-friendly software tools has made  $^{13}\text{C}$  MFA more accessible to experimentalists. INCA 2.0 and other software packages such as METRAN [20], [70] and WuFlux [73] provide the end-user with a graphical interface to construct metabolic models. This allows experimentalists and other metabolism researchers, who may not be programming experts, to construct metabolic models without writing computer code or specifying model configurations in text or XML files [342]. However, INCA 2.0 does not sacrifice functionality or extensibility for user-friendliness. Unlike tcaSIM, tcaCALC, and PINTA, which are hard-coded to describe specific metabolic pathways, INCA allows the user to construct new reaction networks or adapt existing models to describe any type of metabolism ranging from mammals to plants [332] to microbes [331]. An added advantage of these customizable metabolic networks is the flexibility to define and simulate MS- or NMR-based measurements for any metabolite of interest. For example, our cardiac model (Fig. 7.1A) used glutamate measurements to determine fluxes, whereas our liver model (Fig. 7.4A) relied on plasma glucose enrichments to determine hepatic fluxes. By using an optimized EMU-based algorithm [20], [74], INCA 2.0 enables efficient simulation of comprehensive NMR and MS datasets and regression of metabolic fluxes within a user-friendly and cross-compatible MATLAB package. INCA 2.0 also offers built-in statistical tests (see *Methods* for details) to assess the model goodness-of-fit, an important feature that is lacking in some MFA software.

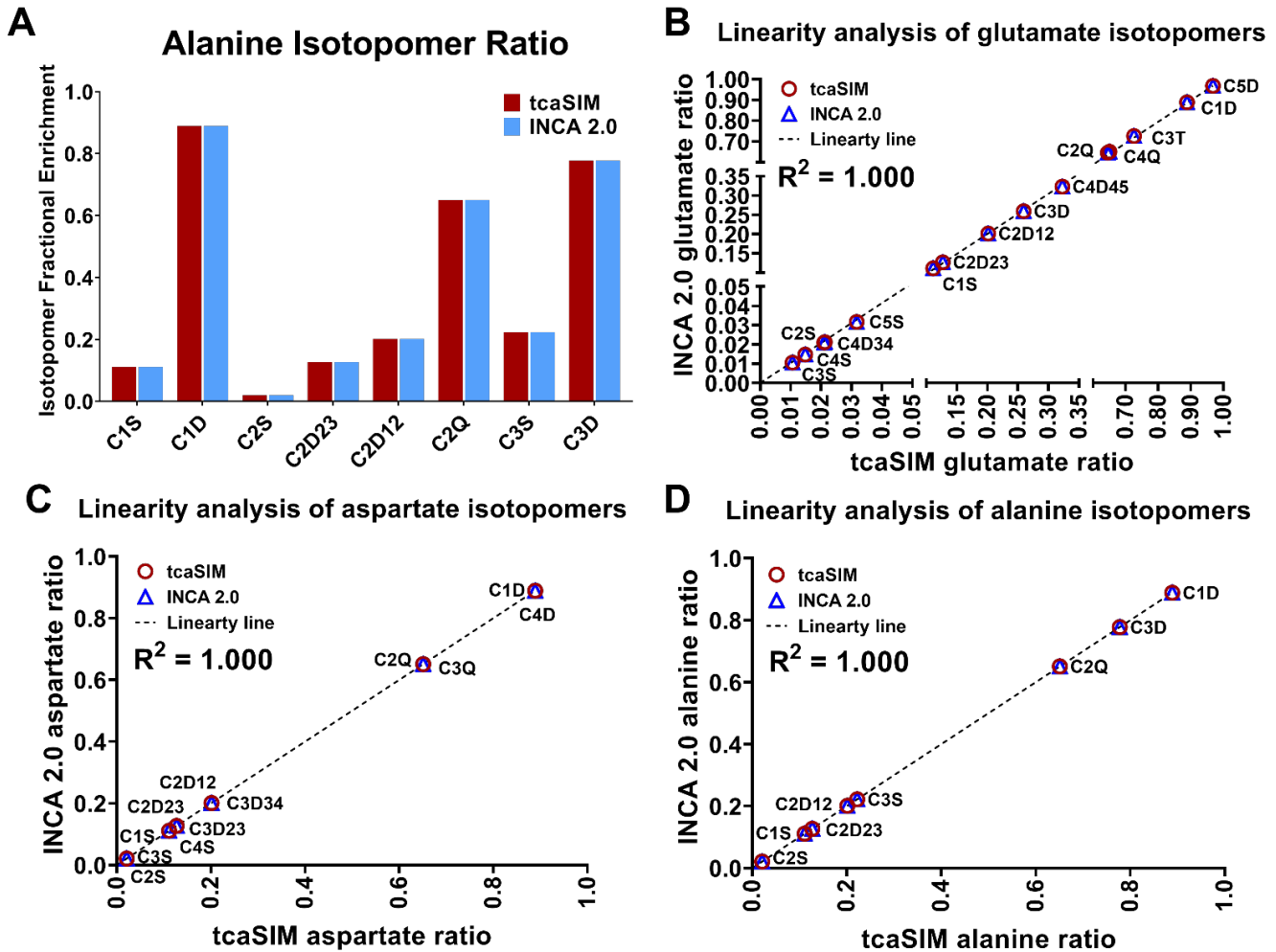
Although numerous software packages have been developed for metabolic flux analysis, few offer support for modeling both NMR and MS datasets, while even fewer provide capabilities to model steady-state or dynamic labeling experiments [68]. Here we have shown examples of how INCA 2.0 can be used to characterize fluxes in two prominent metabolic tissues, liver and heart, using  $^{13}\text{C}$  NMR,  $^2\text{H}$  NMR, and GC-MS data. These biological examples are aimed at providing metabolism researchers with new software tools

and computational models to describe modern metabolic tracer experiments, thus lowering the implementation barriers of  $^{13}\text{C}$  MFA. Our work here can be used to further explore the impact of metabolic diseases, such as type 2 diabetes (T2D), obesity, and non-alcoholic fatty liver disease (NAFLD), on cardiac and hepatic intermediary metabolism. The ability to regress fluxes using both NMR and MS datasets in the same mathematical model is expected to aid in the design of more sophisticated isotope labelling studies and allow for significant advancements in the fields of metabolic engineering, cell culture, and mammalian physiology. We also foresee numerous applications of INCA 2.0 in further characterizing tissue-specific metabolism and understanding organ crosstalk in both normal and diseased states.

## **7.6 Acknowledgements**

This work was supported by NIH R01 DK106348, NIH R01-DK078184, NIH P41-EB- 015908, NIH R21-EB-016197, NIH Grant R01-EB-009772, the Robert A. Welch Foundation Grant I-1804 and the UT Southwestern Center for Human Nutrition. We thank the Merritt group at University of Florida and Burgess group, UT Southwestern for providing the heart and liver NMR datasets, respectfully.

7.7 Appendix: Supplemental figures and tables

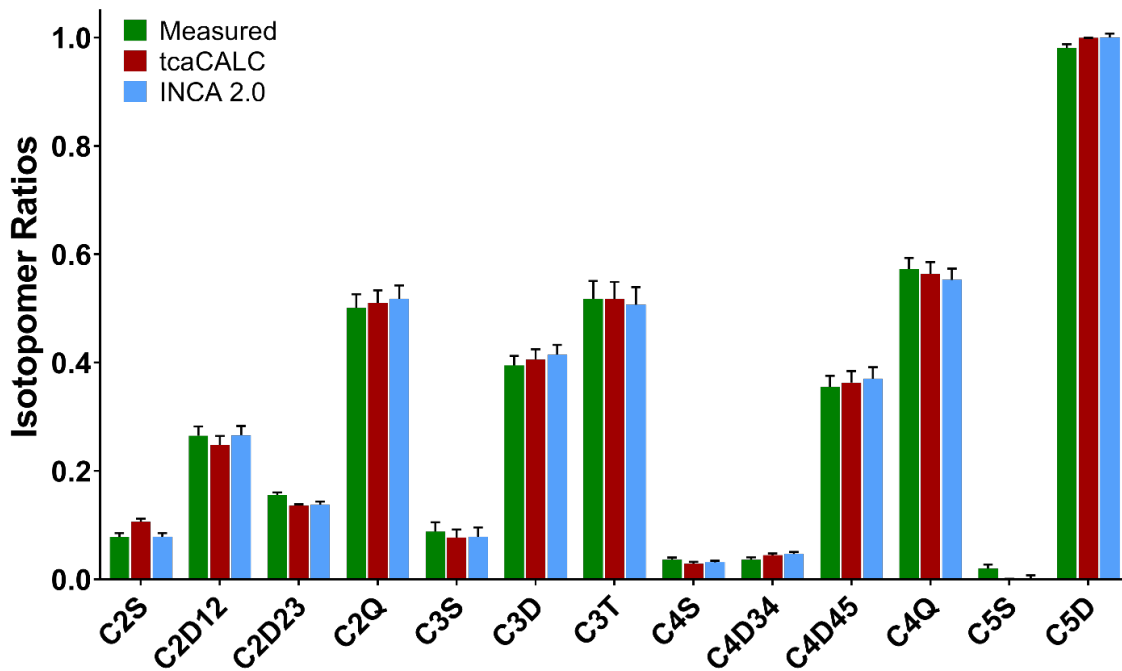


**Figure 7A.1: Comparison of simulated NMR isotopomers using tcaSIM and INCA 2.0**

- A. Simulated isotopomer fractional enrichments of alanine using tcaSIM and INCA 2.0
- B. Regression analysis of glutamate isotopomers simulated using tcaSIM versus INCA 2.0
- C. Regression analysis of aspartate isotopomers simulated using tcaSIM versus INCA 2.0
- D. Regression analysis of alanine isotopomers simulated using tcaSIM versus INCA 2.0

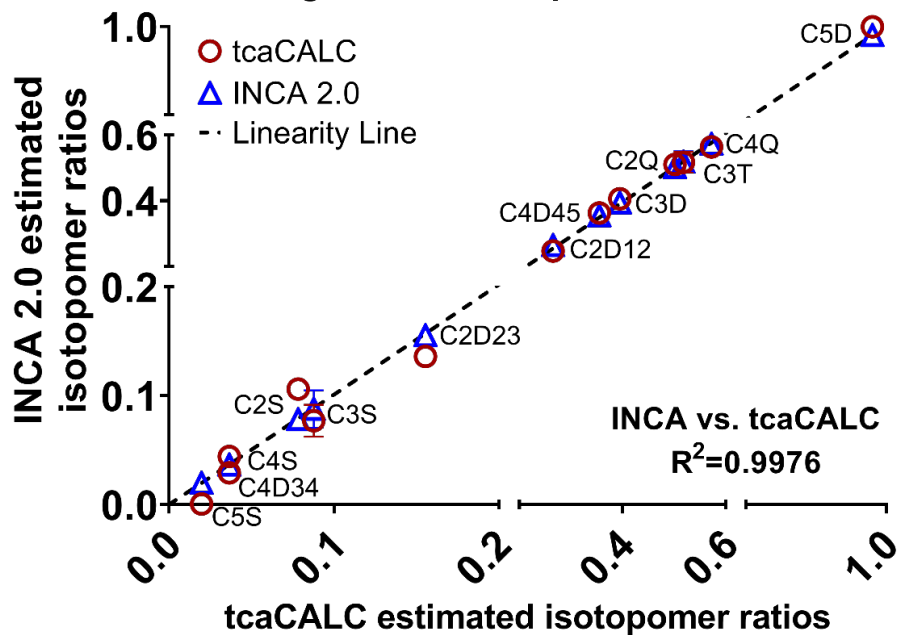
**A**

## Glutamate Isotopomer Ratios



**B**

### Linearity analysis between INCA 2.0 and tcaCALC glutamate isotopomer ratios



**Figure 7A.2: Comparison of measured glutamate isotopomers against those predicted by tcaCALC and INCA 2.0**

**A.** Comparison of measured glutamate isotopomer ratios against predicted values generated by tcaCALC and INCA 2.0

**B.** Linear regression of glutamate isotopomer ratios determined by tcaCALC and INCA 2.0

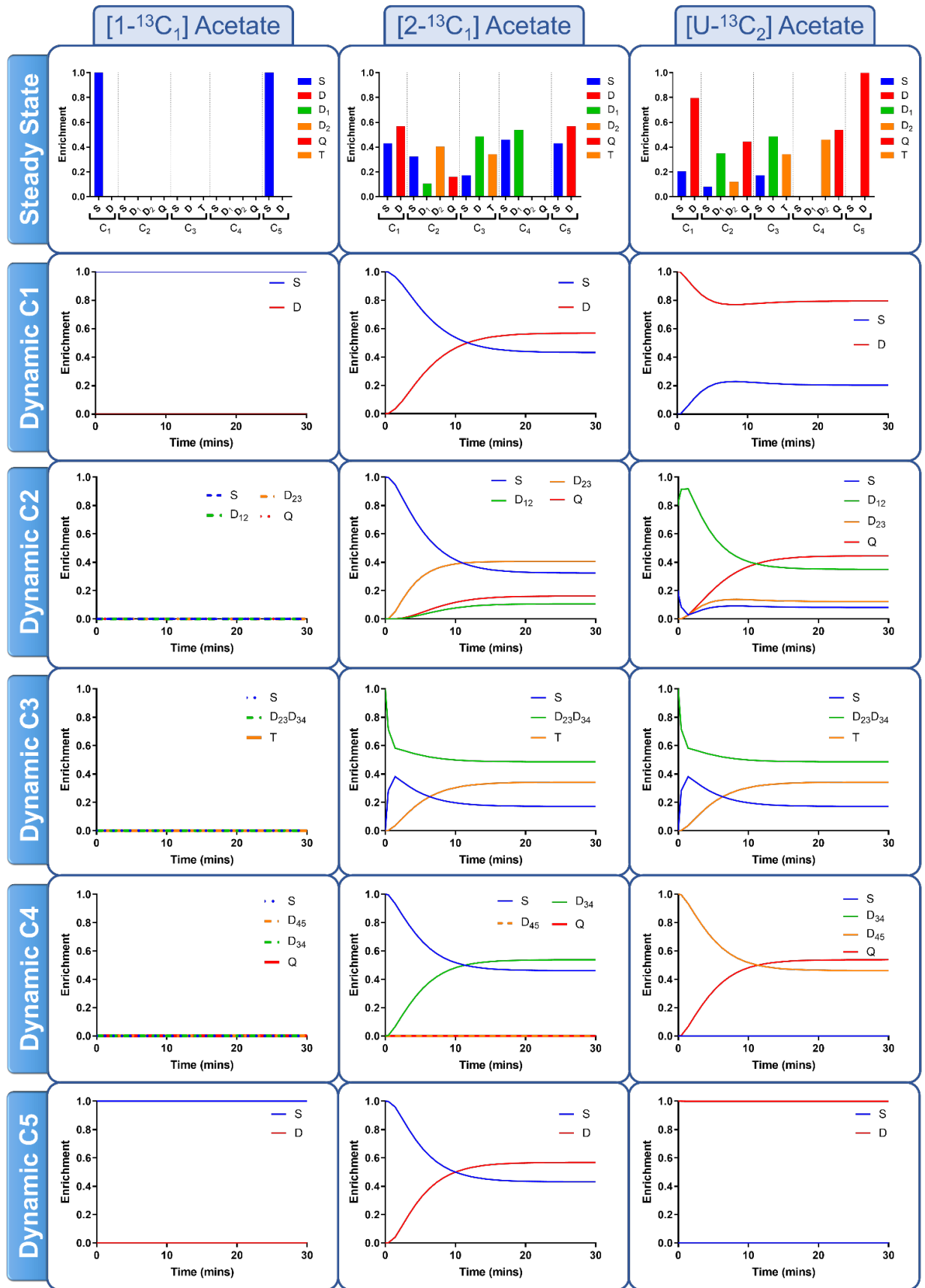
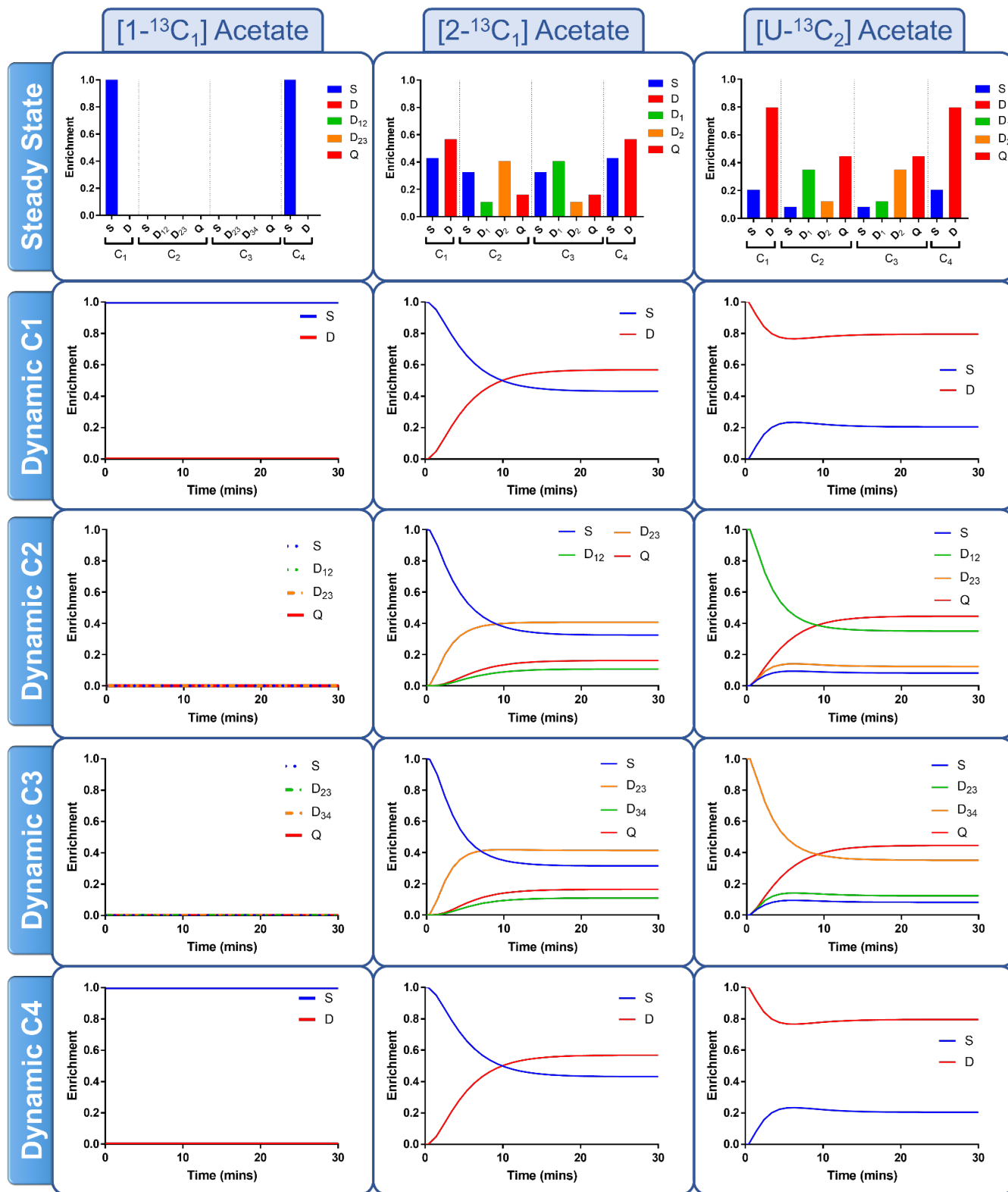


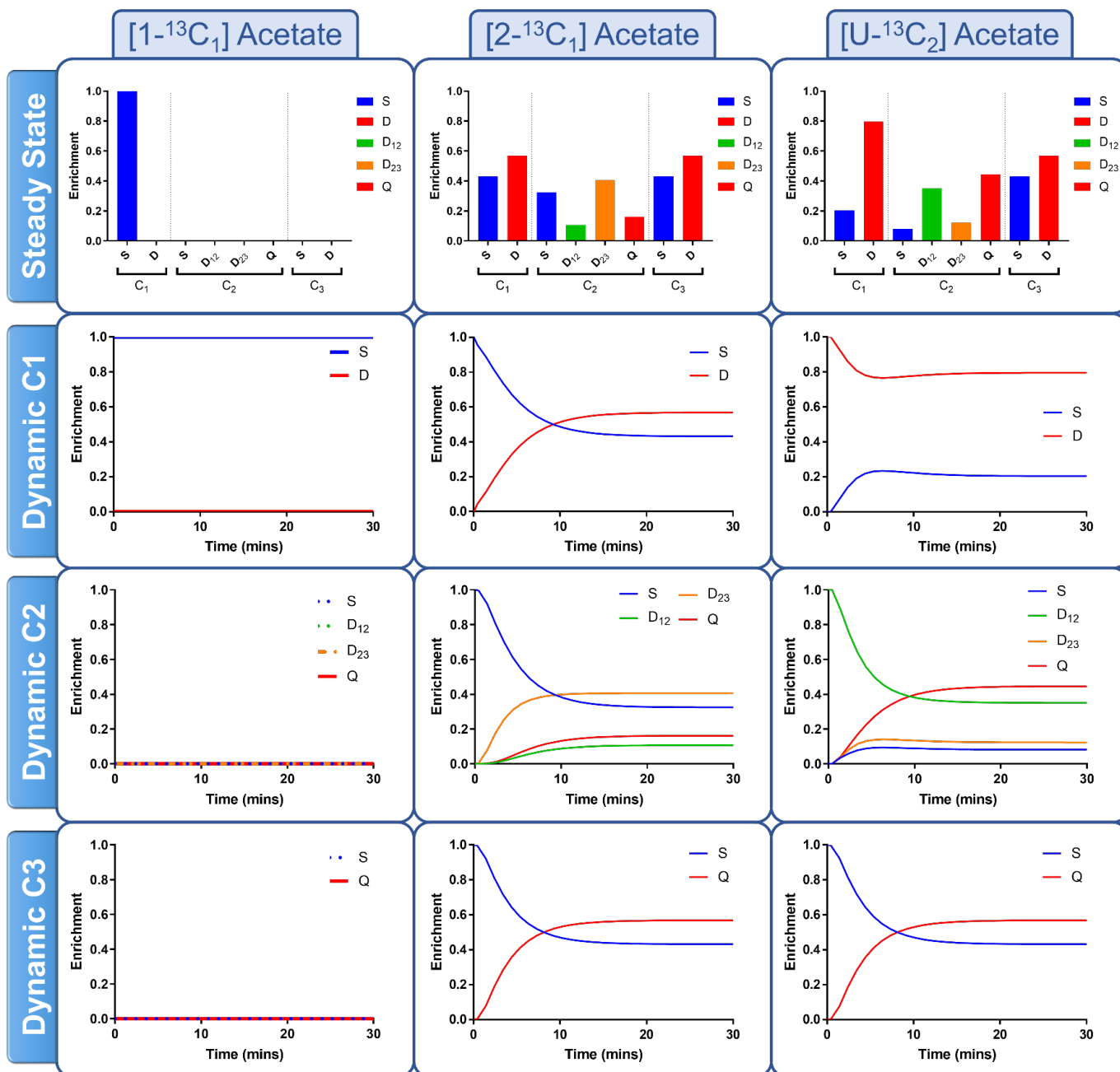
Figure 7A.3: Dynamic and steady-state  $^{13}\text{C}$  NMR glutamate isotopomer ratios  
 Steady-state and transient glutamate isotopomers simulated using  $[1-^{13}\text{C}]$ acetate,  $[2-^{13}\text{C}]$ acetate and  $[\text{U}-^{13}\text{C}_2]$ acetate as tracer





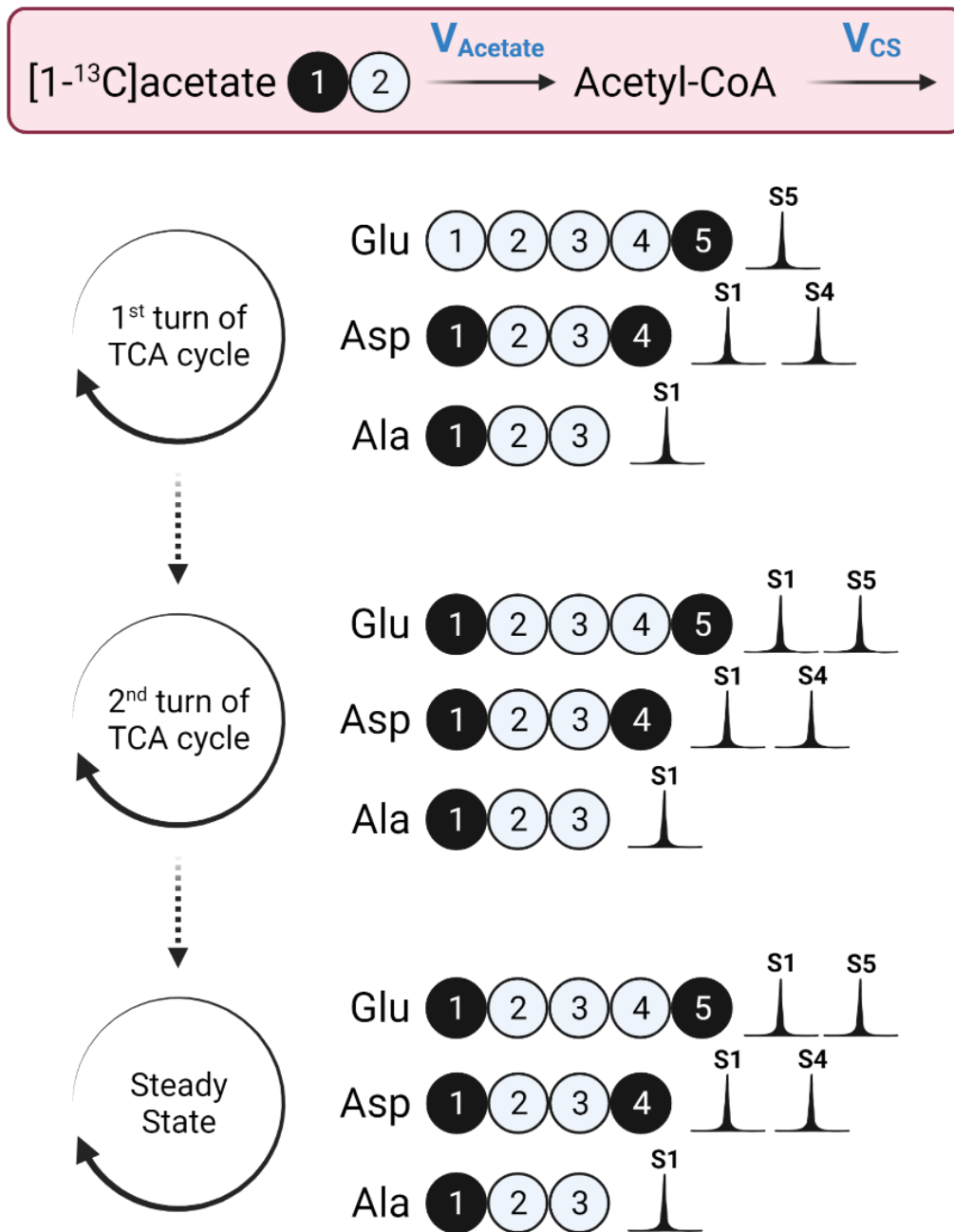
**Figure 7A.4: Dynamic and steady-state  $^{13}\text{C}$  NMR aspartate isotopomer ratios**

Steady-state and transient aspartate isotopomers simulated using  $[1-^{13}\text{C}]$ acetate,  $[2-^{13}\text{C}]$ acetate and  $[\text{U}-^{13}\text{C}_2]$ acetate as tracers



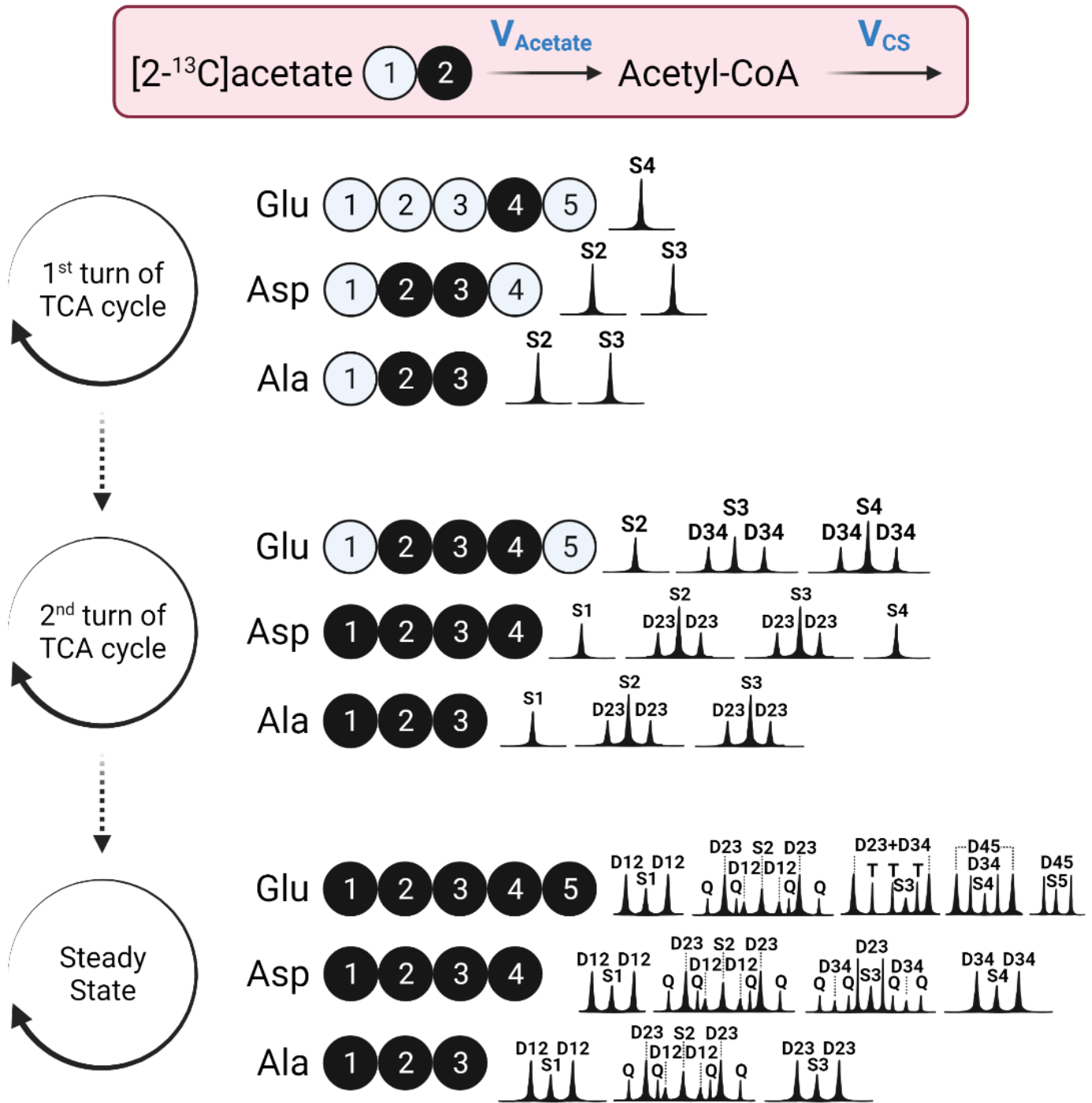
**Figure 7A.5: Dynamic and steady-state NMR alanine Isotopomers**

Steady-state and transient alanine isotopomers simulated using [1-<sup>13</sup>C]acetate, [2-<sup>13</sup>C]acetate and [U-<sup>13</sup>C<sub>2</sub>]acetate as tracers



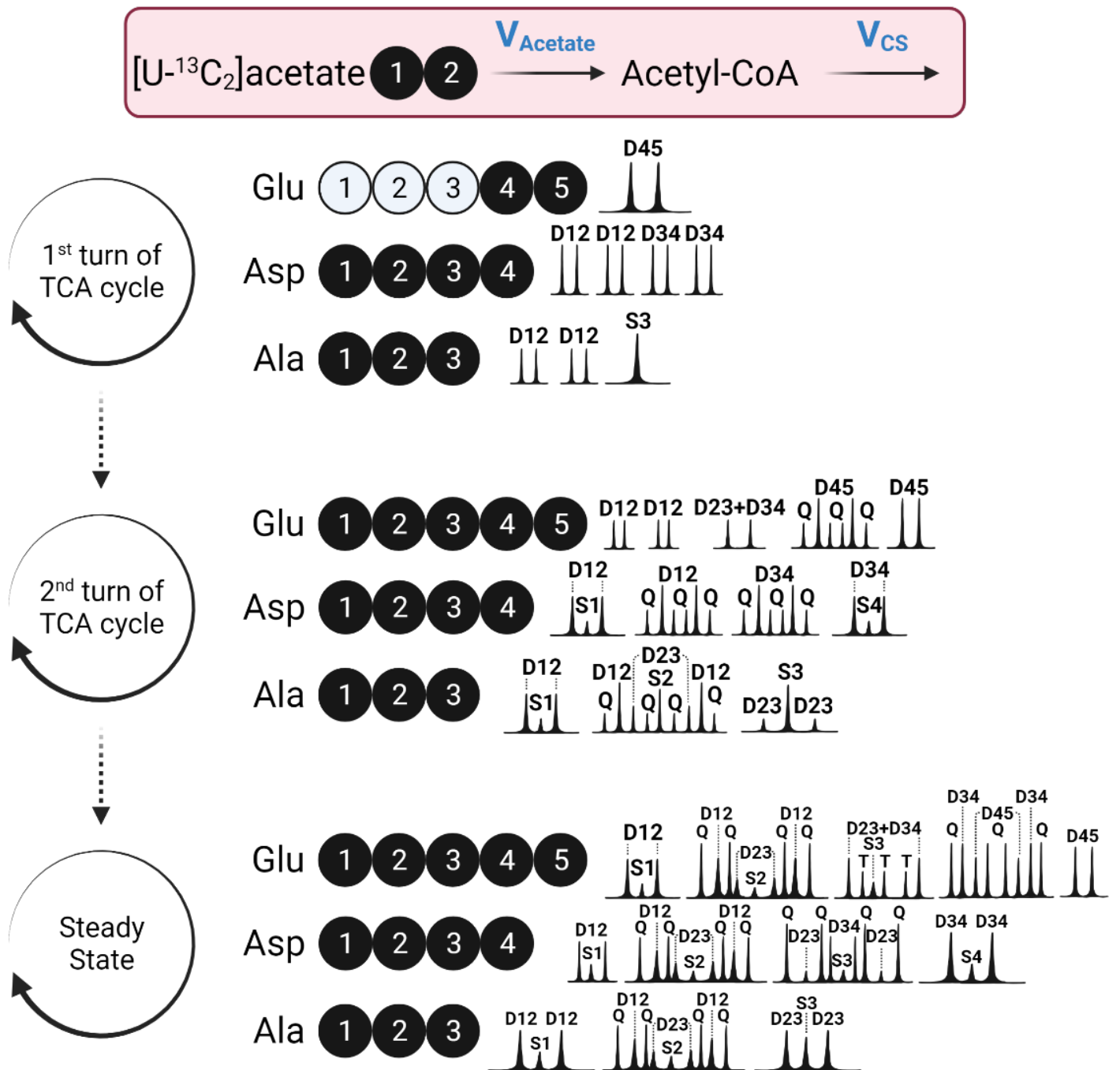
**Figure 7A.6: Formation of glutamate, aspartate and alanine isotopomers over time in the heart when  $[1-^{13}\text{C}]$ acetate is administered as a tracer.**

Different combinations of glutamate, aspartate, and alanine isotopomers are formed at the end of the 1<sup>st</sup> and 2<sup>nd</sup> turns of the TCA cycle when  $[1-^{13}\text{C}]$  acetate is used as a tracer. Carbon atoms highlighted in black represent presence of  $^{13}\text{C}$  enrichment from the tracer. Over time, after many turns of the TCA cycle, all isotopomers reach steady state (See Supplementary Results for details)



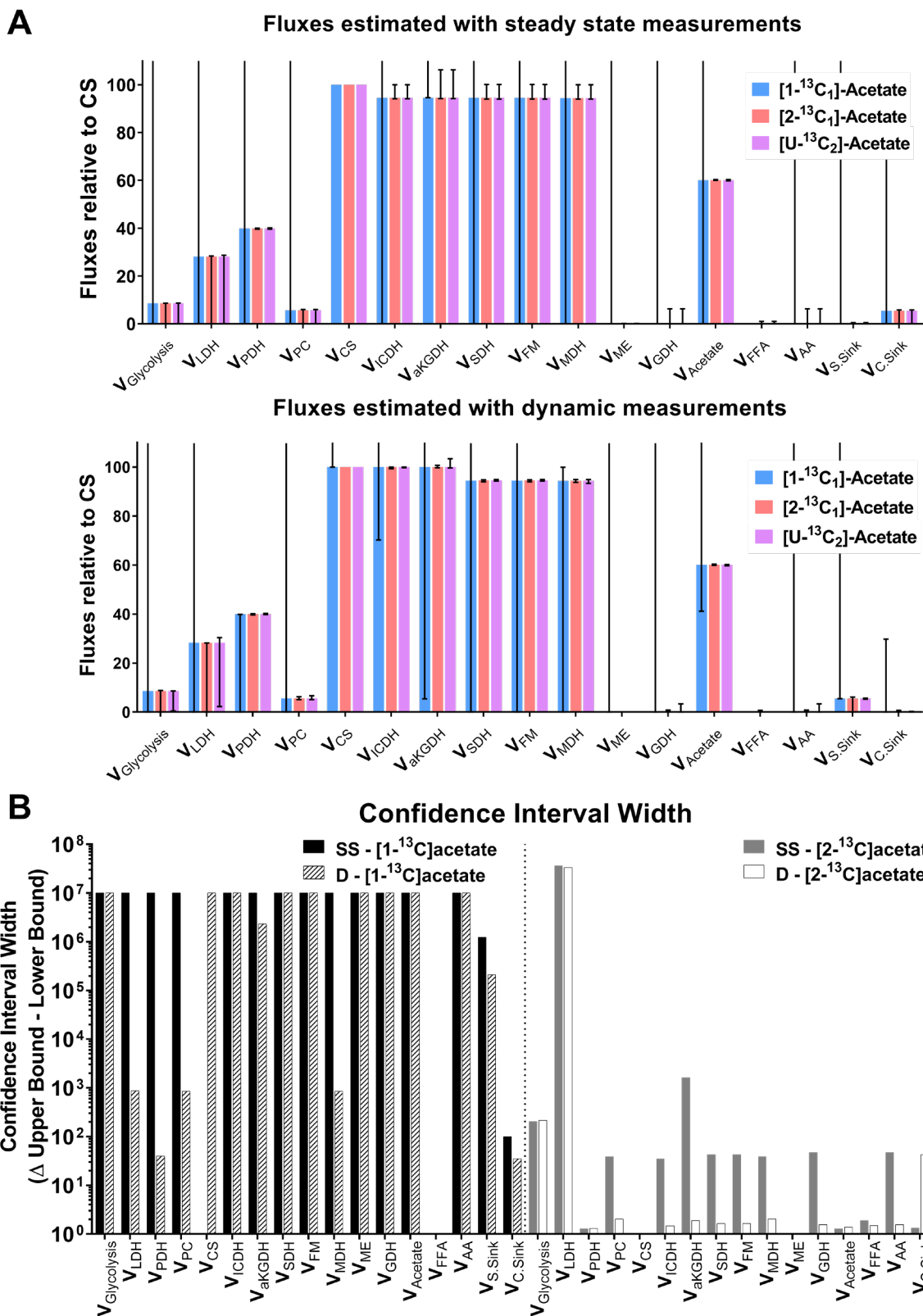
**Figure 7A.7: Formation of glutamate, aspartate and alanine isotopomers over time in the heart when [2-<sup>13</sup>C]acetate is administered as a tracer.**

Different combinations of glutamate, aspartate, and alanine isotopomers are formed at the end of the 1<sup>st</sup> and 2<sup>nd</sup> turns of the TCA cycle when [2-<sup>13</sup>C] acetate is used as a tracer. Carbon atoms highlighted in black represent presence of <sup>13</sup>C enrichment from the tracer. Over time, after many turns of the TCA cycle, all isotopomers reach steady state (See Supplementary Results for details)



**Figure 7A.8: Formation of glutamate, aspartate and alanine isotopomers over time in the heart when  $[U-^{13}C_2]$ acetate is administered as a tracer.**

Different combinations of glutamate, aspartate, and alanine isotopomers are formed at the end of the 1<sup>st</sup> and 2<sup>nd</sup> turns of the TCA cycle when  $[U-^{13}C_2]$  acetate is used as a tracer. Carbon atoms highlighted in black represent presence of  $^{13}C$  enrichment from the tracer. Over time, after many turns of the TCA cycle, all isotopomers reach steady state (See Supplementary Results for details)



**Figure 7A.9: Estimation of cardiac fluxes using steady-state versus dynamic NMR isotopomer measurements**  
**A.** Cardiac fluxes estimated using steady-state versus dynamic glutamate, aspartate and alanine NMR isotopomer measurements.  
**B.** Confidence interval width for fluxes determined from steady-state versus dynamic datasets using  $[1-^{13}\text{C}]$ acetate or  $[2-^{13}\text{C}]$ acetate as tracer. SS=steady state, D=dynamic.

**Table 7A.1: Metabolic parameters used to simulate cardiac metabolism in tcaSIM. All relative fluxes are normalized to citrate synthase (=1).**

<b>tcaSIM parameter</b>	<b>Description</b>	<b>Value</b>
<b>GLY</b>	Glycerol enrichment	0
<b>GK</b>	Glycerol kinase relative flux	0
<b>TPI</b>	Triose phosphate isomerase equilibration	1
<b>PK</b>	Pyruvate kinase relative flux	0
<b>LDH</b>	Lactate enrichment	0.1466
<b>PDH</b>	Pyruvate dehydrogenase relative flux	0.0627
<b>CO2</b>	Carbon dioxide enrichment	0
<b>YPC</b>	Pyruvate carboxylase relative flux	0.0839
<b>FAT12</b>	Fatty acids enrichment	0.7833
<b>GLYOX</b>	Glyoxylate pathway relative flux	0
<b>ROF</b>	Oxaloacetate-fumarate equilibration	1
<b>RSM</b>	Conserved orientation transfer between succinate and fumarate	0.5
<b>YS</b>	Relative anaplerotic flux	0.1302
<b>AS0</b>	Anaplerotic substrate	1
<b>ACS</b>	Acetyl- or acyl-CoA synthetase	0.9373

**Table 7A.2: Cardiac metabolic reaction network constructed in INCA 2.0 for comparison against tcaSIM and tcaCALC.**

A model of cardiac metabolism was developed to track carbon atoms through the reaction network. Metabolite measurements used to regress fluxes are shown in Table S2. <sup>13</sup>C isotopes are introduced into model reactions via glucose and long chain fatty acids. The reaction  $V_{CS}$  was used to constrain the relative citric acid cycle flux to 100.

Flux	Reaction Network
$V_{Glycolysis}$	Glucose (ABCDEF) $\rightarrow$ Pyr (CBA) + Pyr (DEF)
$V_{PDH}$	Pyr (ABC) $\rightarrow$ AcCoA (BC) + CO <sub>2</sub> (A)
$V_{PC}$	Pyr (ABC) + CO <sub>2</sub> (D) $\rightarrow$ Oac (ABCD)
$V_{CS}$	AcCoA (AB) + Oac (CDEF) $\rightarrow$ Cit (FEDBAC)
$V_{IDH}$	Cit (ABCDEF) $\rightarrow$ Akg (ABCDE) + CO <sub>2</sub> (F)
$V_{\alpha KGDH}$	Akg (ABCDE) $\rightarrow$ $\frac{1}{2}$ Suc (BCDE) + $\frac{1}{2}$ Suc (EDCB) + CO <sub>2</sub> (A)
$V_{SDH}$	$\frac{1}{2}$ Suc (ABCD) + $\frac{1}{2}$ Suc (CDBA) $\leftrightarrow$ $\frac{1}{2}$ Fum (ABCD) + $\frac{1}{2}$ Fum (DCBA)
$V_{FM}$	$\frac{1}{2}$ Fum (ABCD) + $\frac{1}{2}$ Fum (DCBA) $\leftrightarrow$ Mal (ABCD)
$V_{MDH}$	Mal (ABCD) $\leftrightarrow$ Oac (ABCD)
$V_{Oac.Sink}$	Oac $\rightarrow$ Sink
$V_{LCFA}$	Acetate (AB) $\rightarrow$ AcCoA (AB)
$V_{FFA}$	FFA (AB) $\rightarrow$ AcCoA (AB)
$V_{Gluc.tracer}$	Glucose.tracer (ABCDEF) $\rightarrow$ Glucose (ABCDEF)
$V_{Suc.source}$	Suc.source (ABCD) $\rightarrow$ $\frac{1}{2}$ Suc (ABCD) + $\frac{1}{2}$ Suc (CDBA)



**Table 7A.3: Isotopomers simulated by tcaSIM and INCA 2.0.**

<b>Glutamate Isotopomer Ratios</b>	<b>tcaSIM</b>	<b>INCA 2.0</b>
<b>GLU1S</b>	0.1575	0.1575
<b>GLU1D</b>	0.8425	0.8425
<b>GLU2S</b>	0.0978	0.0978
<b>GLU2D23</b>	0.1373	0.1373
<b>GLU2D12</b>	0.2496	0.2495
<b>GLU2Q</b>	0.5154	0.5154
<b>GLU3S</b>	0.0721	0.0721
<b>GLU3D</b>	0.4107	0.4107
<b>GLU3T</b>	0.5172	0.5172
<b>GLU4S</b>	0.0287	0.0287
<b>GLU4D34</b>	0.0448	0.0448
<b>GLU4D45</b>	0.3618	0.3618
<b>GLU4Q</b>	0.5647	0.5647
<b>GLU5S</b>	0	0
<b>GLU5D</b>	1	1

<b>Aspartate Isotopomer Ratios</b>	<b>tcaSIM</b>	<b>INCA 2.0</b>
<b>ASP1S</b>	0.1575	0.1575
<b>ASP1D</b>	0.8425	0.8425
<b>ASP2S</b>	0.0978	0.0978
<b>ASP2D23</b>	0.2495	0.2495
<b>ASP2D12</b>	0.1373	0.1373
<b>ASP2Q</b>	0.5154	0.5154
<b>ASP3S</b>	0.0978	0.0978
<b>ASP3D23</b>	0.1373	0.1373
<b>ASP3D34</b>	0.2495	0.2495
<b>ASP3Q</b>	0.5154	0.5154
<b>ASP4S</b>	0.1575	0.1575
<b>ASP4D</b>	0.8425	0.8425

**Table 7A.4: Pool sizes of glycolytic and citric acid cycle metabolites in the heart used for dynamic simulations**

Pool sizes used for metabolites are consistent with those measured within myocardial cells [330]. Pool size values have been normalized to the turnover rate of citrate of  $9.66 \text{ min}^{-1}$  and are thus unit-less [154]. Glutamate pool size was set to 40 times that of citrate while alanine and aspartate pool sizes were set to  $1/10^{\text{th}}$  that of glutamate, consistent with values reported in literature [337], [343].

Metabolite	Pool Size
Acetyl-CoA	0.1806
$\alpha$ -KG	0.096
Citrate	10.3595
Fumarate	0.1681
Glutamate	413.9799
Lactate	6.7479
Malate	1.2784
Oxaloacetate	0.0528
Pyruvate	0.1807
Succinate	2.8744
Alanine	41.3980
Aspartate	41.3980

## 8. CONCLUSIONS AND FUTURE WORK

### 8.1 Conclusions

The research presented here shows the development of novel metabolic models and their applications in answering challenging questions in biology and physiology. The results shown in the prior chapters of this dissertation conclude that metabolic flux analysis is an effective approach to discover and quantify physiological mechanisms in cells, tissues, and the whole body, which would be otherwise impossible to observe. The models and tools developed here can be further applied to help characterize diseased metabolic states and guide the development of drugs and therapeutics in the context of diabetes and obesity.

The data presented in Chapter 3 shows the role of G6PC2 as a negative regulator of glycolytic as well as mitochondrial metabolism. These findings challenge the dogma that GK alone regulates oxidative metabolism and thus insulin secretion in the beta cell. Results shown here validate the hypothesis previously presented by others that *G6pc2* causes a leftward shift in the dose-response curve for GSIS and thus is a potential target for enhancing insulin secretion. Given that *G6PC2* expression is associated with increased fasting blood glucose (FBG) levels and thus heightened risk for cardiovascular-associated mortality (CAM) *in vivo* [199], [207], these data suggest that G6PC2 inhibitors would be useful for lowering FBG and the risk of CAM. However, one needs to be judicious in interpreting these findings as recent studies suggest that under specific physiological conditions, such as prolonged fasting and ketogenic feeding, G6PC2 offers protection against hypoglycemia [178]. More broadly, the flux model developed in this chapter can be further applied to assess the metabolic regulation of primary islets and other pancreatic cell lines under conditions of hypo- and hyperglycemia.

Findings from Chapter 4 establish the significance of secondary tracer effects due to Cori cycling and their impact on estimating hepatic fluxes. The expanded model, which relaxes certain assumptions through the analysis of broader measurement sets, indicates that significant hepatic pyruvate cycling persists under

fasted conditions. Additionally, exogenous propionate administration has no noticeable effects on gluconeogenic or pyruvate cycling fluxes. Overall, the results from this study conclude that secondary tracer effects are significant and the expansion of the hepatic model can help explain the previously seen differences between  $^{13}\text{C}$  propionate and lactate tracers [109], [219].

Results from Chapter 5 highlight the ability of stable isotope-based studies to simultaneously quantify hepatic and renal fluxes. The approach developed in the chapter shows that isotopic tracing and metabolic flux analysis are extensible tools that can aid in shaping our understanding of *in vivo* mammalian metabolism. Application of the dual-organ model shows that mice lacking hepatic PEPCK-C maintain euglycemia by upregulating renal glucose production and oxidative metabolism. Loss of hepatic PEPCK-C diminishes gluconeogenesis, citric acid cycle (CAC) activity, anaplerosis, and pyruvate cycling in the liver. Compensatory increases in expression of both PEPCK isozymes in the kidneys facilitates increased gluconeogenesis and cataplerosis from the CAC. The integration of tissue and plasma metabolites provides a platform to simultaneously evaluate hepatic and renal metabolism *in vivo*.

The research presented in chapter 6 leverages the expanded model presented in chapter 4 to simultaneously assess intermediary metabolism in the liver, heart, gastrocnemius and vastus muscles within a single mouse, using isotope enrichment measurements of tissue and plasma metabolites. Application of this multi-tissue model emphasizes that obesity has organ-specific effects that do not develop in isolation. Additionally, using integrative multi-omics analysis, I was able to identify important regulatory and clinical biomarkers of obesity-induced metabolic dysfunction. The development of this metabolic model provides a flexible platform to simultaneously evaluate *in vivo* fluxes in response to genetic, (patho)physiological and pharmacological interventions.

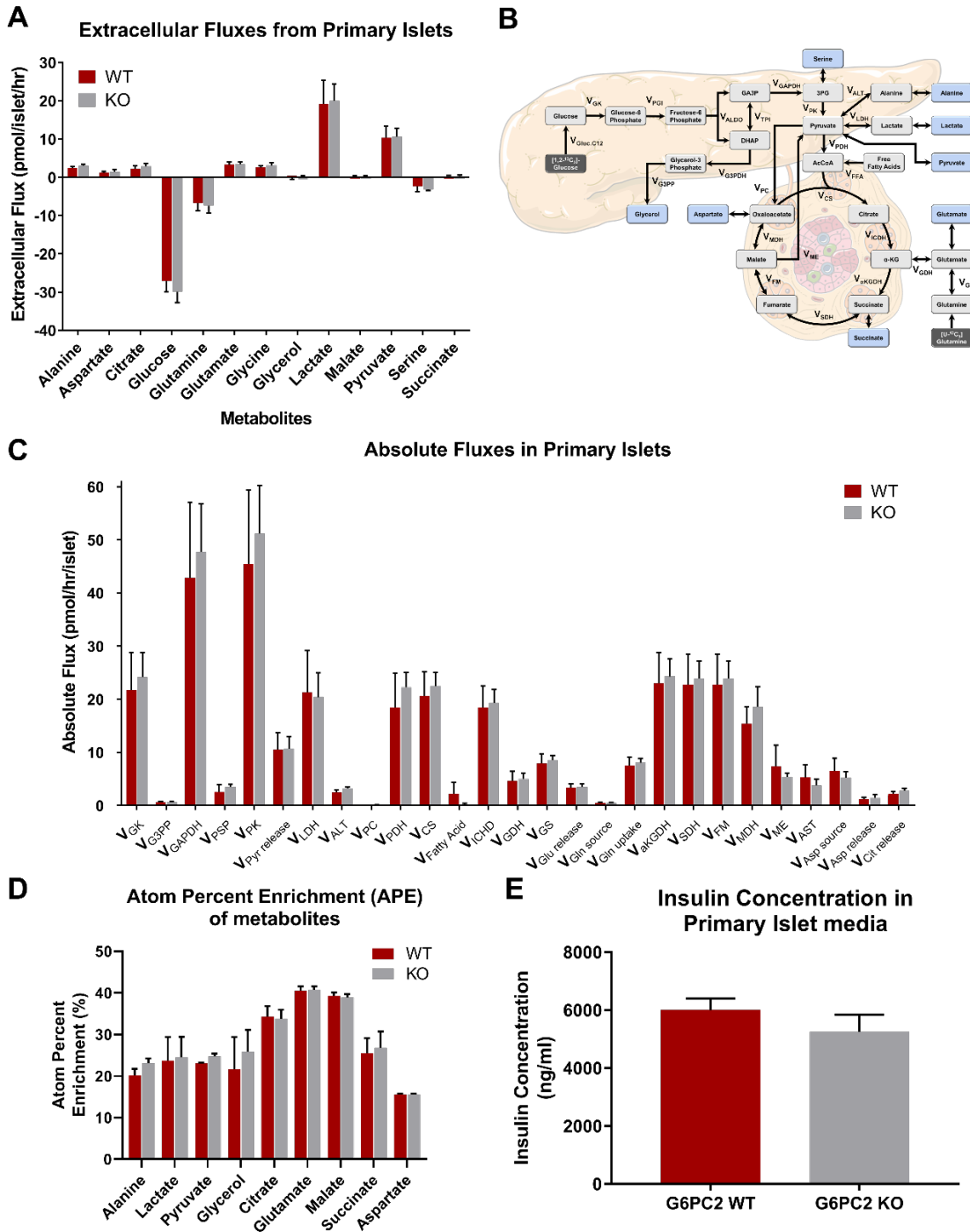
Lastly, the INCA software package was upgraded with the capability to model steady-state and dynamic NMR measurements, and these new features were validated using both synthetic and experimental datasets

to precisely determine cardiac and hepatic fluxes. The ability to regress fluxes using both NMR and MS datasets in the same mathematical model is expected to aid in the design of more sophisticated isotope labelling studies and allow for significant advancements in the fields of metabolic engineering, cell culture, and mammalian physiology. We also foresee numerous applications of INCA 2.0 in further characterizing tissue-specific metabolism and understanding organ crosstalk in both normal and diseased states.

## 8.2 Recommendations for future work

The work presented in this dissertation has merely scratched the surface of all the possible applications of MFA in studying physiology and disease. The *in vitro* models presented here can readily be adapted to better characterize *in vivo* metabolism, and the *in vivo* models can be further applied to study different diseased states in animals and humans.

The beta cell model examined in Chapter 3 establishes the role of G6PC2 as a negative regulator of oxidative metabolism, but operation of the pathways described herein remain to be tested in primary mouse and human islets. Preliminary studies assessing metabolic fluxes in mouse islets show high variability and thus mitigate any significant trends present in glycolytic and mitochondrial fluxes as well as insulin secretion (Fig. 8.1). The variability in these studies partially stems from adaptations that occur *ex vivo* in islets due to longer incubation times (>24h) [144]. Therefore, studies in primary islets need to be optimized for shorter incubation times with enriched media to capture metabolic effects that may not persist in prolonged culture. A starting point for optimizing these media conditions would be to add stable isotopes (glucose or glutamine) in the recovery media in the pre-incubation step and run the isotope labelling experiment for one to three hours. My results from the  $\beta$ TC3 cells showed that isotopic steady state was achieved in glycolytic intermediates within 3h (Fig. 3.3A) while earlier timepoints were not studied. This indicates that primary islets, which generate significantly more insulin than the  $\beta$ TC3 cells (Fig. 8.1E), may well reach steady state even earlier than 3h.



**Figure 8.1: Metabolic effect of *G6pc2* KO in primary mice islets**

- A) Extracellular uptake and excretion measured in primary mice islets at 11 mM glucose concentrations. Positive values represent excretion fluxes while negative values indicate net uptake of metabolite. Data represent means $\pm$ SEM (n=15).
- B) Flux network representing oxidative islet metabolism constructed in INCA. Measured media metabolites are shown in blue.
- C) Absolute extra- and intracellular fluxes in *G6pc2* WT and KO primary mice islets estimated using MFA. Data represent means $\pm$ SEM (n=3).
- D) Atom percent enrichment in glycolytic (labelled using [1,2- $^{13}C_2$ ] glucose) and TCA cycle metabolites (labelled using [U- $^{13}C_5$ ] glutamine). Data represent means $\pm$ SEM (n $\geq$ 6).
- E) Media insulin content after 24h incubation of primary mice islets. Data represent means $\pm$ SEM (n=15).

Another improvement that can help resolve the fluxes in the oxidative pentose phosphate pathway in the  $\beta$ -cell model is the measurement of phosphorylated sugars. Development of LC-MS/MS methods, as previously described [322], or improvements in TMS derivatization for GC-MS systems will allow for the measurement of sugar phosphates. Additionally, assessment of NADPH:NADP<sup>+</sup> ratios from metabolite concentrations can also be further verified using a two-photon excitation microscope accessible at the Vanderbilt Biophotonics Center in the  $\beta$ TC3 cell line and primary mice islets. Ultimately, the metabolic model presented in Chapter 3 has further applications in studying  $\beta$ -cell metabolism under various conditions and can also be further applied to study the effects of type 2 diabetes in islets from human donors.

Lastly, I measured changes in mitochondrial flux, independent from elevated glucose uptake rate. Consistent with these findings, baseline Ca<sup>2+</sup> were also elevated at both 5 and 11 mM glucose concentration. To test whether calcium levels are elevated either in response to higher glycolysis or due to the loss of G6PC2, it would best to conduct flux studies and measure calcium levels in the presence of a K<sub>ATP</sub> channel inhibitor, diazoxide. Additionally, elevated G6P levels are connected with a reduction in the calcium accumulation in the endoplasmic reticulum through the metabolite's ability to lower sarco-endoplasmic reticulum calcium ATPase (SERCA) activity [194]. More importantly, inhibition of glucose-6-phosphatase has been shown to lower Ca<sup>2+</sup> sequestration in endoplasmic reticulum of permeabilized islets [195]. Therefore, it is vital to measure the absolute concentration of G6P in WT and KO cells, where an elevation might suggest lower calcium sequestration in the ER. The experiment to measure levels of G6P can be combined with glucose cycling experiments to determine if rates of intracellular glucose cycling are higher internally than those measured in the media. Lastly, we can also conduct an experiment in WT and KO cells to see if calcium release from the ER is controlling glycolysis by using thapsigargin and measuring intracellular insulin content and media concentration.

The *in vivo* models presented in Chapter 4, 5 and 6 assume that the tissue metabolite enrichment is in isotopic steady state. While plasma enrichment is unchanged during the last 20 minutes of the infusion

studies, further studies need to be conducted to confirm that this assumption holds true for tissue metabolites. A suggested experiment involves taking mice from the same cohort and running a series of infusion studies where tissues are extracted after 100-, 110- and 120-min post  $^{13}\text{C}_3$  lactate administration ( $\sim n=3-5$  per time point). Next steps would be to compare the enrichment across the three time points in a number of tissues, including the liver, kidney, heart, gastrocnemius, and vastus, and verify if the mass isotopomer distribution (MIDs) of metabolites is indeed constant.

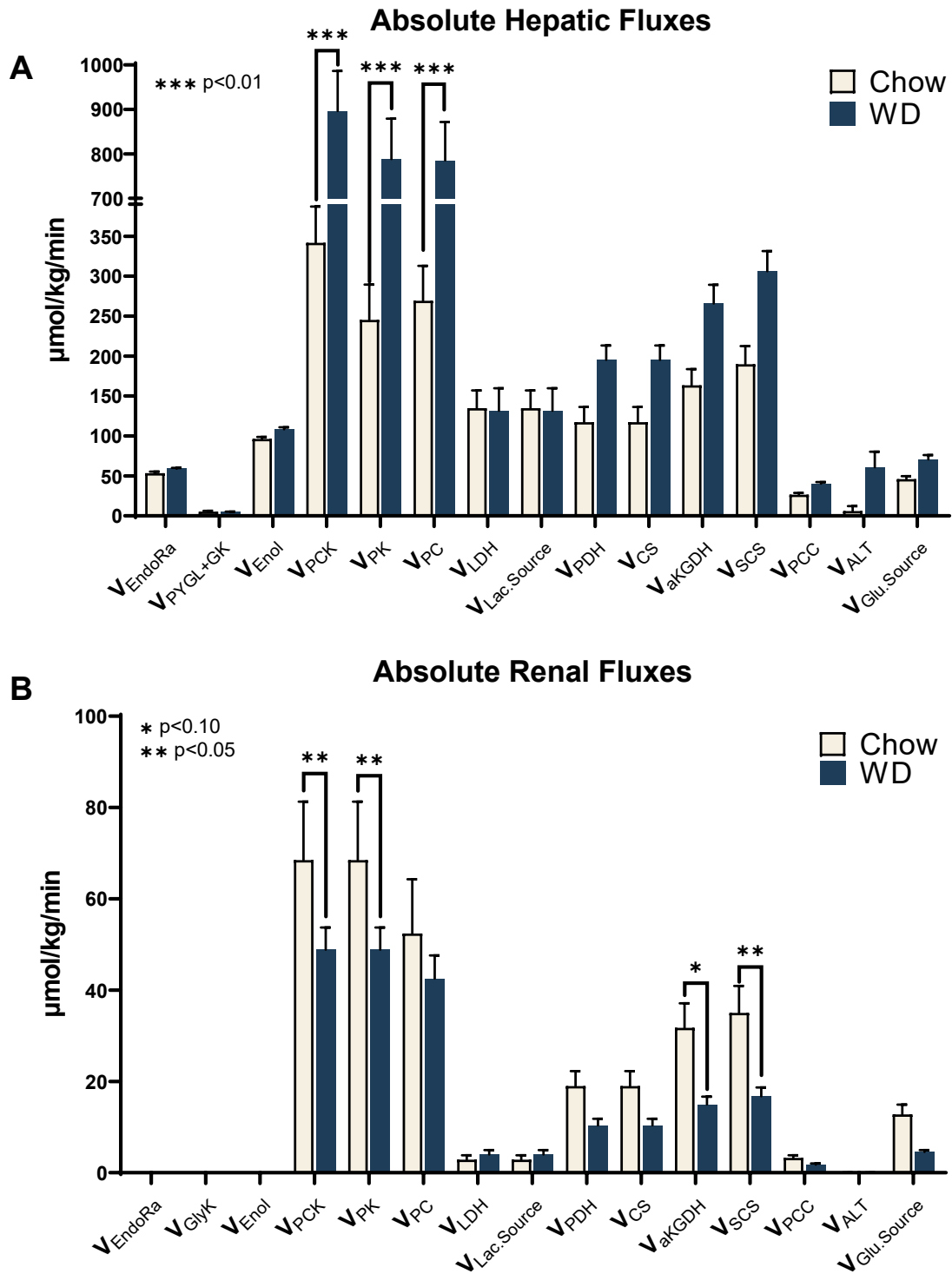
While I showed that the kidney compensates for the loss of hepatic glucose production, the exact mechanism of action was not identified. Plasma glucagon levels were elevated and so was the expression of genes regulated by glucagon's action in the kidneys of KO mice. To further test this hypothesis, a PEPCK-C KO mice with a renal glucagon receptor (GCGR) knockout model will be needed which is difficult to obtain. Alternatively, perfused kidneys from PEPCK-C WT and KO mice could be used under conditions of low glucagon to determine the signaling mechanism responsible for increased renal glucose production in these mice. Additionally, the contributions of the intestines to glucose production were not determined in our current model. Apart from expanding the flux model to encompass glucose production from the intestines, future studies could be conducted with dual knockouts of PEPCK in the liver and intestines as well as in the liver and kidneys. Obviously, these study require obtaining the pertinent mouse model prior to performing isotope infusion studies.

The dual-organ model described in chapter 5 has further applications in studying the effect of obesity on renal and hepatic metabolism. In fact, applying this model on  $\text{MC4R}^{-/-}$  mice fed 20 weeks of Western diet (WD) shows significant elevation in pyruvate cycling in the liver yet a reduction in oxidative and mitochondrial fluxes in the kidneys (Figure 8.2). This model has significant applications in studying the effects of disease and drugs on renal metabolism; for example, it can be applied to elucidate the effects of SGLT2 inhibitors on renal and hepatic metabolism. The multi-tissue model from Chapter 6 has even wider ranging applications in (patho)physiology and disease. It is already being applied in our lab to study the



metabolic effects of CDN1163, a small molecule drug that activates SERCA2, on multiple tissues in the body.

Lastly, the testing and validation of INCA 2.0 performed in Chapter 7 provides a stepping stone for leveraging combined NMR and MS measurements of isotope enrichment. The flux simulations for regressing dynamic isotopomer measurements in the heart (see Section 7.4.3) can be applied to better resolve cardiac flux under conditions of hypertrophy and other cardiometabolic disorders. Furthermore, there are no software packages in the public domain that can model  $^1\text{H}$  and  $^{13}\text{C}$  NMR datasets together. Given that INCA allows the simultaneous regression of these datasets, future studies can take advantage of these features to better constrain the models presented in Chapter 3-6. One potential future application of this approach is to perform  $^{13}\text{C}$  NMR on tissues with low enrichments to acquire position-specific labeling descriptions of glutamate and alanine, two vital metabolites that can help resolve glycolytic and mitochondrial fluxes. This can help further constrain the model presented in Chapter 6 in tissues where isotopic enrichment is low, such as the heart and skeletal muscle. Broadly, this dissertation provides expanded MFA models that hold immense value in assessing *in vitro* and *in vivo* metabolic fluxes in normal and pathological conditions in animals and humans.



**Figure 8.2: Metabolic fluxes in the liver and kidneys of  $MC4R^{-/-}$  KO mice**

Metabolic fluxes were estimated using the dual-organ model in the (A) liver and (B) kidneys of 28-week-old  $MC4R^{-/-}$  KO mice, fed chow (n=4) or WD (n=7) for 20 weeks. Values represent means  $\pm$  SEM, \* $P$ <0.10, \*\* $P$ <0.05, \*\*\* $P$ <0.01.

## LIST OF REFERENCES

- [1] C. M. Metallo and M. G. Vander Heiden, "Understanding metabolic regulation and its influence on cell physiology.," *Mol. Cell*, vol. 49, no. 3, pp. 388–98, Feb. 2013.
- [2] S. C. Burgess *et al.*, "Cytosolic Phosphoenolpyruvate Carboxykinase Does Not Solely Control the Rate of Hepatic Gluconeogenesis in the Intact Mouse Liver," *Cell Metab.*, vol. 5, no. 4, pp. 313–320, Apr. 2007.
- [3] A. K. Groen, C. W. van Roermund, R. C. Vervoorn, and J. M. Tager, "Control of gluconeogenesis in rat liver cells. Flux control coefficients of the enzymes in the gluconeogenic pathway in the absence and presence of glucagon.," *Biochem. J.*, vol. 237, no. 2, pp. 379–89, Jul. 1986.
- [4] A. Varma and B. O. Palsson, "Metabolic Flux Balancing: Basic Concepts, Scientific and Practical Use," *Bio/Technology*, vol. 12, no. 10, pp. 994–998, Oct. 1994.
- [5] J. J. Vallino and G. Stephanopoulos, "Metabolic flux distributions in *Corynebacterium glutamicum* during growth and lysine overproduction. Reprinted from *Biotechnology and Bioengineering*, Vol. 41, Pp 633-646 (1993).," *Biotechnol. Bioeng.*, vol. 67, no. 6, pp. 872–85, Mar. 2000.
- [6] H. King, R. E. Aubert, and W. H. Herman, "Global burden of diabetes, 1995-2025: Prevalence, numerical estimates, and projections," *Diabetes Care*, vol. 21, no. 9, pp. 1414–1431, Sep. 1998.
- [7] "GLOBAL REPORT ON DIABETES WHO Library Cataloguing-in-Publication Data," *ISBN*, vol. 978, pp. 92–4.
- [8] R. Patil and G. K. Sood, "Non-alcoholic fatty liver disease and cardiovascular risk.," *World J. Gastrointest. Pathophysiol.*, vol. 8, no. 2, pp. 51–58, May 2017.
- [9] P. Angulo, "Nonalcoholic Fatty Liver Disease," *N. Engl. J. Med.*, vol. 346, no. 16, pp. 1221–1231, Apr. 2002.
- [10] A. Kotronen and H. Yki-Jarvinen, "Fatty Liver: A Novel Component of the Metabolic Syndrome," *Arterioscler. Thromb. Vasc. Biol.*, vol. 28, no. 1, pp. 27–38, Oct. 2007.
- [11] A. Sánchez López de Nava and A. Raja, *Physiology, Metabolism*. StatPearls Publishing, 2020.
- [12] Nature Education, "Contents of Essentials of Cell Biology | Learn Science at Scitable," *Scitable*, 2014. [Online]. Available: <https://www.nature.com/scitable/ebooks/essentials-of-cell-biology-14749010/118238537/>. [Accessed: 26-Jun-2021].
- [13] K. Aleksandrova, C. Egea Rodrigues, A. Floegel, and W. Ahrens, "Omics Biomarkers in Obesity: Novel Etiological Insights and Targets for Precision Prevention.," *Curr. Obes. Rep.*, vol. 9, no. 3, pp. 219–230, Sep. 2020.
- [14] R. Wang *et al.*, "The transcription factor Myc controls metabolic reprogramming upon T lymphocyte activation.," *Immunity*, vol. 35, no. 6, pp. 871–82, Dec. 2011.
- [15] M. Khairallah, F. Labarthe, B. Bouchard, G. Danialou, B. J. Petrof, and C. Des Rosiers, "Profiling substrate fluxes in the isolated working mouse heart using <sup>13</sup>C-labeled substrates: focusing on the origin and fate of pyruvate and citrate carbons," *Am. J. Physiol. Circ. Physiol.*, vol. 286, no. 4, pp. H1461–H1470, Apr. 2004.
- [16] N. Templeton, J. Dean, P. Reddy, and J. D. Young, "Peak antibody production is associated with increased oxidative metabolism in an industrially relevant fed-batch CHO cell culture," *Biotechnol. Bioeng.*, vol. 110, no. 7, pp. 2013–2024, Jul. 2013.
- [17] U. Sauer, "Metabolic networks in motion: 13C-based flux analysis," *Mol. Syst. Biol.*, vol. 2, p. 62, Nov. 2006.

- [18] W. Wiechert, "13C Metabolic Flux Analysis," *Metab. Eng.*, vol. 3, no. 3, pp. 195–206, Jul. 2001.
- [19] W. Wiechert, M. Mö, N. Isermann, M. Wurzel, and A. A. De Graaf, "Bidirectional Reaction Steps in Metabolic Networks: III. Explicit Solution and Analysis of Isotopomer Labeling Systems," *Biotechnol Bioeng*, vol. 66, pp. 69–85, 1999.
- [20] J. D. Young, J. L. Walther, M. R. Antoniewicz, H. Yoo, and G. Stephanopoulos, "An elementary metabolite unit (EMU) based method of isotopically nonstationary flux analysis," *Biotechnol. Bioeng.*, vol. 99, no. 3, pp. 686–699, Feb. 2008.
- [21] S. B. Crown, C. P. Long, and M. R. Antoniewicz, "Optimal tracers for parallel labeling experiments and 13C metabolic flux analysis: A new precision and synergy scoring system," *Metab. Eng.*, vol. 38, pp. 10–18, Nov. 2016.
- [22] A. G. McAtee Pereira, J. L. Walther, M. Hollenbach, and J. D. Young, "13C Flux Analysis Reveals that Rebalancing Medium Amino Acid Composition can Reduce Ammonia Production while Preserving Central Carbon Metabolism of CHO Cell Cultures," *Biotechnol. J.*, vol. 13, no. 10, p. 1700518, Oct. 2018.
- [23] C. M. Metallo *et al.*, "Reductive glutamine metabolism by IDH1 mediates lipogenesis under hypoxia," *Nature*, vol. 481, no. 7381, pp. 380–384, 2012.
- [24] C. M. Metallo, J. L. Walther, and G. Stephanopoulos, "Evaluation of 13C isotopic tracers for metabolic flux analysis in mammalian cells.," *J. Biotechnol.*, vol. 144, no. 3, pp. 167–74, Nov. 2009.
- [25] S. B. Crown, N. Marze, and M. R. Antoniewicz, "Catabolism of branched chain amino acids contributes significantly to synthesis of odd-chain and even-chain fatty acids in 3T3-L1 adipocytes," *PLoS One*, vol. 10, no. 12, Dec. 2015.
- [26] M. R. Antoniewicz, "A guide to 13 C metabolic flux analysis for the cancer biologist," *Exp. Mol. Med.*, vol. 50, no. 4, 2018.
- [27] T. A. Murphy and J. D. Young, "ETA: Robust software for determination of cell specific rates from extracellular time courses," *Biotechnol. Bioeng.*, vol. 110, no. 6, pp. 1748–1758, Jun. 2013.
- [28] R. F. Kletzien and J. F. Perdue, "Induction of sugar transport in chick embryo fibroblasts by hexose starvation. Evidence for transcriptional regulation of transport," *J. Biol. Chem.*, vol. 250, no. 2, pp. 593–600, Jan. 1975.
- [29] C. M. Hasenour *et al.*, "Mass spectrometry-based microassay of 2H and 13C plasma glucose labeling to quantify liver metabolic fluxes in vivo.," *Am. J. Physiol. Endocrinol. Metab.*, vol. 309, no. 2, pp. E191-203, Jul. 2015.
- [30] M. Schnelle *et al.*, "In vivo [U-13C]glucose labeling to assess heart metabolism in murine models of pressure and volume overload," *Am. J. Physiol. - Hear. Circ. Physiol.*, vol. 319, no. 2, pp. H422–H431, Aug. 2020.
- [31] K. F. Petersen, S. Dufour, G. W. Cline, and G. I. Shulman, "Regulation of hepatic mitochondrial oxidation by glucose-alanine cycling during starvation in humans," *J. Clin. Invest.*, vol. 129, no. 11, pp. 4671–4675, Nov. 2019.
- [32] J. A. Fletcher, S. Deja, S. Satapati, X. Fu, S. C. Burgess, and J. D. Browning, "Impaired ketogenesis and increased acetyl-CoA oxidation promote hyperglycemia in human fatty liver," *JCI Insight*, vol. 4, no. 11, Jun. 2019.
- [33] J. E. Ayala *et al.*, "Hyperinsulinemic-euglycemic clamps in conscious, unrestrained mice.," *J. Vis. Exp.*, no. 57, pp. e3188–e3188, Nov. 2011.
- [34] C. Des Rosiers, S. Lloyd, B. Comte, and J. C. Chatham, "A critical perspective of the use of 13C-isotopomer analysis by GCMS and NMR as applied to cardiac metabolism," *Metab. Eng.*, vol. 6, no. 1, pp. 44–58, Jan. 2004.

- [35] J. C. Chatham, B. Bouchard, and C. Des Rosiers, "A comparison between NMR and GCMS  $^{13}\text{C}$ -isotopomer analysis in cardiac metabolism," *Mol. Cell. Biochem.*, vol. 249, no. 1–2, pp. 105–112, Jul. 2003.
- [36] L. Di Donato, C. Des Rosiers, J. A. Montgomery, F. David, M. Garneau, and H. Brunengraber, "Rates of gluconeogenesis and citric acid cycle in perfused livers, assessed from the mass spectrometric assay of the  $^{13}\text{C}$  labeling pattern of glutamate.," *J. Biol. Chem.*, vol. 268, no. 6, pp. 4170–80, Feb. 1993.
- [37] B. Comte, G. Vincent, B. Bouchard, M. Jetté, S. Cordeau, and C. D. Rosiers, "A  $^{13}\text{C}$  mass isotopomer study of anaplerotic pyruvate carboxylation in perfused rat hearts.," *J. Biol. Chem.*, vol. 272, no. 42, pp. 26125–31, Oct. 1997.
- [38] A. H. M. Emwas, "The strengths and weaknesses of NMR spectroscopy and mass spectrometry with particular focus on metabolomics research," *Methods Mol. Biol.*, vol. 1277, pp. 161–193, 2015.
- [39] K. Schmidt, M. Carlsen, J. Nielsen, and J. Villadsen, "Modeling isotopomer distributions in biochemical networks using isotopomer mapping matrices.," *Biotechnol. Bioeng.*, vol. 55, no. 6, pp. 831–40, Sep. 1997.
- [40] J. Katz, P. Wals, and W. N. P. Lee, "Isotopomer studies of gluconeogenesis and the Krebs cycle with  $^{13}\text{C}$ -labeled lactate," *J. Biol. Chem.*, vol. 268, no. 34, pp. 25509–25521, 1993.
- [41] M. R. Antoniewicz, J. K. Kelleher, and G. Stephanopoulos, "Measuring deuterium enrichment of glucose hydrogen atoms by gas chromatography/mass spectrometry," *Anal. Chem.*, vol. 83, no. 8, pp. 3211–3216, 2011.
- [42] L. Holm *et al.*, "An exploration of the methods to determine the protein-specific synthesis and breakdown rates in vivo in humans.," *Physiol. Rep.*, vol. 7, no. 17, p. e14143, Sep. 2019.
- [43] T. Mairinger, J. Sanderson, and S. Hann, "GC-QTOFMS with a low-energy electron ionization source for advancing isotopologue analysis in  $^{13}\text{C}$ -based metabolic flux analysis," *Anal. Bioanal. Chem.*, vol. 411, no. 8, pp. 1495–1502, 2019.
- [44] O. Al Kadhi, A. Melchini, R. Mithen, and S. Saha, "Development of a LC-MS/MS Method for the Simultaneous Detection of Tricarboxylic Acid Cycle Intermediates in a Range of Biological Matrices," *J. Anal. Methods Chem.*, vol. 2017, pp. 1–12, 2017.
- [45] E. J. Want, A. Nordström, H. Morita, and G. Siuzdak, "From exogenous to endogenous: The inevitable imprint of mass spectrometry in metabolomics," *Journal of Proteome Research*, vol. 6, no. 2. American Chemical Society, pp. 459–468, Feb-2007.
- [46] M. Trötz Müller, A. Triebel, A. Ajsic, J. Hartler, H. Köfeler, and W. Regittnig, "Determination of the Isotopic Enrichment of  $^{13}\text{C}$ - and  $^2\text{H}$ -Labeled Tracers of Glucose Using High-Resolution Mass Spectrometry: Application to Dual- and Triple-Tracer Studies," *Anal. Chem.*, vol. 89, no. 22, pp. 12252–12260, Nov. 2017.
- [47] J. Choi and M. R. Antoniewicz, "Tandem mass spectrometry for  $^{13}\text{C}$  metabolic flux analysis: Methods and algorithms based on EMU framework," *Front. Microbiol.*, vol. 10, no. JAN, pp. 1–8, 2019.
- [48] C. M. Hasenour, M. Rahim, and J. D. Young, "In Vivo Estimates of Liver Metabolic Flux Assessed by  $^{13}\text{C}$ -Propionate and  $^{13}\text{C}$ -Lactate Are Impacted by Tracer Recycling and Equilibrium Assumptions.," *Cell Rep.*, vol. 32, no. 5, p. 107986, Aug. 2020.
- [49] I. Martínez-Reyes and N. S. Chandel, "Waste Not, Want Not: Lactate Oxidation Fuels the TCA Cycle," *Cell Metab.*, vol. 26, no. 6, pp. 803–804, Dec. 2017.
- [50] C. R. Malloy, A. D. Sherry, and F. M. H. Jeffrey, "Analysis of tricarboxylic acid cycle of the heart using  $^{13}\text{C}$  isotope isomers.," *Am. J. Physiol.*, vol. 259, no. 3 Pt 2, pp. H987-95, 1990.

- [51] J. G. Jones, M. A. Solomon, S. M. Cole, A. D. Sherry, and C. R. Malloy, "An integrated  $^2\text{H}$  and  $^{13}\text{C}$  NMR study of gluconeogenesis and TCA cycle flux in humans," *Am. J. Physiol. Metab.*, vol. 281, no. 4, pp. E848–E856, Oct. 2001.
- [52] S. M. Cohen, R. G. Shulman, and A. C. McLaughlin, "Effects of ethanol on alanine metabolism in perfused mouse liver studied by  $^{13}\text{C}$  NMR," *Proc. Natl. Acad. Sci. U. S. A.*, vol. 76, no. 10, pp. 4808–4812, Oct. 1979.
- [53] T. E. Walker, C. H. Han, V. H. Kollman, R. E. London, and N. A. Matwiyoff, " $^{13}\text{C}$  nuclear magnetic resonance studies of the biosynthesis by *Microbacterium ammoniaphilum* of L-glutamate selectively enriched with carbon-13," *J. Biol. Chem.*, vol. 257, no. 3, pp. 1189–95, Feb. 1982.
- [54] A. W. H. Jans and R. Willem, "A  $^{13}\text{C}$ -n.m.r. investigation of the metabolism of amino acids in renal proximal convoluted tubules of normal and streptozotocin-treated rats and rabbits," *Biochem. J.*, vol. 263, no. 1, pp. 231–241, 1989.
- [55] K. SONNTAG, L. EGGELING, A. A. DE GRAAF, and H. SAHM, "Flux partitioning in the split pathway of lysine synthesis in *Corynebacterium glutamicum* Quantification by  $^{13}\text{C}$ - and  $^1\text{H}$ -NMR spectroscopy," *Eur. J. Biochem.*, vol. 213, no. 3, pp. 1325–1331, May 1993.
- [56] C. Zupke and G. Stephanopoulos, "Intracellular flux analysis in hybridomas using mass balances and in vitro  $^{13}\text{C}$  nmr," *Biotechnol. Bioeng.*, vol. 45, no. 4, pp. 292–303, Feb. 1995.
- [57] A. Marx, A. A. de Graaf, W. Wiechert, L. Eggeling, and H. Sahm, "Determination of the fluxes in the central metabolism of *Corynebacterium glutamicum* by nuclear magnetic resonance spectroscopy combined with metabolite balancing," *Biotechnol. Bioeng.*, vol. 49, no. 2, pp. 111–29, Jan. 1996.
- [58] T. Szyperki, "Biosynthetically Directed Fractional  $^{13}\text{C}$ -labeling of Proteinogenic Amino Acids: An Efficient Analytical Tool to Investigate Intermediary Metabolism," *Eur. J. Biochem.*, vol. 232, no. 2, pp. 433–448, 1995.
- [59] K. Schmidt, J. Nielsen, and J. Villadsen, "Quantitative analysis of metabolic fluxes in *Escherichia coli*, using two-dimensional NMR spectroscopy and complete isotopomer models," in *Journal of Biotechnology*, 1999, vol. 71, no. 1–3, pp. 175–189.
- [60] Z. Pan and D. Raftery, "Comparing and combining NMR spectroscopy and mass spectrometry in metabolomics," *Anal. Bioanal. Chem.*, vol. 387, no. 2, pp. 525–527, Jan. 2007.
- [61] J. G. Jones, M. A. Solomon, A. Dean Sherry, F. M. H. Jeffrey, and C. R. Malloy, " $^{13}\text{C}$  NMR measurements of human gluconeogenic fluxes after ingestion of [U- $^{13}\text{C}$ ]propionate, phenylacetate, and acetaminophen," *Am. J. Physiol. - Endocrinol. Metab.*, vol. 275, no. 5, pp. 38–5, 1998.
- [62] M. Beylot, M. V. Soloviev, F. David, B. R. Landau, and H. Brunengraber, "Tracing hepatic gluconeogenesis relative to citric acid cycle activity in vitro and in vivo: Comparisons in the use of [3- $^{13}\text{C}$ ]lactate, [2- $^{13}\text{C}$ ]acetate, and  $\alpha$ -keto[3- $^{13}\text{C}$ ]isocaproate," *J. Biol. Chem.*, vol. 270, no. 4, pp. 1509–1514, 1995.
- [63] B. R. Landau, J. Wahren, V. Chandramouli, W. C. Schumann, K. Ekberg, and S. C. Kalhan, "Contributions of gluconeogenesis to glucose production in the fasted state," *J. Clin. Invest.*, vol. 98, no. 2, pp. 378–385, Jul. 1996.
- [64] E. Ferrannini *et al.*, "The disposal of an oral glucose load in patients with non-insulin-dependent diabetes," *Metabolism*, vol. 37, no. 1, pp. 79–85, 1988.
- [65] S. Deja *et al.*, "Simultaneous tracers and a unified model of positional and mass isotopomers for quantification of metabolic flux in liver," *Metab. Eng.*, vol. 59, pp. 1–14, May 2020.
- [66] C. B. Prasanna, V. Mishra, D. Jaiswal, and P. P. Wangikar, "Mass Isotopologue Distribution of dimer ion adducts of intracellular metabolites for potential applications in  $^{13}\text{C}$  Metabolic Flux

- Analysis,” *PLoS One*, vol. 14, no. 8, p. e0220412, Aug. 2019.
- [67] M. Ying, C. Guo, and X. Hu, “The quantitative relationship between isotopic and net contributions of lactate and glucose to the tricarboxylic acid (TCA) cycle,” *J. Biol. Chem.*, vol. 294, no. 24, pp. 9615–9630, Jun. 2019.
- [68] T. K. Bednarski, M. Rahim, and J. D. Young, “In vivo 2H/13C flux analysis in metabolism research,” *Curr. Opin. Biotechnol.*, vol. 71, pp. 1–8, Oct. 2021.
- [69] J. D. Young, “INCA: A computational platform for isotopically non-stationary metabolic flux analysis,” *Bioinformatics*, vol. 30, no. 9, pp. 1333–1335, May 2014.
- [70] H. Yoo, M. R. Antoniewicz, G. Stephanopoulos, and J. K. Kelleher, “Quantifying reductive carboxylation flux of glutamine to lipid in a brown adipocyte cell line,” *J. Biol. Chem.*, vol. 283, no. 30, pp. 20621–20627, Jul. 2008.
- [71] M. S. Shupletsov, L. I. Golubeva, S. S. Rubina, D. A. Podvyaznikov, S. Iwatani, and S. V Mashko, “OpenFLUX2: 13C-MFA modeling software package adjusted for the comprehensive analysis of single and parallel labeling experiments,” *Microb. Cell Fact.*, vol. 13, no. 1, p. 152, Dec. 2014.
- [72] S. Kajihata, C. Furusawa, F. Matsuda, and H. Shimizu, “OpenMebius: An open source software for isotopically nonstationary 13C-based metabolic flux analysis,” *Biomed Res. Int.*, vol. 2014, 2014.
- [73] L. He, S. G. Wu, M. Zhang, Y. Chen, and Y. J. Tang, “WUFlux: An open-source platform for 13C metabolic flux analysis of bacterial metabolism,” *BMC Bioinformatics*, vol. 17, no. 1, p. 1, Nov. 2016.
- [74] M. R. Antoniewicz, J. K. Kelleher, and G. Stephanopoulos, “Elementary metabolite units (EMU): A novel framework for modeling isotopic distributions,” *Metab. Eng.*, vol. 9, no. 1, pp. 68–86, Jan. 2007.
- [75] M. R. Antoniewicz, J. K. Kelleher, and G. Stephanopoulos, “Determination of confidence intervals of metabolic fluxes estimated from stable isotope measurements,” *Metab. Eng.*, vol. 8, no. 4, pp. 324–337, 2006.
- [76] J. R. Alger, A. D. Sherry, and C. R. Malloy, “tcaSIM: A Simulation Program for Optimal Design of 13C Tracer Experiments for Analysis of Metabolic Flux by NMR and Mass Spectroscopy,” *Curr. Metabolomics*, vol. 6, no. 3, pp. 176–187, Dec. 2018.
- [77] M. C. Dange *et al.*, “Evaluation of freely available software tools for untargeted quantification of 13C isotopic enrichment in cellular metabolome from HR-LC/MS data,” *Metab. Eng. Commun.*, vol. 10, no. August 2019, p. e00120, 2020.
- [78] M. Weitzel, K. Nöh, T. Dalman, S. Niedenführ, B. Stute, and W. Wiechert, “13CFLUX2—high-performance software suite for 13C-metabolic flux analysis,” *Bioinformatics*, vol. 29, no. 1, pp. 143–145, Jan. 2013.
- [79] T. Mairinger *et al.*, “Comprehensive assessment of measurement uncertainty in 13C-based metabolic flux experiments,” *Anal. Bioanal. Chem.*, vol. 410, no. 14, pp. 3337–3348, 2018.
- [80] M. A. Orman, J. Mattick, I. P. Androulakis, F. Berthiaume, and M. G. Ierapetritou, “Stoichiometry based steady-state hepatic flux analysis: Computational and experimental aspects,” *Metabolites*, vol. 2, no. 1. MDPI AG, pp. 268–291, 14-Mar-2012.
- [81] R. A. Egnatchik, A. K. Leamy, D. A. Jacobson, M. Shiota, and J. D. Young, “ER calcium release promotes mitochondrial dysfunction and hepatic cell lipotoxicity in response to palmitate overload,” *Mol. Metab.*, vol. 3, no. 5, pp. 544–553, Aug. 2014.
- [82] R. A. Egnatchik, A. K. Leamy, Y. Noguchi, M. Shiota, and J. D. Young, “Palmitate-induced activation of mitochondrial metabolism promotes oxidative stress and apoptosis in H4IIEC3 rat hepatocytes,” *Metabolism*, vol. 63, no. 2, pp. 283–295, Feb. 2014.

- [83] A. D. Cherrington, "Control of glucose uptake and release by the liver in vivo," in *Diabetes*, 1999, vol. 48, no. 5, pp. 1198–1214.
- [84] D. H. Wasserman and A. D. Cherrington, "Hepatic fuel metabolism during muscular work: Role and regulation," *American Journal of Physiology - Endocrinology and Metabolism*, vol. 260, no. 6 23/6. Am J Physiol, 1991.
- [85] J. Wahren and K. Ekberg, "Splanchnic regulation of glucose production," *Annual Review of Nutrition*, vol. 27. Annu Rev Nutr, pp. 329–345, 2007.
- [86] C. J. Ramnanan *et al.*, "Molecular characterization of insulin-mediated suppression of hepatic glucose production in vivo," *Diabetes*, vol. 59, no. 6, pp. 1302–1311, Jun. 2010.
- [87] K. F. Petersen *et al.*, "Contributions of net hepatic glycogenolysis and gluconeogenesis to glucose production in cirrhosis," *Am. J. Physiol. - Endocrinol. Metab.*, vol. 276, no. 3 39-3, 1999.
- [88] D. L. Rothman, I. Magnusson, L. D. Katz, R. G. Shulman, and G. I. Shulman, "Quantitation of hepatic glycogenolysis and gluconeogenesis in fasting humans with <sup>13</sup>C NMR," *Science (80-. )*, vol. 254, no. 5031, pp. 573–576, 1991.
- [89] B. R. Landau *et al.*, "A limitation in the use of mass isotopomer distributions to measure gluconeogenesis in fasting humans," *Am. J. Physiol. - Endocrinol. Metab.*, vol. 269, no. 1 32-1, 1995.
- [90] S. F. Previs, C. A. Fernandez, D. Yang, M. V. Soloviev, F. David, and H. Brunengraber, "Limitations of the mass isotopomer distribution analysis of glucose to study gluconeogenesis: Substrate cycling between glycerol and triose phosphates in liver," *J. Biol. Chem.*, vol. 270, no. 34, pp. 19806–19815, Aug. 1995.
- [91] S. F. Previs and H. Brunengraber, "Methods for measuring gluconeogenesis in vivo," *Curr. Opin. Clin. Nutr. Metab. Care*, vol. 1, no. 5, pp. 461–465, 1998.
- [92] S. F. Previs, G. W. Cline, and G. I. Shulman, "A critical evaluation of mass isotopomer distribution analysis of gluconeogenesis in vivo," *Am. J. Physiol. - Endocrinol. Metab.*, vol. 277, no. 1 40-1, 1999.
- [93] O. Peroni, V. Large, F. Diraison, and M. Beylot, "Glucose production and gluconeogenesis in postabsorptive and starved normal and streptozotocin-diabetic rats," *Metabolism.*, vol. 46, no. 11, pp. 1358–1363, 1997.
- [94] V. Chandramouli, K. Ekberg, W. C. Schumann, S. C. Kalhan, J. Wahren, and B. R. Landau, "Quantifying gluconeogenesis during fasting," *Am. J. Physiol. - Endocrinol. Metab.*, vol. 273, no. 6 36-6, 1997.
- [95] B. R. Landau, J. Wahren, V. Chandramouli, W. C. Schumann, K. Ekberg, and S. C. Kalhan, "Use of <sup>2</sup>H<sub>2</sub>O for estimating rates of gluconeogenesis: Application to the fasted state," *J. Clin. Invest.*, vol. 95, no. 1, pp. 172–178, 1995.
- [96] R. ROGNSTAD, J. KATZ, and D. G. CLARK, "Glucose Synthesis in Tritiated Water," *Eur. J. Biochem.*, vol. 47, no. 2, pp. 383–388, 1974.
- [97] Z. K. Guo, W. N. Paul Lee, J. Katz, and A. E. Bergner, "Quantitation of Positional isomers of deuterium-labeled glucose by gas chromatography/mass spectrometry," *Anal. Biochem.*, vol. 204, no. 2, pp. 273–282, Aug. 1992.
- [98] B. R. Landau, "Stable isotope techniques for the study of gluconeogenesis in man," *Hormone and Metabolic Research*, vol. 29, no. 7. Georg Thieme Verlag, pp. 334–336, 1997.
- [99] S. Satapati *et al.*, "Elevated TCA cycle function in the pathology of diet-induced hepatic insulin resistance and fatty liver," *J. Lipid Res.*, vol. 53, no. 6, pp. 1080–1092, Jun. 2012.



- [100] S. C. Burgess *et al.*, “Effect of murine strain on metabolic pathways of glucose production after brief or prolonged fasting,” *Am. J. Physiol. Metab.*, vol. 289, no. 1, pp. E53–E61, 2005.
- [101] P. She *et al.*, “Mechanisms by which liver-specific PEPCK knockout mice preserve euglycemia during starvation,” *Diabetes*, vol. 52, no. 7, pp. 1649–54, Jul. 2003.
- [102] A. Wajngot *et al.*, “Quantitative contributions of gluconeogenesis to glucose production during fasting in type 2 diabetes mellitus,” *Metabolism*, vol. 50, no. 1, pp. 47–52, Jan. 2001.
- [103] A. L. Sunehag, M. W. Haymond, R. J. Schanler, P. J. Reeds, and D. M. Bier, “Gluconeogenesis in very low birth weight infants receiving total parenteral nutrition,” *Diabetes*, vol. 48, no. 4, pp. 791–800, 1999.
- [104] E. Dekker *et al.*, “Glucose production and gluconeogenesis in adults with uncomplicated falciparum malaria,” *Am. J. Physiol. - Endocrinol. Metab.*, vol. 272, no. 6 35-6, 1997.
- [105] E. S. Jin, S. A. Beddow, C. R. Malloy, and V. T. Samuel, “Hepatic glucose production pathways after three days of a high-fat diet,” *Metabolism*, vol. 62, no. 1, pp. 152–162, Jan. 2013.
- [106] E. S. Jin, S. C. Burgess, M. E. Merritt, A. D. Sherry, and C. R. Malloy, “Differing mechanisms of hepatic glucose overproduction in triiodothyronine-treated rats vs. Zucker diabetic fatty rats by NMR analysis of plasma glucose,” *Am. J. Physiol. Metab.*, vol. 288, no. 4, pp. E654–E662, 2005.
- [107] N. E. Sunny, E. J. Parks, J. D. Browning, and S. C. Burgess, “Excessive hepatic mitochondrial TCA cycle and gluconeogenesis in humans with nonalcoholic fatty liver disease,” *Cell Metab.*, vol. 14, no. 6, pp. 804–810, 2011.
- [108] B. Kucejova *et al.*, “Hepatic mTORC1 Opposes Impaired Insulin Action to Control Mitochondrial Metabolism in Obesity,” *Cell Rep.*, vol. 16, no. 2, pp. 508–519, Jul. 2016.
- [109] S. Satapati *et al.*, “Mitochondrial metabolism mediates oxidative stress and inflammation in fatty liver,” *J. Clin. Invest.*, vol. 125, no. 12, pp. 4447–4462, Dec. 2015.
- [110] D. A. Cappel *et al.*, “Pyruvate-Carboxylase-Mediated Anaplerosis Promotes Antioxidant Capacity by Sustaining TCA Cycle and Redox Metabolism in Liver,” *Cell Metab.*, vol. 29, no. 6, pp. 1291–1305.e8, 2019.
- [111] J. G. Jones, R. Naidoo, A. D. D. Sherry, F. M. H. M. H. Jeffrey, G. L. L. Cottam, and C. R. Malloy, “Measurement of gluconeogenesis and pyruvate recycling in the rat liver: a simple analysis of glucose and glutamate isotopomers during metabolism of [1,2,3-<sup>13</sup>C<sub>3</sub>]propionate,” *FEBS Lett.*, vol. 412, no. 1, pp. 131–137, Jul. 1997.
- [112] C. R. Malloy, A. D. Sherry, and F. M. H. Jeffrey, “Carbon flux through citric acid cycle pathways in perfused heart by <sup>13</sup>C NMR spectroscopy,” *FEBS Lett.*, vol. 212, no. 1, pp. 58–62, Feb. 1987.
- [113] E. H. STRISOWER, G. D. KOHLER, and I. L. CHAIKOFF, “Incorporation of acetate carbon into glucose by liver slices from normal and alloxan-diabetic rats,” *J. Biol. Chem.*, vol. 198, no. 1, pp. 115–26, Sep. 1952.
- [114] E. O. WEINMAN, E. H. STRISOWER, and I. L. CHAIKOFF, “Conversion of fatty acids to carbohydrate; application of isotopes to this problem and role of the Krebs cycle as a synthetic pathway,” *Physiol. Rev.*, vol. 37, no. 2, pp. 252–72, Apr. 1957.
- [115] B. R. LANDAU, G. E. BARTSCH, J. KATZ, and H. G. WOOD, “ESTIMATION OF PATHWAY CONTRIBUTIONS TO GLUCOSE METABOLISM AND OF THE RATE OF ISOMERIZATION OF HEXOSE 6-PHOSPHATE,” *J. Biol. Chem.*, vol. 239, no. 3, pp. 686–96, Mar. 1964.
- [116] J. H. Exton and C. R. Park, “Control of gluconeogenesis in liver. I. General features of gluconeogenesis in the perfused livers of rats,” *J. Biol. Chem.*, vol. 242, no. 11, pp. 2622–36, Jun. 1967.

- [117] R. Rognstad and J. Katz, "Gluconeogenesis in the kidney cortex. Effects of D-malate and aminoxyacetate.," *Biochem. J.*, vol. 116, no. 3, pp. 483–91, Feb. 1970.
- [118] J. Katz, "Determination of gluconeogenesis in vivo with <sup>14</sup>C-labeled substrates.," *Am. J. Physiol.*, vol. 248, no. 4 Pt 2, pp. R391-9, Apr. 1985.
- [119] J. K. Kelleher, "Gluconeogenesis from labeled carbon: estimating isotope dilution.," *Am. J. Physiol.*, vol. 250, no. 3 Pt 1, pp. E296-305, Mar. 1986.
- [120] W.-N. N. Lee, "Appendix. Analysis of tricarboxylic acid cycle using mass isotopomer ratios.," *J. Biol. Chem.*, vol. 268, no. 34, pp. 25522–6, Dec. 1993.
- [121] S. F. Previs and D. E. Kelley, "Tracer-based assessments of hepatic anaplerotic and TCA cycle flux: practicality, stoichiometry, and hidden assumptions," *Am J Physiol Endocrinol Metab*, vol. 309, pp. 727–735, 2015.
- [122] S. Deja, B. Kucejova, X. Fu, J. D. Browning, J. D. Young, and S. Burgess, "In Vivo Estimation of Ketogenesis Using Metabolic Flux Analysis—Technical Aspects and Model Interpretation," *Metabolites*, vol. 11, no. 5, p. 279, Apr. 2021.
- [123] J. C. Henquin, "Regulation of insulin secretion: A matter of phase control and amplitude modulation," *Diabetologia*, vol. 52, no. 5. Springer, pp. 739–751, 14-May-2009.
- [124] T. C. Alves *et al.*, "Integrated, Step-Wise, Mass-Isotopomeric Flux Analysis of the TCA Cycle," *Cell Metab.*, vol. 22, no. 5, pp. 936–947, Nov. 2015.
- [125] A. Khan, Z. C. Ling, and B. R. Landau, "Quantifying the carboxylation of pyruvate in pancreatic islets," *J. Biol. Chem.*, vol. 271, no. 5, pp. 2539–2542, Feb. 1996.
- [126] D. Lu *et al.*, "<sup>13</sup>C NMR isotopomer analysis reveals a connection between pyruvate cycling and glucose-stimulated insulin secretion (GSIS)," *Proc. Natl. Acad. Sci. U. S. A.*, vol. 99, no. 5, pp. 2708–2713, Mar. 2002.
- [127] F. Schuit *et al.*, "Metabolic fate of glucose in purified islet cells. Glucose-regulated anaplerosis in  $\beta$  cells," *J. Biol. Chem.*, vol. 272, no. 30, pp. 18572–18579, 1997.
- [128] D. Lu *et al.*, "<sup>13</sup>C NMR isotopomer analysis reveals a connection between pyruvate cycling and glucose-stimulated insulin secretion (GSIS)," *Proc. Natl. Acad. Sci. U. S. A.*, vol. 99, no. 5, pp. 2708–2713, Mar. 2002.
- [129] V. Attali, M. Parnes, Y. Ariav, E. Cerasi, N. Kaiser, and G. Leibowitz, "Regulation of insulin secretion and proinsulin biosynthesis by succinate," *Endocrinology*, vol. 147, no. 11, pp. 5110–5118, Nov. 2006.
- [130] S. Farfari, V. Schulz, B. Corkey, and M. Prentki, "Glucose-regulated anaplerosis and cataplerosis in pancreatic  $\beta$  cells: Possible implication of a pyruvate/citrate shuttle in insulin secretion," *Diabetes*, vol. 49, no. 5, pp. 718–726, 2000.
- [131] U. Fransson, A. H. Rosengren, F. C. Schuit, E. Renström, and H. Mulder, "Anaplerosis via pyruvate carboxylase is required for the fuel-induced rise in the ATP:ADP ratio in rat pancreatic islets," *Diabetologia*, vol. 49, no. 7, pp. 1578–1586, Jul. 2006.
- [132] G.-F. Zhang *et al.*, "Reductive TCA cycle metabolism fuels glutamine- and glucose-stimulated insulin secretion," *Cell Metab.*, vol. 33, no. 4, pp. 804-817.e5, Apr. 2021.
- [133] M. Ferdaoussi *et al.*, "Isocitrate-to-SEN1 signaling amplifies insulin secretion and rescues dysfunctional  $\beta$  cells," *J. Clin. Invest.*, vol. 125, no. 10, pp. 3847–3860, Oct. 2015.
- [134] M. A. Kalwat and M. H. Cobb, "Mechanisms of the amplifying pathway of insulin secretion in the  $\beta$  cell," *Pharmacology and Therapeutics*, vol. 179. Elsevier Inc., pp. 17–30, 01-Nov-2017.
- [135] P. Spéjel *et al.*, "Time-resolved metabolomics analysis of  $\beta$ -cells implicates the pentose phosphate

- pathway in the control of insulin release,” *Biochem. J.*, vol. 450, no. 3, pp. 595–605, Mar. 2013.
- [136] I. Goehring *et al.*, “Identification of an intracellular metabolic signature impairing beta cell function in the rat beta cell line INS-1E and human islets,” *Diabetologia*, vol. 54, no. 10, pp. 2584–2594, 2011.
- [137] M. Huang and J. W. Joseph, “Assessment of the metabolic pathways associated with glucose-stimulated biphasic insulin secretion,” *Endocrinology*, vol. 155, no. 5, pp. 1653–1666, 2014.
- [138] S. R. Jesinkey *et al.*, “Mitochondrial GTP Links Nutrient Sensing to  $\beta$  Cell Health, Mitochondrial Morphology, and Insulin Secretion Independent of OxPhos,” *Cell Rep.*, vol. 28, no. 3, pp. 759–772.e10, Jul. 2019.
- [139] R. G. Kibbey, R. L. Pongratz, A. J. Romanelli, C. B. Wollheim, G. W. Cline, and G. I. Shulman, “Mitochondrial GTP Regulates Glucose-Stimulated Insulin Secretion,” *Cell Metab.*, vol. 5, no. 4, pp. 253–264, Apr. 2007.
- [140] J. R. Gooding *et al.*, “Adenylosuccinate Is an Insulin Secretagogue Derived from Glucose-Induced Purine Metabolism,” *Cell Rep.*, vol. 13, no. 1, pp. 157–167, Oct. 2015.
- [141] S. L. Lewandowski *et al.*, “Pyruvate Kinase Controls Signal Strength in the Insulin Secretory Pathway,” *Cell Metab.*, vol. 32, no. 5, pp. 736–750.e5, Nov. 2020.
- [142] L. D. Pound *et al.*, “G6PC2: A negative regulator of basal glucose-stimulated insulin secretion,” *Diabetes*, vol. 62, no. 5, pp. 1547–1556, 2013.
- [143] M. L. Wall, L. D. Pound, I. Trenary, R. M. O’Brien, and J. D. Young, “Novel Stable Isotope Analyses Demonstrate Significant Rates of Glucose Cycling in Mouse Pancreatic Islets,” *Diabetes*, vol. 64, no. 6, pp. 2129–2137, 2015.
- [144] M. Morsi, T. Schulze, E. Früh, D. Brüning, U. Panten, and I. Rustenbeck, “Fresh and cultured mouse islets differ in their response to nutrient stimulation,” *Endocr. Connect.*, vol. 9, no. 8, pp. 769–782, 2020.
- [145] K. J. Bosma *et al.*, “Pancreatic islet beta cell-specific deletion of G6pc2 reduces fasting blood glucose,” *J. Mol. Endocrinol.*, vol. 64, no. 4, pp. 235–248, May 2020.
- [146] X. Li *et al.*, “Additive effects of genetic variation in GCK and G6PC2 on insulin secretion and fasting glucose,” *Diabetes*, vol. 58, no. 12, pp. 2946–2953, Dec. 2009.
- [147] C. Zusi *et al.*, “Haplotypes of the genes (GCK and G6PC2) underlying the glucose/glucose-6-phosphate cycle are associated with pancreatic beta cell glucose sensitivity in patients with newly diagnosed type 2 diabetes from the VNDS study (VNDS 11),” *J. Endocrinol. Invest.*, pp. 1–8, Jun. 2021.
- [148] J. C. Chatham, J. R. Forder, J. D. Glickson, and E. M. Chance, “Calculation of absolute metabolic flux and the elucidation of the pathways of glutamate labeling in perfused rat heart by  $^{13}\text{C}$  NMR spectroscopy and nonlinear least squares analysis,” *J. Biol. Chem.*, vol. 270, no. 14, pp. 7999–8008, Apr. 1995.
- [149] F. M. H. Jeffrey, V. Diczku, A. D. Sherry, and C. R. Malloy, “Substrate selection in the isolated working rat heart: effects of reperfusion, afterload, and concentration,” *Basic Res. Cardiol.*, vol. 90, no. 5, pp. 388–396, Sep. 1995.
- [150] A. K. Olson, B. Bouchard, X.-H. Ning, N. Isern, C. Des Rosiers, and M. A. Portman, “Triiodothyronine increases myocardial function and pyruvate entry into the citric acid cycle after reperfusion in a model of infant cardiopulmonary bypass,” *Am. J. Physiol. Heart Circ. Physiol.*, vol. 302, no. 5, pp. H1086–93, Mar. 2012.
- [151] B. Lagerwaard, J. Keijer, K. K. McCully, V. C. J. de Boer, and A. G. Nieuwenhuizen, “In vivo assessment of muscle mitochondrial function in healthy, young males in relation to parameters of

- aerobic fitness,” *Eur. J. Appl. Physiol.*, vol. 119, no. 8, pp. 1799–1808, Aug. 2019.
- [152] O. J. Rider *et al.*, “Noninvasive In Vivo Assessment of Cardiac Metabolism in the Healthy and Diabetic Human Heart Using Hyperpolarized <sup>13</sup> C MRI,” *Circ. Res.*, vol. 126, no. 6, pp. 725–736, Mar. 2020.
- [153] S. B. Crown, J. K. Kelleher, R. Rouf, D. M. Muoio, and M. R. Antoniewicz, “Comprehensive metabolic modeling of multiple <sup>13</sup>C-isotopomer data sets to study metabolism in perfused working hearts,” *Am. J. Physiol. - Hear. Circ. Physiol.*, vol. 311, no. 4, pp. H881–H891, 2016.
- [154] C. Purmal, B. Kucejova, A. D. Sherry, S. C. Burgess, C. R. Malloy, and M. E. Merritt, “Propionate stimulates pyruvate oxidation in the presence of acetate,” *AJP Hear. Circ. Physiol.*, vol. 307, no. 8, pp. H1134–H1141, 2014.
- [155] A. K. Olson, B. Bouchard, X. H. Ning, N. Isern, C. des Rosiers, and M. A. Portman, “Triiodothyronine increases myocardial function and pyruvate entry into the citric acid cycle after reperfusion in a model of infant cardiopulmonary bypass,” *Am. J. Physiol. - Hear. Circ. Physiol.*, vol. 302, no. 5, p. H1086, Mar. 2012.
- [156] R. A. DeFronzo, “Insulin resistance: A multifaceted syndrome responsible for NIDDM, obesity, hypertension, dyslipidaemia and atherosclerosis,” *Neth. J. Med.*, vol. 50, no. 5, pp. 191–197, May 1997.
- [157] E. Horton and R. Terjung, *Exercise, nutrition, and energy metabolism*. 1988.
- [158] L. Szczepaniak, E. E. Babcock, C. R. Malloy, and A. D. Sherry, “Oxidation of acetate in rabbit skeletal muscle: Detection by <sup>13</sup>C NMR spectroscopy in vivo,” *Magn. Reson. Med.*, vol. 36, no. 3, pp. 451–457, 1996.
- [159] M. E. Walton, D. Ebert, and R. G. Haller, “Relative rates of anaplerotic flux in rested and contracted rat skeletal muscle measured by <sup>13</sup>C NMR spectroscopy,” *J. Physiol.*, vol. 548, no. 2, pp. 541–548, Apr. 2003.
- [160] D. E. Befroy, K. F. Petersen, S. Dufour, G. F. Mason, D. L. Rothman, and G. I. Shulman, “Increased substrate oxidation and mitochondrial uncoupling in skeletal muscle of endurance-trained individuals,” *Proc. Natl. Acad. Sci. U. S. A.*, vol. 105, no. 43, pp. 16701–16706, Oct. 2008.
- [161] D. E. Befroy *et al.*, “Impaired Mitochondrial Substrate Oxidation in Muscle of Insulin-Resistant Offspring of Type 2 Diabetic Patients,” *Diabetes*, vol. 56, no. 5, pp. 1376–1381, May 2007.
- [162] B. M. Jucker *et al.*, “Assessment of mitochondrial energy coupling in vivo by <sup>13</sup>C/<sup>31</sup>P NMR,” *Proc. Natl. Acad. Sci. U. S. A.*, vol. 97, no. 12, pp. 6880–4, Jun. 2000.
- [163] S. Hui *et al.*, “Glucose feeds the TCA cycle via circulating lactate,” *Nature*, vol. 551, no. 7678, pp. 115–118, Oct. 2017.
- [164] S. Liu, Z. Dai, D. E. Cooper, D. G. Kirsch, and J. W. Locasale, “Quantitative Analysis of the Physiological Contributions of Glucose to the TCA Cycle,” *Cell Metab.*, vol. 32, no. 4, pp. 1–10, 2020.
- [165] Y. Wang, H. Kwon, X. Su, and F. E. Wondisford, “Glycerol not lactate is the major net carbon source for gluconeogenesis in mice during both short and prolonged fasting,” *Mol. Metab.*, vol. 31, no. November 2019, pp. 36–44, 2020.
- [166] T. TeSlaa *et al.*, “The Source of Glycolytic Intermediates in Mammalian Tissues,” *Cell Metab.*, vol. 33, no. 2, pp. 367–378.e5, 2021.
- [167] S. Hui *et al.*, “Quantitative Fluxomics of Circulating Metabolites,” *Cell Metab.*, vol. 32, no. 4, pp. 676–688.e4, Oct. 2020.
- [168] J. C. Hutton and R. M. O’Brien, “Glucose-6-phosphatase catalytic subunit gene family,” *J. Biol.*

- Chem.*, vol. 284, no. 43, pp. 29241–29245, Oct. 2009.
- [169] M. Veiga-da-Cunha *et al.*, “Failure to eliminate a phosphorylated glucose analog leads to neutropenia in patients with G6PT and G6PC3 deficiency,” *Proc. Natl. Acad. Sci. U. S. A.*, vol. 116, no. 4, pp. 1241–1250, 2019.
- [170] E. K. Brinkman, T. Chen, M. Amendola, and B. Van Steensel, “Easy quantitative assessment of genome editing by sequence trace decomposition,” *Nucleic Acids Res.*, vol. 42, no. 22, pp. e168–e168, Dec. 2014.
- [171] Y. Noguchi, J. D. Young, J. O. Aleman, M. E. Hansen, J. K. Kelleher, and G. Stephanopoulos, “Effect of anaplerotic fluxes and amino acid availability on hepatic lipoapoptosis,” *J. Biol. Chem.*, vol. 284, no. 48, pp. 33425–33436, Nov. 2009.
- [172] J. D. Young, D. K. Allen, and J. A. Morgan, “Isotopomer measurement techniques in metabolic flux analysis II: Mass spectrometry,” *Methods Mol. Biol.*, vol. 1083, pp. 85–108, 2014.
- [173] L. D. Pound *et al.*, “The Physiological Effects of Deleting the Mouse Slc30a8 Gene Encoding Zinc Transporter-8 Are Influenced by Gender and Genetic Background,” *PLoS One*, vol. 7, no. 7, p. e40972, Jul. 2012.
- [174] T. Bock, K. Svenstrup, B. Pakkenberg, and K. Buschard, “Unbiased estimation of total  $\beta$ -cell number and mean  $\beta$ -cell volume in rodent pancreas,” *APMIS*, vol. 107, no. 8, pp. 791–799, 1999.
- [175] H. A. Krebs and R. L. Veech, “Equilibrium relations between pyridine nucleotides and adenine nucleotides and their roles in the regulation of metabolic processes,” *Adv. Enzyme Regul.*, vol. 7, no. C, pp. 397–413, Jan. 1969.
- [176] T. D. Schmittgen and K. J. Livak, “Analyzing real-time PCR data by the comparative CT method,” *Nat. Protoc.*, vol. 3, no. 6, pp. 1101–1108, 2008.
- [177] C. Berger and D. Zdzieblo, “Glucose transporters in pancreatic islets,” *Pflügers Arch. - Eur. J. Physiol.* 2020 4729, vol. 472, no. 9, pp. 1249–1272, May 2020.
- [178] K. J. Bosma, M. Rahim, J. K. Oeser, O. P. McGuinness, J. D. Young, and R. M. O’Brien, “G6PC2 confers protection against hypoglycemia upon ketogenic diet feeding and prolonged fasting,” *Mol. Metab.*, vol. 41, p. 101043, Nov. 2020.
- [179] C. C. Martin *et al.*, “Cloning and Characterization of the Human and Rat Islet-specific Glucose-6-phosphatase Catalytic Subunit-related Protein (IGRP) Genes,” *J. Biol. Chem.*, vol. 276, no. 27, pp. 25197–25207, Jul. 2001.
- [180] W. Palm and C. B. Thompson, “Nutrient Acquisition Strategies of Mammalian Cells,” *Nature*, vol. 546, no. 7657, p. 234, Jun. 2017.
- [181] J. E. Campbell and C. B. Newgard, “Mechanisms controlling pancreatic islet cell function in insulin secretion,” *Nat. Rev. Mol. Cell Biol.*, vol. 22, no. 2, pp. 142–158, Feb. 2021.
- [182] S. M. Ronnebaum *et al.*, “A Pyruvate Cycling Pathway Involving Cytosolic NADP-dependent Isocitrate Dehydrogenase Regulates Glucose-stimulated Insulin Secretion \*,” 2006.
- [183] F. M. Matschinsky and J. E. Ellerman, “Metabolism of glucose in the islets of Langerhans,” *J. Biol. Chem.*, vol. 243, no. 10, pp. 2730–2736, May 1968.
- [184] F. M. Matschinsky, “Regulation of pancreatic  $\beta$ -cell glucokinase: From basics to therapeutics,” in *Diabetes*, 2002, vol. 51, no. SUPPL. 3, pp. S394–S404.
- [185] R. Stark *et al.*, “Phosphoenolpyruvate Cycling via Mitochondrial Phosphoenolpyruvate Carboxykinase Links Anaplerosis and Mitochondrial GTP with Insulin Secretion \* □ S,” 2009.
- [186] Y. Mugabo *et al.*, “Metabolic fate of glucose and candidate signaling and excess-fuel detoxification pathways in pancreatic  $\beta$ -cells,” *J. Biol. Chem.*, vol. 292, no. 18, pp. 7407–7422, 2017.

- [187] R. M. Malinowski *et al.*, “Pancreatic  $\beta$ -cells respond to fuel pressure with an early metabolic switch,” *Sci. Rep.*, vol. 10, no. 1, pp. 1–11, Dec. 2020.
- [188] Y. Mugabo *et al.*, “Identification of a mammalian glycerol-3-phosphate phosphatase: Role in metabolism and signaling in pancreatic  $\beta$ -cells and hepatocytes,” *Proc. Natl. Acad. Sci.*, p. 201514375, 2016.
- [189] S. Malmgreh *et al.*, “Tight coupling between glucose and mitochondrial metabolism in clonal  $\beta$ -cells is required for robust insulin secretion,” *J. Biol. Chem.*, vol. 284, no. 47, pp. 32395–32404, Nov. 2009.
- [190] R. L. Pongratz, R. G. Kibbey, G. I. Shulman, and G. W. Cline, “Cytosolic and mitochondrial malic enzyme isoforms differentially control insulin secretion,” *J. Biol. Chem.*, vol. 282, no. 1, pp. 200–207, Jan. 2007.
- [191] I. R *et al.*, “Redox control of exocytosis: regulatory role of NADPH, thioredoxin, and glutaredoxin,” *Diabetes*, vol. 54, no. 7, pp. 2132–2142, Jul. 2005.
- [192] X.-Q. Dai *et al.*, “SUMOylation Regulates Insulin Exocytosis Downstream of Secretory Granule Docking in Rodents and Humans,” *Diabetes*, vol. 60, no. 3, p. 838, Mar. 2011.
- [193] J. Wu, Z. Jin, H. Zheng, and L.-J. Yan, “Sources and implications of NADH/NAD(+) redox imbalance in diabetes and its complications,” *Diabetes. Metab. Syndr. Obes.*, vol. 9, pp. 145–53, May 2016.
- [194] J. T. Cole, W. S. Kean, H. B. Pollard, A. Verma, and W. D. Watson, “Glucose-6-phosphate reduces calcium accumulation in rat brain endoplasmic reticulum,” *Front. Mol. Neurosci.*, vol. 0, no. APRIL, p. 51, Apr. 2012.
- [195] B. A. Wolf, J. R. Colca, P. G. Comens, J. Turk, and M. L. McDaniel, “Glucose 6-phosphate regulates  $\text{Ca}^{2+}$  steady state in endoplasmic reticulum of islets. A possible link in glucose-induced insulin secretion,” *J. Biol. Chem.*, vol. 261, no. 35, pp. 16284–16287, 1986.
- [196] R. M. Denton, “Regulation of mitochondrial dehydrogenases by calcium ions,” *Biochim. Biophys. Acta*, vol. 1787, no. 11, pp. 1309–16, Nov. 2009.
- [197] R. M. O’Brien, “Moving on from GWAS: Functional Studies on the G6PC2 Gene Implicated in the Regulation of Fasting Blood Glucose,” *Curr. Diab. Rep.*, vol. 13, no. 6, pp. 768–777, Dec. 2013.
- [198] E. Wheeler, G. Marenne, and I. Barroso, “Genetic aetiology of glycaemic traits: Approaches and insights,” *Human Molecular Genetics*, vol. 26, no. R2. Oxford University Press, pp. R172–R184, 01-Oct-2017.
- [199] D. A. Baerenwald *et al.*, “Multiple functional polymorphisms in the G6PC2 gene contribute to the association with higher fasting plasma glucose levels,” *Diabetologia*, vol. 56, no. 6, pp. 1306–1316, Jun. 2013.
- [200] K. A. Boortz *et al.*, “Functional analysis of mouse G6pc1 mutations using a novel in situ assay for glucose-6-phosphatase activity and the effect of mutations in conserved human G6PC1/G6PC2 amino acids on G6PC2 protein expression,” *PLoS One*, vol. 11, no. 9, pp. 1–24, 2016.
- [201] R.-H. Chung *et al.*, “Multi-omics analysis identifies CpGs near G6PC2 mediating the effects of genetic variants on fasting glucose,” *Diabetologia*, pp. 1–13, Apr. 2021.
- [202] N. H. J. J. Ng *et al.*, “Tissue-Specific Alteration of Metabolic Pathways Influences Glycemic Regulation,” *bioRxiv*, vol. 29, p. 60, Oct. 2019.
- [203] J. Ren *et al.*, “Pancreatic islet cell therapy for type I diabetes: Understanding the effects of glucose stimulation on islets in order to produce better islets for transplantation,” *Journal of Translational Medicine*, vol. 5, no. 1. BioMed Central, p. 1, 03-Jan-2007.

- [204] J. M. Berg, J. L. Tymoczko, and L. Stryer, *The Citric Acid Cycle Oxidizes Two-Carbon Units*, 5th editio. W H Freeman, 2002.
- [205] C. A. Lewis *et al.*, “Tracing Compartmentalized NADPH Metabolism in the Cytosol and Mitochondria of Mammalian Cells,” *Mol. Cell*, vol. 55, no. 2, pp. 253–263, 2014.
- [206] W. N. P. Lee, L. G. Boros, J. Puigjaner, S. Bassilian, S. Lim, and M. Cascante, “Mass isotopomer study of the nonoxidative pathways of the pentose cycle with [1,2-13C2]glucose,” *Am. J. Physiol. - Endocrinol. Metab.*, vol. 274, no. 5 37-5, pp. E843–E851, May 1998.
- [207] N. Bouatia-Naji *et al.*, “A Polymorphism Within the G6PC2 Gene Is Associated with Fasting Plasma Glucose Levels,” *Science (80-. )*, vol. 320, no. 5879, pp. 1085–1088, May 2008.
- [208] B. R. Landau, “Correction of tricarboxylic acid cycle exchange in gluconeogenesis: why the y’s are wrong,” *Am. J. Physiol. Metab.*, vol. 261, no. 5, pp. E673–E676, Nov. 1991.
- [209] J. Katz, P. Wals, and W.-N. P. Lee, “Isotopomer studies of gluconeogenesis and the Krebs cycle with 13C-labeled lactate,” *J. Biol. Chem.*, vol. 268, no. 34, pp. 25509–21, Dec. 1993.
- [210] W. C. Schumann, I. Magnusson, V. Chandramouli, K. Kumaran, J. Wahren, and B. R. Landau, “Metabolism of [2-14C]acetate and its use in assessing hepatic krebs cycle activity and gluconeogenesis,” *J. Biol. Chem.*, vol. 266, no. 11, pp. 6985–6990, 1991.
- [211] B. R. Landau, W. C. Schumann, V. Chandramouli, I. Magnusson, K. Kumaran, and J. Wahren, “14C-labeled propionate metabolism in vivo and estimates of hepatic gluconeogenesis relative to Krebs cycle flux,” *AJP - Endo*, vol. 265, no. 4, pp. 636–647, 1993.
- [212] J. E. Ayala, D. P. Bracy, O. P. McGuinness, and D. H. Wasserman, “Considerations in the design of hyperinsulinemic-euglycemic clamps in the conscious mouse,” *Diabetes*, vol. 55, no. 2, pp. 390–397, 2006.
- [213] I. Magnusson *et al.*, “Noninvasive tracing of Krebs cycle metabolism in liver,” *J. Biol. Chem.*, vol. 266, no. 11, pp. 6975–6984, 1991.
- [214] R. J. Perry *et al.*, “Propionate increases hepatic pyruvate cycling and anaplerosis and alters mitochondrial metabolism,” *J. Biol. Chem.*, vol. 291, no. 23, pp. 12161–12170, Jun. 2016.
- [215] R. J. Perry *et al.*, “Hepatic acetyl CoA links adipose tissue inflammation to hepatic insulin resistance and type 2 diabetes,” *Cell*, vol. 160, no. 4, pp. 745–758, 2015.
- [216] B. Faubert *et al.*, “Lactate Metabolism in Human Lung Tumors,” *Cell*, vol. 171, no. 2, pp. 358–371.e9, 2017.
- [217] C. M. Hasenour *et al.*, “Vitamin E does not prevent Western diet-induced NASH progression and increases metabolic flux dysregulation in mice,” *J. Lipid Res.*, vol. 61, no. 5, pp. 707–721, May 2020.
- [218] D. E. Befroy *et al.*, “Direct assessment of hepatic mitochondrial oxidative and anaplerotic fluxes in humans using dynamic 13 C magnetic resonance spectroscopy,” *Nat. Med.*, vol. 20, no. 1, pp. 98–102, 2014.
- [219] D. E. Befroy, R. G. Kibbey, R. J. Perry, K. F. Petersen, D. L. Rothman, and G. I. Shulman, “Response to burgess,” *Nat. Med.*, vol. 21, no. 2, pp. 109–110, Feb. 2015.
- [220] K. F. Petersen, D. E. Befroy, S. Dufour, D. L. Rothman, and G. I. Shulman, “Assessment of Hepatic Mitochondrial Oxidation and Pyruvate Cycling in NAFLD by (13)C Magnetic Resonance Spectroscopy,” *Cell Metab.*, vol. 24, no. 1, pp. 167–71, 2016.
- [221] S. C. Burgess, M. E. Merritt, J. G. Jones, J. D. Browning, A. D. Sherry, and C. R. Malloy, “Limitations of detection of anaplerosis and pyruvate cycling from metabolism of [1-13C] acetate,” *Nat. Med.*, vol. 21, no. 2, pp. 108–109, Feb. 2015.

- [222] J. P. Riou, C. Audigier, M. Laville, M. Beylot, P. Pigeon, and R. Mornex, “Dephosphorylation of l-pyruvate kinase during rat liver hepatocyte isolation,” *Arch. Biochem. Biophys.*, vol. 236, no. 1, pp. 321–327, 1985.
- [223] V. Large, H. Brunengraber, M. Odeon, and M. Beylot, “Use of labeling pattern of liver glutamate to calculate rates of citric acid cycle and gluconeogenesis,” *Am. J. Physiol.*, vol. 272, no. 1 Pt 1, pp. E51–8, Jan. 1997.
- [224] V. Large and M. Beylot, “Modifications of citric acid cycle activity and gluconeogenesis in streptozotocin-induced diabetes and effects of metformin,” *Diabetes*, vol. 48, no. 6, pp. 1251–1257, Jun. 1999.
- [225] J. B. Blair, D. E. Cook, and H. A. Lardy, “Interaction of propionate and lactate in the perfused rat liver. Effects of glucagon and oleate,” *J. Biol. Chem.*, vol. 248, no. 10, pp. 3608–14, May 1973.
- [226] P. She, M. Shiota, K. D. Shelton, R. Chalkley, C. Postic, and M. A. Magnuson, “Phosphoenolpyruvate Carboxykinase Is Necessary for the Integration of Hepatic Energy Metabolism,” *Mol. Cell. Biol.*, vol. 20, no. 17, pp. 6508–6517, 2000.
- [227] S. C. Burgess *et al.*, “Impaired tricarboxylic acid cycle activity in mouse livers lacking cytosolic phosphoenolpyruvate carboxykinase,” *J. Biol. Chem.*, vol. 279, no. 47, pp. 48941–48949, 2004.
- [228] Y. E. Cheah, C. M. Hasenour, and J. D. Young, “<sup>13</sup>C Flux Analysis in Biotechnology and Medicine,” in *Systems Biology*, Weinheim, Germany: Wiley-VCH Verlag GmbH & Co. KGaA, 2017, pp. 25–70.
- [229] L. Goedeke *et al.*, “Acetyl-CoA Carboxylase Inhibition Reverses NAFLD and Hepatic Insulin Resistance but Promotes Hypertriglyceridemia in Rodents,” *Hepatology*, vol. 68, no. 6, pp. 2197–2211, Dec. 2018.
- [230] D. A. d’Avignon *et al.*, “Hepatic ketogenic insufficiency reprograms hepatic glycogen metabolism and the lipidome,” *JCI Insight*, vol. 3, no. 12, Jun. 2018.
- [231] S. F. Previs, D. Z. Brunengraber, and H. Brunengraber, “Is There Glucose Production Outside of the Liver and Kidney?,” *Annu. Rev. Nutr.*, vol. 29, no. 1, pp. 43–57, 2009.
- [232] G. Martin *et al.*, “Glutamine gluconeogenesis in the small intestine of 72 h-fasted adult rats is undetectable,” *Biochem. J.*, vol. 401, no. 2, pp. 465–73, Jan. 2007.
- [233] M. Watford, “Is the Small Intestine a Gluconeogenic Organ?,” *Nutr. Rev.*, vol. 63, no. 10, pp. 356–360, Oct. 2005.
- [234] A. Potts *et al.*, “Cytosolic phosphoenolpyruvate carboxykinase as a cataplerotic pathway in the small intestine,” *Am. J. Physiol. Gastrointest. Liver Physiol.*, vol. 315, no. 2, pp. G249–G258, 2018.
- [235] J. E. Gerich, C. Meyer, H. J. Woerle, and M. Stumvoll, “Renal Gluconeogenesis: Its importance in human glucose homeostasis,” *Diabetes Care*, vol. 24, no. 2, pp. 382–391, Feb. 2001.
- [236] G. Weber, “Kidney Enzymes of Gluconeogenesis, Glycogenesis, Glycolysis and Direct Oxidation,” *Exp. Biol. Med.*, vol. 108, no. 3, pp. 631–634, Dec. 1961.
- [237] W. G. Guder and B. D. Ross, “Enzyme distribution along the nephron,” *Kidney Int.*, vol. 26, no. 2, pp. 101–111, 1984.
- [238] E. Mutel *et al.*, “Control of blood glucose in the absence of hepatic glucose production during prolonged fasting in mice: Induction of renal and intestinal gluconeogenesis by glucagon,” *Diabetes*, vol. 60, no. 12, pp. 3121–3131, Dec. 2011.
- [239] E. D. Berglund *et al.*, “Hepatic energy state is regulated by glucagon receptor signaling in mice,” *J. Clin. Invest.*, vol. 119, no. 8, pp. 2412–2422, Aug. 2009.
- [240] E. D. Montal *et al.*, “PEPCK Coordinates the Regulation of Central Carbon Metabolism to Promote



- Cancer Cell Growth,” *Mol. Cell*, vol. 60, no. 4, pp. 571–83, Nov. 2015.
- [241] A. Penhoat, L. Fayard, A. Stefanutti, G. Mithieux, and F. Rajas, “Intestinal gluconeogenesis is crucial to maintain a physiological fasting glycemia in the absence of hepatic glucose production in mice,” *Metabolism*, vol. 63, no. 1, pp. 104–11, Jan. 2014.
- [242] A. Battezzati *et al.*, “Nonhepatic glucose production in humans,” *Am. J. Physiol. Endocrinol. Metab.*, vol. 286, no. 1, pp. E129–35, Jan. 2004.
- [243] R. Stark *et al.*, “A role for mitochondrial phosphoenolpyruvate carboxykinase (PEPCK-M) in the regulation of hepatic gluconeogenesis,” *J. Biol. Chem.*, vol. 289, no. 11, pp. 7257–7263, Mar. 2014.
- [244] T. J. Wiese, D. O. Lambeth, and P. D. Ray, “The intracellular distribution and activities of phosphoenolpyruvate carboxykinase isozymes in various tissues of several mammals and birds,” *Comp. Biochem. Physiol. B*, vol. 100, no. 2, pp. 297–302, Jan. 1991.
- [245] R. C. Nordlie and H. A. Lardy, “Mammalian liver phosphoenolpyruvate carboxykinase activities,” *J. Biol. Chem.*, vol. 238, no. 7, pp. 2259–63, Jul. 1963.
- [246] A. Méndez-Lucas *et al.*, “PEPCK-M expression in mouse liver potentiates, not replaces, PEPCK-C mediated gluconeogenesis,” *J. Hepatol.*, vol. 59, no. 1, pp. 105–113, Jul. 2013.
- [247] A. Klyuyeva, A. Tuganova, N. Kedishvili, and K. M. Popov, “Tissue-specific kinase expression and activity regulate flux through the pyruvate dehydrogenase complex,” *J. Biol. Chem.*, vol. 294, no. 3, pp. 838–851, Jan. 2019.
- [248] R. G. Kibbey, “PEPCK-M,” in *Encyclopedia of Signaling Molecules*, Springer New York, 2016, pp. 1–9.
- [249] C. M. Croniger, Y. Olswang, L. Reshef, S. C. Kalhan, S. M. Tilghman, and R. W. Hanson, “Mini-Series: Modern Metabolic Concepts Phosphoenolpyruvate Carboxykinase Revisited,” *Biochem. Mol. Biol. Educ.*, vol. 30, no. 1, pp. 14–20, 2002.
- [250] K. Kida, S. Nakajo, F. Kamiya, Y. Toyama, T. Nishio, and H. Nakagawa, “Renal net glucose release in vivo and its contribution to blood glucose in rats,” *J. Clin. Invest.*, vol. 62, no. 4, pp. 721–726, Oct. 1978.
- [251] E. Cersosimo, R. L. Judd, and J. M. Miles, “Insulin regulation of renal glucose metabolism in conscious dogs,” *J. Clin. Invest.*, vol. 93, no. 6, pp. 2584–9, Jun. 1994.
- [252] K. Ekberg *et al.*, “Contributions by kidney and liver to glucose production in the postabsorptive state and after 60 h of fasting,” *Diabetes*, vol. 48, no. 2, pp. 292–8, Feb. 1999.
- [253] C. Jang *et al.*, “Metabolite Exchange between Mammalian Organs Quantified in Pigs,” *Cell Metab.*, vol. 30, no. 3, pp. 594–606.e3, Sep. 2019.
- [254] D. H. Wasserman, “Four grams of glucose,” *American Journal of Physiology - Endocrinology and Metabolism*, vol. 296, no. 1. American Physiological Society, 2009.
- [255] G. Stephanopoulos, “Metabolic engineering,” *Biotechnol. Bioeng.*, vol. 58, no. 2–3, pp. 119–20, 1998.
- [256] I.-Y. Kim *et al.*, “In Vivo and In Vitro Quantification of Glucose Kinetics: From Bedside to Bench,” *Endocrinol. Metab.*, vol. 35, no. 4, pp. 733–749, 2020.
- [257] M. Rahim, C. M. Hasenour, T. K. Bednarski, C. C. Hughey, D. H. Wasserman, and J. D. Young, “Multitissue 2H/13C flux analysis reveals reciprocal upregulation of renal gluconeogenesis in hepatic PEPCK-C–knockout mice,” *JCI Insight*, vol. 6, no. 12, Jun. 2021.
- [258] N. Stride *et al.*, “Decreased mitochondrial oxidative phosphorylation capacity in the human heart with left ventricular systolic dysfunction,” *Eur. J. Heart Fail.*, vol. 15, no. 2, pp. 150–157, Feb. 2013.

- [259] S. Larsen *et al.*, “Biomarkers of mitochondrial content in skeletal muscle of healthy young human subjects,” *J. Physiol.*, vol. 590, no. 14, pp. 3349–3360, Jul. 2012.
- [260] J. Kempainen, T. Fujimoto, K. K. Kalliokoski, T. Viljanen, P. Nuutila, and J. Knuuti, “Myocardial and skeletal muscle glucose uptake during exercise in humans,” *J. Physiol.*, vol. 542, no. 2, pp. 403–412, Jul. 2002.
- [261] J. D. Song *et al.*, “Dissociation of Muscle Insulin Resistance from Alterations in Mitochondrial Substrate Preference,” *Cell Metab.*, vol. 32, no. 5, pp. 726–735.e5, Nov. 2020.
- [262] J. A. Bastiaansen, M. E. Merritt, and A. Comment, “Real time measurement of myocardial substrate selection in vivo using hyperpolarized <sup>13</sup>C magnetic resonance,” *J. Cardiovasc. Magn. Reson.*, vol. 17, no. S1, pp. 1–3, Dec. 2015.
- [263] K. X. Moreno, S. M. Sabelhaus, M. E. Merritt, A. D. Sherry, and C. R. Malloy, “Competition of pyruvate with physiological substrates for oxidation by the heart: Implications for studies with hyperpolarized [1-<sup>13</sup>C]pyruvate,” *Am. J. Physiol. - Hear. Circ. Physiol.*, vol. 298, no. 5, pp. 1556–1564, May 2010.
- [264] C. von Morze and M. E. Merritt, “Cancer in the crosshairs: targeting cancer metabolism with hyperpolarized carbon-13 MRI technology,” *NMR Biomed.*, vol. 32, no. 10, pp. 1–12, 2019.
- [265] D. Huszar *et al.*, “Targeted disruption of the melanocortin-4 receptor results in obesity in mice,” *Cell*, vol. 88, no. 1, pp. 131–141, Jan. 1997.
- [266] C. Depre, J. L. J. Vanoverschelde, and H. Taegtmeyer, “Glucose for the heart,” *Circulation*, vol. 99, no. 4, Lippincott Williams and Wilkins, pp. 578–588, 02-Feb-1999.
- [267] C. A. Schneider, V. T. B. Nguyen, and H. Taegtmeyer, “Feeding and fasting determine postischemic glucose utilization in isolated working rat hearts,” *Am. J. Physiol. - Hear. Circ. Physiol.*, vol. 260, no. 2 29-2, 1991.
- [268] J. Jensen, P. I. Rustad, A. J. Kolnes, and Y. C. Lai, “The role of skeletal muscle glycogen breakdown for regulation of insulin sensitivity by exercise,” *Frontiers in Physiology*, vol. 2 DEC. Frontiers Media SA, 2011.
- [269] G. Van Hall, M. Sacchetti, G. Rådegran, and B. Saltin, “Human skeletal muscle fatty acid and glycerol metabolism during rest, exercise and recovery,” *Journal of Physiology*, vol. 543, no. 3. Wiley-Blackwell, pp. 1047–1058, 15-Sep-2002.
- [270] J. E. Ayala *et al.*, “Standard operating procedures for describing and performing metabolic tests of glucose homeostasis in mice,” *DMM Disease Models and Mechanisms*, vol. 3, no. 9–10. The Company of Biologists Ltd, pp. 525–534, 01-Sep-2010.
- [271] E. W. Kraegen, D. E. James, A. B. Jenkins, D. J. Chisholm, A. Jen-kins, and D. J. Chi, “Dose-response curves for in vivo insulin sensitivity in individual tissues in rats,” 1985.
- [272] Z. Pang *et al.*, “MetaboAnalyst 5.0: narrowing the gap between raw spectra and functional insights,” *Nucleic Acids Res.*, no. 1, May 2021.
- [273] P. Bedossa *et al.*, “Utility and appropriateness of the fatty liver inhibition of progression (FLIP) algorithm and steatosis, activity, and fibrosis (SAF) score in the evaluation of biopsies of nonalcoholic fatty liver disease,” *Hepatology*, vol. 60, no. 2, pp. 565–575, Aug. 2014.
- [274] R. Nakata *et al.*, “In vivo redox metabolic imaging of mitochondria assesses disease progression in non-alcoholic steatohepatitis,” *Sci. Rep.*, vol. 7, no. 1, pp. 1–12, Dec. 2017.
- [275] Z. Chen, R. Tian, Z. She, J. Cai, and H. Li, “Role of oxidative stress in the pathogenesis of nonalcoholic fatty liver disease,” *Free Radical Biology and Medicine*, vol. 152. Elsevier Inc., pp. 116–141, 20-May-2020.

- [276] D. Häussinger, “Liver glutamine metabolism.,” *JPEN. Journal of parenteral and enteral nutrition*, vol. 14, no. 4 Suppl. 1990.
- [277] F. De Chiara *et al.*, “Urea cycle dysregulation in non-alcoholic fatty liver disease,” *J. Hepatol.*, vol. 69, no. 4, pp. 905–915, Oct. 2018.
- [278] P. L. Eriksen *et al.*, “Non-alcoholic fatty liver disease alters expression of genes governing hepatic nitrogen conversion,” *Liver Int.*, vol. 39, no. 11, pp. 2094–2101, Nov. 2019.
- [279] K. Kobayashi and J. R. Neely, “Control of Maximum Rates of Glycolysis in Rat Cardiac Muscle,” 1979.
- [280] S. E. Seiler *et al.*, “Obesity and lipid stress inhibit carnitine acetyltransferase activity.,” *J. Lipid Res.*, vol. 55, no. 4, pp. 635–44, Apr. 2014.
- [281] S. E. Seiler *et al.*, “Carnitine Acetyltransferase Mitigates Metabolic Inertia and Muscle Fatigue during Exercise,” *Cell Metab.*, vol. 22, no. 1, pp. 65–76, 2015.
- [282] P. J. Randle, P. B. Garland, C. N. Hales, and E. A. Newsholme, “THE GLUCOSE FATTY-ACID CYCLE ITS ROLE IN INSULIN SENSITIVITY AND THE METABOLIC DISTURBANCES OF DIABETES MELLITUS,” *Lancet*, vol. 281, no. 7285, pp. 785–789, Apr. 1963.
- [283] E. P. Wijekoon, C. Skinner, M. E. Brosnan, and J. T. Brosnan, “Amino acid metabolism in the Zucker diabetic fatty rat: Effects of insulin resistance and of type 2 diabetes,” *Can. J. Physiol. Pharmacol.*, vol. 82, no. 7, pp. 506–514, Jul. 2004.
- [284] C. B. Newgard *et al.*, “A Branched-Chain Amino Acid-Related Metabolic Signature that Differentiates Obese and Lean Humans and Contributes to Insulin Resistance,” *Cell Metab.*, vol. 9, no. 4, pp. 311–326, Apr. 2009.
- [285] P. Würtz *et al.*, “Metabolic signatures of insulin resistance in 7,098 young adults.,” *Diabetes*, vol. 61, no. 6, pp. 1372–80, Jun. 2012.
- [286] T. E. Jones *et al.*, “Plasma lactate as a marker of metabolic health: Implications of elevated lactate for impairment of aerobic metabolism in the metabolic syndrome,” in *Surgery (United States)*, 2019, vol. 166, no. 5, pp. 861–866.
- [287] R. J. Perry *et al.*, “Non-invasive assessment of hepatic mitochondrial metabolism by positional isotopomer NMR tracer analysis (PINTA),” *Nat. Commun.*, vol. 8, no. 1, pp. 1–9, Dec. 2017.
- [288] T. Utriainen *et al.*, “Insulin resistance characterizes glucose uptake in skeletal muscle but not in the heart in NIDDM,” *Diabetologia*, vol. 41, no. 5, pp. 555–559, 1998.
- [289] P. Nuutila *et al.*, “Insulin resistance is localized to skeletal but not heart muscle in type 1 diabetes,” *Am. J. Physiol. - Endocrinol. Metab.*, vol. 264, no. 5 27-5, 1993.
- [290] J. Vom Dahl *et al.*, “Myocardial glucose uptake in patients with insulin-dependent diabetes mellitus assessed quantitatively by dynamic positron emission tomography,” *Circulation*, vol. 88, no. 2, pp. 395–404, 1993.
- [291] D. H. Tran and Z. V. Wang, “Glucose Metabolism in Cardiac Hypertrophy and Heart Failure,” *Journal of the American Heart Association*, vol. 8, no. 12. American Heart Association Inc., 18-Jun-2019.
- [292] O. J. Rider, P. Cox, D. Tyler, K. Clarke, and S. Neubauer, “Myocardial substrate metabolism in obesity,” *International Journal of Obesity*, vol. 37, no. 7. Nature Publishing Group, pp. 972–979, 16-Jul-2013.
- [293] J. R. Ussher *et al.*, “Insulin-stimulated cardiac glucose oxidation is increased in high-fat diet-induced obese mice lacking malonyl CoA decarboxylase,” *Diabetes*, vol. 58, no. 8, pp. 1766–1775, Aug. 2009.

- [294] J. Buchanan *et al.*, “Reduced cardiac efficiency and altered substrate metabolism precedes the onset of hyperglycemia and contractile dysfunction in two mouse models of insulin resistance and obesity,” *Endocrinology*, vol. 146, no. 12, pp. 5341–5349, Dec. 2005.
- [295] J. R. Ussher and G. D. Lopaschuk, “Cardiac insulin resistance: It’s sweeter than you think,” *Endocrinology*, vol. 154, no. 8, pp. 2575–2578, Aug. 2013.
- [296] A. A. Gupte *et al.*, “High-fat feeding-induced hyperinsulinemia increases cardiac glucose uptake and mitochondrial function despite peripheral insulin resistance,” *Endocrinology*, vol. 154, no. 8, pp. 2650–2662, Aug. 2013.
- [297] L. Zhang, J. R. Ussher, T. Oka, V. J. J. Cadete, C. Wagg, and G. D. Lopaschuk, “Cardiac diacylglycerol accumulation in high fat-fed mice is associated with impaired insulin-stimulated glucose oxidation,” *Cardiovasc. Res.*, vol. 89, no. 1, pp. 148–156, Jan. 2011.
- [298] M. Baranowski *et al.*, “Myocardium of type 2 diabetic and obese patients is characterized by alterations in sphingolipid metabolic enzymes but not by accumulation of ceramide,” *J. Lipid Res.*, vol. 51, no. 1, pp. 74–80, 2010.
- [299] K. F. Petersen, S. Dufour, D. Befroy, R. Garcia, and G. I. Shulman, “Impaired Mitochondrial Activity in the Insulin-Resistant Offspring of Patients with Type 2 Diabetes,” *N. Engl. J. Med.*, vol. 350, no. 7, pp. 664–671, Feb. 2004.
- [300] T. R. Koves *et al.*, “Mitochondrial Overload and Incomplete Fatty Acid Oxidation Contribute to Skeletal Muscle Insulin Resistance,” *Cell Metab.*, vol. 7, no. 1, pp. 45–56, Jan. 2008.
- [301] H. M. De Feyter *et al.*, “Increased intramyocellular lipid content but normal skeletal muscle mitochondrial oxidative capacity throughout the pathogenesis of type 2 diabetes,” *FASEB J.*, vol. 22, no. 11, pp. 3947–3955, Nov. 2008.
- [302] H. M. De Feyter, N. M. A. Van den Broek, S. F. E. Praet, K. Nicolay, L. J. C. Van Loon, and J. J. Prompers, “Early or advanced stage type 2 diabetes is not accompanied by in vivo skeletal muscle mitochondrial dysfunction,” *Eur. J. Endocrinol.*, vol. 158, no. 5, pp. 643–653, May 2008.
- [303] C. R. Hancock *et al.*, “High-fat diets cause insulin resistance despite an increase in muscle mitochondria,” *Proc. Natl. Acad. Sci. U. S. A.*, vol. 105, no. 22, pp. 7815–7820, Jun. 2008.
- [304] T. P. Gavin *et al.*, “High incomplete skeletal muscle fatty acid oxidation explains low muscle insulin sensitivity in poorly controlled T2D,” *J. Clin. Endocrinol. Metab.*, vol. 103, no. 3, pp. 882–889, Mar. 2018.
- [305] P. R. Baker *et al.*, “Metabolomic analysis reveals altered skeletal muscle amino acid and fatty acid handling in obese humans,” *Obesity*, vol. 23, no. 5, pp. 981–988, May 2015.
- [306] L. Hue and H. Taegtmeyer, “The Randle cycle revisited: A new head for an old hat,” *American Journal of Physiology - Endocrinology and Metabolism*, vol. 297, no. 3. American Physiological Society, pp. 578–591, Sep-2009.
- [307] M. C. Sugden and M. J. Holness, “Mechanisms underlying regulation of the expression and activities of the mammalian pyruvate dehydrogenase kinases,” *Archives of Physiology and Biochemistry*, vol. 112, no. 3. Taylor & Francis, pp. 139–149, 01-Jun-2006.
- [308] B. Wessels, J. Ciapaite, N. M. A. van den Broek, S. M. Houten, K. Nicolay, and J. J. Prompers, “Pioglitazone treatment restores in vivo muscle oxidative capacity in a rat model of diabetes,” *Diabetes, Obes. Metab.*, vol. 17, no. 1, pp. 52–60, Jan. 2015.
- [309] D. M. Muoio and P. D. Neuffer, “Lipid-induced mitochondrial stress and insulin action in muscle,” *Cell Metabolism*, vol. 15, no. 5. Cell Metab, pp. 595–605, 02-May-2012.
- [310] J. L. Ivy, A. L. Katz, C. L. Cutler, W. M. Sherman, and E. F. Coyle, “Muscle glycogen synthesis after exercise: Effect of time of carbohydrate ingestion,” *J. Appl. Physiol.*, vol. 64, no. 4, pp. 1480–

- 1485, Apr. 1988.
- [311] J. B. Lyon, "Muscle and Liver Glycogen Levels in Lean and Obese Strains of Mice," *Am. J. Physiol. Content*, vol. 190, no. 3, pp. 434–438, Sep. 1957.
- [312] P. Damsbo, A. Vaag, O. Hother-Nielsen, and H. Beck-Nielsen, "Reduced glycogen synthase activity in skeletal muscle from obese patients with and without Type 2 (non-insulin-dependent) diabetes mellitus," *Diabetologia*, vol. 34, no. 4, pp. 239–245, Apr. 1991.
- [313] S. B. Pedersen, J. D. Børglum, O. Schmitz, J. F. Bak, N. S. Sørensen, and B. Richelsen, "Abdominal obesity is associated with insulin resistance and reduced glycogen synthase activity in skeletal muscle," *Metabolism*, vol. 42, no. 8, pp. 998–1005, 1993.
- [314] K. Aleksandrova, C. Egea Rodrigues, A. Floegel, and W. Ahrens, "Omics Biomarkers in Obesity: Novel Etiological Insights and Targets for Precision Prevention," *Current obesity reports*, vol. 9, no. 3. NLM (Medline), pp. 219–230, 01-Sep-2020.
- [315] D. Greco *et al.*, "Gene expression in human NAFLD," *Am. J. Physiol. - Gastrointest. Liver Physiol.*, vol. 294, no. 5, May 2008.
- [316] K. Pei *et al.*, "An Overview of Lipid Metabolism and Nonalcoholic Fatty Liver Disease," *BioMed Research International*, vol. 2020. Hindawi Limited, 2020.
- [317] C. Lerin *et al.*, "Defects in muscle branched-chain amino acid oxidation contribute to impaired lipid metabolism," *Mol. Metab.*, vol. 5, no. 10, pp. 926–936, Oct. 2016.
- [318] J. David, D. Dardevet, L. Mosoni, I. Savary-Auzeloux, and S. Polakof, "Impaired skeletal muscle branched-chain amino acids catabolism contributes to their increased circulating levels in a non-obese insulin-resistant fructose-fed rat model," *Nutrients*, vol. 11, no. 2, Feb. 2019.
- [319] A. Katsuki *et al.*, "Homeostasis model assessment is a reliable indicator of insulin resistance during follow-up of patients with type 2 diabetes," *Diabetes Care*, vol. 24, no. 2, pp. 362–365, Feb. 2001.
- [320] H. G. Zimmer, "The oxidative pentose phosphate pathway in the heart: Regulation, physiologic significance, and clinical implications," *Basic Research in Cardiology*, vol. 87, no. 4. Steinkopff-Verlag, pp. 303–316, Jul-1992.
- [321] G. E. Glock and P. McLean, "Levels of enzymes of the direct oxidative pathway of carbohydrate metabolism in mammalian tissues and tumours.," *Biochem. J.*, vol. 56, no. 1, pp. 171–5, Jan. 1954.
- [322] D. McCloskey, J. D. Young, S. Xu, B. O. Palsson, and A. M. Feist, "MID Max: LC-MS/MS Method for Measuring the Precursor and Product Mass Isotopomer Distributions of Metabolic Intermediates and Cofactors for Metabolic Flux Analysis Applications," *Anal. Chem.*, vol. 88, no. 2, pp. 1362–1370, Jan. 2016.
- [323] R. Schoenheimer and D. Rittenberg, "Deuterium as an indicator in the study of intermediary metabolism," *Science*, vol. 82, no. 2120, pp. 156–7, Aug. 1935.
- [324] I. Magnusson *et al.*, "Noninvasive tracing of Krebs cycle metabolism in liver.," *J. Biol. Chem.*, vol. 266, no. 11, pp. 6975–84, Apr. 1991.
- [325] C. Des Rosiers *et al.*, "Isotopomer analysis of citric acid cycle and gluconeogenesis in rat liver. Reversibility of isocitrate dehydrogenase and involvement of ATP-citrate lyase in gluconeogenesis.," *J. Biol. Chem.*, vol. 270, no. 17, pp. 10027–36, Apr. 1995.
- [326] L. J. Jazmin, J. P. O'Grady, F. Ma, D. K. Allen, J. A. Morgan, and J. D. Young, "Isotopically Nonstationary MFA (INST-MFA) of Autotrophic Metabolism," Humana Press, Totowa, NJ, 2014, pp. 181–210.
- [327] S. G. Lloyd, H. Zeng, P. Wang, and J. C. Chatham, "Lactate isotopomer analysis by <sup>1</sup>H NMR spectroscopy: Consideration of long-range nuclear spin–spin interactions," *Magn. Reson. Med.*, vol.

- 51, no. 6, pp. 1279–1282, Jun. 2004.
- [328] Y. Fu, J. M. Yoon, L. Jarboe, and J. V. Shanks, “Metabolic flux analysis of *Escherichia coli* MG1655 under octanoic acid (C8) stress,” *Appl. Microbiol. Biotechnol.*, vol. 99, no. 10, pp. 4397–4408, May 2015.
- [329] S. Sokol, P. Millard, and J.-C. Portais, “influx\_s: increasing numerical stability and precision for metabolic flux analysis in isotope labelling experiments,” *Bioinformatics*, vol. 28, no. 5, pp. 687–693, Mar. 2012.
- [330] M. Ragavan, A. Kirpich, X. Fu, S. C. Burgess, L. M. McIntyre, and M. E. Merritt, “A comprehensive analysis of myocardial substrate preference emphasizes the need for a synchronized fluxomic/metabolomic research design,” *Am. J. Physiol. - Hear. Circ. Physiol.*, vol. 312, no. 6, pp. H1215–H1223, Jun. 2017.
- [331] Y. E. Cheah *et al.*, “Systematic identification and elimination of flux bottlenecks in the aldehyde production pathway of *Synechococcus elongatus* PCC 7942,” *Metab. Eng.*, vol. 60, pp. 56–65, Jul. 2020.
- [332] F. Ma, L. J. Jazmin, J. D. Young, and D. K. Allen, “Isotopically nonstationary <sup>13</sup>C flux analysis of changes in *Arabidopsis thaliana* leaf metabolism due to high light acclimation.,” *Proc. Natl. Acad. Sci. U. S. A.*, vol. 111, no. 47, pp. 16967–72, Nov. 2014.
- [333] Y. Sekiyama and J. Kikuchi, “Towards dynamic metabolic network measurements by multi-dimensional NMR-based fluxomics,” *Phytochemistry*, vol. 68, no. 16–18, pp. 2320–2329, Aug. 2007.
- [334] F. M. Jeffrey, A. Rajagopal, C. R. Malloy, and A. D. Sherry, “<sup>13</sup>C-NMR: a simple yet comprehensive method for analysis of intermediary metabolism.,” *Trends Biochem. Sci.*, vol. 16, no. 1, pp. 5–10, Jan. 1991.
- [335] A. D. Sherry, F. M. H. Jeffrey, and C. R. Malloy, “Analytical solutions for <sup>13</sup>C isotopomer analysis of complex metabolic conditions: Substrate oxidation, multiple pyruvate cycles, and gluconeogenesis,” *Metab. Eng.*, vol. 6, no. 1, pp. 12–24, 2004.
- [336] F. M. H. Jeffrey, C. J. Storey, A. D. Sherry, and C. R. Malloy, “<sup>13</sup>C isotopomer model for estimation of anaplerotic substrate oxidation via acetyl-CoA,” *Am. J. Physiol. - Endocrinol. Metab.*, vol. 271, no. 4, pp. 34–4, 1996.
- [337] H. E. Morgan, D. C. Earl, A. Broadus, E. B. Wolpert, K. E. Giger, and L. S. Jefferson, “Regulation of protein synthesis in heart muscle. I. Effect of amino acid levels on protein synthesis.,” *J. Biol. Chem.*, vol. 246, no. 7, pp. 2152–62, Apr. 1971.
- [338] F. M. Jeffrey *et al.*, “Modeling of brain metabolism and pyruvate compartmentation using <sup>13</sup>C NMR in vivo: Caution required,” *J. Cereb. Blood Flow Metab.*, vol. 33, no. 8, pp. 1160–1167, Aug. 2013.
- [339] A. Cherix, R. Sonti, B. Lanz, and H. Lei, “In vivo metabolism of [1,6-<sup>13</sup>C<sub>2</sub>]glucose reveals distinct neuroenergetic functionality between mouse hippocampus and hypothalamus,” *Metabolites*, vol. 11, no. 1, pp. 1–14, Jan. 2021.
- [340] M. T. Judge *et al.*, “Continuous in vivo Metabolism by NMR,” *Front. Mol. Biosci.*, vol. 0, no. APR, p. 26, 2019.
- [341] P. G. Henry *et al.*, “In vivo <sup>13</sup>C NMR spectroscopy and metabolic modeling in the brain: a practical perspective,” *Magn. Reson. Imaging*, vol. 24, no. 4, pp. 527–539, May 2006.
- [342] M. Beyß, S. Azzouzi, M. Weitzel, W. Wiechert, and K. Nöh, “The design of FluxML: A universal modeling language for <sup>13</sup>C metabolic flux analysis,” *Front. Microbiol.*, vol. 10, no. MAY, p. 1022, May 2019.

- [343] K. Sahlin, A. Katz, and S. Broberg, "Tricarboxylic acid cycle intermediates in human muscle during prolonged exercise," *Am. J. Physiol. - Cell Physiol.*, vol. 259, no. 5 28-5, 1990.

## APPENDIX OF DETAILED PROTOCOLS

### Metabolite extraction from plasma

#### Materials:

- 10 mL Methanol (MeOH) at -20°C
- 10 mL Chloroform (ChCl<sub>3</sub>) at -20°C
- 10 mL of UltraPure H<sub>2</sub>O on ice
- 5 mM Norvaline
- Crushed ice to hold samples
- Microcentrifuge tubes
- Vortexer with access to 4°C freezer
- Centrifuge set to 0°C

#### Procedure:

1. Prepare 650µL mixture of MeOH/ChCl<sub>3</sub> (2:1) for every 30-50 µL of plasma
2. Add the 650µL mixture of MeOH/ChCl<sub>3</sub> (2:1) to a sample and vortex for ~30s
3. Add 10 uL of 5 mM norvaline to each sample; place the sample on ice
4. Vortex all samples simultaneously for 10min at 4°C
5. Place samples in crushed ice for 20min
6. Add 200 µL of cold ChCl<sub>3</sub> followed by 385 µL of ice cold H<sub>2</sub>O to a sample
7. Vortex for ~1min and place on ice
8. Repeat (7.) for remaining samples
9. Centrifuge samples at 0°C for 10min at 14,000 RPM
10. Isolate the aqueous phase with a fine-tipped pipette and place in a microcentrifuge tube
11. Overnight dry samples at room temperature under gentle air flow



## Metabolite extraction from frozen tissues

### Materials:

- 10 mL Methanol (MeOH) at -20°C
- 10 mL Chloroform (ChCl<sub>3</sub>) at -20°C
- 10 mL of Pure DI Water kept cold on crushed ice
- 5 mM norvaline
- Crushed ice to hold samples
- Vortexer
- Centrifuge set to 0°C and 12,000 RPM
- 30-50 mg of tissues aliquoted in tubes and stored on Liquid Nitrogen (LN<sub>2</sub>)
- Reacti-Vap Evaporator

### Tissue Extraction:

1. Add beads to screw-cap conical sample tubes.
2. Prepare 2:1 mixture of MeOH/CHCl<sub>3</sub> and place it on Ice
3. Add 650 µL mixture of MeOH/CHCl<sub>3</sub> (2:1) to each sample tube (1mL tube) containing 30 to 50 mg of tissue
4. Add 10 µl of 5 mM Norvaline as Internal Standard
5. Homogenize each sample using the BeadBug (highest speed, 2 cycles, 60 seconds each)  
**Important: Place samples on ice for 5 minutes between cycles**
6. Place samples in crushed ice for 20 min
7. Add 200µL of cold ChCl<sub>3</sub> followed by 385µL of ice-cold DI Water to each sample
8. Vortex for ≈1min and place on ice
9. Centrifuge samples at 0°C for 5 min at 12,000 RPM
10. Isolate the aqueous phase (top layer) with a fine-tipped pipette and place in a microcentrifuge tube (1.7/2 mL)
11. Overnight dry samples at room temperature under gentle air flow
12. Store samples at -80°C for GC-MS analysis or add 50 µL of solution A for LC-MS analysis

## RNA and protein extraction from cells

**Cleaning:** Buffer RLT contains a guanidine salt and is therefore not compatible with disinfecting reagents containing bleach. Buffer RPE is supplied as a concentrate.

Before using for the first time, add 4 volumes of ethanol (96–100%) as indicated on the bottle to obtain a working solution.

A maximum of 100 µg RNA can be cleaned up in this protocol. This amount corresponds to the RNA binding capacity of the RNeasy spin column.

### RNA and protein extraction from Cells

NOTE: The centrifugation temperature should be 20–25°C. This can cause formation of precipitates that can clog the RNeasy spin column. If this happens, set the centrifugation temperature to 25°C. Warm the ethanol-containing lysate to 37°C before transferring it to the RNeasy spin column.

- 1. Aspirate media and gently rinse cells with PBS
- 2. Add **350ul** of **RLT Lysis buffer** (1mL + 10ul of b-mercaptoethanol) and disrupt the cells by vigorously pipetting up and down (Note: Check under microscope)

Note: < 5 x10<sup>6</sup> add 350ul RLT and up to 10<sup>7</sup> cells add 600 µL

- 3. Pipet the lysate directly into a **QIAshredder** spin column placed in a 2 ml collection tube, and centrifuge for **2 min at full speed**.

**Collect flow-through.**

- 4. Add **350µL volume of 70% ethanol** to the homogenized lysate and mix well by pipetting. Do not centrifuge.

- 5. Transfer up to **700 µl** of the sample, including any precipitate that may have formed, to a RNeasy spin column placed in a 2 ml collection tube. Close the lid gently, and centrifuge for **15 s at ≥8000 x g** (≥10,000 rpm).

\*\*\*Save flow-through for protein quantification\*\*\* → Go to protein extraction for details

- 6. Add **700 µl Buffer RW1** to the RNeasy spin column. Close the lid gently, and centrifuge for **15 s at ≥8000 x g** (≥10,000 rpm) to wash the spin column membrane.

**Discard the flow-through.**

- 7. Continue from step 8.

### RNase Free DNase Set (Qiagen: 79254)

- Set at room temp for 15 mins
- Using a needle and syringe, add 550µL of RNase free water into vial of lyophilized Dnase
- Gently mix by inverting, do not vortex
- Store: -20C for months, 2-8C for 6 weeks
- For each sample: 10µL of reconstituted DNase + 70µL of RDD buffer

- 8. Add **350 µl Buffer RW1** to the RNeasy spin column. Incubate for **5 mins at room temp** (helps remove DNA contamination)

- 9. Close the lid gently, and centrifuge for **15 s at ≥8000 x g** (≥10,000 rpm) to wash the spin column membrane.

**Discard the flow-through.**

- Add **10 µl DNase I** stock solution (see above) to **70 µl Buffer RDD**. Mix by gently inverting the tube, and centrifuge briefly to collect residual liquid from the sides of the tube.
- Add the **DNase I** incubation mix (**80 µl**) directly to the RNeasy spin column membrane, and place on the benchtop (**20–30°C**) for **15 min**.
- Add **350 µl Buffer RW1** to the RNeasy spin column. Close the lid gently, and centrifuge for **15 s** at **≥8000 x g** (≥10,000 rpm) to wash the spin column membrane.

**Discard the flow-through.**

- Add **500 µl Buffer RPE** to the RNeasy spin column. Close the lid gently, and centrifuge for **15 s** at **≥8000 x g** (≥10,000 rpm) to wash the spin column membrane.

**Discard the flow-through.**

- Add **500 µl Buffer RPE** to the RNeasy spin column. Close the lid gently, and centrifuge for **2 mins** at **≥8000 x g** (≥10,000 rpm) to wash the spin column membrane.

**Discard the flow-through.**

**ENSURE THAT THE PREVIOUS STEP IS DONE AT RT and NOT at 4C. NECESSARY FOR COMPLETE REMOVAL OF ETHANOL IMPURITIES IN RPE.**

- Place the RNeasy spin column in a new 2 ml collection tube and discard the old collection tube with the flow-through. Close the lid gently, and centrifuge at full speed for **1 min**
- Place the RNeasy spin column in a new 1.5 ml collection tube. Add **40 µl RNase-free water** directly to the spin column membrane. Close the lid gently, and centrifuge for **1 min** at **≥8000 x g** (≥10,000 rpm) to elute the RNA
- Repeat previous step, collect **40µL** flow through from pervious step, add it to the spin column and centrifuge for **1 min** at **8000 x g**

**Note: Repeat RNA elution and incubate the RNeasy spin column on the benchtop for 10 min with RNase-free water before centrifuging if your yield is low.**

#### ***Protein extraction from Buffer RLT Lysates***

**Note: Precipitated, denatured protein obtained using this protocol is suitable for SDS-Page, western blotting and 2D gel electrophoresis**

- Transfer flow-through from the 2 mL tube to a 15 mL falcon tube.
- Add 4 volumes of ice-cold acetone to the flow-through:
  - a. So, for example, if you had added 350 µL of RLT + 350 µL of 70% ethanol in step 2 and 4, the flow-through volume will be ~700 µL, therefore add 2800 µL of ice-cold acetone.
  - b. If you added 600 µL of RLT + 600 µL of 70% ethanol, add 4800 µL of ice-cold acetone to the flow-through
- Incubate for 30 min on ice or at –20°C.
- Centrifuge for 10 min at maximum speed in a benchtop centrifuge. Discard the supernatant and air-dry the pellet.
- Optional: Wash the pellet with 100 µl ice-cold ethanol and air-dry. Do not over dry the pellet as this may make resuspension more difficult.
- Freeze down pellet at -80C for later analysis.

## Quantification, and Determination of Quality of RNA

- RNA should be determined by measuring the absorbance at 260 nm ( $A_{260}$ ) in a spectrophotometer
- To ensure significance,  $A_{260}$  readings should be greater than 0.15.
- An absorbance of 1 unit at 260 nm corresponds to 44  $\mu\text{g}$  of RNA per ml ( $A_{260}=1 \rightarrow 44 \mu\text{g/ml}$ )
- The ratio between the absorbance values at 260 and 280 nm gives an estimate of RNA purity.
- the  $A_{260}/A_{280}$  ratio is influenced considerably by pH. Since water is not buffered, the pH and the resulting  $A_{260}/A_{280}$  ratio can vary greatly. Lower pH results in a lower  $A_{260}/A_{280}$  ratio and reduced sensitivity to protein contamination.
- Pure RNA has an  $A_{260}/A_{280}$  ratio of 1.9–2.1 in 10 mM Tris·Cl, pH 7.5.

## Di-O-isopropylidene propionate derivatization of glucose

### I. Chemicals

- a. Acetone, stored at 4°C ((CH<sub>3</sub>)<sub>2</sub>CO; Sigma-Aldrich #179124-4L)
- b. 96% Sulfuric acid (H<sub>2</sub>SO<sub>4</sub>; EMD Millipore #SX1244-5 2.5L)
- c. 0.44 M Sodium Carbonate solution (Na<sub>2</sub>CO<sub>3</sub>; Fisher Scientific #S495-500)
- d. Saturated sodium chloride solution (Fisher Scientific #S271-1)
- e. Propionic anhydride (C<sub>6</sub>H<sub>10</sub>O<sub>3</sub>; Sigma-Aldrich #240311-50G)
- f. Pyridine (C<sub>5</sub>H<sub>5</sub>N; Sigma-Aldrich #270970-100ML)
- g. Ethyl acetate (CH<sub>3</sub>COOCH<sub>2</sub>CH<sub>3</sub>; Fisher Scientific #E195-1 1L)
- h. 5 mM U-<sup>13</sup>C<sub>6</sub>-D<sub>7</sub>-Glucose (Cambridge Isotopes); Optional

### II. Materials

- a. 1.5 mL microcentrifuge tubes
- b. 10 mL screw-cap culture tubes (Fisher Scientific #14-959-25A)
- c. 100 mL glass vials or test tubes
- d. Pipettes and tips
- e. 1 mL glass Pasteur pipettes and bulb
- f. 1.5 mL GC injection vial and injection caps (Agilent 5182-0716, 5182-0717)
- g. 250 µL glass inserts (Agilent 5181-1270)

### III. Equipment

- a. Sample dryer (e.g. Pierce Reacti-Therm III and Reacti-Vap III)
- b. Heating block
- c. Microcentrifuge
- d. Vortex

### IV. Procedure

- a. *Sample Preparation – protein precipitation*
  - i. Transfer 20 µL of sample or standard to a labeled microcentrifuge tube
  - ii. If needed, spike in 20 µL of 5 mM U-<sup>13</sup>C<sub>6</sub>-D<sub>7</sub>-Glucose to use as an internal standard for estimating absolute glucose concentration; pipette up and down to mix
  - iii. Add 300 µL cold acetone
  - iv. Vortex vigorously for 10 seconds
  - v. Centrifuge for 5 minutes at 14,000 rpm
  - vi. Carefully transfer the supernatant by pipetting to a labeled 10 mL screw-top culture tube
- vii. Evaporate samples to dryness under air flow at 60°C
  1. Drying takes approximately 20 minutes
  2. Breakpoint; samples can sit at 4 °C overnight before proceeding
- b. *Derivatization*
  - i. In a glass vial or test tube, carefully mix 1 part sulfuric acid:46 parts acetone v/v; swirl to mix
    1. Must be prepared fresh
  - ii. Add 500 µL of acetone/sulfuric acid solution to each sample
  - iii. Vortex 10 seconds
  - iv. Incubate at room temperature for 60 minutes
  - v. Add 400 µL of 0.44mM sodium carbonate solution to stop the reaction; swirl to mix until bubbling ceases
  - vi. Add 1 mL of saturated sodium chloride solution
  - vii. Add 1 mL of ethyl acetate
  - viii. Vortex vigorously for 15 seconds

- ix. Allow tubes to incubate 2 minutes or until the two layers are fully separated
  1. If bottom layer has a lot of bubbles, add an additional 400  $\mu\text{L}$  of 0.44mM sodium carbonate solution
- x. Using a glass pipette tip with the Drummond pipet-aid, carefully transfer the top organic layer to a labeled microcentrifuge tube
  1. The top layer should be  $> 1$  mL
- xi. Evaporate to dryness under air flow at room temperature
  1. Drying takes approximately 45 minutes – 1 hour
  2. The dried samples are usually white powder
  3. Breakpoint; samples can sit at 4  $^{\circ}\text{C}$  overnight before proceeding
- xii. In a glass vial or test tube (I.I.c.), prepare a 2:1 solution of propionic anhydride:pyridine; swirl to mix
  1. Must be prepared fresh
- xiii. Add 150  $\mu\text{L}$  of propionic anhydride/pyridine solution to each sample; scrape powder with tip to dissolve and pipette up and down to mix
- xiv. Incubate for 30 minutes at 60 $^{\circ}\text{C}$  on the heating block
- xv. Centrifuge for 30 seconds at 14,000 rpm to remove condensation
- xvi. Evaporate samples to dryness under air flow at 60 $^{\circ}\text{C}$ . Takes around 20-30 minutes
- xvii. Dissolve the samples in 100  $\mu\text{L}$  ethyl acetate
- xviii. Centrifuge 10 minutes at 14,000 rpm to remove solid debris
- xix. Transfer supernatant to a GC injection vial containing a 150  $\mu\text{L}$  glass insert
  1. Close vials tightly and store at -20 $^{\circ}\text{C}$

## MOX-TBDMS derivatization of metabolite extracts

### 1. Introduction

This protocol describes the derivatization of intracellular metabolites for subsequent GC/MS analysis.

### 2. Required Materials and Equipment

- MOX reagent (Pierce Biotechnology, product# 45950)
- TBDMS: MTBSTFA + 10% TBDMCS, 1 mL ampules (Pierce Biotechnology, product# 48927)
- 2 mL amber glass injection vial
- 150 uL insert for injection vial
- Evaporator (Pierce Reacti-Vap)
- Sonicator
- Heating block

### 3. Sample preparation

- Dry frozen sample under air flow at room temperature (approximately 60 min)

### 4. MOX derivatization protocol

- Dissolve dried sample in 50 uL MOX reagent
- Spin samples for 30 seconds at 14,000 rpm
- Place in sonication bath for 30 min. at room temperature
- Spin samples for 30 seconds at 14,000 rpm
- Incubate for 90 min. at 40 °C on a heating block

### 5. TBDMS derivatization protocol

For TBDMS:

- Add 70 uL of MTBSTFA +1 % TBDMCS directly into the sample, pipette up and down to mix
- Spin samples for 30 seconds at 14,000 rpm
- Incubate for 30 min. at 70 °C on a heating block
- To drive the reaction to completion, leave samples at room temperature overnight

### 6. Preparation for GC/MS

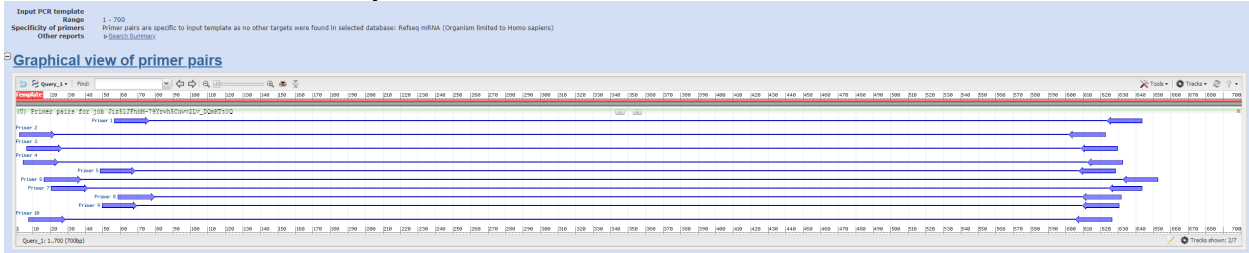
- Centrifuge for 5 min at 14,000 rpm to remove solid debris
- Transfer liquid to injection vial containing a 150 uL microvolume insert







- Click 'get primers' and the program will design the top primers based on optimizing  $T_m$ , GC%, and self-complementarity. The primers will vary in length. Typically, any of these top primers should work sufficiently.



**Detailed primer reports**

Primer pair 1	Sequence (5'→3')	Template strand	Length	Start	Stop	$T_m$	GC%	Self complementarity	Self 3' complementarity
Forward primer	TCGGCTTCGACCCCTCAGTT	Plus	20	67	86	60.18	55.00	3.00	0.00
Reverse primer	CCTCTTAGCACCCTCCACAT	Minus	20	643	624	59.46	55.00	3.00	2.00
Product length	587								
Primer pair 2	Sequence (5'→3')	Template strand	Length	Start	Stop	$T_m$	GC%	Self complementarity	Self 3' complementarity
Forward primer	CAAGGCTAAGGGGAGAACC	Plus	20	3	22	59.74	60.00	3.00	2.00
Reverse primer	CACAGCAGACTAGCAGCTCCGA	Minus	21	622	602	59.93	52.38	2.00	0.00
Product length	620								
Primer pair 3	Sequence (5'→3')	Template strand	Length	Start	Stop	$T_m$	GC%	Self complementarity	Self 3' complementarity
Forward primer	GCTAAGGGGAGAACCCCTGGA	Plus	20	7	26	60.62	60.00	4.00	1.00
Reverse primer	CCACATGCACACCACATACC	Minus	21	629	609	59.80	52.38	4.00	0.00
Product length	623								

- Order the top primer sequence from IDT. Several primer pairs can be ordered to ensure that they will work properly in PCR and for the cheap cost of ordering primers. Primers will arrive within a couple of days after ordering.

### Performing PCR on Genomic DNA

- Extract DNA from your control sample (Cas9 cell line without any crRNA delivery) and test sample (Cas9 cell line with crRNA delivery), according to the DNA extraction protocol (see protocol). Make sure that the DNA is efficiently dilute in the QuickExtract reagent. Too concentrated DNA will not allow PCR amplification to occur, clog gel lanes, and make pipetting difficult. Too dilute DNA will require an extra concentration step to load enough DNA into each PCR reaction.
- Measure the DNA concentration using the Qubit fluorometer in Lippmann lab.
- Set up a standard PCR reaction according to the Taq polymerase instructions with your designed primers, aiming for ~50 ng per reaction. Scale up the reaction to ensure enough yield at the end (typically 8 Rxns in a PCR tube strip).

	NEB Taq DNA Polymerase with Standard Taq Buffer	
	1 Rxn (50 uL) [uL]	8 Rxn (400 uL) [uL]
10X Standard Buffer	5	40
10 mM dNTPs	1	8
10 uM FP	2	16
10 uM RP	2	16
Genomic DNA	X (~50 ng)	X (~400 ng)
Polymerase	0.25	2
Ultrapure Water	Fill to 50 uL	Fill to 400 uL

4. Perform the PCR reaction on the thermocycler for 30 cycles. Combine the reactions.

Step	Temperature	Time
Initial Denaturation	95C	30 seconds
30 cycles	95C	30 seconds
	58C	30 seconds
	68C	1 minute
Final Extension	68C	5 minutes
Hold	4C	∞

5. Following the PCR reaction, the DNA needs to be cleaned up. This can either be done with a PCR cleanup spin column kit or PCR cleanup gel extraction kit (see protocols).
6. Use the Qubit Fluorometer to measure the concentration of the DNA after cleanup.
7. Perform phenol/chloroform extraction with ethanol precipitation (see protocol) to concentrate the sample according to the following guidelines. A sequence of ~700 bp of purified PCR products should be ~2 ng/uL, in 10 uL of water for ~20 ng of total mass.
8. Add 25 pmol of forward primer in 5 uL of volume to the 10 uL of sample, for a total volume of 15 uL. Mix the solution by pipetting up and down a few times. The samples are now ready to be sent in for sequencing and can be placed in the fridge for storage for up to one week. Freeze in the -20 freezer for long term storage.



#### US & UK PreMixed

In the same tube, mix template (10 µl) and your primer (5 µl) according to the table below. To use a GENEWIZ Universal Primer, simply submit template at the requested concentration in 10 µl. See the Technical Notes section for tips on how to purify PCR products

DNA Type	DNA Length (include vector)	Template Concentration in 10 µl	Template Total Mass	Your Primer Total Picomoles	Premixed Volume* (Template + Your Primer)
Plasmids	<6 kb	~50 ng / µl	~500 ng	25 pmol	15 µl
	6 - 10 kb	~80 ng / µl	~800 ng		
	> 10 kb	~100 ng / µl	~1000 ng		
Purified PCR Products	<500 bp	~1 ng / µl	~10 ng	25 pmol	15 µl
	500 - 1000 bp	~2 ng / µl	~20 ng		
	1000 - 2000 bp	~4 ng / µl	~40 ng		
	2000 - 4000 bp	~6 ng / µl	~60 ng		
	> 4000 bp	Treat as plasmid	Treat as plasmid		

\*If you use a GENEWIZ Universal Primer, submit the required amount of template in 10 µl.

\*For PCR products purified with an enzymatic cleanup protocol (e.g. ExoSAP-IT), a spectrophotometer cannot be used for accurate DNA quantitation. Reaction components, such as degraded primers and nucleotides, will absorb UV light and inflate the calculated DNA concentration. Instead, use the band intensity on an agarose gel relative to that of mass standards to estimate DNA concentration. Alternatively, a fluorometer, which employs a dye that specifically binds dsDNA, can provide accurate quantitation.

## Genewiz Sample Submission

1. Log into Genewiz (create account if you haven't already done so and make sure to contact support to get an educational account for Vanderbilt):  
<https://clims4.genewiz.com/RegisterAccount/Login?returnUrl=https://clims4.genewiz.com//CustomerHome?language=en-US&language=en-US>
2. Click 'PCR Product-Purified.' Select 'PCR Product-Purified' under DNA Type, 'Premix' under Service type, 'same day' for service priority, either 'column' or 'gel extracted' for purification type and input the number of samples. In the chart, type your sample name, select 501-1000 bp under length, and type the name of the primer. Then click save and review.

Home / Sanger Sequencing Download/Upload [New](#) Excel Form Auto Save

Note: **Sameday only due to an institutional upgrade**

DNA Type: PCR Product - Purified  
 Service Type: Premix  
 Service Priority: Same Day  
 Purification Type: Column  
 # of Samples: 1 Add Sample Entry

Order Name: g017 example TCR  
 Order Comments:  
 Special ID:  
 Provision Code:  
 Coupon Code: + +

**SAMPLE SUBMISSION GUIDELINES** 1 To 1 samples of total 1 samples Preview ?

Tube View: ?  
 Plate: 1 ?

Legend: ● Valid ● Invalid

HEAT Columns ? Add Order ? Close All Samples ? Register Samples to Event ? Spreadsheet Functionality Key

Plate	Tube	Sample #	Sample	Length (bp)	My Primer	Genewiz Primer	Selection Tool	Difficult Template	Notes
1	A-1	1	EXAMPLE	501-1000	es80a	es77	es209pbp		

3. Look over the summary sheet then click add to cart.
4. Click 'sample pickup at Vanderbilt University Light Hall 902 by 2:00pm'. Then click 'checkout'.
5. Print two copies of the order form, one is for your records. The other copy is to tape the tube samples to. Fold the sheet in half with the samples and bring to Light Hall a little before 2:00pm. The dropoff box is at room temperature, so it is best to wait to as close to 2:00pm before dropping off to make sure the samples are not left sitting out.
6. Sequencing can take a of couple days to get the results back. When the results are available, an email will be sent to you. Click the link or log onto your Genewiz account to view your results.
7. The results list the QS and CRL from the sequencing. Values of QS over 40 and CRL over 500 are good results with minimal background. Too low of values of QS may require a redo with the difficult sequencing option. If the QS and CRL still fail after a redo, the sample may be bad and this procedure must be performed again to ensure as little background as possible from sequencing.
8. Once the sequences pass the QS and CRL thresholds, download all the files in .ab1 format.

## TIDE Analysis

1. Login to your TIDE profile (create one if you haven't). <http://shinyapps.datacurators.nl/tide/>
2. Begin by typing the name of your data, selecting spCas9, selecting your 20 bp guide sequence, selecting your control sample in .ab1 format and your test sample in .ab1 format.

The screenshot shows the 'Upload Data' section of the TIDE web interface. It contains the following elements:

- Upload Data:** The main heading for the section.
- Title plot (e.g. sample name):** A text input field containing 'G6PC2 Sequence 1 - Clone 4'.
- Guide sequence:** A text input field containing 'GACTCCTGGAGTGTGTTCAA'. Below it is a small instruction: 'Submit 20nt guide sequence upstream of PAM (5'-3)'. There is a small icon in the bottom right corner of the input field.
- Control Sample Chromatogram (.ab1 or .scf):** A file upload area with a 'Browse...' button and a file name 'A6-CT2\_G6PC2A.ab1'. Below the file name is a blue bar with the text 'Upload complete'.
- Test Sample Chromatogram (.ab1 or .scf):** A file upload area with a 'Browse...' button and a file name 'A4-KO4\_G6PC2A.ab1'. Below the file name is a blue bar with the text 'Upload complete'.
- Load Example Data**

3. Click advanced settings to view the alignment window, decomposition window, indel size range, and P-value threshold. The default settings should be sufficient. Click Update View.

**Parameters**

All parameters have default settings but can be adjusted by checking the 'advance settings' box.

Advanced settings

**Alignment window (bp)**

The sequence segment used to align the control and test sample

left boundary

1 100 700

1 71 141 211 281 351 421 491 561 631 700

right boundary

automatically set at breaksite - 10bp

**Decomposition window (bp)**

The sequence segment used for decomposition.  
Default is maximum window possible

1 115 685 700

1 71 141 211 281 351 421 491 561 631 700

**Indel size range**

Maximum size of insertions and deletions modeled in decomposition

2 10 50

2 7 12 17 22 27 32 37 42 47 50

**P-value threshold**

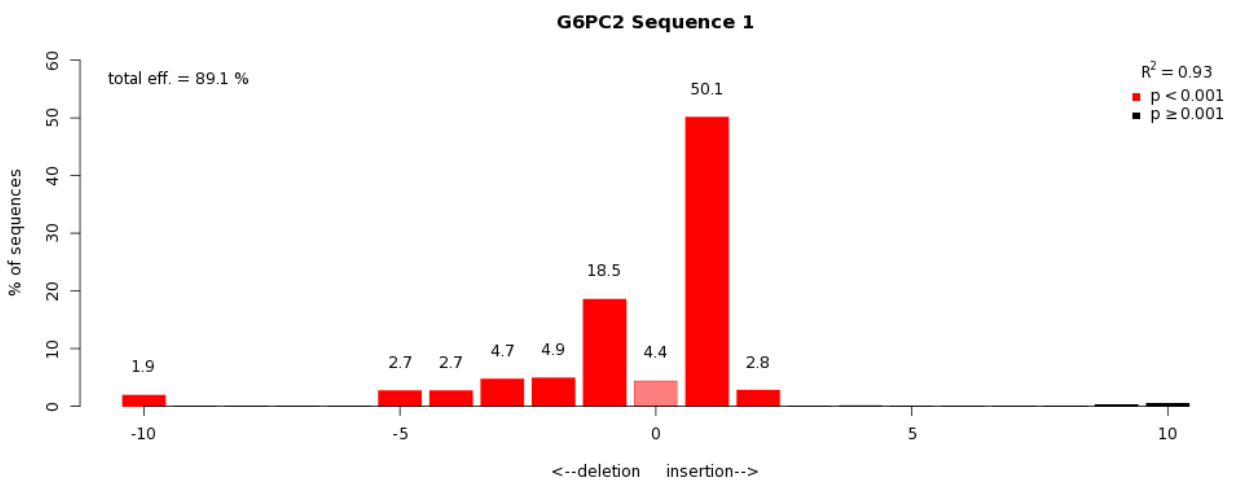
Significance cutoff for decomposition

0.001

Update View

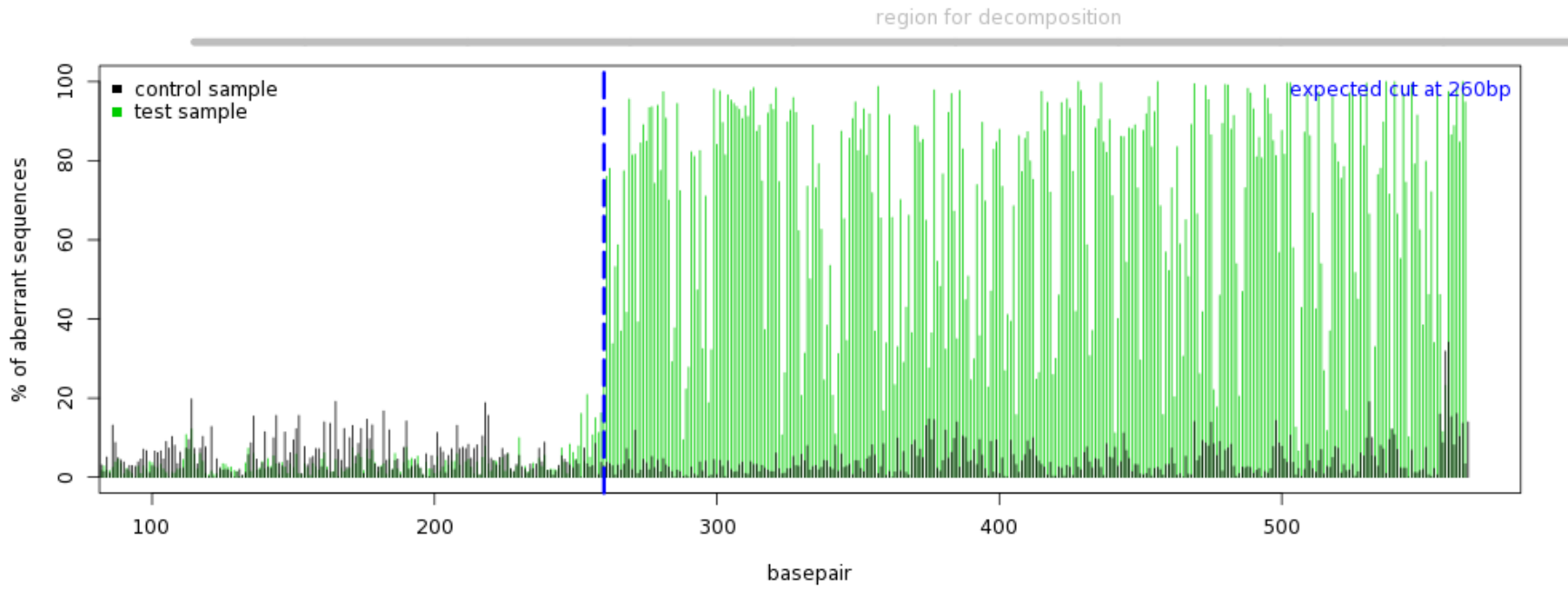
4. The results will then be displayed. The most important information is the efficiency of the indel spectrum. In the following graph, there is an efficiency of 89.1% indel formation, with 11.9% of the sequences showing no difference between the control and test samples. An  $R^2$  value above 0.93 means that the two sequencing files align well and that the data can be trusted

Indel Spectrum



- 5. Other information is generated including quality control to look for aberrant sequence signals, ctrl/edit align to show the sequence that the program uses to align the two files, and quantification of indel frequencies to show the indel spectrum in more detail.

Quality control - Aberrant sequence signal



Ctrl align: GACTCCTGGAGTGTGTTCAA  
edit align: GACTCCTGGAGTGTGTTCAA

### Quantification Indel Frequencies

overall efficiency = 89.1 %

<b>percentage</b>	<b>pvalue</b>
1.90	3.1e-05
0.00	1
0.00	1
0.00	1
0.00	1
2.70	2.3e-09
2.70	3.8e-09
4.70	1.5e-25
4.90	2.4e-27
18.50	0
4.40	4e-22
50.10	0
2.80	8e-10
0.00	1
0.10	0.89
0.00	1
0.00	1
0.00	1
0.00	0.97
0.30	0.57
0.50	0.29